Investigation of the nuclear structure of ^{69}As and ^{69}Se with the EUROBALL spectrometer

Inaugural-Dissertation
zur
Erlangung des Doktorgrades
der Mathematisch-Naturwissenschaftlichen Fakultät
der Universität zu Köln

vorgelegt von
Irina Stefania Stefanescu
aus Radomiresti, Rumänien

Köln 2004

Abstract

Excited levels in the nuclei ^{69}Se and ^{69}As were studied using the reaction ^{40}Ca(^{32}S,2pn)^{69}Se and ^{40}Ca(^{32}S,3p)^{69}As, respectively, at 95 and 105 MeV beam energy. γ rays were detected with the EUROBALL spectrometer operated in conjunction with the Neutron Wall and the charged-particle detector array EUCLIDES. New level sequences with positive and negative parity were identified from *particle*-$\gamma\gamma$ and $\gamma\gamma\gamma$ coincidences. The level scheme of ^{69}Se was extended with 21 new levels and 50 new transitions. In ^{69}As, 50 new levels and 70 new transitions were newly identified. Spins were assigned to many of the levels on the basis of angular distributions and directional correlation of oriented states (DCO).

The excitation energies of the positive-parity yrast bands in both nuclei are compared with the predictions of the Rigid Triaxial Rotor plus Particle model (RTRP). The model reproduces very well the properties of the yrast states in ^{69}Se such as the signature splitting, excitation energies and branching ratios only when a substantial deviation from axial symmetry is taken into account. The calculations with fixed shape parameters in ^{69}As could not reproduce the $15/2^+$ yrast state above the $17/2^+$ yrast state, suggesting a change in shape or γ-softness in the low-spin region.

The high-spin bands in both nuclei are discussed within the Cranked Nilsson-Strutinsky (CNS) formalism. The model predicts that the yrast line in ^{69}Se is dominated by the competition of triaxial-prolate and triaxial-oblate minima which survive separately up to high rotational frequencies. The observed bands are believed to correspond to such minima. The positive-parity bands are interpreted as $\pi(g_{9/2})^2\nu(g_{9/2})^3$ configurations whereas $\pi(g_{9/2})^2\nu(g_{9/2})^2$ configurations are associated to the negative-parity bands. Configurations of type $\pi(g_{9/2})^1\nu(g_{9/2})^2$ and $\pi(g_{9/2})^2\nu(g_{9/2})^3$ are proposed for the positive-parity bands in ^{69}As. For the negative-parity bands, configurations of $\pi(g_{9/2})^2\nu(g_{9/2})^2$ and $\pi(g_{9/2})^1\nu(g_{9/2})^3$ nature are proposed. Experimental bands have been observed in both nuclei up to spin values very close to those predicted by the theory for their respective terminations.

Zusammenfassung

Die angeregten Zustände in den neutronenarmen Kernen ^{69}Se und ^{69}As wurden mittels der Compoundkernreaktionen ^{40}Ca(^{32}S,2pn)^{69}Se bzw. ^{40}Ca(^{32}S,3p)^{69}As bei den Strahlenergien 95 und 105 MeV untersucht.
Die γ-Zerfälle wurden mit dem EUROBALL-Spektrometer beobachtet. Die evaporierten Neutronen und geladenen Teilchen wurden mit der Neutronenwand und dem EUCLIDES-Detektorensystem identifiziert.

Es wurden $Teilchen - \gamma\gamma$ und $Teilchen - \gamma\gamma\gamma$-Koinzidenzen ausgewertet.
Das Termschema des ^{69}Se konnte um 21 neue Niveaus und 50 neue γ-Übergänge erweitert werden. Für den Kern ^{69}As wurden 50 neue Niveaus und 70 neue γ-Übergänge gefunden. Mit Hilfe von DCO-Verhältnissen und Winkelverteilungsanalysen konnten die Spins der meisten Zuständen bestimmt werden.

Die Eigenschaften der $g_{9/2}$ Yrastbande in ^{69}Se lassen sich mit dem starren triaxialen Rotor-plus-Teilchen-Modell sehr gut beschreiben. Die Signaturaufspaltung zwischen favorisierten und unfavorisierten Zuständen konnte zur Bestimmung des Deformationsparameters γ genutzt werden. Ein Fit mit axialer Symmetrie konnte im Rahmen dieses Modells keine akzeptablen Ergebnisse liefern.

Das Modell kann auch die Niveauenergien der entkoppelter $g_{9/2}$ Bande in ^{69}As gut beschreiben. Die richtige Reihenfolge der Niveaus liess sich aber nicht reproduzieren.

Die Hochspin-Rotationsbanden und die speziellen Nukleonenkonfigurationen, auf denen sie aufbauen, wurden im Rahmen des Cranked-Nilsson-Strutinsky Modells untersucht. Das Modell sagt vorher, dass die Zustände nahe der Yrast-Linie in ^{69}Se von konkurrierenden Minima in den Potentialfläche mit triaxial-prolater und triaxial-oblater Form, die bis zu hohe Rotationsfrequenzen stabil bleiben, dominiert werden. Die Banden positiver Parität werden als $\pi(g_{9/2})^2\nu(g_{9/2})^3$ Konfigurationen interpretiert, während der Banden negativer Parität die Konfigurationen $\pi(g_{9/2})^2\nu(g_{9/2})^2$ zugeordnet werden.

Die Konfigurationen $\pi(g_{9/2})^1\nu(g_{9/2})^2$ und $\pi(g_{9/2})^2\nu(g_{9/2})^3$ werden für die Banden positiver Parität in ^{69}As vorgeschlagen. Der Banden negativer Parität werden die Konfigurationen $\pi(g_{9/2})^1\nu(g_{9/2})^3$ und $\pi(g_{9/2})^2\nu(g_{9/2})^2$ zugeordnet. In beiden Kernen konnten die Banden experimentell bis zu Spins beobachtet werden, die nahe bei dem theoretisch vorhergesagte Bandenabschluss liegen.

Contents

Chapter 1

Introduction

Since many years, nuclear structure studies focused on the nuclei in the A$\sim$70 mass-region due to their complex structure ([Ham76, Lim81, Wio88a, Her95, Bec97, Bru00, Rai02]).

These nuclei have long been proposed as good candidates for well-deformed oblate rotors ($\beta_2 \sim -0.35$) due to the presence of the N, Z=34, 36 shell gap at oblate deformations. Indeed, well-deformed oblate shapes have been suggested from lifetimes measurements [Hee86] and angular distribution information [Wio88a] in the very light selenium nuclei.

Competing oblate and prolate structures are also predicted to be favored in this region, due to the presence of the shell gaps at nucleon numbers 34 and 38, corresponding to well-deformed prolate minima ($\beta_2 \sim 0.3 - 0.4$). Adding or removing few nucleons, can, therefore, have a dramatic effect on the nuclear shape.

Experimental evidence for shape-coexistence at low spins comes mainly from the study of the positive-parity bands in the even-even nuclei. It consists of the observation of low-lying excited 0^+ states, which can be interpreted as the "ground state" of a different shape. First evidence for such a state was reported in ^{72}Se by Hamilton *et al.* [Ham74]. The identification of similar low-lying 0^+ states in ^{72,74}Kr nuclei [Bou03, Cha97] and the irregularities observed at the bottom of the rotational bands in ^{68,70}Se [Lis00, Myl89] confirmed the predicted scenario of oblate-prolate shape coexistence in this mass-region.

The study of the $g_{9/2}$ yrast band in the odd-A nuclei offered the best experimental evidence for drastic changes in structure with increasing nucleon number. Investigations revealed positive-parity yrast bands showing decoupling (odd-As and odd-Br isotopes, [Her95, Hel78, Arr90]), weak coupling (^{69}Ge, [Bec97]) or strong coupling (^{69}Se, [Wio88a]). Since the Fermi level for the odd nucleons lies at the beginning of the $g_{9/2}$ orbital in all these nuclei, the different structures of the yrast bands indicate strong polarization effects introduced by the odd-particle.

The advent of heavy-ion accelerators and the new generation of Ge-detectors systems coupled with better data-analysis techniques made it possible to extend the investigation of the structure of the A$\sim$70 nuclei to high spin. Extensive experimental information consisting of quasiparticle alignments, band crossings, shape coexistence and band termination was obtained [Myl89, Sko90, Her92, Bec97, Lis00, Rai02, Ste03].

In the $N \approx Z$ even-even nuclei, where the protons and neutrons occupy the same orbitals, simultaneous alignment of protons and neutron was observed [Fis03], in agreement

with the theoretical predictions [Pet2, Pet02, Wys01]. The identification of high-spin states in the odd-even and odd-odd nuclei allowed to study the blocking effect introduced by the odd-particles [Bru00, Jen01, Jen02].

The coexistence of different shapes in the same nucleus was found to play an important role at high-spin as well. In ^{70}Se, two negative-parity high-spin bands were recently observed and they were interpreted to correspond to two distinct minima in the potential-energy surface [Rai02].

Recently, Plettner *et al.* [Ple00] and Ward *et al.* [War00] reported the observation of terminating bands in ^{73}Br and ^{68}Ge, respectively. Their results established this phenomenon in the A$\sim$70 mass-region for the first time and showed that the progress in the experimental techniques made it possible to investigate shape competition at the highest excitation energy and angular momentum.

Despite the intensive experimental and theoretical efforts, there are still difficulties in understanding the complex structure of the nuclei in the $A \sim$70 mass-region. These difficulties arise mainly from the incomplete experimental information about the structure of several nuclei. There are still nuclei whose experimental bands could be observed only in a very limited spin range and information about the electromagnetic properties of the corresponding states is missing. Among these are the ^{69}Se and ^{69}As nuclei.

^{69}Se is the first nucleus in the A$\sim$70 mass-region which was found to exhibit an oblate deformation at low-spin [Wio88a]. The principal features of the level scheme reported in that work included a band consisting of two $E2$ transitions and four competing mixed $M1/E2$ transitions built on an isomeric $9/2^+$ state. The oblate deformation has been determined from the sign of the measured mixing ratio of the lowest $E2/M1$ member of the $g_{9/2}$ band. Due to the poor statistics, the $g_{9/2}$ oblate band identified in Ref. [Wio88a] could only be observed up to spin $17/2^+$. Within the same work, information has also been obtained on the negative-parity states.

Recently, high-spin states in ^{69}Se have been reported by Jenkins and coworkers [Jen01]. They extended the previously known $g_{9/2}$ band up to a tentative spin of $(41/2^+)$.

In ^{69}As, the $g_{9/2}$ band has been observed for the first time by Hellmeister *et al.* [Hel78]. Their proposed level scheme consists of a favored band extending up to spin $I = 25/2^+$ and an unfavored band consisting of the $11/2^+$ and $15/2^+$ levels. The decoupled character of the $g_{9/2}$ band suggests a prolate deformation at low spin. Later on, Bruce and coworkers [Bru00] managed to extend the yrast band up to spin $37/2^+$. Negative-parity states up to spin $(29/2^-)$ in ^{69}As have been reported in Ref. [Sef88] and partially confirmed in Refs. [Mit97, Bru00].

There are still multiple problems in ^{69}Se and ^{69}As which were not clarified in the previous works. In both nuclei, the experimental information about low-lying non-yrast states is rather scarce. The study of these states would offer important evidence about the shapes involved at low excitation energies. Furthermore, the ground-state bands were observed only up to spin $21/2^+$ in both nuclei. Their extension beyond this spin value is important because it can provide information about the stability of the deformation of the ground-state bands.

The low-lying negative-parity states in ^{69}Se and ^{69}As were found to consists of se-

quences of levels with irregular spacing, suggesting predominant shell model characteristics and therefore much smaller deformations than those of the positive-parity states. This is somewhat surprising, since in the neighboring nuclei ^{71}Br and ^{71}As rotational negative-parity bands built on the ground-state were identified [Arr90, Fot99]. In ^{71}As, the observed low-lying negative-parity band was found to show properties similar to those of a $f_{7/2}$ band [Fot99]. This orbital approaches the Fermi surface for Z=33 only at large ϵ_2 >0.25 deformations. It will be therefore interesting to search for low-lying negative-parity bands in ^{69}Se and ^{69}As which would help to solve the puzzle of the deformations involved in this part of the level scheme.

Despite the previous intense efforts to extend the level schemes of ^{69}Se and ^{69}As to high rotational frequencies, the information about the high-spin structure in both nuclei is still rather poor: the yrast bands have been observed only in a limited spin range and high-spin near-yrast bands are not yet identified. The investigation of the high-spin states near the yrast line is needed in order to get a better understanding of the shapes and structures involved at high-excitation energies in these two nuclei. Since previous works in the A$\sim$70 mass-region showed that it became possible to reach the terminations of the yrast bands, it will be of a great interest to find experimentally the limit of the discrete nuclear states in ^{69}Se and ^{69}As and to investigate the effects of reducing the pairing correlations at high angular momentum.

The open questions mentioned above can be answered only by performing detailed measurements employing heavy-ion fusion-evaporation reactions and beam energies which should contain sufficient information to allow the construction of unambiguous γ-ray decay schemes. For establishing the long deexcitation cascades, a high efficiency and high resolution detection system is required. Since such heavy-ion reactions populate several nuclei, in order to improve the selectivity of the reaction channel of interest, the γ-ray detector array must be operated in conjunction with neutron and charged-particles detectors.

The present work reports the results obtained from the analysis of two EUROBALL+EUCLIDES+NWALL experiments, concerning the level-structure of the nuclei ^{69}Se and ^{69}As. The reaction used to populate these nuclei was ^{32}S + ^{40}Ca at 95 and 105 MeV beam energies. In the experiment at 95 MeV a foil of 1 mg/cm^2 of enriched 99.9% ^{40}Ca evaporated onto a 15 mg/cm^2 gold backing was used. In the second experiment, performed at 105 MeV, the target consisted of a 860μg/cm^2 selfsupporting foil of enriched 99.965% ^{40}Ca. Population at low beam energies should allow the low-lying sequence to be established and ordered, while population at higher beam-energies should allow the cascades to be extended to higher angular momenta.

A detailed description of the experimental devices and techniques used in the present work is given in chapter 2. The experimental results obtained from the analysis of the data acquired in the two experiments are presented in chapter 3.

The extension of the level scheme of ^{69}Se and ^{69}As not only expands the experimental knowledge of these nuclei, but also gives a significantly more precise test of theoretical predictions. The A$\sim$70 mass-region represents not only an experimental but also a theoretical challenge. Many models have been proposed over the years for describing this complex area of the nuclear structure. None of the models can offer a complete descrip-

tion of the observed properties in the nuclei in this mass-region. A short presentation of the most important theoretical approaches used and their limitations is presented in chapter 4. In the second part of chapter 4, the low-lying positive-parity states in ^{69}Se and ^{69}As are compared with the predictions of the Rigid Triaxial Rotor plus Particle (RTRP) model. The high-spin rotational bands are discussed in the framework of the Cranked Nilsson-Strutinsky (CNS) formalism. By applying the RTRP model one may hope to gain some physical insight and certainly, it is interesting to see to what extent a simple phenomenological model which proved its success in other mass-regions can describe the complicate structure of these two nuclei. Furthermore, by comparing the experimental data with the predictions of the CNS model, important information concerning the shapes and single-particle structures of the high-spin rotational bands can be obtained.

Chapter 2

Experimental Techniques

2.1 Fusion-evaporation reactions

In studies of high-spin states one obviously searches for reactions which transfer to the nucleus the highest possible angular momentum l with the largest possible cross-section σ. It was found that fusion evaporation reactions provide the most efficient way to achieve this. Such a process usually produces compound nuclei which are highly excited, with a large amount of angular momentum. On formation, the energy of the compound nucleus is above the particle emission threshold, and consequently, the decay from hot state to cold residual nuclei is initially dominated by statistical particle emission, each nucleon taking away the order of 5 MeV from the excitation energy, but each taking only about $1\hbar$ of angular momentum. These particles are evaporated approximately isotropically in the center of mass frame of reference. After the evaporation of a number of particles, the recoiling nuclei have cooled in terms of excitation energy, but they still retain the high internal angular momentum. This is ideal for the study of the high spin states in the reaction product nuclei. Below the particle separation energies, statistical γ-ray emission dominates, until, at lower excitation energy, the nature of the states changes from continuum to discrete, e.g. states quantum mechanically well defined. The nuclei complete their decay to the ground state by γ-ray emission from these discrete states. The states which are preferentially populated in this type of decay are yrast or near yrast. Figure 2.1 presents the sequence of the decay of the compound nucleus to the ground state, in terms of energy and spin.

For near stable and neutron-rich compound nuclei, neutron evaporation is favored over charged particle evaporation due to the Coulomb barrier in the nucleus. For very neutron deficient compound nuclei, the separation energy of the protons is less than that of the neutrons, making energetically favorable to evaporate protons or α-particles. Thus, the production cross-sections for nuclei coming out of reaction channels containing neutrons are much lower than those of the nuclei obtained by evaporating charged particles from the compound nucleus.

In the present work, the excited states in ^{69}Se and ^{69}As were populated via the ^{32}S + ^{40}Ca reaction at 95 and 105 MeV beam energy delivered by the VIVITRON accelerator of the IReS Strasbourg. In the experiment at 105 MeV, the target consisted of a 860 μg/cm^2 self-supporting foil of enriched 99.965% ^{40}Ca. In the second experiment, performed at 95

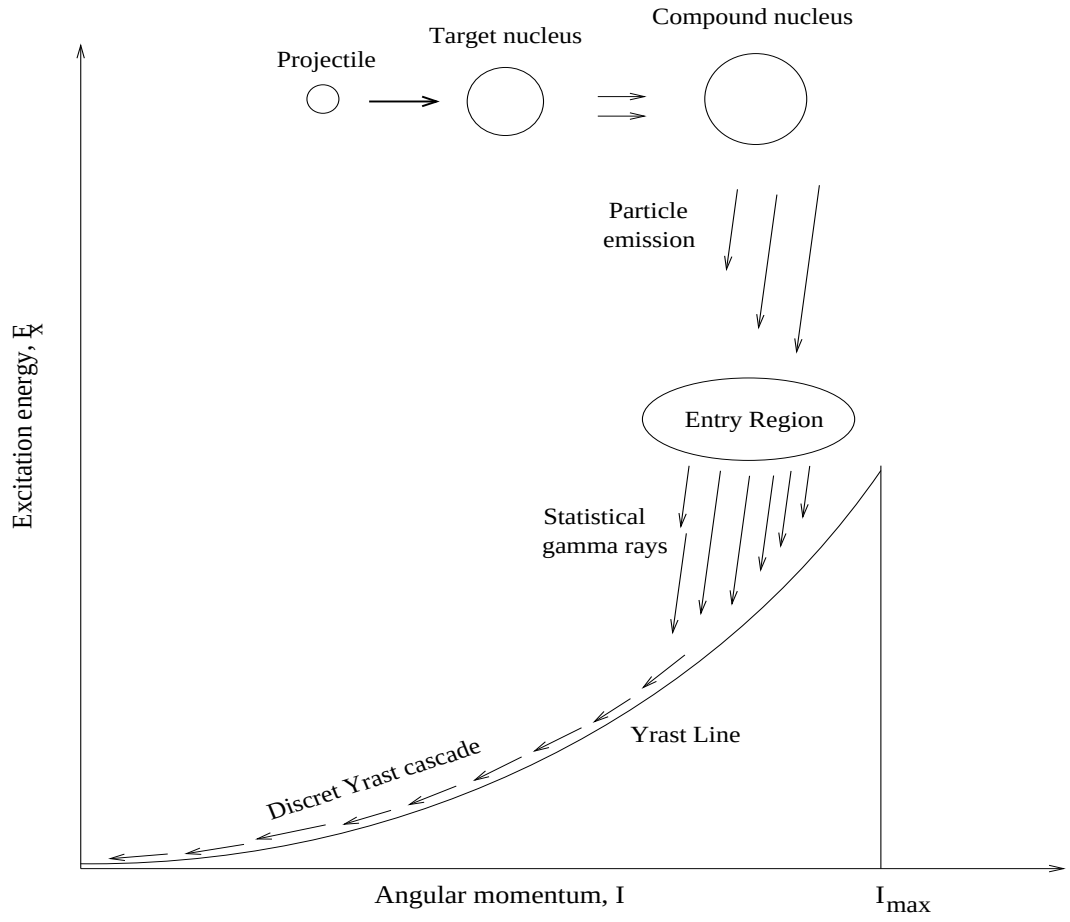

Figure 2.1: *Decay of a compound nucleus obtained in fusion-evaporation reactions to the ground state of a residual nucleus.*

MeV, a foil of 1 mg/cm^2 of ^{40}Ca (99.9%) evaporated on a 15 mg/cm^2 gold backing has been used. The Coulomb barrier in the ^{32}S on ^{40}Ca reaction is V_{coul} ≈81 MeV, and, for beam energies above this value, the reaction leads to the formation of the compound nucleus ^{72}Kr (see 2.2). This target-beam combination has the advantage of using both $N = Z$ beam and target of roughly the same mass, such that the reaction is almost symmetrical in the center-of mass frame. This helps to populate higher angular momentum states. In practical terms, sulphur beams and calcium targets are readily available and permit a reasonable high beam current. The only disadvantage in using calcium targets is that the calcium oxidizes rapidly leading to a contamination of the spectra with γ-rays emitted by the nuclei formed in the reaction ^{32}S + ^{16}O. The degree of oxidation depends on the thickness of the Ca-target. Thus, a special care has to be paid in the analysis of the data, by identifying the contaminant lines among those of interest.

CASCADE [Pul77] calculations predict a maximum in the cross-section around 90-100 MeV for both the $2pn$ (^{69}Se) and $3p$ channels (^{69}As) (see Table 2.3). Allowing for about 5 MeV energy loss of the 105 MeV beam to the center of the 860 μg/cm^2, ^{40}Ca target

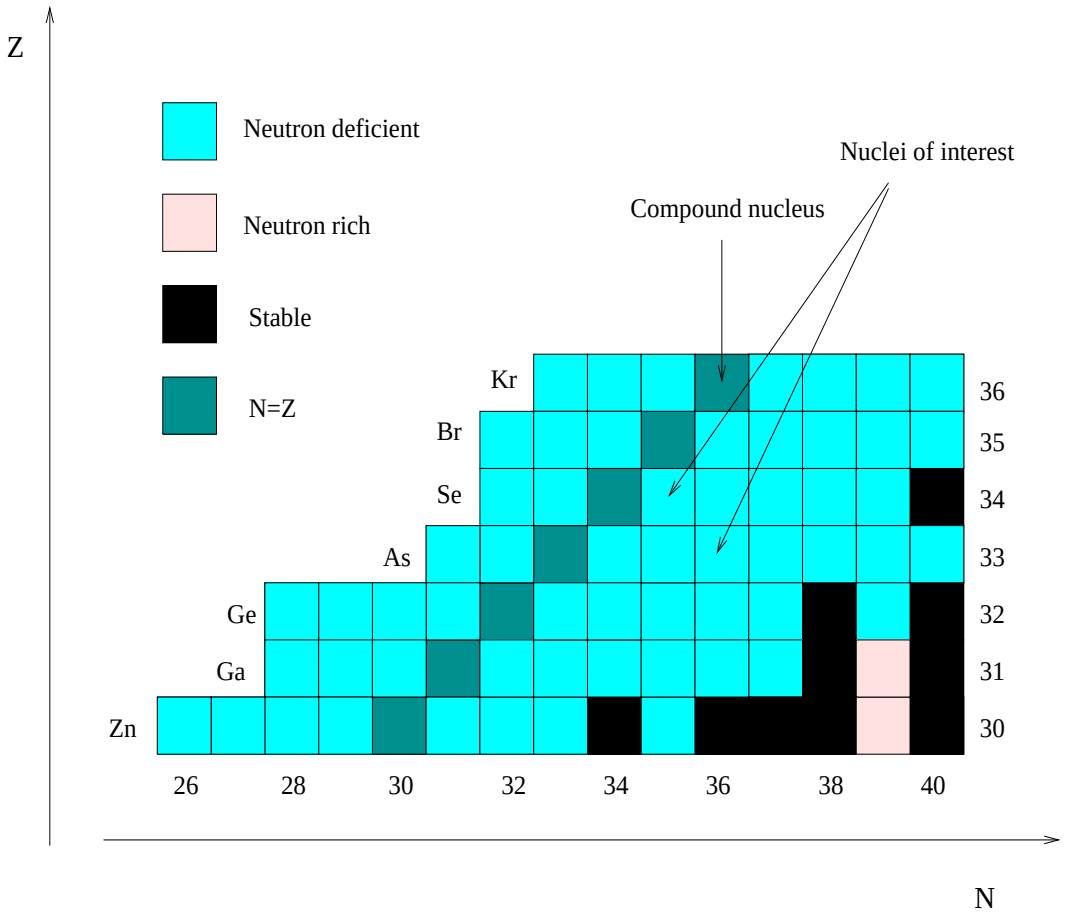

Figure 2.2: *The A∼70 mass-region. The two nuclei of interest to this study are the neutron deficient nuclei* ^{69}*Se and* ^{69}*As.*

used in the first experiment and an energy loss of about 6.4 MeV of the 95 MeV beam to the center of the 1mg/cm^2 target in the second experiment, in both experiments the beam energies have been chosen to optimize the production of nuclei of interest ^{69}Se and ^{69}As at high angular momentum, in order to investigate their high spin structure.

2.2 Experimental setup

The residual nuclei produced by fusion-evaporation reactions are populated at high excitation energies and angular momentum. The number of γ-rays emitted by these nuclei can be large. Typically, a fusion-evaporation reaction in the A∼70 mass-region, opens around 20 reaction channels with varying cross sections from tens of μb up to 150 mb. For a ^{32}S + ^{40}Ca reaction at 105 MeV bombarding energy, the $A \sim 70$ nuclei are expected to be populated at $E^* \sim 50$ MeV excitation energy and to deexcite by emitting γ-rays of multiplicity ∼15 with energies between few keV and 3 MeV. This requires that the detection system has a high efficiency and high energy resolution for the γ-ray detection.

CASCADE Calculation LaTeX Output © F. Seiffert code vers.: F. Pühlhofer, Nucl.Phys.A 280(1977)267									Target: **40Ca** Projectile: **32S**			
Date of calc: 20030505					Compound Nucleus: 72Kr			Vcoul.= 81.15 MeV			Lcrit.= 44$\hbar$	
E	[MeV]	70.00	75.00	80.00	85.00	90.00	95.00	100.00	105.00	110.00	115.00	120.00
Cl0	$\hbar$	1.00	1.00	1.00	11.53	18.10	22.76	26.55	29.79	32.66	35.25	37.61
Nuc.	chan.	σ / mb										
70Br	np				0.25	0.33	0.15	0.02	0.05	0.02	0.01	
69Br	2np								0.01	0.01	0.01	
70Se	2p			0.13	1.89	2.59	1.34	0.52	0.24	0.10	0.04	0.14
69Se	n2p			0.54	13.17	19.15	19.24	15.25	6.58	3.92	3.56	2.25
68Se	2n2p								0.62	1.44	1.14	1.42
67Se	nα				0.01							
69As	3p			5.12	76.70	106.79	122.78	98.25	62.74	33.81	23.21	13.63
68As	n3p					12.07	29.15	47.39	65.41	80.30	63.50	52.15
67As	pα				0.31	0.43	0.38	0.32	0.20	0.13	0.01	0.11
67As	2n3p										0.78	1.65
66As	npα				0.10	0.63	1.27	1.46	1.47	1.12	1.03	0.58
68Ge	4p					48.79	77.08	104.67	127.62	141.93	123.01	104.33
67Ge	n4p										18.90	30.44
66Ge	2pα			0.99	21.29	47.12	73.61	83.36	83.04	69.02	58.48	40.92
65Ge	n2pα					1.32	6.24	15.57	29.63	41.30	34.68	31.95
64Ge	2α				0.04	0.11	0.13	0.14	0.15	0.12	0.07	
64Ge	2n2pα										0.58	0.94
63Ge	n2α							0.06	0.16	0.13	0.08	0.18
67Ga	5p										12.37	20.21
65Ga	3pα					11.33	33.42	90.66	156.07	215.05	220.49	219.69
64Ga	n3pα										27.23	55.10
63Ga	p2α				0.77	2.52	5.99	10.96	15.11	18.64	19.53	20.31
62Ga	np2α							0.17	0.64	1.58	2.61	4.02
64Zn	4pα										32.89	59.65
62Zn	2p2α					0.77	5.05	13.76	26.88	49.87	79.28	110.83
61Zn	n2p2α										1.72	2.53
60Zn	3α							0.07	0.23	0.43	0.65	0.86
61Cu	3p2α										2.67	12.56
59Cu	p3α								0.23	0.84	2.77	7.82
58Ni	2p3α										1.02	2.76
σ_{fusion}			0.05	7.45	115.88	256.15	378.57	486.04	580.25	663.40	737.26	802.62

Figure 2.3: *CASCADE calculations for the ^{32}S + ^{40}Ca reaction at different projectile energies.*

High-Purity Germanium (HPGe)-detectors coupled together in arrays constitute powerful tools in the investigation of the high spin states in nuclei. Such detector arrays have been in use for a decade and their development significantly contributed to the observation of new phenomena in the nuclear structure field. The most efficient and sensitive are EUROBALL in Europe and GAMMASPHERE in USA. These arrays are designed to measure efficiently the energies of cascades of γ-rays depopulating the high-spin nuclear

states and the correlations between these γ-rays. Their high total photopeak efficiency and granularity allows the exploitation of high-statistics, high-fold coincidence data. The availability of such large statistics data sets with high-fold coincidence data allows high-fold selection criteria (gates) on γ-ray transitions in order to enhance specific interesting features. Both EUROBALL and GAMMASPHERE can be operated in conjunction with particle detectors improving the selectivity of the reaction channels of interest.

The present experiments have been carried out at the Institut de Recherches Subatomiques (IReS), Strasbourg, France. The EUROBALL spectrometer [Bec92, Sim97] has been used to detect γ-rays from the employed reactions. Charged particles have been detected and discriminated in the silicon ball EUCLIDES [Gad99] encapsulating the target. The detection of the neutrons has been made by using the Neutron WALL (NWALL) [Ske99].

2.2.1 The Euroball Spectrometer

The EUROBALL spectrometer (Figure 2.4) was built by an European collaboration involving France, United Kingdom, Germany, Italy, Denmark and Sweden. It was first operated at the Laboratori Nationali di Legnaro, Italy (1997-1999) and later at the Institut de Recherches Subatomiques (IReS), Strasbourg, France (1999-2003). It consisted of 15 Cluster and 26 Clover composite Ge-detectors each surrounded by a BGO-shield providing Compton suppression. The idea of using composite Ge-detectors is to increase the granularity in order to improve the energy resolution and the photopeak efficiency.

The Cluster detector

The Cluster detector [Ebe93] has been developed in a collaboration of University of Cologne and KFA-Jülich, Germany and the Eurisys company, France. It consists of seven large hexagonal tapered Ge detectors closely packed in a common cryostat (see Figure 2.5). In order to achieve the very close packing, the technique of encapsulating the crystals was developed. The main idea of encapsulation is to decouple the crystal vacuum from the cryostat vacuum, by housing the crystal in a sealed aluminum capsule of wall thickness 0.7 mm with the capsule 0.5 mm from the surface of the crystal. The detector can be handled safely and easily annealed. Its energy resolution at 1332 keV is better than 2.3 keV.

The Cluster detectors are arranged to form the backward 1π shell of EUROBALL at $\sim$44.5 cm from the target, with a total-absorption efficiency of about 4% at E_γ=1.3 MeV. The advantages of using Cluster detectors are:

- their high granularity allows the Doppler broadening in accelerator based experiments to be minimized;
- an improvement of the isolated-hit probability for high multiplicity events.
- a high sensitivity to the linear polarization of gamma-rays;
- improved efficiency by using the cluster detector in add-back mode.

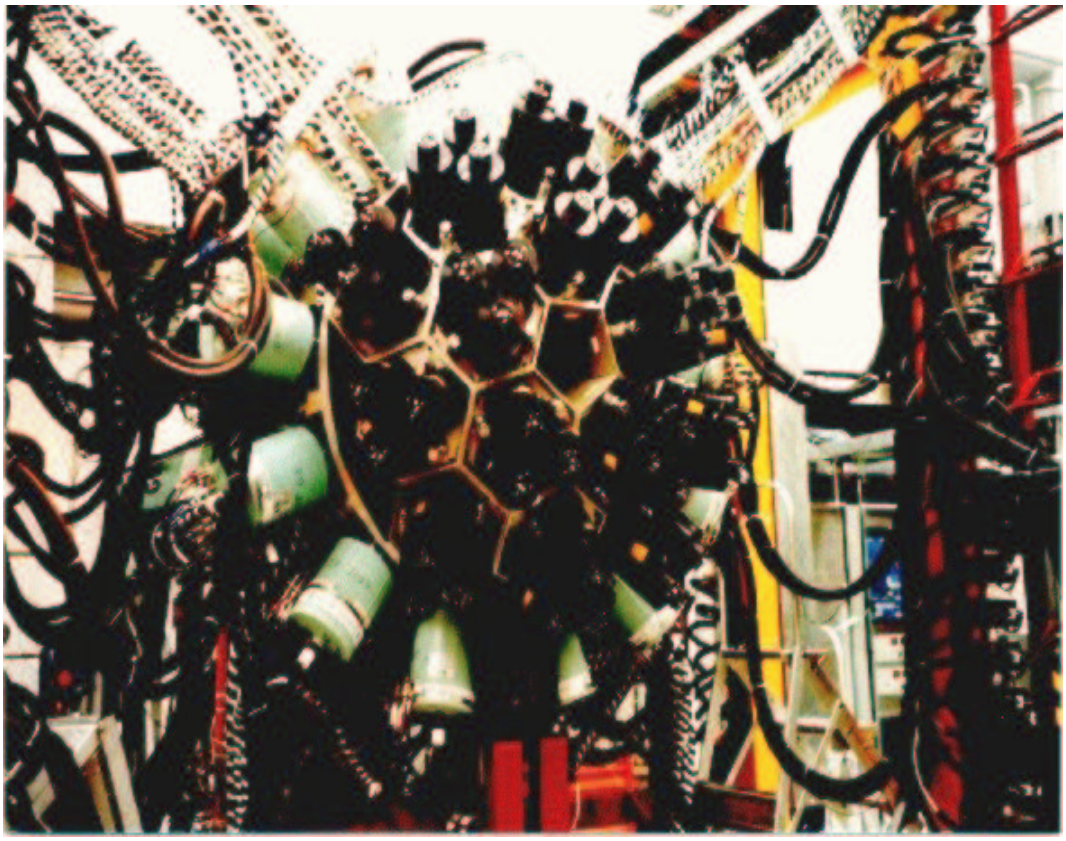

Figure 2.4: *The EUROBALL IV spectrometer at Strasbourg, France. The photograph shows the forward hemisphere of the spectrometer.*

The Clover detector

The Clover detector has been proposed and developed by a France/U.K. collaboration as part of Euroball. It consists of four coaxial n-type Ge crystals arranged in the configuration of a "four-leaf clover", and housed in the same cryostat (see Figure 2.6). To optimize the packing of the crystals the outer faces are tapered at the front. The Clover detectors are arranged to form a 2π shell around the 90° direction to the beam axis and at ~26.5 cm from the target. The total-absorption efficiency is of about 4% at E_γ=1.3 MeV.

The advantages of using Clover detectors are:

- a reduction of the Doppler broadening;
- a high sensitivity to the linear polarization of gamma-rays.
- improved efficiency by using the clover detector in add-back mode.

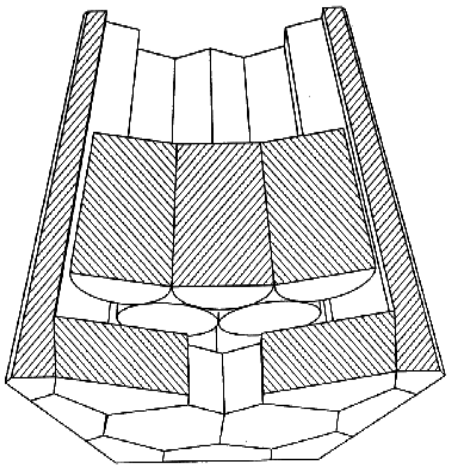

Figure 2.5: *The Euroball Cluster detector.*

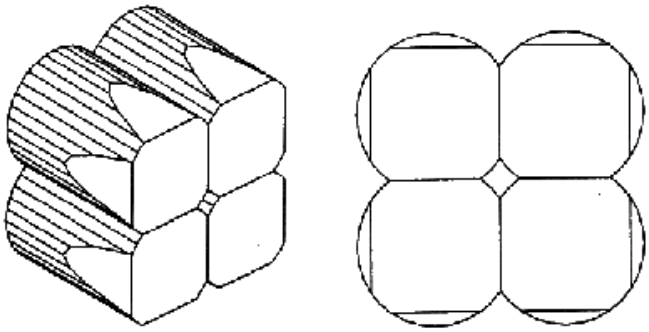

Figure 2.6: *The Euroball Clover detector.*

The BGO shield

To reduce the Compton background, each of the Ge detectors is surrounded by a shield of bismuth germanate scintillator crystals - the BGO crystals. The way in which the Compton suppression works is to detect those γ-rays which are Compton scattered out of the detector before depositing all of their energy. All these "bad" events are vetoed electronically. By using Compton suppression, the peak-to-total ratio for ^{60}Co in the Ge spectrum is improved from $\sim$25% to typically 65%. This improvement in the peak-to-total ratio (PT) is crucial in coincidence spectroscopy. For example, in a doubles ($\gamma - \gamma$ or γ^2) or coincidence experiment, the photopeak-photopeak coincidence probability is

proportional to $(PT)^2$. Therefore, the use of the suppression shield typically results in a improvement of more than a factor of eight in the photopeak coincidences, when compared with the background. Even larger improvements are obtained when higher fold coincidence events are recorded. The improvement are typically a factor of 21 for triples (γ^3), 57 for quadruples (γ^4) and 157 for quintuples (γ^5).

The EUROBALL rings

The 209 Ge-crystals (26×4=104 clover crystals and 15×7=105 cluster crystals) are arranged in 13 rings. The 26 Clover detectors form 4 rings situed at ∼90° about the beam axis. The Clusters are arranged in 9 rings at backward angles between 163° and 123° with respect to the beam axis. In this configuration the total photopeak efficiency is ∼8%.

Table 2.1: The EUROBALL rings and their associated angles. The angle $\theta = 0$ defines the beam axis (z-axis).

Ring no	No of detectors	Type of detectors	Angle
0	10	Clusters (C)	163.46°
1	15	Clusters (C)	155.85°
2	10	Clusters (C)	149.28°
3	5	Clusters (C)	145.72°
4	10	Clusters (C)	141.01°
5	15	Clusters (C)	137.13°
6	10	Clusters (C)	132.79°
7	20	Clusters (C)	129.35°
8	10	Clusters (C)	122.63°
9	26	Clovers (Q)	107.54°
10	26	Clovers (Q)	99.05°
11	26	Clovers (Q)	80.94°
12	26	Clovers (Q)	72.15°

2.2.2 EUCLIDES (EUropean Charged Light Ions DEtector Sphere)

The Si 4π array EUCLIDES is a light charged particle ancillary detector developed and built within a collaboration of the INFN laboratories in Legnaro, Padua and Florence, Italy, as well as the University of Liverpool and the Daresbury Laboratory, England. It consists of 40 silicon $\Delta E - E$ telescopes, 130 μm + 1000 μm thick. The EUCLIDES array is used to detect the evaporated light charged particles (protons and alphas) from

the compound nucleus decay. The five forward elements are electrically segmented in four parts. The segmentation was designed to reduce the probability of multiple hits in one detector. The charged particles are essentially evaporated isotropically in the center of mass system but the nucleus is moving in the laboratory frame in the direction of the beam, resulting in a forward focused cone of recoils in the laboratory frame. There is, consequently, an increased probability of detection at forward angles, requiring an increased granularity. Even though the α-particles have on average higher energy than the protons, they are more forward focused in the laboratory frame due to their lower velocity. The energy lost ΔE by a proton or an alpha particle traveling the Si material is given by the Bethe-Bloch formula

$$\frac{dE}{dx} = \left(\frac{e^2}{4\pi\epsilon_0}\right)\frac{4\pi z^2 N_0 Z\rho}{mc^2\beta^2 A}\left[\ln\left(\frac{2mc^2\beta^2}{I}\right) - \ln(1-\beta^2) - \beta^2\right] \tag{2.1}$$

where $\beta = v/c$ is the velocity of the particle, e is the electric charge, Z, A and ρ are the atomic number, atomic weight and density of the stopping material, z is the proton number of the projectile, N_0 is Avogadro's number, and m is the electron mass. I represents the mean excitation energy of the atomic electrons and it is generally regarded as an empirical constant with a value in eV of the order of $10Z$.

A plot of ΔE versus E will show different loci for different species according to their mass and charge number. This allows for particle identification.

When the Silicon ball is used in conjunction with EUROBALL the channel selectivity, which is of great importance when studying weak reaction channels, is increased considerably.

2.2.3 The Neutron Wall (NWALL)

The Neutron Wall consists of 50 liquid scintillation detectors covering a solid angle of about 1π in the forward direction with respect to the beam direction. The array consists of 15 pseudohexaconical detector units subdivided into three, 149 mm high, hermetically separated segments and a smaller central pentagonal unit subdivided into five segments. The detectors are filled with a BC501A liquid scintillator [Ske99]. Each section of the detectors is viewed by a photomultiplier. When a neutron emitted from the compound nucleus passes through the liquid scintillator, photons are emitted as the neutron excites the atoms within the liquid. This light strikes the photosensitive surface of the multiplier tube, releasing at least one electron per photon. These secondary electrons are then multiplied, accelerated and formed into the output pulse in the photomultiplier tube. Because liquid scintillator detectors are also sensitive to the γ-rays, a good $n-\gamma$ discrimination is required. The $n-\gamma$ separation can be made by a combinations of zero-crossover (ZCO) time signal and the difference in measured time of flight (TOF) of neutrons and γ-rays. Neutrons interact in the detectors mainly by elastic scattering against the protons of the scintillation liquid. When the recoiling protons are slowed down in the liquid, they give rise to a larger proportion of the slow component of the scintillation light than the recoiling electrons, which are produced by γ-ray interactions. This gives rise to a difference in the pulse shape of the anode signal, a difference which is observed as a delayed ZCO time signal for neutrons interacting in the detector compared to γ-rays.

The combination of detectors for neutron and light charged particle detection with efficient γ-ray detector arrays has been proven to be a powerful tool in the spectroscopy of exotic neutron deficient nuclei close to $N = Z$ and the proton drip-line.

A schematic representation of the Euroball experimental set-up used in the present work is represented in Figure 2.7.

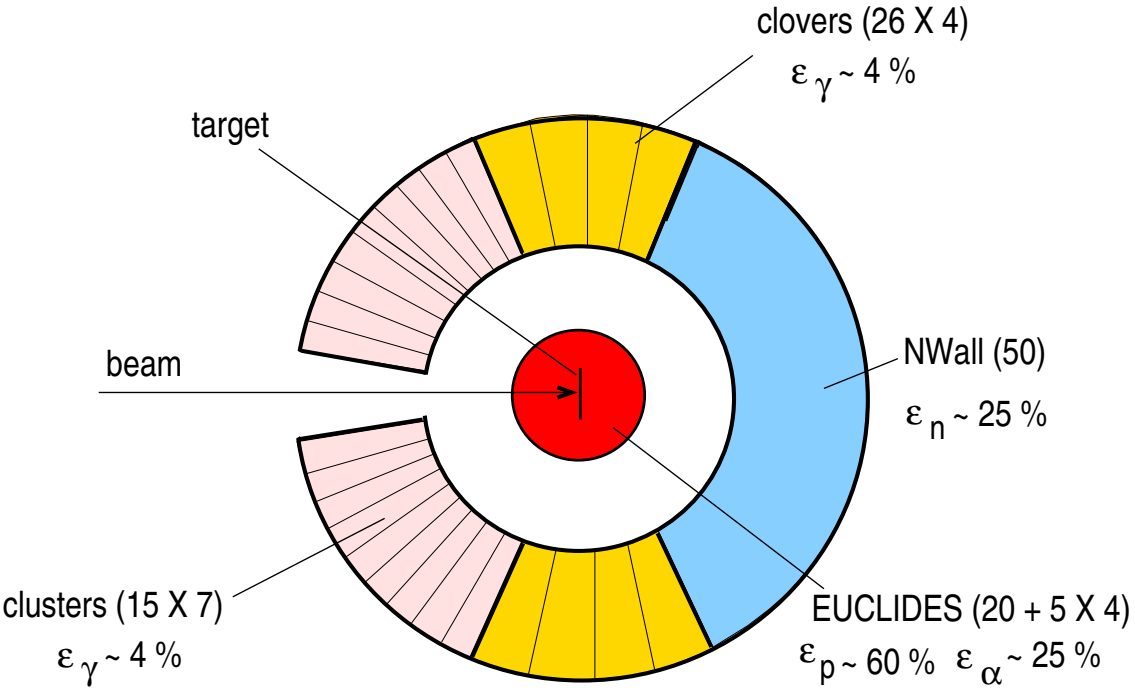

Figure 2.7: *The experimental setup used in the present experiments.*

2.3 Data analysis

Each of the two experiments using the ^{32}S beam at energies 105 and 95 MeV and the ^{40}Ca targets ran for about 6 days. At the end of the beam time a short calibration run using a ^{152}Eu source was performed. The data were stored on magnetic tapes (~560 GB from the experiment at 105 MeV and ~250 GB from the experiment at 95 MeV). The main information written on the tapes consisted of energy (E) and time (T) from the Ge detectors, time-of-flight (TOF) and zero/crossover (Z/C) from the NWALL and energy (E) and the energy loss (ΔE) from the silicon detectors. For the offline sorting the computer package GASPware was used [Bazz97].

The events (trigger) were defined as following:

- a minimum of two Compton-suppressed Ge detectors fired in coincidence with one event (neutron or γ) in NWALL in the experiment performed at 95 MeV;
- a minimum of two Compton-suppressed Ge detectors fired in coincidence with one neutron in NWALL in the experiment at 105 MeV;

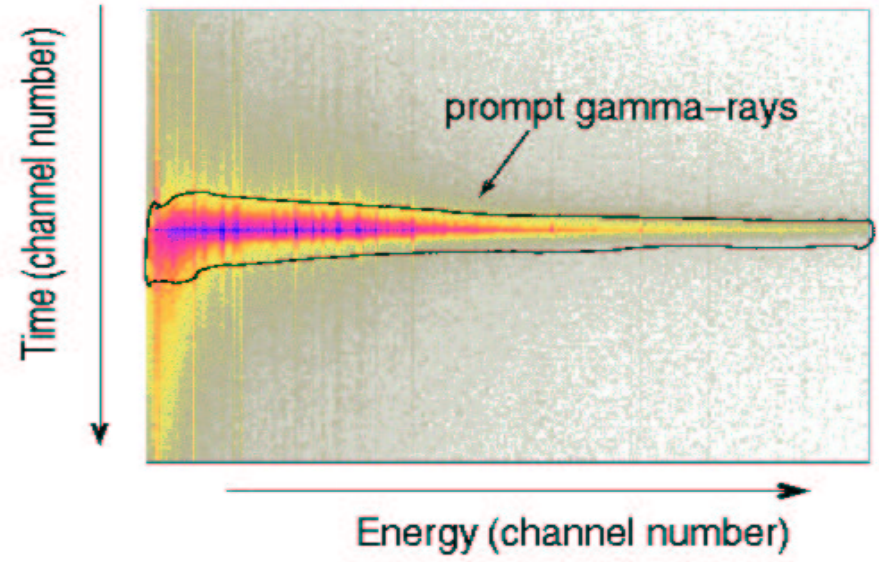

Figure 2.8: *An energy versus time matrix for the Ge-detectors. The contour represents the gate defining the prompt γ-rays.*

- a minimum of three Compton-suppressed Ge detectors fired in coincidence with one event in NWALL in the experiment performed at 105 MeV beam energy.

The first steps in the offline sorting of the data are the gain matching, the Doppler and the add-back corrections and the efficiency calibration.

Gain matching

Gain matching is very important when using detector arrays which consist of a large number of detectors because each detector within the array or each segment of a composite detector has its own set of coefficients used to describe its gain. These gains can change throughout the run time of an experiment. The gains were calculated using data taken from the run with the ^{152}Eu calibration source.

Time gates

The times of the Ge detectors were aligned and the prompt γ-ray transitions were defined using a two-dimensional gate in a Ge-time versus Ge-energy matrix (see 2.8). On the y-axis is given the time difference of the individual Ge-detectors with respect to the centre of gravity of the average time of all Ge-detectors.

The time signals from the EUCLIDES and NWALL were also aligned throughout the experiment. In the final sort of the data, wide gates on EUCLIDES time signals were used.

Doppler correction

Doppler broadening or Doppler shift is the spread in the measured energy due to the Doppler effect caused when gamma rays from moving nuclei are observed using a stationary detector whose opening angle is large enough to accept varying angles of incidence. The effect gets worse as the velocity of the nucleus increases and as the detector size (and hence opening angle seen by the projectile nucleus) is increased. The calibrated γ-rays need to be corrected for the Doppler shift, using the equation

$$E'_\gamma = E_\gamma \left(1 + \frac{v}{c}\cos\theta\right) \tag{2.2}$$

where E'_γ is the energy of the γ-ray emitted from the moving nucleus, E_γ is the energy of the γ-ray emitted from rest, θ is the angle between the detector (ring) position and the beam axis and c is the speed of light. From the equation above, the shift in energy is greatest at forward (0°) and backward angles (180°) with respect to the beam axis.

In the present work, a Doppler correction has been performed for the γ-rays obtained from the experiment using the selfsupporting ^{40}Ca target. The correction has been made by plotting the shifted energy E'_γ against $\cos\theta$ for the E_γ=1098 keV transition in ^{69}As. The θ angles represent the angles of the 13 EUROBALL rings given in Table 2.1. From the slope of the fitting curve (see Figure 2.9) a v/c=2.67% was extracted and further used for an event-by-event correction of the γ-energies.

The Doppler effect affects also the peak resolution (Doppler broadening). Finite opening angles of the Ge detectors, finite target thickness (the energy loss in the target will be different if the reaction occurs at the front of the target than if it occurs at the back) and the effect of evaporated particles (they have different velocities when the particles are evaporated in a forward direction from the compound nucleus than if they are evaporated backwards) induce uncertainties in θ and v/c which causes an uncertainty in E_γ.

The application of the gain matching and Doppler correction procedures for each detector is of vital importance, otherwise photopeaks within the various spectra for single detectors will not be in the same channels thus losing resolution when adding them together.

Add-back correction

The "add-back" correction is a procedure of *add*ing-*back* the energies of γ-ray hits in individual elements within a composite Ge detector system such as an EUROBALL Cluster or Clover. Thus, when the γ-ray scatters from one element to another, thereby depositing its full energy over two or more elements, the energy of the incident γ-ray can be recovered by summing the individual hits together and correcting for Doppler effects appropriately. There are two possible reasons for two capsules of a cluster or clover detector being hit together: either due to two separate γ-rays which is more probable if the reaction has a high multiplicity, or due to scattering from one detector to the other which is more probable for higher γ-ray energies. In a Clover detector there are two types of double hits, whilst higher multiplicity hits are disregarded. For clusters there are also two types of double hit and higher multiplicities cannot be necessarily rejected. In the present work, the add-back

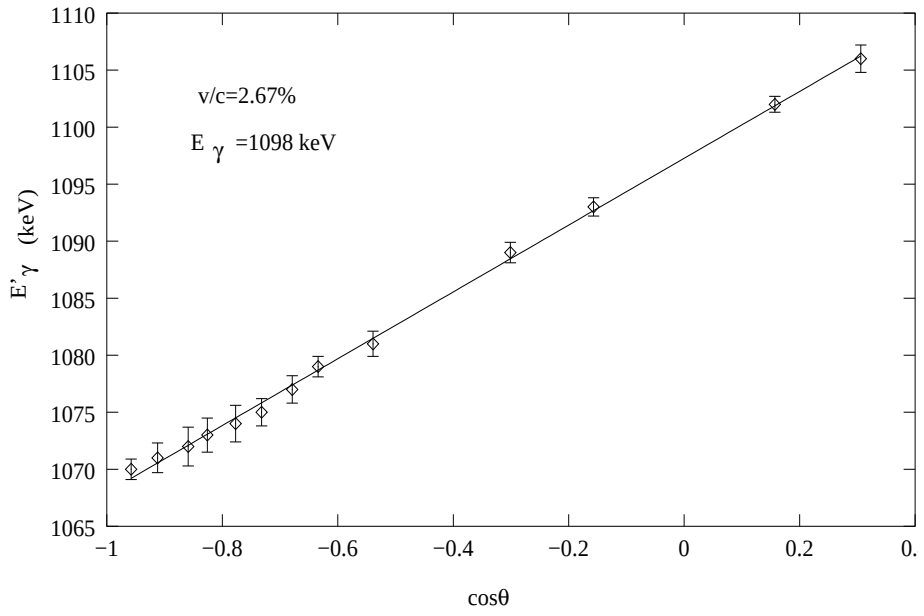

Figure 2.9: *The 1098-keV transition in ^{69}As is detected at 13 different angles corresponding to the 13 EUROBALL rings. The peak is shifted to higher energy at forward angles and to lower energy at backward angles. From the slope of the line which fits the experimental points a value v/c=2.67% is obtained.*

procedure is applied when 2 or 3 neighboring segments of the same composite detector fired in coincidence:

- Clusters
  - all the possible combinations of two neighboring segments; when the two segments are not neighboring, the signals are treated as two different events;
  - combinations of two neighboring segments plus the central one.
- Clovers
  - combinations of two neighboring segments excluding the diagonal case.

In all cases the sum energy is attributed to the segment in which the major energy was released. Applying the addback correction the sensitivity of the array is increased by improving the overall peak-to-total of the device. An example of spectra without and with addback mode, acquired in the experiment at 105 MeV beam energy is given in Fig. 2.11.

Efficiency calibration

Since the detection efficiency for γ-rays changes as a function of γ-ray energy, an efficiency correction is required. In the present work the efficiency corrections were made by using

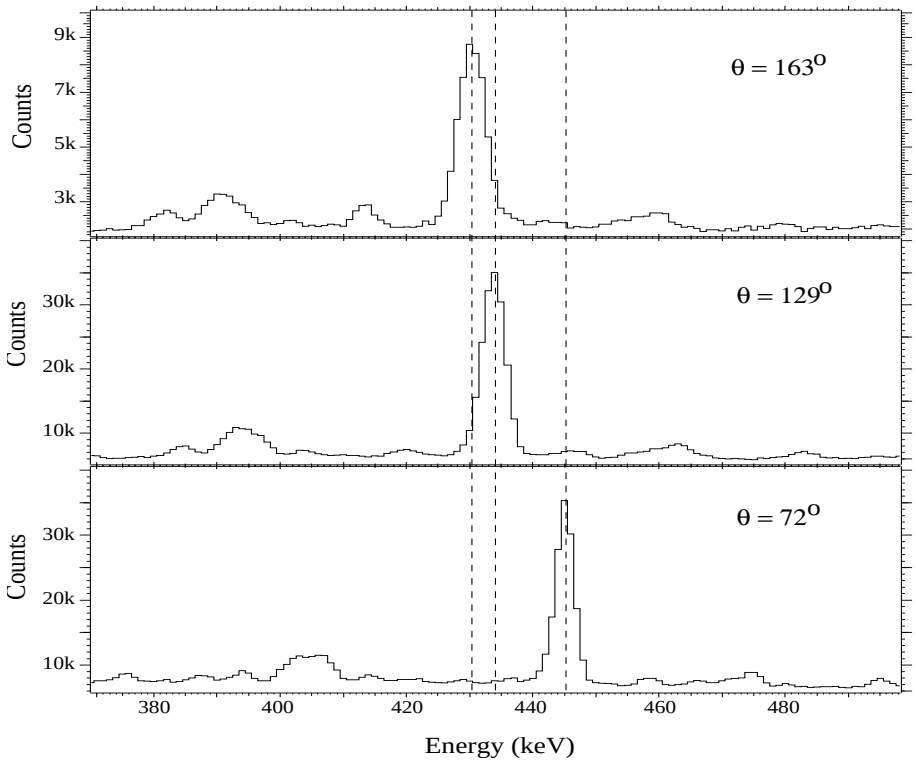

Figure 2.10: *The 442-keV transition in ^{69}As detected at three different angles in EUROBALL. The peak is shifted to higher energy at the forward angle (θ=72°), and to lower energies at backward angles (θ=163°, 129°) of the array.*

the known γ-ray intensities from the ^{152}Eu and ^{56}Co radioactive sources. The efficiency correction was fitted for the relative efficiency ϵ_γ according to [Rad95]:

$$ln(\epsilon_\gamma) = \left[\left(A + Bx + Cx^2\right)^{-G} + \left(D + Ey + Fy^2\right)^{-G}\right]^{-1/G} \tag{2.3}$$

where

$$x = ln\left(\frac{E_\gamma}{100}\right) \tag{2.4}$$

$$y = ln\left(\frac{E_\gamma}{1000}\right). \tag{2.5}$$

In the equation above, E_γ is the γ-ray energy in keV and the $A-G$ are the fit parameters. The parameter G determines the shape of the turn-over region between the high and the low energy efficiency curves.

Figure 2.12 shows the efficiency curve of EUROBALL array. Above ≈100 keV the efficiency decreases steeply as the probability of the photoelectric and Compton effects decreases. At high energies there is a large probability that the γ-rays will not interact with the crystal. Figure 2.13 shows the efficiencies of two different rings of the EUROBALL.

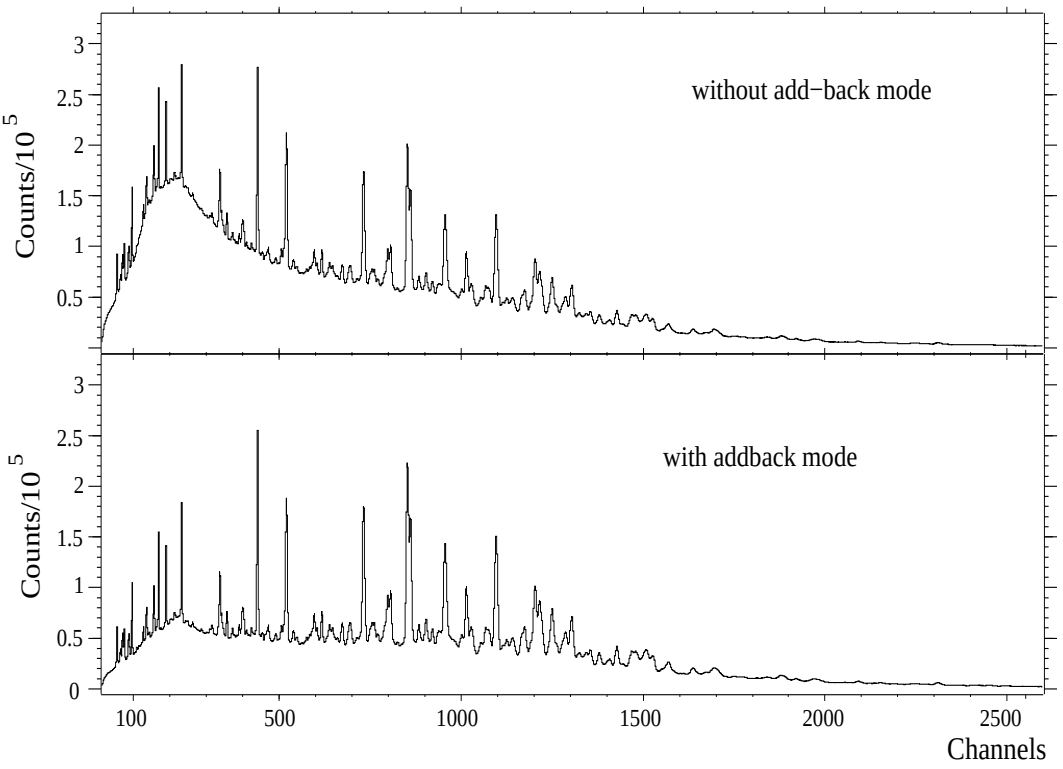

Figure 2.11: *Spectra acquired without (top) and with (bottom) addback mode. The spectra where obtained from the reaction at 105 MeV beam energy.*

The efficiencies of the different rings of the EUROBALL were used when analyzing the angular distribution and directional correlations (DCO) (see subsection 2.4.1).

2.3.1 Channel selection

Due to the statistical nature of the nucleon emission from the compound system, the fusion evaporation reactions tend to populate more than one residual nucleus. Therefore in order to associate a γ-ray with a specific nucleus some form of extra channel selection is required. There are several ways of determining the nucleus which emitted the gamma ray, by the identification of the nucleus itself via a recoil separator, X-ray-γ coincidences or measuring the particles which have been evaporated from the compound system via the use of charged particle balls or neutron detectors.

The EUCLIDES silicon ball and the Neutron WALL detector arrays were used in the selection of the final reaction channel studied. $TOF-ZC$ (see subsection 2.2.3 for details) and $\Delta E - E$ matrices were created for each neutron and silicon detector, respectively. An example of such matrices is presented in Figure 2.14. The top part of the figure presents a typical TOF (time-of-flight) versus ZCO (zero-crossover) matrix for one of the EUROBALL neutron detectors. The matrix was obtained after the calibration of both TOF and ZC spectra for each neutron detector in the ball. A very good discrimination

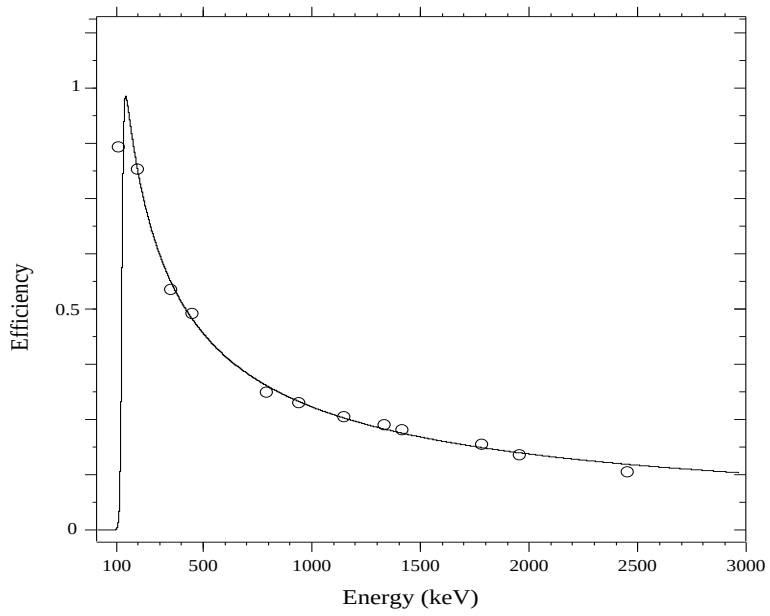

Figure 2.12: *A plot showing how the detector response varies for the EUROBALL array with γ-ray energies. The fit shows the relative efficiency of the array normalized to 1, obtained using ^{152}Eu and ^{56}Co sources.*

between the neutron and gamma ray induced events could be achieved. The bottom part of the Figure 2.14 shows a $\Delta E - E$ matrix for one of the backward silicon detectors. The darker loci at low energies corresponds to the protons. The loci at high energies correspond to the alpha particles. A good discrimination between these two types of charged particles is obtained. Gates are applied to these 2D matrices in order to select events corresponding to different reaction channels. The charged particles reaction channels with a certain multiplicity for protons and alphas were selected by defining offline a multiplicity spectrum by counting all the events with the right fold inside the particle gates.

2.3.2 Coincidence data

Particle gates

A total of about 20 different residual nuclei in the A$\sim$70 mass region were populated in the present experiment (see Table 2.3). According to CASCADE calculations presented in Table 2.3, the most populated nuclei are those coming out of the xp and $xpy\alpha$ channels such as ^{68}Ge (4p), ^{66}Ge (2pα), ^{69}As (3p) and ^{65}Ga (3pα). Figures 2.15 and 2.16 (top) show the total projection spectra obtained from the ^{32}S + ^{40}Ca reaction at 105 MeV and 95 MeV, respectively . The spectra were obtained by projecting the content of the corresponding $E_\gamma - E_\gamma$ matrices onto one axis. While ^{69}As belongs to the nuclei strongly populated by the reaction and its γ-rays predominate the total projection spectra, the γ-rays of ^{69}Se are not easy to identify.

Clearly, the single and double γ-gating and particle identification techniques are

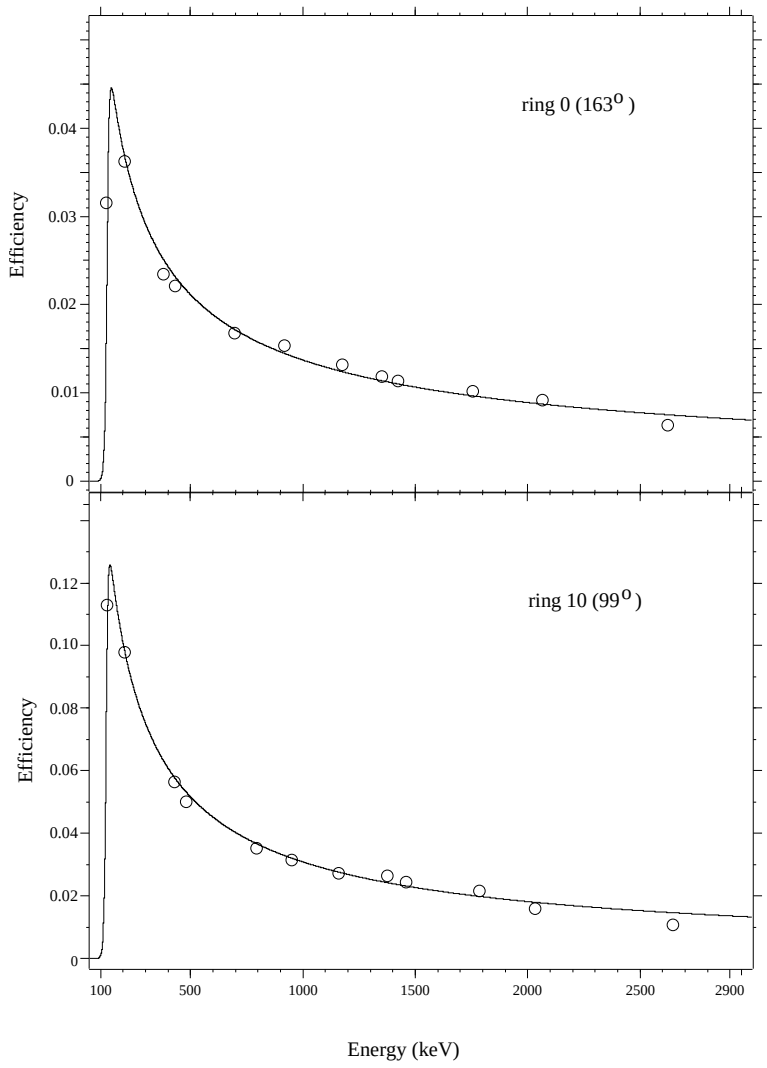

Figure 2.13: *Relative efficiency calibration curves for the most backward EUROBALL ring (ring 0 at 163°) consisting of 10 cluster capsules (top) and for the ring no. 10 (99°) consisting of 26 clover capsules (bottom). The curves were obtained by normalizing to the efficiency of the whole EUROBALL.*

needed in order to clean the spectra and select the channel of interest. An advantage of using the ^{32}S on ^{40}Ca reaction is that in the neutronic channels only two nuclei are produced: the nucleus ^{68}As (3p1n) and one of the nuclei of interest, ^{69}Se (2p1n). The middle spectra given in Figures 2.15 and 2.16 were produced by requiring that 1 neutron is detected in the NWALL in coincidence with 2 protons in EUCLIDES. Demanding one neutron in coincidence with the γ-rays, the peaks from ^{69}Se and ^{68}As are nicely enhanced over those deexciting the nuclei populated from non-neutronic channels. Requiring 3 protons in coincidence with the prompt γ-rays, an improvement of the quality of the ^{69}As data is obtained, as can be seen for the bottom spectra of Fig. 2.15 and 2.16. If the

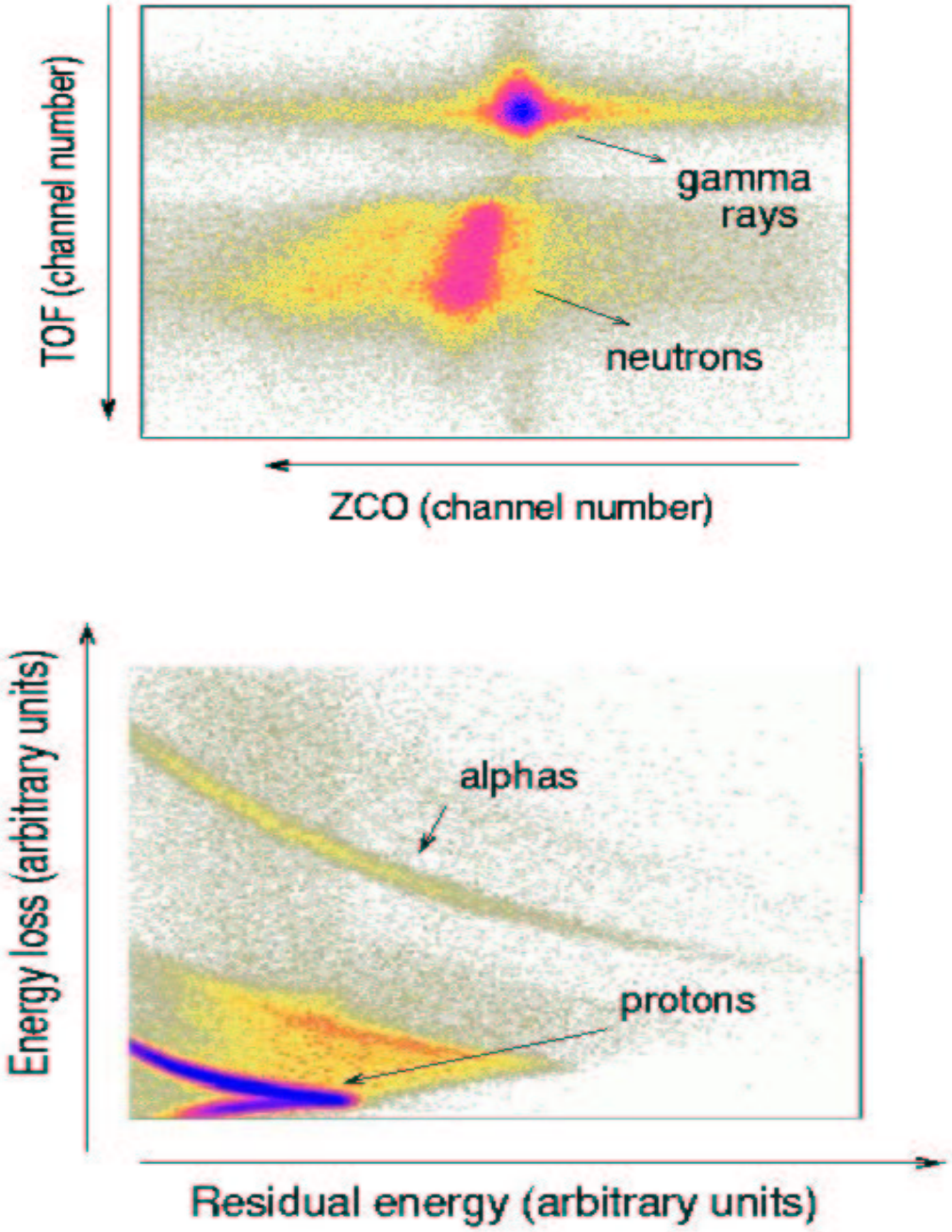

Figure 2.14: *Top: A TOF versus ZCO histogram for the detector number 0 illustrating the very good neutron-γ discrimination achieved with the Neutron Wall. Bottom: An $E-\Delta E$ matrix for the detector number 36 showing the discrimination between protons and alpha particles achieved with EUCLIDES.*

efficiency of detecting neutrons were 100% then the spectra acquired in coincidence with one neutron should contain only γ-rays from ^{69}Se and ^{68}As. Since, in general, the particle

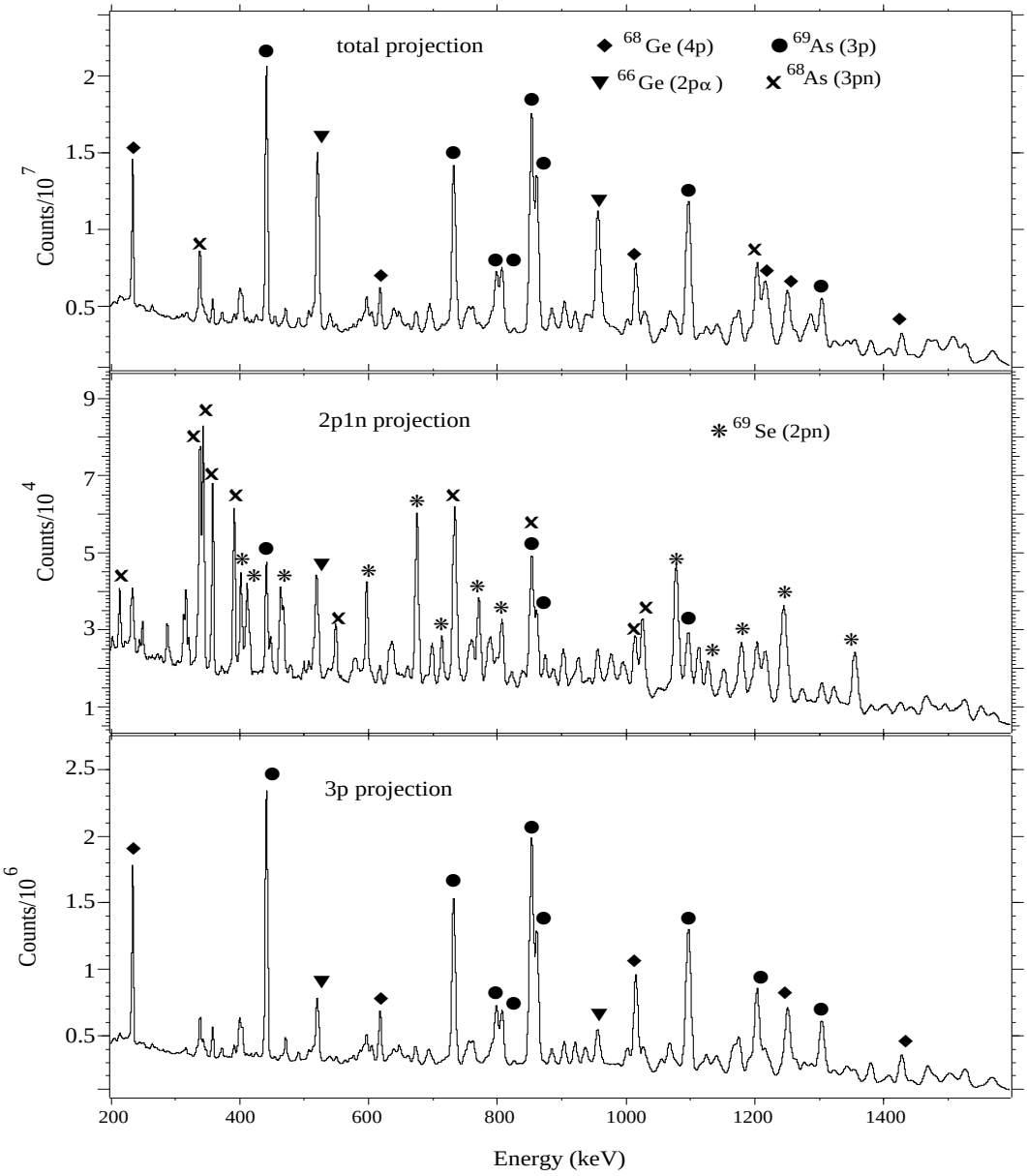

Figure 2.15: *γ-ray projection spectra without any gate on particles (top), 2p1n-gated (middle) and 3p-gated (bottom). The spectra are obtained from the experiment at 105 MeV beam energy.*

detection efficiency is less than 100% both for neutrons and charged particles, contaminant lines from nuclei obtained in other reaction channels are present in the spectra. The particle detection efficiency is worsened mainly by the insufficient neutron-γ or proton-α discrimination, by the solid angle Ω subtended by the neutron detectors which is limited to the forward 1π section of EUROBALL, or by the presence of inactive regions near the detector edges in the Si ball. The efficiencies of detecting charged particles were esti-

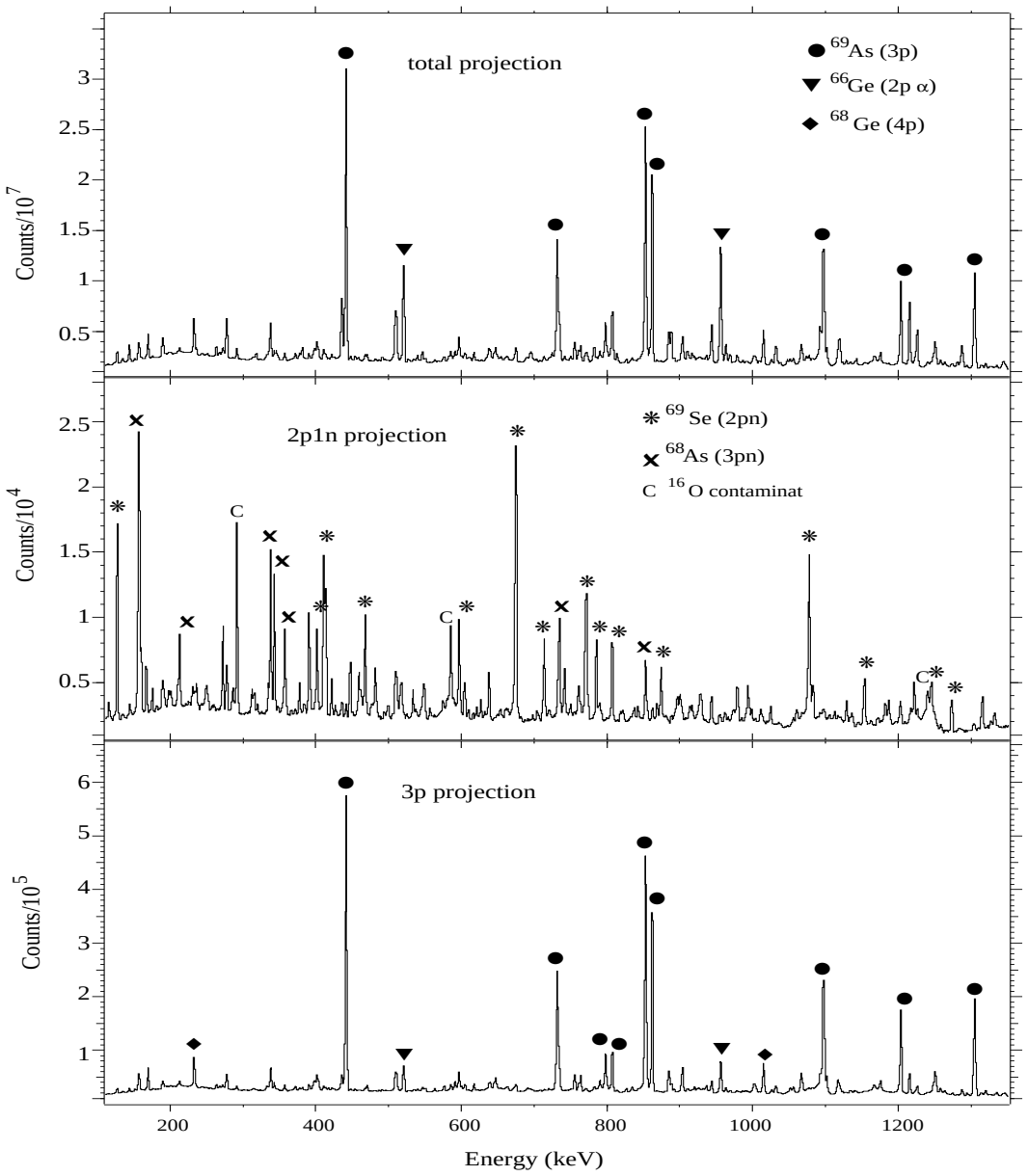

Figure 2.16: *γ-ray projection spectra without any gate on particles (top), 2p1n-gated (middle) and 3p-gated (bottom). The spectra are obtained from the experiment at 95 MeV beam energy.*

mated from the present data to be around 60% for protons and 25% for alpha particles. The efficiency of the NWALL for detecting neutrons is tipically around 25-30% [Ske99], depending on the reaction kinematics.

Despite a good energy resolution (estimated to be around 2.6(2) at 1.3 MeV), the 2p1n-gated spectrum obtained from the experiment at 95 MeV (Figure 2.16, middle) becomes more difficult to analyze than its correspondent from the experiment at 105

MeV because of the contamination with γ-lines deexciting the nuclei populated in the reaction of the ^{32}S beam with ^{16}O, produced by the oxidation of the ^{40}Ca target. The main contaminants, ^{46}V and ^{45}Ti are populated by the 2p1n reaction channel.

Particle$-\gamma-\gamma$ coincidences

One of the most used and known criterion to assign the γ-rays to a nucleus of interest is the $\gamma-\gamma$ coincidence analysis. Such an analyzing procedure needs the sorting of the coincidence data into matrices - two-dimensional "spectra" of correlated γ-rays. In each fusion-evaporation event defined by a time window, there are typically $\sim$20-30 γ-rays emitted (depending on the angular momentum transferred). Due to the limited γ-ray detection efficiency, only a few of these are observed. Every time more than one γ is detected from each cascade, the corresponding element of the coincidence matrix is incremented. Setting a gate on a γ-ray on one axis, an energy spectrum is obtained on the other axis, containing all the other transitions which are coincident with the γ-ray used as gate.

Particle$-\gamma-\gamma-\gamma$ coincidences

A large detector array like EUROBALL can offer three-, four- or even five-fold coincidence data in useful quantities. The analysis of three-fold coincidence data involves the sorting of the data respecting the coincidence condition into cubes - three-dimensional "spectra". These cubes are analyzed by specifying energy gates for all but one of the axes and inspecting the projection onto the remaining axis.

By gating the particle$-\gamma-\gamma$ matrices and the particle$-\gamma-\gamma-\gamma$ cubes by the known γ-rays of the nuclei of interest and noting which transitions are present and which are absent in each gate, it becomes possible to built up the decay schemes of the nuclei of interest. Ordering of transitions in a cascade may also be inferred from such gated spectra because the intensity of transitions in a cascade generally increases at lower excitation energy due to side feeding from other non-yrast states. Thus, the intensity of the transitions above a gate will generally have the same intensity (if there is no decay out of the cascade) as the feeding decay path has been defined by the gate. By measuring intensities in different gates, it is therefore possible to ascertain the ordering of the decay. Example of doubly gated spectra, revealing transitions deexciting the levels of ^{69}Se and ^{69}As populated in the present experiments are shown in Figs. 2.17 and 2.18.

2.4 Spin and parity assignment to the nuclear states

A complete determination of the level scheme includes the assignment of the spins and parities of the excited states and the determination of the mixing ratio of the γ transitions. The spin and the parity assignments to the nuclear ground states are often based on β-decay measurements whereas for excited states, angular distribution and correlation measurements are usually employed. These methods are based on the fact that the probability of emission of a γ-ray by a radioactive nucleus depends, in general, on the

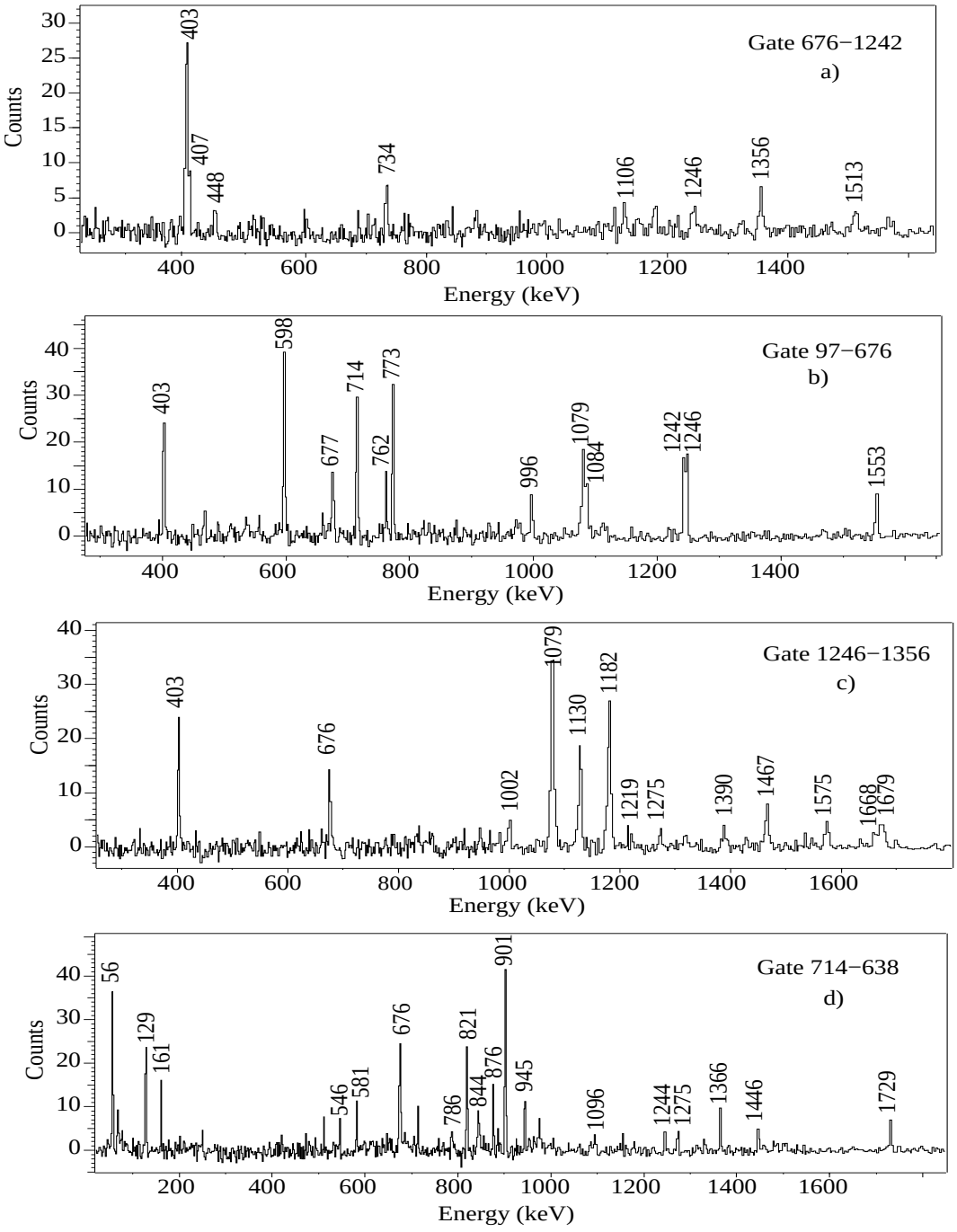

Figure 2.17: *Examples of doubly-gated coincidence spectra from the n-$\gamma\gamma\gamma$ cube. Figures a) and b) present spectra acquired from the experiment at 105 MeV using the thin ^{40}Ca target and Figures c) and d) contain spectra acquired from the experiment at 95 MeV using a gold-backed ^{40}Ca target. Peaks labeled with their energies in keV are assigned to ^{69}Se.*

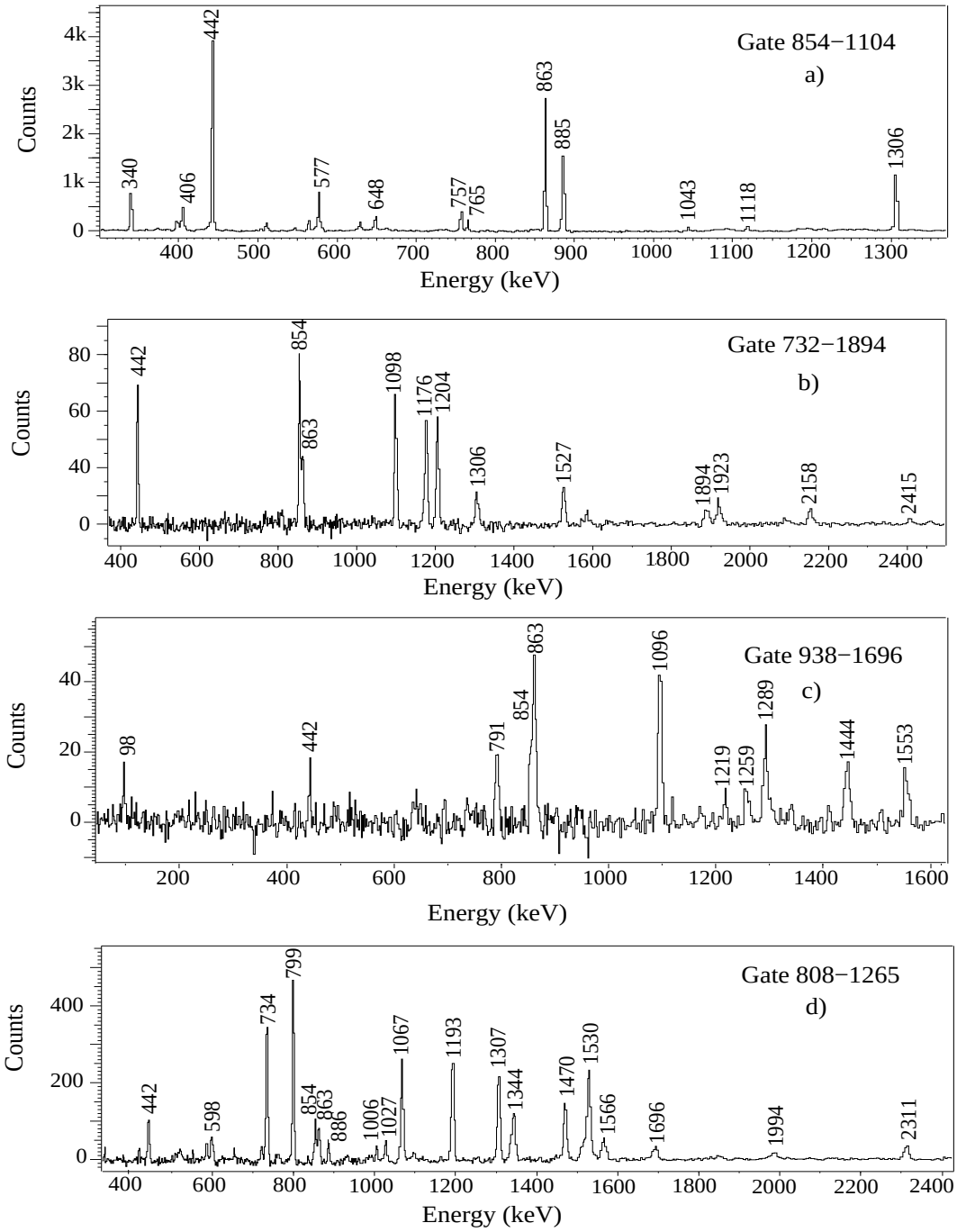

Figure 2.18: *Examples of doubly-gated coincidence spectra from the $\gamma\gamma\gamma$ cube. Figure a) presents a spectrum acquired from the experiment at 95 MeV using the gold-backed ^{40}Ca target and Figures b), c) and d) contain spectra acquired from the experiment at 105 MeV. Peaks labeled with their energies in keV are assigned to ^{69}As.*

angle between the nuclear spin axis and the direction of emission. Under ordinary circumstances, the total radiation from a radioactive sample is isotropic because the nuclei are randomly oriented in space. An anisotropic radiation pattern can be observed only from an ensemble of nuclei that are not randomly oriented. Oriented nuclei can be produced by nuclear reactions, by placing a radioactive sample at low temperature in a strong magnetic field or electric field gradient, etc.

The spins can be assigned to the nuclear states on the basis of angular distribution or correlation methods. For parity assignments, polarization measurements are performed. In the following, these methods will be briefly discussed.

2.4.1 Spin assignments to the nuclear states

Angular distributions

Angular distribution measurements for spin assignments have become a standard technique of in-beam γ-ray spectroscopy taking advantage of the fact that heavy ions bring into the compound system large amounts of orbital angular momentum (average values of twenty to fifty are common) so that, even if the target and projectiles have non-zero spins, the compound nucleus will, on average, have its angular momentum vector strongly aligned. This strong alignment of the compound nucleus is essentially preserved through the evaporation process of the light particles leading to a residual nucleus whose angular momentum of the initial state will still be strongly aligned, though less than that of the compound nucleus.

An initial state of spin J_i has several magnetic substates available. If one denotes these magnetic substates by m then there are $2J_i+1$ values of m; $m = -J_i \ldots J_i$. For aligned states of high spin populated in heavy ion reactions the resulting magnetic substate distribution is concentrated around $m = 0$ taking the beam axis as the axis of quantization. The highly aligned state will then decay via to a cascade of γ-ray transitions leading finally to the ground state. The lower levels are populated via cascade feeding and also directly via side feeding from evaporated particles and the high energy dipole γ-ray transitions. All these processes introduce a loss in alignment. The loss of nuclear alignment throughout the decay of the residual nucleus is minimized when it decays via a stretched (dipole or quadrupole) spin sequence from the initial levels to its ground state. Large loss of nuclear alignment of a level can be caused by non-stretched transitions, isomeric states or β-decay feeding. However, it is quite reasonable to expect a Gaussian distribution of substates for the initial state since that state is fed via a large number of paths, none of which is dominant [New67, Zob80b]:

$$\wp(m) = \frac{e^{-m^2/2\sigma^2}}{\sum_{m=-j}^{j} e^{-m^2/2\sigma^2}}. \tag{2.6}$$

When a nucleus in such a state emits a γ-radiation, the relative intensities at different angles with respect to the beam axis depend on the multipolarity of the transition. The angular distribution function at a given angle θ can be expressed as [Sie65]:

$$I(\theta) = W^{exp}(\theta) = \sum_{\kappa=even} A_\kappa^{exp} P_\kappa(\cos\theta). \tag{2.7}$$

The experimental coefficients A_κ^{exp} depend not only on the spins of the respective initial and final states and on the multipolarities of the connecting γ-ray transition but also on the population distribution of the initial level, distribution described by the Gaussian of eq. 2.6. The degree of alignment of the state J_i is specified by the so-called attenuation coefficients $\alpha_K(J_i, \sigma)$, $(0 \leq \alpha_K(J_i) \leq 1)$, where K takes positive even values because of the parity conservation [Yam67]. Thus, the experimental coefficients may be split into two factors:

$$A_\kappa^{exp} = \alpha_\kappa A_\kappa^{max}(J_i, J_f, \delta) \tag{2.8}$$

were the A_κ^{max} and α_κ coefficients are tabulated in ref. [Yam67] and [Mat74], respectively. For strongly aligned states, $\sigma \to 0$ and $\alpha_K \approx 1$. Since only the lowest two coefficients $\alpha_{2,4}$ can be derived from experiment and since one assumes that the population parameters are represented by a distribution function involving only the parameter σ, then α_4 is uniquely related to α_2 and α_2 can be expressed as a function of J and σ/J [Yam67, Mat74].

A standard angular distribution measurement consists of measurements of the γ-rays using detectors placed at different angles between 0° and 180° with respect to the beam axis. When the experimental setup involves only a small number of detectors, then one of them is used as a monitor detector and the rest are used as movable counters. Because in such type of experiment the spectra at different angles cannot be acquired simultaneously, systematic errors can appear due to changes in beam energy, integrated beam intensities or different dead times and absolute efficiencies of the detectors. A normalization needs to be done, usually achieved by using some intense peaks in the spectra acquired in the monitor detector.

The use of the detector arrays in the angular distribution measurements has the advantage of reduced systematic errors due to the changes in beam energy or intensity. The normalization is required only to correct for the dead times and absolute efficiencies.

The assignment of the spins to the excited levels are carried out by a χ^2-analysis of the angular distributions. The value of χ^2 is calculated as a function of δ, the mixing ratio of the transition under investigation, for each spin-hypothesis made on the initial and final levels involved. The reduced χ^2-distribution is defined as

$$\chi^2 = \frac{1}{N-1} \sum_i \frac{[W_E(\theta_i) - W_T(\theta_i)]^2}{\Delta W_E(\theta_i)^2} \tag{2.9}$$

were the sum is carried out over all measured angles; $W_E(\theta_i)$ and $\Delta W_E(\theta_i)$ are the experimental angular distribution data and their errors at each angle and $W_T(\theta_i)$ is the theoretical angular distribution function calculated for a given sequence of initial and final spin. The experimental and the theoretical yields are normalized such as $\sum W_T = \sum W_E$; N is the number of angles at which measurements are performed minus 1 to account for the variable width of the Gaussian substate distribution. A spin value is rejected if its χ^2 lies completely above the 0.1% confidence limit. The analysis of the χ^2-distributions for all possible spin hypotheses of the transition of interest allows the determination of the best spin hypotheses in most cases.

Particle gated angular distributions were analyzed in order to extract the multipole mixing ratios of the γ-rays in ^{69}Se. The data from the experiment at 105 MeV beam energy data set were sorted into spectra for each of the rings of EUROBALL. To increase the

statistics, the resulting spectra of the neighboring rings were added up forming pseudorings at weighted angles given by:

$$\theta_{av} = \frac{\sum_i n_i \theta_i}{\sum_i n_i} \tag{2.10}$$

where i represents the number of rings included, n_i and θ_i are the number of detectors and the angle of the ring i, respectively. The average angles of the pseudorings are given in Table 2.2.

Table 2.2: The angles of the EUROBALL detectors used for the angular distribution measurements in the present work.

Pseudoring#	No of detectors	Ring#	Type of detectors	Ring angle	Pseudoring angle
1	35	0	C	163.46°	156.15°
		1	C	155.85°	
		2	C	149.28°	
2	30	3	C	145.72°	139.86°
		4	C	141.01°	
		5	C	137.13°	
3	40	6	C	132.79°	128.53°
		7	C	129.35°	
		8	C	122.63°	
4	52	10	Q	99.05°	90°
		11	Q	80.94°	
5	52	9	Q	107.54°	89.84°
		12	Q	72.15°	

Due to the high bombarding energy used in the present experiments, the assumption of a strong alignment of the angular momentum with the beam axis in the compound nucleus ^{72}Kr is reasonable. The evaporated particles (neutrons, alphas, protons) and the γ-rays emitted subsequently in random directions do not change the alignment very much. Therefore a Gaussian distribution centered at $m = 0$ can be used to describe the $m-$substate population with a half width σ for a given spin. The quantity σ/J is

Table 2.3: Angular distribution coefficients and mixing ratios in ^{69}Se from the ^{40}Ca(^{32}S,2pn)^{69}Se reaction at 105 MeV beam energy.

E_γ (keV)	$I_i^{\pi_i} \rightarrow I_f^{\pi_f}$	$A_2/A_0 \pm \Delta(A_2/A_0)$	$A_4/A_0 \pm \Delta(A_4/A_0)$	$\delta \pm \Delta\delta$
714.2	$23/2^- \rightarrow 19/2^-$	0.238±0.06	-0.0807±0.01	$-0.067^{+0.063}_{-0.073}$
598.2	$21/2^- \rightarrow 19/2^-$	-0.142±0.04	-0.085±0.03	0.05±0.03
468.0	$19/2^- \rightarrow 15/2^-$	0.157±0.05	-0.11±0.07	-0.16±0.06
448.2	$19/2^- \rightarrow 17/2^+$	0.245±0.6	0.025±0.01	0.32±0.05[a]
412.0	$17/2^- \rightarrow 15/2^-$	-0.172±0.05	-0.02±0.01	0.50±0.4
1130.2	$29/2^+ \rightarrow 25/2^+$	0.511±0.04	0.007±0.002	0.17±0.4[b]
1182.3	$25/2^+ \rightarrow 21/2^+$	0.359±0.03	-0.154±0.06	0.0±0.01
1079.1	$13/2^+ \rightarrow 9/2^+$	0.29±0.03	-0.06±0.03	0.0±0.01
403.1	$13/2^+ \rightarrow 11/2^+$	0.005±0.001	-0.0015±0.0007	0.16±0.05
773.3	$13/2^+ \rightarrow 11/2^+$	0.47±0.1	0.105±0.075	2.30±0.39
675.9	$11/2^+ \rightarrow 9/2^+$	0.35±0.07	0.057±0.02	$0.57^{+0.10}_{-0.07}$ $2.52^{+0.55}_{-0.44}$ $0.57^{+0.10}_{-0.08}$

[a]small contamination at backward-angles with the 442.9-keV transition in ^{69}As.
[b]small contamination at backward-angles with the 1125.3-keV transition in ^{68}Ge.

approximately constant over a wide spin range. A deviation from this empirical fact may occur only in the low-spin region, $J \leq 6$ [Tar75]. Angular distributions for some intensive stretched electric quadrupole ($E2$) transitions in the same spin region as the transitions of interest in ^{69}Se, were analyzed initially in order to extract the alignment parameter σ/J. In the analysis, the computer code CHIPLO-2 has been used [Wei94]. There was no detectable spin dependence. A mean value for σ/J_i=0.35±0.05, where J_i is the spin of the initial state, was found to minimize the χ^2 function and to reproduce the angular distribution coefficients given in literature for the testing transitions [Her95, Her90]. This value has been used as a reference value for the final analysis of all angular distribution measurements. The results of the angular distribution measurements for some intense lines in ^{69}Se are summarized in Table 2.3. Sample data are shown in Fig. 2.19.

The use of heavy-ion-induced fusion-evaporation reactions to study high-spin states introduces some problems with singles angular distribution measurements. Firstly, these reactions produce very complicated spectra since many bands of several nuclei are usually populated. Secondly, in the reactions using thin targets, due to the finite size of the angle subtended by a cluster or clover crystal, the peaks are Doppler broadened worsening the energy resolution. In the reactions with thick targets, due to the large recoil velocity, the peaks are Doppler shifted by different amounts for different lifetimes. All these aspects make single spectra difficult to analyze.

Directional correlations of oriented states (DCO-ratios)

The measurement of directional correlations of coincident γ-rays with multidetector arrays is a powerful tool for determining the multipolarity of a emitted radiation. The use

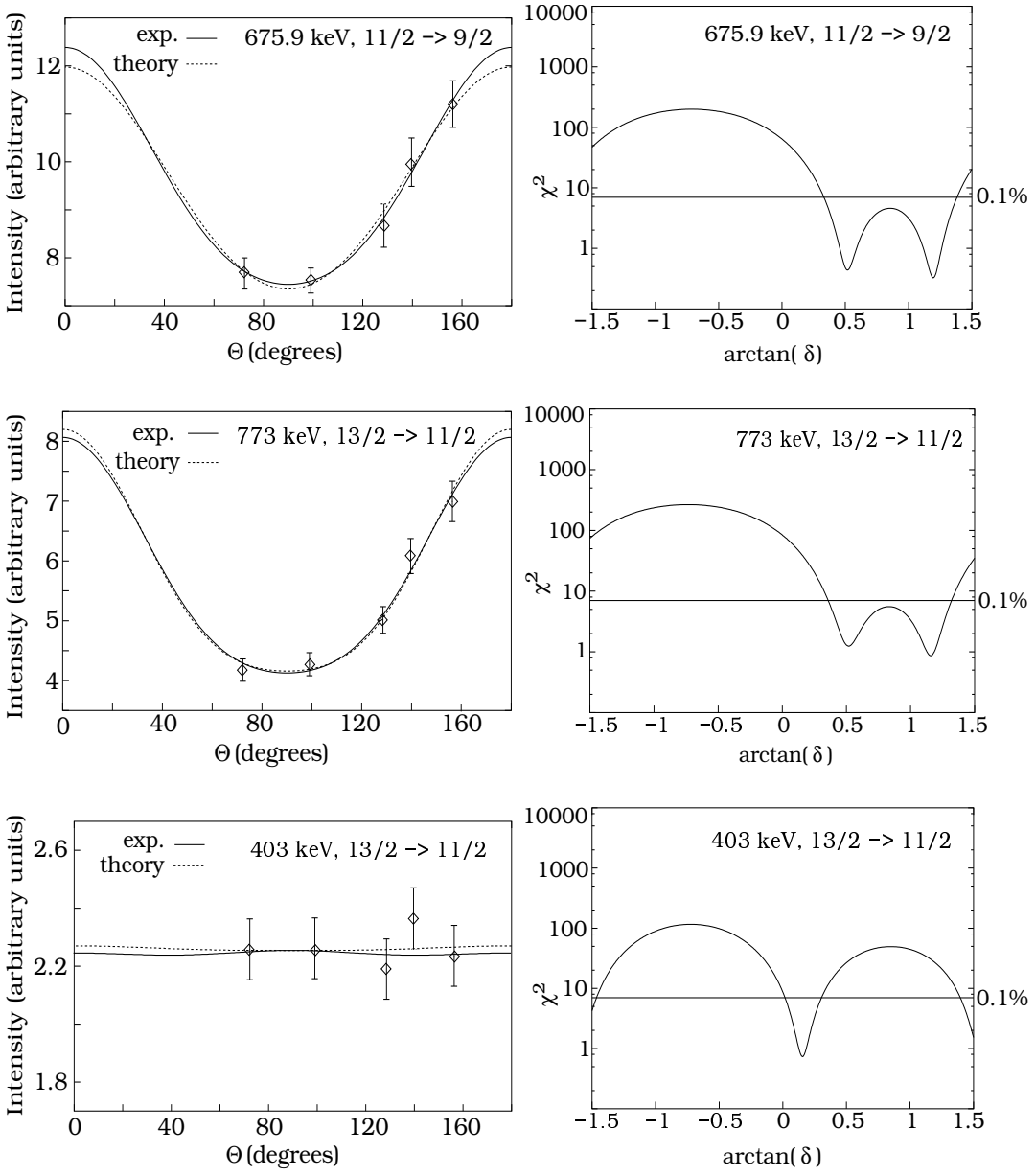

Figure 2.19: *Left: angular distribution data for the the 675.9-, 773.2-, and 403.1-keV* ^{69}Se *γ-rays. Right: plots of χ^2 vs the mixing ratio δ for the angular distribution of the respective γ-rays. The initial- and final-spin states which were tested are indicated on the plots.*

of $\gamma - \gamma$ coincidence data has the advantage over singles γ-ray angular distribution measurements in that the γ-ray peaks are better separated in two dimensions with a lower background contamination. The advent of the highly efficient γ-ray spectrometers such as EUROBALL, offers the opportunity of extending the precise measurements of γ-ray directional correlations to even weaker transitions. Thus, definite spin assignments of nuclear states can be pushed to much higher spin regime than previously possible.

The theory of directional correlations of γ-radiation emitted from oriented states is well developed and was discussed by Steffen and Alder [Ste75b] and by Krane *et al.* [Kra73]. In an directional correlation work, a nucleus emits two coincident γ-rays γ_1 and γ_2. One asks for the relative probability $W(\theta)d\Omega$ that γ_2 is emitted into the solid angle $d\Omega$ at an angle θ with respect to the direction of emission of γ_1. Two detectors placed at angles θ_1 and θ_2 are necessary to determine the angular correlation of the cascade $\gamma_1 - \gamma_2$, where $\theta_{1,2}$ are the angle between the beam axis, assumed to be z and the direction of emission of $\gamma_{1,2}$, respectively. To describe the angular position of the detectors, a third angle $\Delta\Phi = \Phi_1 - \Phi_2$ is required, which is the angle between the two planes opened by each detector and the beam axis. The intensity of the transition γ_2 determined from the spectrum in detector 2 gated on the transition γ_1 in detector 1 is denoted by $W(\theta_1, \theta_2, \Delta\Phi)$. The intensity of the transition γ_2, determined from a spectrum of detector 1 gated on the transition γ_1 in detector 2 (reverse case) is denoted by $W(\theta_2, \theta_1, \Delta\Phi)$. The theoretical DCO ratio is:

$$R_{DCO}^{th} = \frac{W(\theta_1, \theta_2, \Delta\Phi)}{W(\theta_2, \theta_1, \Delta\Phi)}. \tag{2.11}$$

An exchange of the angles or of the gating and observed transitions will invert the DCO ratio. The theoretical expression for the correlation function $W(\theta_1, \theta_2, \Delta\Phi)$ of γ-rays depends on the spins of the involved levels, the multipolarities and the mixing ratios of the γ transitions [Kra73]. For most applications the theory of DCO ratios can be simplified with respect to the general directional correlation theory by taking into account the experimental conditions such as (i) unpolarized beams are used, (ii) multidetectors systems are used for the detection of γ-rays, (iii) the detectors are insensitive to the polarization of the γ-rays. Therefore, detectors placed at forward and backward angles with respect to the beam direction can be treated in the same way.

The following symmetries can be deduced for the theoretical angular correlation function [Eks92]:

$$\begin{aligned} W(\theta_1, \theta_2, \Delta\Phi) &= W(180^\circ - \theta_1, 180^\circ - \theta_2, \Delta\Phi) \\ &= W(\theta_1, 180^\circ - \theta_2, 180^\circ + \Delta\Phi) \\ &= W(180^\circ - \theta_1, \theta_2, 180^\circ + \Delta\Phi) \\ &= W(\theta_1, 180^\circ - \theta_2, 180^\circ - \Delta\Phi) \\ &= W(180^\circ - \theta_1, \theta_2, 180^\circ - \Delta\Phi). \end{aligned} \tag{2.12}$$

The first symmetry follows from the fact that the initial state is aligned, which implies equivalence of "beam up" and "beam down" directions. The second and the third symmetries follow from the relation:

$$\cos(q\Delta\Phi) = (-1)^q \cos(q(180^\circ + \Delta\Phi)) = (-1)^q \cos(q(180^\circ - \Delta\Phi)) \tag{2.13}$$

and

$$P_\lambda^q(\cos\theta) = (-1)^q P_\lambda^q(\cos(180^\circ - \theta)). \tag{2.14}$$

with q an arbitrary integer.

An experimental DCO ratio is often defined as:

$$R_{DCO}^{exp} = \frac{I_{\gamma\gamma}(\theta_1, \theta_2[gate])}{I_{\gamma\gamma}(\theta_2, \theta_1[gate])} \tag{2.15}$$

which must be equal to the R_{DCO}^{th} defined by the eq. 2.11. In the experimental ratio in the equation above, all the detectors in the rings at θ_1 and θ_2 ($\theta_1 \neq \theta_2$) with respect to the beam axis are considered, irrespective to their $\Delta\Phi$ values. Typically, a single $E_{\gamma_1} - E_{\gamma_2}$ correlation matrix is constructed of γ-rays detected at θ_1 against γ-rays detected at θ_2, from which the coincidence intensities $I_{\gamma_1\gamma_2}(\theta_1, \theta_2)$ and $I_{\gamma_1\gamma_2}(\theta_2, \theta_1)$ are extracted. Since the theoretical angular correlation function can be developed in powers of $\cos(\theta)$ (Legendre polynomials), the largest difference in the DCO ratios for a cascade of γ-rays is observed if one detector is placed at 0° (180°) and the other one at 90° with respect to the beam axis.

The EUROBALL array contains 209 Ge-detectors when used with the Neutron Wall. The 209 detectors constitute 21736 (209×208/2) detector pairs. Due to the high degree of symmetry in the setup, these 21736 combinations can be reduced to 13 distinct geometries with the help of the symmetries given by the eq. 2.12. The 13 distinct geometries correspond to the 13 EUROBALL rings discussed in subsection 2.2.1. In the present work, due to poor statistics of the weak γ-rays in the particle - gated correlation matrices sorted for each of the 13 rings, the matrices from the 4 most backward- angle (163°, 156°, 149° and 146°) and the 4 rings near 90° (72°, 81°, 99° and 107°), (see Table 2.1) were added up, resulting a total correlation matrix $E_{\gamma_1(155°)} - E_{\gamma_2(90°)}$, were θ=155° and θ=90° are the angles obtained by weighting over the angles of the 4 rings in each case. In this geometry, if one gates on a stretched quadrupole transition, the theoretical DCO ratios are ∼1 for stretched quadrupole transitions and ∼0.5 for pure dipole transitions. If, on the contrary, gates are set on a pure dipole transition, the extracted DCO ratios are ∼2 for pure quadrupole transitions and ∼1 for pure dipole transitions. Mixed $M1/E2$ transitions can have a DCO ratio ranging from ≈0.3 up to ≈1.2. This can lead to ambiguities in the multipolarity assignment, but one advantage is that the sign of the mixing ratio, δ, can in theory be determined for the mixed transitions [Kra73]. A negative mixing ratio for an $I \rightarrow I - 1$ transition will lead to a reduction in the DCO ratio. A positive mixing ratio leads to an increased DCO ratio compared to that of the unmixed transition.

The results of the angular distribution and directional correlation analyses for ^{69}Se and ^{69}As will be presented and discussed in conjunction with the associated level schemes in the next chapter.

2.4.2 Parity assignments to the nuclear states

In order to deduce the parities of nuclear states one needs to measure the electric or magnetic character of the connecting transitions. The most efficient method is to measure the linear polarization P of the γ-rays. Assuming spin alignment, this method uses the fact that the γ-rays undergo Compton scattering and that the direction of the Compton scattered γ-ray depends on its electric or magnetic character. The polarization measurements make usually use of a linear Compton polarimeter [But73]. This polarimeter consists of

three Ge crystals, one scatterer and two absorbers. The scatterer and one absorber crystals define the reaction plan which is parallel to the beam axis while the other absorber defines with the scatterer the vertical plan. In an EUROBALL experiment, the Cluster and Clover detectors can be used for polarization measurements, with each of the individual crystals playing the role of the scatterer and the two adjacent detectors being the absorbers [Duc99]. Linear polarization measurements were already performed with the Clover detectors, since they are placed around 90° with respect to the beam axis [Kor01].

Besides the direct method of measuring the polarization of the γ-rays, indirect methods can be used to assign the parities of the excited states of a nucleus. In the parity assignments one can account on the well known fact that transitions with electric character are about 100 times more probable than transitions with magnetic character for a given multipolarity (see, for instance, Ref. [Ste75b]). Assuming that the lowest allowed multipole often dominates, one can conclude that a transition whose angular distribution and correlation measurements is consistent with a quadrupole character is more likely a parity conserving $E2$ transition. Using these arguments, a transition whose angular distribution and correlation measurements is consistent with a dipole character can either be parity conserving $E2/M1$ mixed transition or a parity breaking $E1/M2$ transition. In addition, by comparing with the corresponding excited levels with well assigned spins and parities from the neighboring nuclei, one can make assumptions about the involved parities in the nucleus under investigation.

Chapter 3

Experimental results

The current investigations confirm the previously observed yrast transitions and extend the level schemes of ^{69}Se and ^{69}As further. Combining the experimental information obtained from both experiments, new levels were found in both positive- and negative-parity parts of the level schemes. The new levels are arranged in band structures feeding into the yrast bands of the respective parity.

The level scheme shown in Figs. 3.1 and 3.2-3.4 result from the analysis of the data obtained in the present work. The transitions have been placed in the level schemes according to the coincidence relationships and relative intensities. Spins and parities were deduced, whenever possible, from the analysis of the DCO ratios and angular distributions and from a comparison with the systematics.

3.1 ^{69}Se

The level scheme of ^{69}Se (Fig. 3.1) is organized into 7 bands labeled from 1 to 7 plus additional single states or structures which cannot be included in rotational-like bands yet.

The spectroscopic information of the γ-rays belonging to ^{69}Se is listed in Table A.1. The first two columns give the levels energies and the energies of the γ-transitions resulting from the analysis of the n-$\gamma\gamma$ matrices obtained form the experiment at 105 MeV. The next three columns give the relative intensities of the γ-rays, the DCO ratios and the energy of the gating transition, respectively. The intensities are normalized to the intensity of the 773.3 keV transition which is set to be 100. Finally, the sixth and the seventh columns of Table A.1 give the assigned multipolarities and the corresponding spin sequence, based on the measured DCO ratios and angular distributions.

3.1.1 Positive-parity states

The first spectroscopic information about ^{69}Se was given by the study of its β^+ decay ($T_{1/2}$=27.4 s) to the known low-lying levels of ^{69}As [Mac77]. Within that work, a negative-parity ground-state was established. The low-lying excited states were reported later by two different groups whose in-beam results were partially consistent [Wio88a, Ram88].

In Ref. [Ram88], information about the $g_{9/2}$ isomeric state ($T_{1/2}$=853±78 ns) was compared to the properties of the $9/2^+$ states in the N =35 isotones and systematic trends concerning the level structures at low energy and the electromagnetic properties of the γ-transitions between these levels were discussed. A detailed study of Wiosna *et al.* [Wio88a] established a $g_{9/2}$ band showing a strong coupling-like pattern. The work of Arrison *et al.* [Arr89] tried to solve the discrepancy between the two previous studies with respect to the lifetime of the isomeric $9/2^+$ level. It provided a conclusive identification of ^{69}Se and confirmed the experimental evidence found by Wiosna *et al.* concerning the major change in the yrast structure compared to other odd-neutron isotopes in the A∼70 mass region.

Low-lying positive-parity states in ^{69}Se

A strong coupled-like band, labeled Band 1, becomes yrast at low excitation energies. In ref. [Jen01], two ΔI=1 transitions, 838.6 and 406.7 keV were newly reported, as well as the ΔI =2, 1242.2-keV transition, as being the extension of the previous $9/2^+$-$11/2^+$-$13/2^+$ observed sequence. The present data support this assignment. A new level at 4006.3 keV with spin $(19/2^+)$ is proposed, as belonging to the oblate yrast band, depopulating by a ΔI =2, 1512.6-keV γ ray on the 2492.7-keV level and a ΔI =1, 1106.3-keV transition on the 2900.0-keV level. The newly observed state shows a similar degree of signature splitting as the previously known $9/2^+$-$11/2^+$-$13/2^+$-$15/2^+$-$17/2^+$ sequence. Figure 2.17(a) shows a spectrum double-gated on the 675.9- and 1242.2-keV gamma rays in which the extension of the ground-state band can be observed. Although the statistics are low, the double-gating procedure leads to extremely clean spectra.

The fact that the low-spin states were favorably populated in the reaction on the 1 mg/cm^2 ^{40}Ca target at 95 MeV allowed to identify the second $9/2^+$ state at 1361.8 keV excitation energy, which is very close in energy to the first $11/2^+$ at 1250.7 keV and decays to the first $9/2^+$ level by the 787.2-keV transition. Three new levels at 2581.0, 3498.3 and 3576.5 keV were also well populated in the reaction at 95 MeV beam energy. Good statistics made it possible to extract the multipole order of the transitions depopulating these levels supporting the spin assignments of $13/2^+$, $17/2^+$ and $17/2^+$, respectively. Up to now, four levels with spin $17/2^+$ have been found in ^{69}Se. The yrast state at 2900.0 keV excitation energy is only populated by transitions decaying from the higher positive-parity yrast levels. The other three levels - at 3227.1, 3498.3 and 3576.5 keV - are populated by transitions decaying from the negative-parity state with spin $19/2^-$ at 3673.6 keV. In the spectrum from Fig. 2.17(b) the 996.3-, 1083.8-, 677.2-, and 1553-keV γ rays which deexcite the newly found level at 3576.5 keV can be observed.

In Table 2.3 the angular distribution coefficients A_2/A_0 and A_4/A_0 and mixing ratios δ are listed. As an example for the quality of the data, the left side of Fig. 2.19 shows the angular distributions of the 675.9- $(11/2^+ \rightarrow 9/2^+)$, 773.2- $(13/2^+ \rightarrow 11/2^+)$ and 403.1-keV $(13/2^+ \rightarrow 11/2^+)$ γ rays.

The angular distribution results for the 675.9-keV transition (Fig. 2.19, top) agree with the two values for the mixing ratios obtained by Jenkins *et al.* [Jen01]. As they pointed out, the smaller value of the mixing ratio fully agrees with the expected value for the quadrupole moment Q_0 ≈-2 eb when considering an oblate shape and a deformation

parameter $\beta_2 \approx$-0.3, in agreement with the theoretical predictions. But the large value of the mixing ratio cannot be excluded because it may explain the quadrupole behavior of the 675.9-keV transition in the angular correlation analysis (see Table A.1). For example, gating on the 714.2-keV γ-ray, which from the angular distribution and correlation data was found to have a quadrupole character, or gating on the stretched quadrupole 1355.7-keV transition, the values obtained for the DCO ratios are 0.95(16) and 1.20(13), respectively, consistent with a ΔI=2 multipolarity or a large dipole-quadrupole mixing ratio for the 675.9-keV γ ray.

The same situation occurs in the angular correlation analysis of the 773.3-keV transition. With a gate on the ΔI=2, 714.2-keV transition, a DCO value of 1.08(11) is obtained, suggesting a quadrupole character and a spin assignment of $15/2^+$ for the level at 2023.8 keV. In the analysis of the angular distribution data for the 773.3-keV transition, again two solutions are found, one corresponding to a large multipole mixing ratio δ=2.30$\pm$0.39 and the other to a small multipole mixing ratio $\delta=0.57^{+0.10}_{-0.07}$ (see Fig. 2.19 and Table 2.3). The former solution has a reduced χ^2=0.867 value whereas the latter has χ^2=1.245. No other minima were found in the plot of χ^2 vs. δ as represented in Fig. 2.19. With such a large value of δ for the 773.3-keV transition, a mixed E2/M1 character and a spin of $13/2^+$ for the 2023.8-keV level is assumed, in agreement with the systematics of the light germanium isotopes [Her95, Bec97, Zob80]. A spin of $13/2^+$ for the 2023.8-keV level is also consistent with the results of the directional correlations analysis for the 1203.3-, 448.2-, and 1183.2-keV transitions populating the level. The angular distribution of the 403.1-keV transition shows an isotropic character, giving the value δ=0.16$\pm$0.05 for the mixing ratio (Fig. 2.19, bottom).

Large values of the mixing ratios for the low members of the yrast band have also been measured in ^{69}Ge [Bec97] and ^{75}Kr [Sko90, Sko98]. A simple prolate-oblate mixing model is proposed in ref. [Sko90], in order to describe the anomalous behavior of transition probabilities in ^{75}Kr.

Positive-parity high-spin states in ^{69}Se

At spin $21/2^+$ the oblate structure was found by Jenkins and coworkers to be crossed by a prolate configuration which continues at high spin (Band 2 in Fig. 3.1). Above spin $21/2^+$ additional structures occur. The $25/2^+$ state at 5438.0 keV excitation energy belongs to the prolate configuration found by Jenkins *et al.* [Jen01]. The second $25/2^+$ state is depopulated by the 1575.1-keV transition. In the work of Jenkins *et al.* [Jen01] this state was found to be populated by the 1002.2-keV transition. The present data support the existence of the 1002.2-keV transition but not its placement. The double gating procedure applied in the n-$\gamma\gamma\gamma$ cubes obtained from the present experiments does not show any coincidence relation between the 1575.1- and the 1002.2-keV transition. Instead, a rotational-like cascade consisting of 1273.5- and 1389.8-keV lines (see Fig. 2.17(c)) extends the non-yrast structure built on the second $25/2^+$ state and labeled Band 3 in Fig. 3.1. The 1002.2-keV transition is found to feed the $21/2^+$ yrast state directly with a very low intensity which does not allow to extract its DCO value and determine the spin of the level at 5257.9 keV. This level is populated by the 1219.4-keV transition which decays from the newly observed state at 6477.2 keV excitation energy.

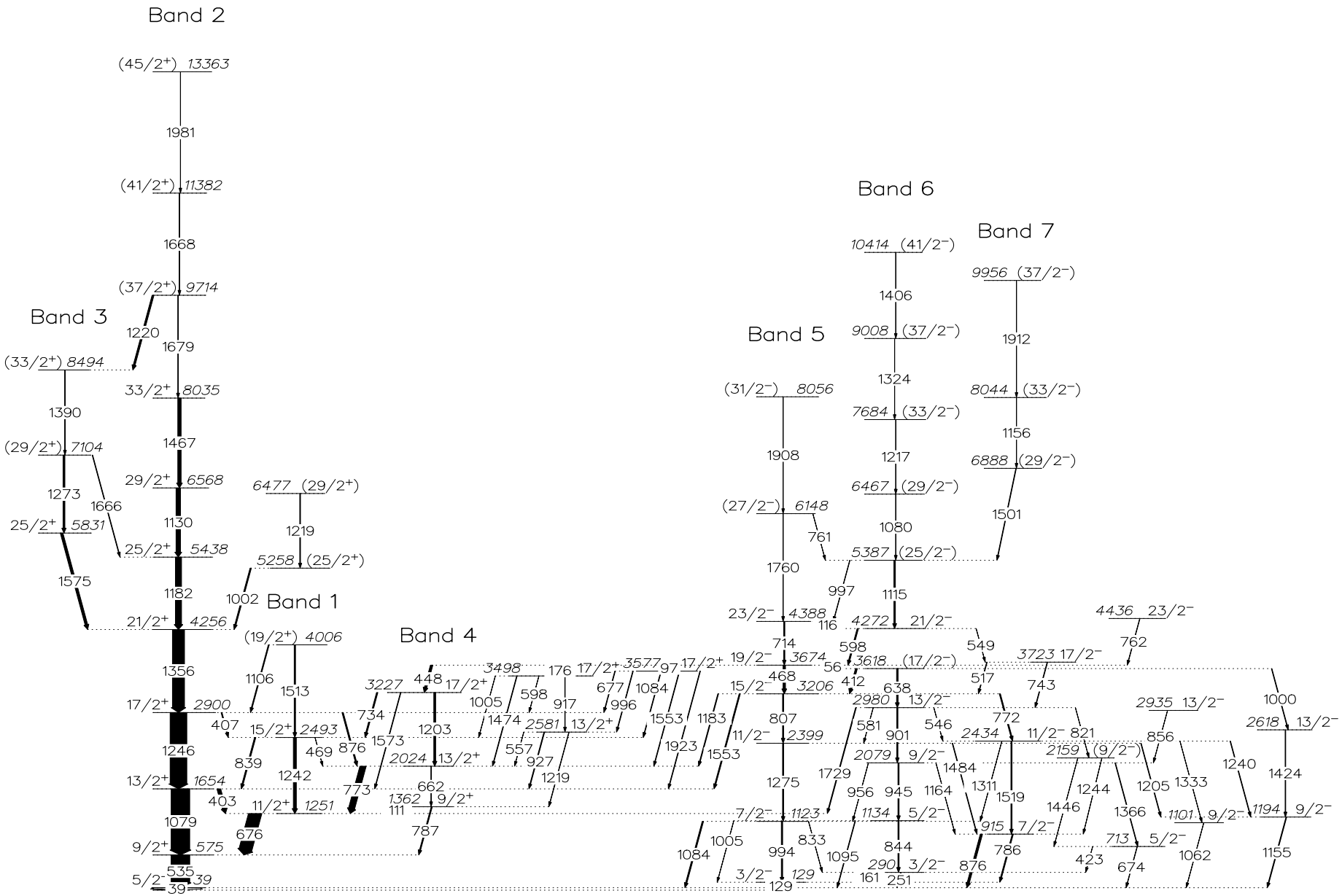

Figure 3.1: *Level scheme of ^{69}Se obtained from the present work. The widths of the arrows are proportional to the γ-ray intensities. The ground state has the spin and parity $1/2^-$.*

3.1.2 Negative-parity states

The single-particle level structure of negative parity below the $9/2^+$ isomer was investigated by Pohl *et al.* [Poh95]. The half-life $T_{1/2}$=2.0±0.2 μs of the first excited negative parity state has been measured, which, together with the internal conversion coefficient of the γ ray deexciting this level, strongly favored a spin and parity assignment of $1/2^-$ for the ^{69}Se ground state.

Low-lying negative-parity states in ^{69}Se

The first three negative-parity levels lie at very low excitation energies. The DCO values for the 129.1- and 161.3-keV transitions show their dipole and quadrupole character, respectively. While a $3/2^-$ value for the spin of the level at 129.1 keV was already assigned by Jenkins *et al.* [Jen01], the systematics of nuclei with N=35 as ^{63}Ni and ^{67}Ge suggest the spin $3/2^-$ as well for the level at 290.1 keV. In general, the negative-parity part of the level scheme shows a large density of levels mostly concentrated below 3.5 MeV excitation energy. They were very strongly populated in the experiment using a thick target and the small peak width characteristic of the experiments using thick targets made possible the disentanglement of the doublets, their placement in the level scheme with good accuracy in energy and clean gates with good statistics in the DCO-ratio measurements. These states can be classified into two groups:

(i) The new levels at 1134.7, 2079.4 and 2979.6 keV, together with the levels at 1193.8 and 2618.1 keV found by Wiosna [Wio88a] and confirmed by Jenkins *et al.* [Jen01] and in the present work are populated from the $17/2^-$ state at 3617.6 keV.

(ii) The levels at 1123.5 and 2398.6 keV and the levels at 914.6 and 2433.9 keV are populated from the state at 3205.6 keV and they show similar spin sequences and energy spacings. The spin assignments for these levels were confirmed by the DCO ratios extracted in the present experiment.

The γ-rays depopulating the newly observed cascade consisting of 2979.6-, 2079.4-, 1134.7-, and 290.1-keV levels are clearly seen in the spectrum presented in Fig. 2.17d. Based on DCO measurements, the spins $13/2^-$, $9/2^-$, $5/2^-$ and $3/2^-$, respectively, have been assigned to these levels. The $15/2^-$ and $19/2^-$ yrast states are fed by the $E2$ transitions of 468.0 and 714.2 keV, respectively and by a parallel $M1/E2$ cascade via the 56.2-412.0 keV and 116.4-598.2 keV γ rays.

Negative-parity high-spin states in ^{69}Se

Built on the top of the $15/2^-$ state at 3205.6 keV a strong coupled sequence is observed (Band 5 in Fig. 3.1). At tentative spin $(25/2^-)$ Band 5 is crossed by a decoupled band, labeled Band 6. The band is weakly populated in the present reaction and the spin of the excited levels have been only tentatively given. However, the regular rotational character and the large energies of the connecting transitions suggest that Band 6 is more likely a ΔI=2 band. Band 6 has been observed up to an excitation energy of 10414.4 keV.

3.2 ^{69}As

The low-lying level scheme of ^{69}As deduced from the present coincidence measurements is shown in Figs. 3.2 (positive-parity states) and 3.4 (negative-parity states). The high-spin structure is presented in Fig. 3.3. It is organized into 8 bands labeled from 1 to 8 plus additional single states or structures which cannot be included in rotational-like bands yet. The level structure contains many newly introduced levels compared to the previous work [Bru00].

The results of the level determinations, with energies, intensities, multipolarities, spin assignments and DCO ratios are given in Table A.2. For those levels for which no definite conclusion could be drawn about the spin and parity, the corresponding columns in Table A.2 were left vacant.

3.2.1 Positive-parity states

The ground-state spin of $I^{\pi}=5/2^{-}$ of ^{69}As has been determined in an atomic beam nuclear magnetic resonance NMR experiment [Hel76]. Low-lying positive-parity states up to an excitation energy of 5.2 MeV have been firmly identified in the work of Hellmeister *et al.* [Hel78]. Within that work, on the basis of $\gamma-\gamma$ coincidences, angular distributions and excitation functions, a rotational aligned $g_{9/2}$ proton band is established. Their proposed level scheme consists of the 443-, 733-, 854-, 864-, 904-, 1099-, 1103-, 1205-, and 1307-keV γ-rays (see Fig. 3.2). The angular distribution coefficients of the 1307-, 854-, 1099-, and 733-keV transitions were found to be typical for stretched quadrupole transitions, whereas those of the 443- and 904-keV lines were found to exhibit a dipole and a mixed dipole/quadrupole character. Thus, the 854-, 1099-, 1205-, and 733-keV γ-rays were assigned to the yrast favored band. The short lifetime of the level at 2211 keV level (τ <2 ps, [Iva76]) and the small intensity and large negative mixing ratio (δ=-1.0±0.5) of the 904 keV depopulating transition led to the spin and parity assignment of $11/2^{+}$ for the state at 2211 keV [Hel78]. As a consequence, the observed states at 2211 and 3264 keV were interpreted by Hellmeister *et al.* as being the lowest members of the unfavored band, in agreement with the systematics and the theoretical predictions (see ref. [Hel78] and the references quoted therein). The proposed protonic character for the $g_{9/2}$ band has been later confirmed by the measurement of the magnetic moment (μ=(4.64±0.59) nm) of the $I^{\pi}=9/2^{+}$, 1305.6-keV level [Ber80].

The recent works of Mitarai *et al.* [Mit97] and Bruce *et al.* [Bru00] confirmed the existence of the levels found by Hellmeister and coworkers [Hel78] and extended the yrast band up to spin $33/2^{+}$ and $(37/2^{+})$, respectively.

A large number of new positive-parity states were assigned to ^{69}As in the current analysis. Examples of doubly gated coincidence spectra, revealing the newly observed transitions in are shown in Fig. 2.18. The respective spectra were extracted mainly from the $\gamma\gamma\gamma$-cube because of the better statistics compared to the $3p$-$\gamma\gamma\gamma$-cube. The low-lying non-yrast states have been better populated in the experiment at 95 MeV, therefore the data acquired at 95 MeV have been mainly used in the investigation of these states. For the high spin analysis, the 105 MeV data set has been exclusively used.

Low-lying positive-parity states in ^{69}As

The current analysis confirms the previous found states at 2210.7 and 3263.2 keV of spin $11/2^+$ and $15/2^+$, respectively. A new level at 4306.1 keV is proposed. The low intensity of the decaying 1042.9 keV transition to the $15/2^+$ state at 3263.5 keV does not allow DCO measurements and firm spin assignment for the level at 4306.1 keV. However, the level at 4306.1 keV shows the same degree of signature splitting with the previously observed $11/2^+$-$15/2^+$ unfavoured yrast structure. Therefore, a tentative spin of $19/2^+$ is suggested for this state. The double gating procedure using at least one of the transitions depopulating the unfavored structure led to the identification of new states at 2808.0, 3216.8, 3507.1, 3660.4, 3840.2, and 4148.2 keV (see Fig. 3.2). Good statistics allowed the extraction of the multipole order of the transitions depopulating these levels supporting the spin assignments of $13/2^+$, $13/2^+$, $15/2^+$, $17/2^+$, $17/2^+$ and $17/2^+$, respectively. The spectrum presented in Fig. 2.18(a) shows a double gate on the 853.8-1103.8 keV transitions. All the $17/2^+$ states enumerated above have a decay branch on the $15/2^+$ state at 3263.2 keV via the 397.2-, 577.0-, and 885.0-keV γ-rays. The investigation of the doubly gated spectra using as gates intense transitions depopulating the yrast band revealed a second decay path of the newly observed levels on the yrast levels, thus confirming their placement in the level scheme of ^{69}As.

A new state at 2169.0 keV has been found, populated by the 639.0-keV γ-ray and decaying by the 635.0-, 952.7-, and 1305.8-keV transitions (see Fig. 3.2). The measured DCO ratio for the 1305.8-keV transition, obtained by gating on the intense 863.2-keV γ-ray (ΔI=1) is consistent with a ΔI=1 character for the 1305.8-keV line, suggesting an I=9/2 spin assignment for the level at 2169.0 keV. The level is populated by the 639.0 keV transition decaying from the positive parity state at 2808.0 keV. No feeding from higher negative-parity levels has been observed. Therefore, a positive parity is tentatively proposed for the 2169.0-keV level, although negative parity cannot be excluded. The coincidence data revealed the existence of the state at 1534.0 keV whose main decay path is to the first negative-parity excited level of 98.2 keV. A $5/2^+$ state closely spaced with the yrast $9/2^+$ state exists in the heavier ^{71,73,75,77}As isotopes, investigated by transfer reactions in the work of Betts *et al.* [Bet71]. Within that work, spin and parity $5/2^+$ for the respective states have been assigned, based on measured deuteron angular distributions. Such a spin and parity assignment is in agreement with the theoretical predictions [Bet71]. Following these arguments, a spin-parity $(5/2^+)$ is proposed for the state at 1534.0 keV in ^{69}As.

The DCO ratios of the 340.5-, 648.5-, and 828.3-keV transitions populating the three $17/2^+$ non-yrast newly observed states indicate a dipole, which results in the assignment of I=19/2 for the level at 4488.7 keV (see Fig. 3.2 and Table A.2). A positive parity assignment for the level at 4488.7 keV would imply the existence of at least one stretched $E2$ transition to one of the $15/2^+$ states but there is no experimental evidence for such a transition. Similar decay sequences have been observed in the light even-odd Ge isotopes. Polarization measurements for the $19/2 \rightarrow 17/2^+$ connecting transitions were always consistent with an electric character, leading to a negative-parity assignment for the states of spin I=19/2 [Her95, Zob80, Bec97]. Such decays have already been observed in ^{71}As, where three presumably $19/2^{(-)}$ levels have been found, all populating at least one of the

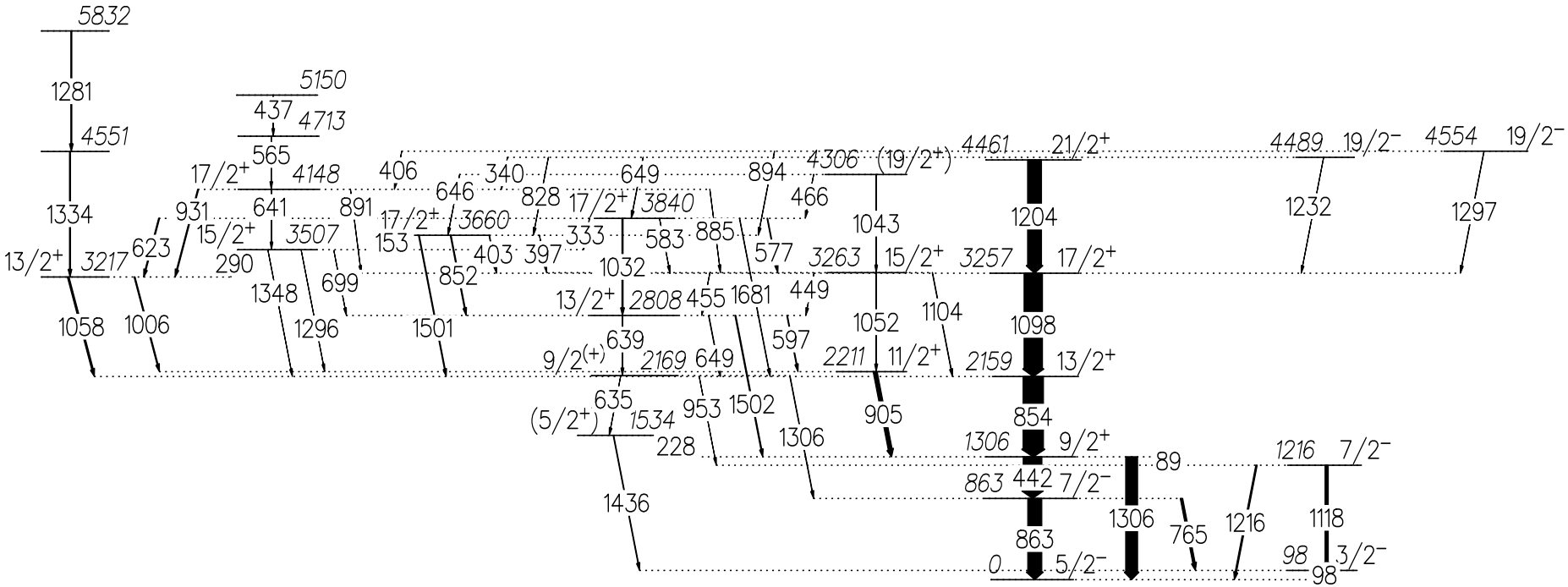

Figure 3.2: *Partial level scheme of* ^{69}*As showing the low-lying positive-parity states obtained from the present work. The widths of the arrows are proportional to the* γ*-ray intensities. The ground state has the spin and parity* $5/2^-$.

$17/2^+$ levels of ^{71}As [Zig94]. As a consequence, a negative-parity assignment for the state at 4488.7 keV is clearly favored by a detailed consideration of the decay pattern of the γ-cascades, the observed and expected yrast states and the systematics of the odd-A Ge and As isotopes.

The coincidence data for ^{69}As show a clear evidence for the existence of a second I^π=19/2 state at 4554.0 keV (see Fig. 3.2). The spin of this level has been fixed by the DCO values of the 893.6- and 1297.0-keV transitions which both indicate a dipole character. The observation of several decaying transitions toward the negative-parity states and accounting for the systematic features presented above in connection with the first I=19/2 state, a negative-parity is assigned to the level at 4554.0 keV.

Positive-parity high-spin states in ^{69}As

At high-spin, the positive-parity states in ^{69}As can be organized into four rotational-like bands, labeled from 1 to 4 in the level scheme of Fig. 3.3. Among them, the Band 3 is mostly populated and it was partially investigated in the previous works [Mit97, Bru00]. Bands 2 and 4 have been observed for the first time, as well as most of the additional levels forming short sequences parallel to bands 1, 2, 3 and 4.

Band 1

The band labeled *Band 1* in Fig. 3.3 includes the previously known yrast levels at 2159.4, 3257.0, and 4461.2 keV and the new levels at 5941.0, 7446.5 and 7627.2 keV. The DCO ratios of the 1479.8- and 1686.2-keV γ-rays, are both consistent with a stretched $E2$ character (see Table A.2), supporting the $25/2^+$ and $29/2^+$ spin assignments for the levels at 5941.0 and 7627.2 keV, respectively. The state of spin $23/2^+$ at 5711.1 keV found in ref. [Mit97] has been confirmed in the present analysis. Besides, this state was found in the present analysis to be populated by the 1735.4-keV transition, decaying from the state at 7446.5 keV. The DCO ratio of the 1505.5 keV transition is consistent with that expected for a dipole radiation, supporting the spin asignment of I=$27/2^+$ for the state at 7446.5 keV. In fact, the sequence consisting of levels at 5711.1, 5941.0, 7446.5, and 7627.2 keV exhibit the same degree of signature splitting as the yrast sequence below spin $21/2^+$. This makes the newly observed sequence a candidate for the continuation of the ground-state band at higher spins.

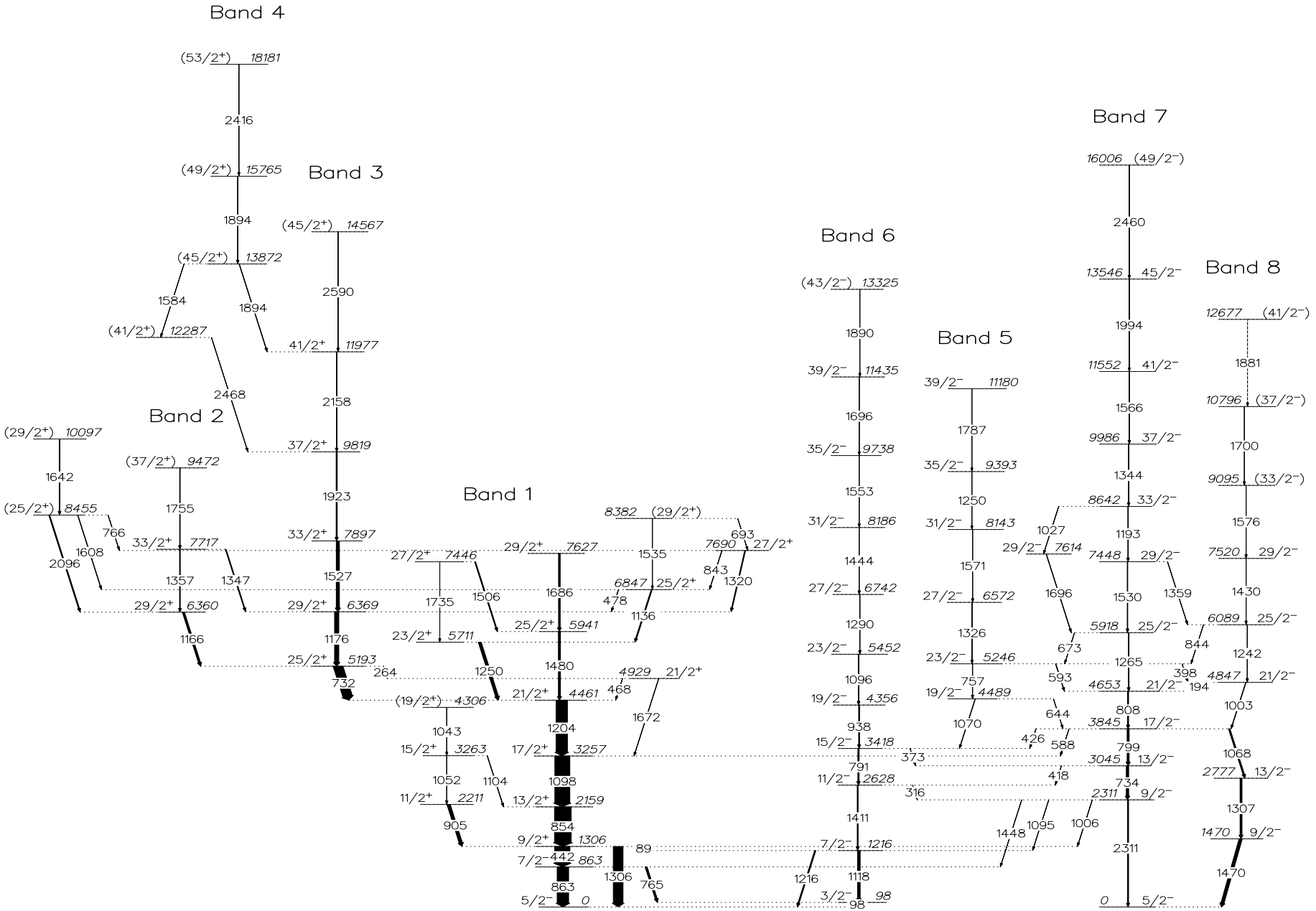

Figure 3.3: *Partial level scheme of* ^{69}*As showing the rotational bands obtained from the present work. The widths of the arrows are proportional to the* γ*-ray intensities. The ground state has the spin and parity* $5/2^-$*.*

Band 2

Above spin $I^{\pi}=25/2^{+}$ a forking into two almost degenerate $I^{\pi}=29/2^{+}$ states occurs. On each of these states rotational-like structures develop (bands 2 and 3 in Fig. 3.3). The level at 6359.7 keV is yrast and is fed by a cascade consisting of 1357.1- and 1755.4-keV transitions depopulating the $33/2^{+}$ and $(37/2^{+})$ yrast states at 7716.8 keV and 9472.2 keV, respectively. The spin $I^{\pi}=29/2^{+}$ of the 6359.7 keV yrast state is fixed by the DCO ratio of the depopulating 1166.4-keV γ-ray, whereas the spin $I^{\pi}=33/2^{+}$ of the 7716.8 keV yrast level is fixed by the DCO ratio of the 1347.4-keV γ-ray populating the second $29/2^{+}$ state at 6369.4 keV (see Table A.2). The $\Delta I = 2$ spin difference between the newly reported levels in Band 2 suggests the $I^{\pi}=37/2^{+}$ spin assignment for the state at 9472.2 keV. Although Band 2 is yrast in the spin region it is observed it carries little flux and the higher spin configurations decay mainly to the second $29/2^{+}$ state (Band 3 in Fig. 3.3).

Band 3

The results of the current investigations have confirmed the states up to spin $37/2^{+}$ in Band 3 (see Fig. 3.3). A γ-ray of 2091 keV has been observed previously [Bru00] as feeding the $37/2^{+}$ level of Band 3. The data from the present experiments do not show any coincidence relation which would support the placement of the 2091 keV transition in the top of the level at 9819.4 keV. Instead, this level was found in the present work to be populated by two γ-rays of energies 2157.8 and 2460.8 keV. The DCO ratio of the 2157.8 keV transition is consistent with a stretched $E2$ character. A tentative spin of $(45/2^{+})$ has been asigned for the maximum observed state in Band 3, the level at 14567.0 keV.

Band 4

At spin $41/2^{+}$ Band 3 is found from the present analysis to be crossed by another configuration, labeled Band 4 in the level scheme of Fig. 3.3. The poor statistics and the presence of the 1894 keV doublet did not make DCO measurements possible above the 11977.2-keV level. The high excitation energy of the levels they depopulate suggests an $E2$ character for these transitions. Band 4 has been observed in the up to a tentative spin $(53/2^{+})$ and an excitation energy of 18180.6 keV.

Figure 2.18(b) shows a 732.1-1894.3 keV doubly-gated spectrum. The chosen double-gate selects only the transitions in bands 3 and 4, and constitutes a firm evidence for the placement of the second 1893.5-keV transition in the level scheme of ^{69}As.

The coincidence analysis supports the placement in the level scheme of ^{69}As of other two irregular positive-parity structures. The states at 6847.3, 7689.9 and 8382.4 keV form a sequence of spins $25/2^{+}$-$27/2^{+}$-$(29/2^{+})$. The spin $27/2^{+}$ assigned to the level at 7689.9

is based on the DCO value of the 1320.5-keV transition which is consistent with a dipole character. A 1322-keV transition has been reported in ref. [Mit97] which is most likely the 1320.5-keV transition discussed above. The present data support its placement but not the spin. The second new sequence consists of the 8455.4- and 10097.0-keV states. The DCO ratio of the 2095.7-keV transition, consistent with a quadrupole character, suggests a $I^{\pi}=33/2^{+}$ spin assignment for the level at 8455.4 keV. The observation of the 765.5- and 1608.1-keV transitions populating the firmly established $27/2^{+}$ state at 7689.9 keV and the $25/2^{+}$ state at 6847.3 keV, respectively, rules out the $I^{\pi}=33/2^{+}$ spin value for the state at 8455.4 keV. Therefore, a spin $I^{\pi}=25/2^{+}$ has been proposed for this state.

3.2.2 Negative-parity states

The negative-parity part of the level scheme of ^{69}As has been considerably extended with respect to the previous works [Mit97, Bru00].

Low-lying negative-parity states

The states below 3 MeV excitation energy show a irregular energy spacing (see Fig. 3.4), presumably being of single-particle character. The first excited state lies at only 98.2 keV excitation energy. From angular distribution measurements, a spin $I^{\pi}=3/2^{-}$ has been assigned to this level [Nol74].

Two new $9/2^{-}$ levels at 1470.3 and 2311.2 keV have been reported by Mitarai *et al.* in ref. [Mit97]. The state at 1470.3 keV was found to be fed by a quadrupole 1306.8-keV transition decaying from the state at 2777.1 keV. Furthermore, the sequence consisting of the 1470.3-, 1306.8-, and 1067.5-keV quadrupole transitions was found to form a decay path parallel to the 2311.2-, 734.2-, and 799.2-keV transitions with the level at 3844.6 keV as a common level [Mit97]. Bruce and coworkers confirmed the decay pattern observed by Mitarai *et al.* and assigned spin and parities to the involved states [Bru00].

The two sequences have been well populated in both data sets used in the present analysis. Therefore, DCO ratios for the connecting transitions could be extracted with good accuracy. The ratios are all consistent with a quadrupole character supporting the $13/2^{-}$ spin assignment for the states at 2777.1 and 3045.4 keV, $17/2^{-}$ for the state at 3844.7 keV and $21/2^{-}$ for the state at 4652.9 keV.

A third new rather well populated sequence consisting of the levels at 1216.3, 2627.6, and 3418.5 keV and has been observed in the top of the 98.2 keV level. The DCO ratios of the 1118.1-, 1411.3-, and 790.9-keV γ-rays are compatible with a $\Delta I=2$ character, supporting the $7/2^{-}$, $11/2^{-}$ and $15/2^{-}$ spin assignment for the respective levels. The crossover transitions of 1322.0- and 1259.1-keV between the newly observed structure and the yrast positive-parity states at 1305.6 and 2159.4 keV, respectively, have been used for a cross-check of the DCO ratios for multipole determination and spin assignment. The negative parity assignment to the levels at 1216.3, 2627.6, and 3418.5 keV is also supported by the observation of the weak cascade of dipole γ-rays between these levels and the levels at 2311.1, 3045.4, and 3844.6 keV (see Fig. 3.4). Thus, the newly observed sequence appears to be the signature partner of this latter sequence. The excitation energy of 3418.5 keV and the existence of the decay branch to the yrast $13/2^{+}$ state makes the

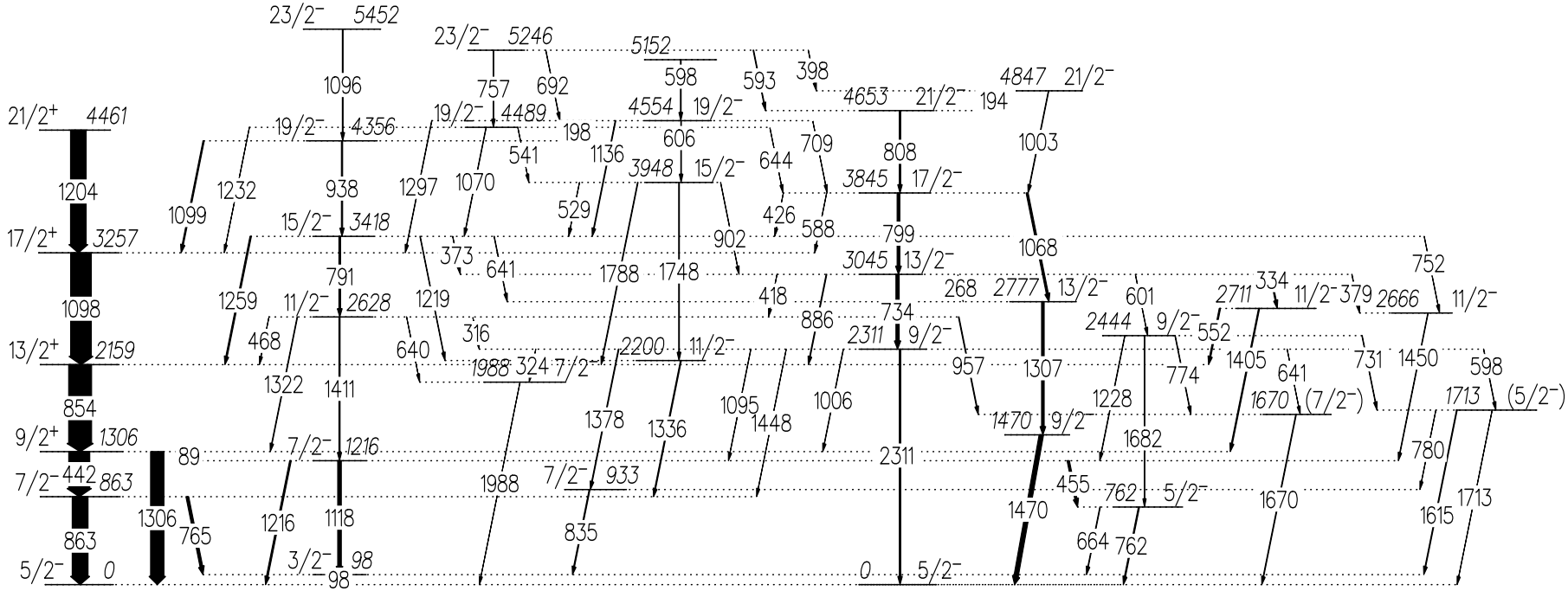

Figure 3.4: *Partial level scheme of ^{69}As showing the low-lying negative-parity states obtained from the present work. The widths of the arrows are proportional to the γ-ray intensities. The ground state has the spin and parity $5/2^-$.*

I^{π}=15/2^{-} state a certain candidate for the octupole state in ^{69}As, in agreement with the systematics [Her95, Bec97]. On the top of this state two rotational-like cascades have been observed (bands 5 and 6 in Fig. 3.3). The second candidate for the octupole state in ^{69}As is the level at 4554.0 keV, observed for the first time in the present work.

Several other low-lying states of negative parity have been placed in the level scheme of ^{69}As, based on the coincidence data acquired in the experiment at 95 MeV. They are weakly populated and decay by γ-rays with energies between 250 keV and 2 MeV.

High-spin negative-parity states in ^{69}As

Four rotational-like structures start to develop above 3 MeV excitation energy and they were labeled from 5 to 8 in the level scheme of Fig. 3.3. Placement of the levels in the bands is based on the measured relative intensities of the transitions depopulating the respective levels and γ-ray coincidence data.

Band 5

Band 5 was observed in the present analysis up to an excitation energy of 11180.3 keV. The spin assignments were deduced from the measured DCO ratios which are close to 1.0 for all in-band transitions, hence giving evidence for the ΔI=2 nature of these γ-rays (see Table A.2). Since the 19/2^{-} state at 4488.7 keV has decay branches to states of both positive and negative parity, it is more likely single particle in origin and may constitute the bandhead for Band 5. The band becomes yrast and shows an irregularity around spin 31/2^{-}.

Band 6

The state at 4356.2 keV is more likely the bandhead of Band 6. This band shows the same spin sequence as Band 5. The DCO ratios of the inband transitions are all consistent with a stretched quadrupole character. Band 6 has been observed up to a tentative spin of (43/2^{-}) corresponding to an excitation energy of 13325.0 keV. The coincidence spectrum obtained by gating on the 937.7- and 1696.1-keV transitions is shown in Fig. 2.18(c). The transitions assigned to Band 6 in ^{69}As are marked in the figure. No interband transitions connecting this band with the bands 7 and 8 could be identified (see Fig. 3.3).

Band 7

On the top of the level at 3844.6 keV two bands start to develop (bands 7 and 8 in Fig. 3.3). Band 7 is yrast and is well populated in the experiment at 105 MeV beam

energy. The levels at 4652.9 and 5918.3 keV have been previously reported [Mit97]. In the present analysis, Band 7 has been extended up to an excitation energy of 16005.6 keV and a tentative spin of $(49/2^+)$. The γ-ray spectrum in Fig. 2.18(d) shows several transitions, e.g. the 1530.0-, 1193.2-, and 1344.2-keV lines which were firmly assigned to the negative-parity Band 7 in ^{69}As. DCO analysis for the inband transitions yields stretched $E2$ multipolarity for all band members. Around 7.5 MeV excitation energy a duplication of the $I^\pi=29/2^-$ level occurs, maybe connected with the irregularity in rotational energy observed in this spin region.

Band 8

Band 8 has been populated in the present experiments up to a tentative spin of $(41/2^-)$ and 12677.0 keV excitation energy. Based on DCO measurements, the spins could be firmly assigned only to the low members of the band. However, Band 8 does not show any irregularity in the spin region it is observed, appearing consistent with a rotational cascade of $E2$ transitions.

Chapter 4

Theoretical considerations

4.1 A∼70 mass region

Figure 4.1 presents the Nilsson diagram for the A∼70 mass region. The structure of the proton and neutron single-particle spectra is very similar and the relevant single-particle properties can be sufficiently well illustrated by showing only diagrams of one kind of particles. The orbitals are labeled by the shell model quantum numbers lj at zero deformation, where l is the orbital angular momentum and j is the particle angular momentum. The microscopic structure of the nuclei in the A∼70 mass region is primarily determined by the $1g_{9/2}$, $2p_{1/2}$, $1f_{5/2}$ and $2p_{3/2}$ orbitals. At zero deformation the spherical shell model is valid, as shown by the large energy gaps at Z, N=28, 50. In the shell model limit, the $g_{9/2}$ orbital is a high particle state and the lowest $9/2^+$ state would lie at high excitation energy. If however, nuclei were becoming more deformed, the orbits resulting from the splitting of the $g_{9/2}$ orbital under the influence of the deformed field come down in energy and the excitation of the lowest $9/2^+$ state decrease. As the deformation $\mid \beta_2 \mid$ increases, new energetically competing gaps occurs, generating a kind of deformed magic numbers at Z, N=34, 36 for large oblate deformations and at Z, N=34, 38 at prolate deformations. These gaps give rise to a strong shape variation as a function of both particle number and spin and lead to pronounced shape coexistence effects. In the case of shape coexistence the collective potential possesses two (or more) local minima and in each of these minima rotational bands develop. Depending on the depth of these various minima, the different bands change their position and can become yrast or excited bands. With the discovery of the first excited 0^+ state close in energy with the first 2^+ state in ^{72}Se [Ham74, Ham76] the possibility of nuclear shape coexistence was taken into account for the first time in the A∼70 mass-region. Prolate-oblate shape coexistence has been theoretically predicted and experimentally established in the Br, Se and Kr isotopes [Pie81, Her87, Luh85, Hee86].

An inspection of the Nilsson diagram in Fig. 4.1 seems to show no preference of nuclei in the mass region for oblate or prolate shapes. Small prolate deformations around 0.2-0.25 were found to characterize the ground states of most of the light Ge (Z=32) isotopes. Large prolate deformations are experimentally well established in the light Kr (Z=36) and Sr (Z=38) isotopes. Oblate ground state rotational bands were found in $N = Z$, $^{68}_{34}$Se [Fis00, Lis00] and $^{72}_{36}$Kr nuclei [Kel01, Bou03]. The competing gaps between

the Nilsson single particle levels at prolate and oblate deformations and the fact that a collective oblate rotation perpendicular to the symmetry axis involves a lower moment of inertia making the oblate rotational band energetically unfavored, are both responsible for the rare occurrence of the oblate ground-state structures in nuclei.

In the following, some general features of the even-even and odd-A nuclei will be discussed, because they are considered to be the most relevant for the present work. Systematic trends based on experimental observations are pointed out, as well as some of the theoretical models which provided the most successful interpretation of the experimental results and proved their predicting power concerning the structure of these nuclei.

The rotational positive-parity bands of the odd-even nuclei in the region are dominated by the $g_{9/2}$ intruder orbital. Their structure depends on the position of the Fermi level and deformation. Thus, strong-coupled structures are expected to occur when the odd particle lies on the high-K orbit under the influence of a weak Coriolis interaction ($\sim< j, K \pm 1 \mid j_{\pm} \mid j, K >$). In such a case, the rotational bands follow the I, $I+1$, $I+2$, ... pattern and the corresponding states are connected by strong $E2$ and $M1/E2$ transitions. For low-K orbits the Coriolis interaction is strong, leading to rotational aligned structures. In this case, the strong Coriolis interaction lowers the states belonging to the favored band (j, $j+2$, ...) more than those of the unfavored band ($j+1$, $j+3$, ...). A cascade of intense $E2$ intraband transitions dominates a rotational aligned band.

For odd nuclei with Z or $N \approx 34$, low-K orbits are available at prolate deformations, whereas high-K orbits are close to the Fermi level at oblate deformations. The strong-coupling-like pattern which develop at low spin in ^{69}Se can only occur if the odd-neutron occupies the $K^{\pi}=9/2^{+}[404]$ Nilsson orbit at an oblate deformation. The decoupled structure of the ground state band in ^{69}As involves low-K underlying orbits, leading to a Coriolis force which is strong enough to be able to produce the large signature splitting observed at low excitation energies. Since the Fermi level for the $Z = 33$ nuclei lies at the bottom of the $g_{9/2}$ orbital, low-K values are involved only at prolate deformations (see Fig. 4.1).

With increasing spin, new phenomena occur, such as multiple backbendings in the yrast spectrum caused by particle alignments. In the ground-state configuration all nucleons except the odd nucleon are assumed to be paired to spin 0 under the influence of the pairing interaction. The nucleus can be regarded as a superfluid having low rigidity and correspondingly, a small moment of inertia. With increasing the rotational velocity, however, the Coriolis force acting on a pair of nucleons becomes strong enough to counteract the pairing force acting between particles, the pair breaks and the Coriolis force will tend to align the single-particle angular momenta along the rotation axis. This process is called rotational alignment (RAL, [Ste72]) or rotational decoupling. The strongest rotational alignment takes place for high-j particles. The RAL mechanism provides the natural explanation for the backbending phenomenon. In terms of band crossings this is the so-called S-band crossing, e.g. the crossing of the ground-state band with a 2qp-band which has a larger moment of inertia [Joh72]. In this way, the nucleus gains angular momentum. At still higher rotational frequencies a second pair of high-j particles align, then a third one, and so on.

In the $N = Z$ even-even nuclei the alignments are expected to occur simultaneously for protons and neutrons. In the situation where the nuclei have two coexisting shapes,

in each minimum, particle alignment will proceed and cause the traditional S-band type crossing. As the two minima are associated with different deformations and implicitly with different moment of inertia, the minima themselves can have an additional crossing as the rotational frequency changes to favor one shape or another.

In the A∼70 mass region, the nuclei gain angular momentum by the breaking of the $g_{9/2}$ nucleon pairs. The maximum gain in angular momentum could be obtained from one such a broken pair is $8\hbar$ (=9/2+7/2). In the light Ge, As, and Se isotopes, the first particle alignment usually occurs in the I^{π} ≈6^{+}-10^{+} spin region (I^{π} ≈$21/2^{+}$-$29/2^{+}$ in the odd-even nuclei) and at rotational frequencies $\hbar\omega$ ≈0.55-0.6 MeV [Lim81, Jen01, Mit97].

Since the shape of nuclei in this mass-region is not stable, a band crossing can also represent the crossing of shapes. Several bands with different deformations and completely unrelated structure might compete near the yrast line, leading to crossings as the one or the other becomes favored in energy at a certain angular momentum. Such crossings usually occur between collective and less collective shapes, since the collective shapes involve a larger deformation and consequently, a larger moment of inertia [Fis03].

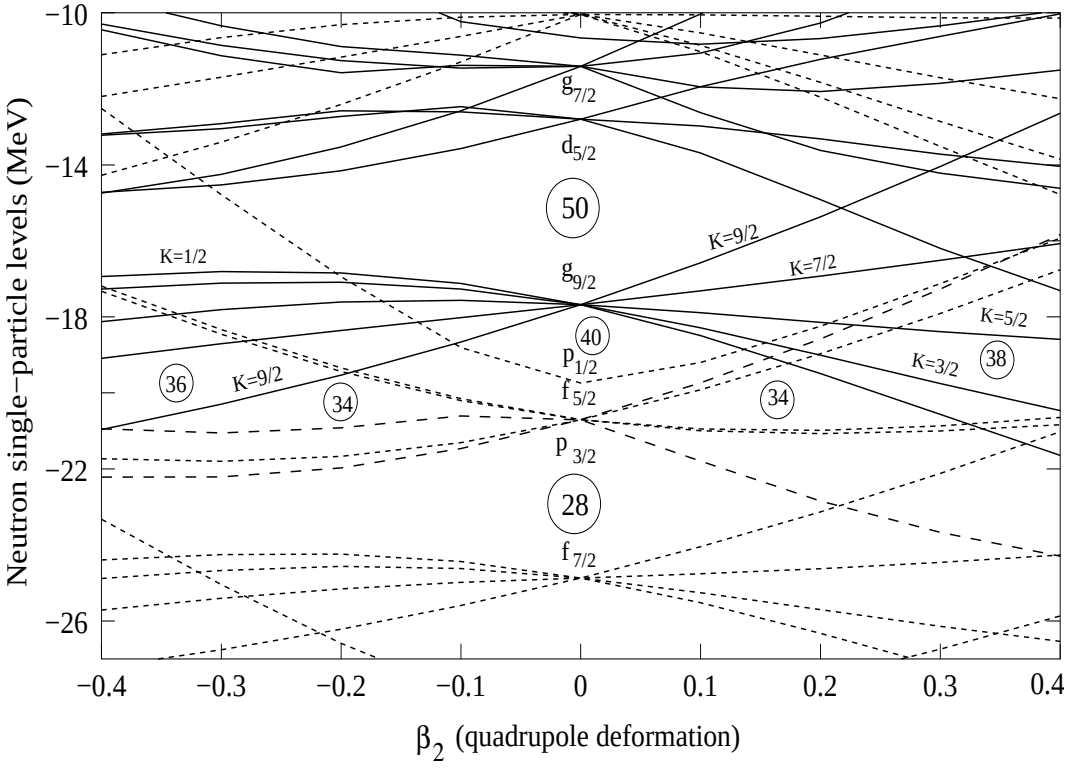

Figure 4.1: *Nilsson diagram for neutrons with N ≥28. Solid (dashed) lines indicate positive (negative) parity states.*

The negative-parity states in the nuclei in the A∼70 mass region are mainly generated by the valence-particles lying in the negative-parity orbitals $p_{3/2}$, $f_{5/2}$ and $p_{1/2}$ (see Fig. 4.1). At low spins, the light odd-Ge, -As, and -Se isotopes show a large density of levels, in general concentrated below 3.5 MeV excitation energy, suggesting small deformations

and possibly predominant shell model characteristics in the low-energy region. With increasing the neutron number, as the nuclei become more deformed, the negative-parity orbitals mentioned above constitute bandheads for rotational bands.

Negative-parity high-spin states ($I^{\pi} > 7^{-}$ in the even-even nuclei or $I^{\pi} > 23/2^{-}$ in the odd-A nuclei) involve particles in the $g_{9/2}$ orbital. By the alignment of the $g_{9/2}$ particles, the nucleus can gain angular momentum and, consequently, built high-spin negative-parity values.

The classification and interpretation of the structure of nuclei in the A$\sim$70 mass-region has always been a challenge to theoretical nuclear structure physics. Models which were rather successfull in describing the observed properties in nuclei in other mass-regions were applied also to the A$\sim$70 nuclei. Below, a short enumeration of the most used models is given.

- *The IBM model.* Within this formalism the nucleus is viewed as a system of boson-like nucleon pairs coupled to low angular momenta (usually only 0 or 2) and interacting via a phenomenological Hamiltonian. The interacting boson approximation, first introduced by Arima and Iachello [Ari75] with its countless extensions developed since then, has, in particular, yielded a good description of the excitation energies of many yrast and non-yrast states, in various mass-regions. In the A$\sim$70 mass-region, the IBA formalism was applied, for example, to the even Ge [Hsi92] and ^{68,70,72}As [Soh98, Pod95, Soh99] isotopes.

- *The cranked Nilsson-Strutinsky (CNS) approach* - it describes the nucleus as a system of independent nucleons moving in a deformed rotating field [Afa99]. The model was able to explain a lot of high-spin phenomena such as band crossings and band terminations in a rather simple and intuitive way. It has been used to describe the properties of the high-spin rotational bands observed in ^{70}Se, ^{68}Ge and ^{70,72,73}Br [Rai02, War00, Jen02, Ple00, Ple01].

- *The VAMPIR approach* - it has been developed to describe the complex structure of the nuclei in the A$\sim$70 mass-region. In the approaches included in the VAMPIR family (**V**ariational **A**fter **M**ean-field **P**rojection **I**n **R**ealistic model spaces) [Sch84], the states of a nuclear spectrum are approximated by several symmetry-projected Hartree-Fock-Bogoliubov (HFB) vacua. The underlying mean-field is determined by a chain of variational calculations after projection. These methods were applied with good success to the rather complex shape-coexistence phenomena in ^{68,70}Se, ^{72,74}Kr and ^{68}Ge [Pet2, Pet02, Pet90].

- Models with one, two or three nucleons coupled to a phenomenological core were also applied to describe the nuclei in this mass-region [Sou82, Hel78, Joh97, Paa76a, Paa76b]. For the core, a rigid axial [Boh52] or a triaxial rotor [Dav58] is used. The additional nucleons are described as quasiparticles moving in the deformed potential of the core.

Unfortunately, all these models have their limitations. For example, the cranking model does not yield proper quantum mechanical wavefunctions and hence cannot be

used to obtain quantitative information about electromagnetic transitions or form factors. The boson models, at least in their simple versions, are not suitable for studying high-spin phenomena. The VAMPIR approaches are unable to describe the odd mass nuclear systems on the same level of sophistication as the even-even ones. A particle-rotor model applied to nuclei with coexisting shapes can describe only a very limited number of states as long as in these models the shape parameters are kept constant throughout the calculations. However, despite these restrictions, the models enumerated above can offer a good description of the basic properties of the nuclei in the $A \sim 70$ mass-region.

4.2 Low-lying states

The positive-parity states of nuclei in the A$\sim$70 nuclei are the most populated in the heavy-ion reactions. The $I^\pi = 9/2^+$ constitutes the band-head of the yrast positive-parity rotational bands of the odd-Ge, odd-As and light odd-Se isotopes. Apart from the yrast band, several low-lying non-yrast states have also been observed, the yrare $13/2^+$ and $17/2^+$ states being identified in almost all odd-A nuclei in the mass-region. In the following two subsections, the systematic features observed in the experimental spectra of the light odd-As, odd-Se isotopes and the adjacent even-even cores are shortly outlined. The models employed to describe the experimental results and their achievements are also presented.

4.2.1 Positive-parity states

Odd-As isotopes

The low-lying positive-parity level schemes of the odd As isotopes show systematic features. General trends like the small splitting between the lowest $11/2^+$ and $13/2^+$ states and between the $15/2^+$ and $17/2^+$ or the presence of the $9/2^+$-$5/2^+$ doublet at low excitation energies have already been discussed in the past [Hei77, Hei76, Hel78]. The comparison between the low-lying positive-parity yrast structures of odd-As nuclei and the structures of the corresponding even-even cores suggested moderate deformations for these nuclei [Hel78].

Figure 4.2 shows the systematics of the $g_{9/2}$ bands in the ^{69,71,73}As nuclei and the rotational bands in the neighboring even-even Ge and Se nuclei, as proposed in Refs. [Hei77, Hel78]. In the references quoted above, the details of such an analysis are discussed in terms of a simple particle-core coupling:

- The positive-parity states in the odd-As isotopes result from an excited particle in the $g_{9/2}$ shell coupled to the even-even core. The yrast states form decoupled-like bands $I = j, j+2, j+4 \ldots$ built on the lowest positive-parity state, $9/2^+$.

- The excitation energies of the $g_{9/2}$ band in the odd-As isotopes are considerably

lower than the Ge core states and much closer to the respective states of the even Se isotopes.

- The signature splitting between the $11/2^+$ and $13/2^+$ states increases from 51 keV in ^{69}As to 256 keV in ^{73}As whereas the $15/2^+$-$17/2^+$ splitting increases from 5 keV in ^{69}As to 100 keV in ^{73}As.

- Going from ^{68}Ge to ^{72}Ge, the $B(E2, 2^+ \rightarrow 0^+)$ values increase slightly. The $E2$ strengths of the $13/2^+ \rightarrow 9/2^+$ transitions in the ^{69,71,73}As nuclei also increase, but they are in all cases a factor of 1.2 to 2 larger than the core transition probabilities. These facts rules out a simple weak-coupling interpretation.

In the last decades, several models have been proposed to understand the properties of the low-lying states in the odd-As nuclei. The investigations within the particle-core [Sch68, Hei76, Hel78] formalism indicated that a deformed picture with the inclusion of the Coriolis coupling provides the most adequate first-order representation of odd-A isotopes. A better parameterization for the core taking into account the γ deformation and a variable moment of inertia (VMI) has been proposed by Toki and Faessler [Tok75]. Within that approach, the small energy splitting between the $13/2^+$ and $11/2^+$ states and between the $17/2^+$ and $15/2^+$ states in ^{71,73}As are closely related to the triaxiality of the core [Tok76]. Recently, an IBFM treatment has been applied to the states below 1.5 MeV excitation energy in ^{73}As [Soh97].

Odd-Se isotopes

The structure of the odd-Se isotopes is more complex than the structure of odd-As isotopes due to the shape coexistence effect which is more pronounced in the Se nuclei. Calculations employing the Strutinsky method with a folded Yukawa potential including pairing effects predicted two minima in the potential energy curves for the light Se, Kr and Sr isotopes, one at large prolate deformations ($\beta_2 \approx$0.35-0.40) and the other at oblate deformations ($\beta_2 \approx$-0.30) [Naz85]. The energy of the oblate minimum is several hundred keV higher than the prolate one for $Z = N$=38 but it decreases with the neutron number to be some hundred keV below the prolate minimum for systems with Z, N=35, 36. Besides the more pronounced shape-coexistence phenomena, the selenium isotopes were found to exhibit larger deformations than the As-nuclei.

In Fig. 4.3 the positive-parity ground-state bands in ^{69,71,73}Se are compared. The energy of the $9/2^+$ bandhead decreases from 575 keV in ^{69}Se to 260 keV in ^{71}Se and becomes the ground-state in ^{73}Se. The $g_{9/2}$ band in ^{69}Se exhibits a fairly regular rotational character and a signature splitting which is smaller than the splitting observed in ^{71,73}Se. The δ values for the $11/2^+ \rightarrow 9/2^+$ transitions in ^{69,71}Se [Wio88b] and the $13/2^+ \rightarrow 11/2^+$ transition in ^{69}Se (present work) have been found to have a positive sign, indicating an oblate deformation for the $g_{9/2}$ yrast band in the low-spin region. In ^{73}Se, the $g_{9/2}$ band shows at low spin a large signature splitting, similar to that in ^{71}Se. Also in this nucleus a positive δ value has been derived for the $11/2^+ \rightarrow 9/2^+$ transition, which again pointed to

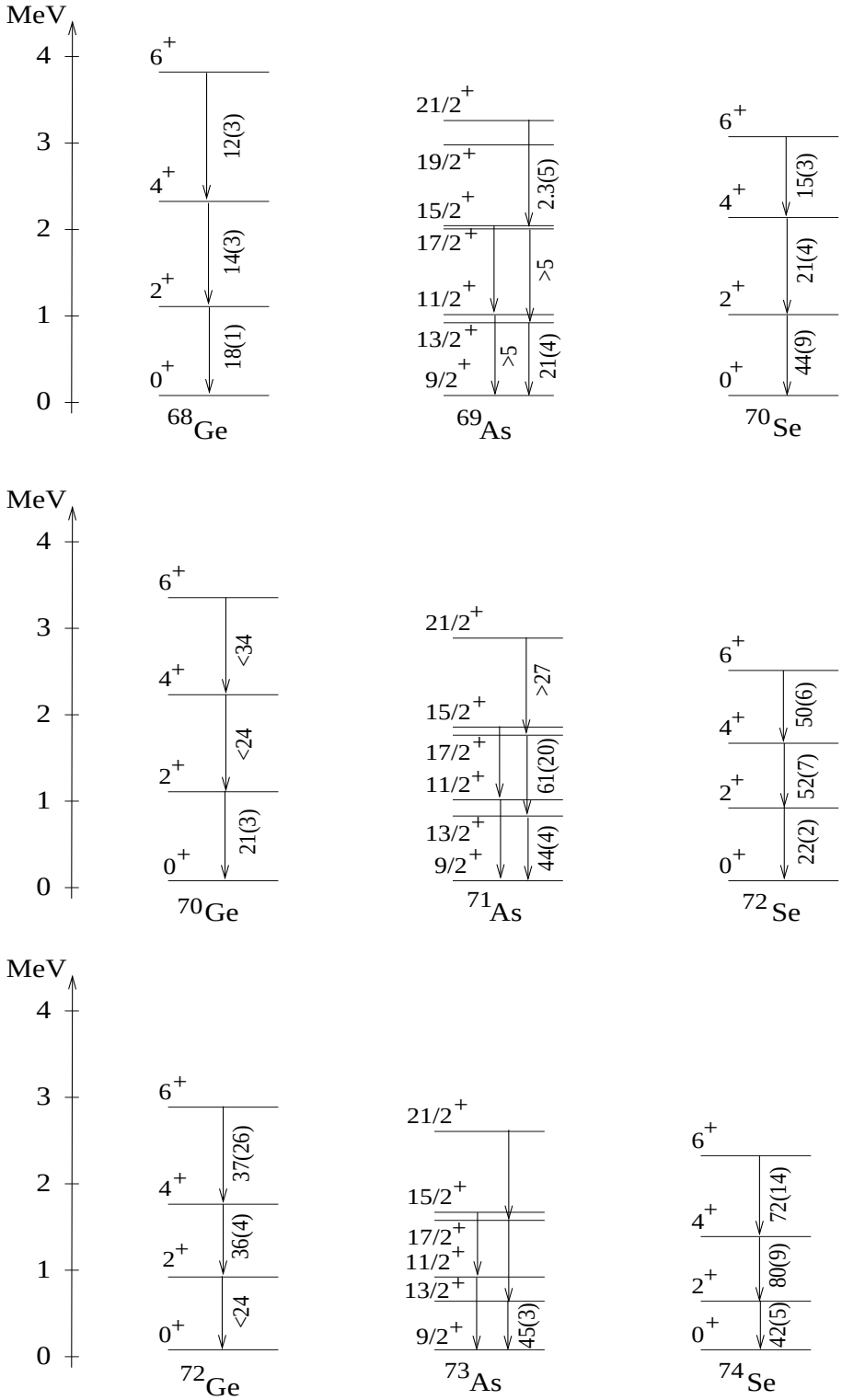

Figure 4.2: *Comparison of yrast positive parity states in odd-As isotopes with the core spectra of the even-Ge and -Se isotopes. $B(E2)$ values are given in W.u. The spectra of the odd-A nuclei have been shifted in order to bring the respective $9/2^+$ states to zero excitation energy.*

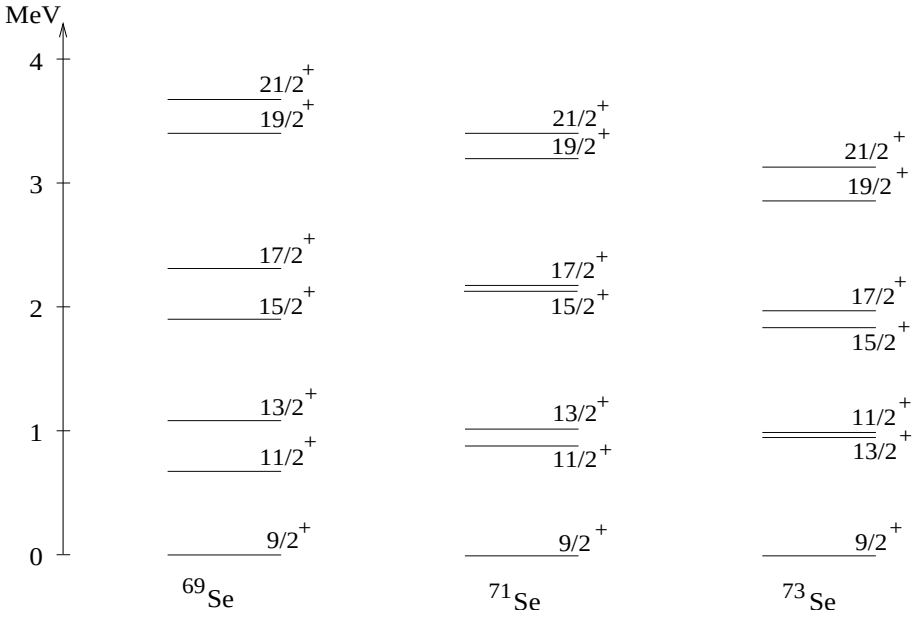

Figure 4.3: *Yrast sequences of the ^{69,71,73}Se isotopes. Each spectra has been normalized to the energy of the respective $9/2^+$ state.*

an oblate deformation. In contrast, the $15/2^+ \rightarrow 13/2^+$ transition has a negative δ value indicating a configuration different than that of the ground state.

The low-lying positive-parity structures in the odd-Se nuclei have been described in the past within the particle-rotor formalism introduced by Toki and Faessler [Tok75]. In ^{69,71}Se isotopes, the $g_{9/2}$ bands could only be reproduced if an oblate deformation with γ close to $-60°$ is assumed, but not for triaxial ($0° < \gamma < -60°$) or prolate shapes ($\gamma = 0°$) [Wio88a]. A relatively good overall agreement for excitation energies and transition probabilities has been obtained for ^{73}Se [Dew87]. Within that work, by introducing triaxiality ($\gamma = -33°$), it was possible to reproduce the experimental situation that the $9/2^+$-level is the lowest positive-parity state.

A description of the one-quasiparticle yrast positive-parity states in ^{69}As and ^{69}Se in the framework of Rigid Triaxial Rotor plus Particle (RTRP) model is also proposed in the present work. The model describes an odd system of nucleons by coupling a quasiparticle to a triaxial Davydov even-even core [Dav58]. Within this model, the shape of the nucleus is defined by two deformation parameters, namely the quadrupole deformation ε_2 and the asymmetry parameter γ. These parameters are kept fixed throughout the calculation (rigid rotor). In literature, the results of the RTRP-calculations are usually defined with respect to the "Bohr-Mottelson convention" [Boh69] according to which $\varepsilon_2 \geq 0$ and $0° \leq \gamma \leq 60°$ define a shape of a triaxial rotor with collective rotation. Since in a later section of this thesis, calculations employing the cranked Nilsson-Strutinsky model will be compared with the experimental data, for consistency, the results of the RTRP fit will be given with respect to the Lund convention [And76]. In this convention, the collective rotation is defined in the $\gamma = (-60°, 0°)$ interval.

The codes employed in this work [Gam, Asy, Pro] allow also calculations with a variable moment of inertia (VMI).

RTRP model

The RTRP model is described in detail in the original paper of Larsson, Leander and Ragnarsson [Lar78]. A particle couples to a rigid rotor so that the Hamiltonian of the odd-system can be written as

$$H = H_{sp} + H_{pair} + H_{core}. \tag{4.1}$$

The single-particle Hamiltonian H_{sp} describes the odd-particle in a deformed modified oscillator potential characterized by the deformation parameters ε_2, ε_4 and γ. The calculations are based on the modified oscillator model [Lar73], where it is assumed that the interaction of the odd nucleon with the nuclear field can by described by the one-body Hamiltonian expressed in stretched coordinates:

$$H_{sp} = T + V = \tfrac{1}{2}\hbar\omega_0^t(-\Delta + \rho^2) - \hbar\omega_0^t \tfrac{2}{3}\epsilon_2\sqrt{\tfrac{4\pi}{5}}\rho^2\left[\cos\gamma Y_{20} - \tfrac{\sin\gamma}{\sqrt{2}}(Y_{22} + Y_{2-2})\right] -$$

$$-\kappa(N)\hbar\omega_0^0\{2l_t \cdot s + \mu(N)(l_t^2 - < l_t^2 >_N)\} + 2\hbar\omega_0^t\rho^2\epsilon_4 V_4(\gamma) \tag{4.2}$$

where ε_2 and γ specify the degree of deformation and the departure from axial symmetry, respectively. This type of nonisotropic oscillator was studied in detail in e.g., ref [New60]. In the limit $\gamma = 0°$ and $\gamma = -60°$, the Hamiltonian 4.2 becomes the Nilsson Hamiltonian for the axial symmetric case. The parameters $\kappa(N)$ and $\mu(N)$ are the shell parameters and their values are chosen in such a way that they vary with N in a smooth way and for $\epsilon_2 = \epsilon_4 = \gamma = 0$, the sequence of levels of the shell model is reproduced. The standard values for these parameters are given in literature [Ben85].

H_{pair} represents the pairing force acting between like nucleons and it is included in the model by a standard BCS calculation, so that the single-particle energies are replaced with quasiparticle energies and appropriate pairing factors are attached to all single-particle matrix elements.

The core Hamiltonian has the typical form

$$H_{core} = \sum_{\kappa=1}^{3} \frac{\hbar^2}{2\Theta_\kappa} R_\kappa^2 = \sum_{\kappa=1}^{3} \frac{(I_\kappa - j_\kappa)^2}{2\Theta_\kappa}, \tag{4.3}$$

where R is the core angular momentum which can be expressed through the total angular momentum I and the particle angular momentum j. The moments of inertia Θ_κ are assumed to be of hydrodynamical type

$$\Theta_\kappa = \frac{4}{3}\Theta_0 \sin^2\left(\gamma + \frac{2\pi}{3}\kappa\right). \tag{4.4}$$

The fixed moment of inertia Θ_0 can be derived from the core excitation energy $E(2^+)$.

The strong-coupling basis is used for the diagonalization of the particle-rotor Hamiltonian

$$|IMK\nu> = \sqrt{\frac{2I+1}{16\pi^2}} \sum_{Nlj\Omega} c_{Nlj\Omega}^{(\nu)} \left(D_{MK}^I |Nlj\Omega> + (-1)^{I+K} D_{M-K}^I |Nlj-\Omega>\right). \tag{4.5}$$

The symbol ν labels the different deformed single-particle states. Up to 15 single particle orbitals can be included in the calculations. The strong coupling basis states of the complete system $|IMK\nu>$ are labeled by the projection K of I on the intrinsic axis-3 (quantization axis); due to triaxiality, the relation $K = \Omega$ is not longer valid. The calculations have been extended to include the variable moment of inertia (VMI) of the core [Tok75, Rag88]. The VMI description for axially symmetric nuclei is based on the equations:

$$E_R(\Theta_{0R}) = \frac{\hbar^2}{2\Theta_{0R}} R(R+1) + \frac{1}{2} C \left[\frac{\Theta_{0R}}{\hbar^2} - \frac{\Theta_{00}}{\hbar^2} \right]^2, \tag{4.6}$$

$$\frac{\partial E_R}{\partial \Theta_{0R}} = 0. \tag{4.7}$$

Here Θ_{0R} is the moment of inertia for an axially symmetric even-mass nucleus for the angular momentum R. Θ_{00} and C are the VMI parameters of Mariscotti *et al.* [Mar69]. Minimization of the rotational energy E_R as a function of the moment of inertia Θ_{0R} according to Eq. 4.7 yields the VMI equation for axially symmetric nuclei:

$$\epsilon_R^3 - \epsilon_0 \epsilon_R^2 - \frac{1}{2C} R(R+1) = 0, \tag{4.8}$$

where $\epsilon_R = \Theta_{0R}/\hbar^2$ and $\epsilon_0 = \Theta_{00}/\hbar^2$. The moment of inertia Θ_{0R} which depends on the angular momentum is given by solving the VMI equation 4.8. For an asymmetric nucleus, the three moments of inertia are given by (κ=1,2,3)

$$\Theta_{\kappa R} = \frac{4}{3} \Theta_{0R} \sin^2 \left(\gamma + \frac{2\pi}{3} \kappa \right). \tag{4.9}$$

In the RTRP-VMI code, the VMI parameters are $A00 = 1/2\Theta_{00}$ (in MeV) and C (in MeV^3).

The agreement between the experimental and calculated spectra can be improved by introducing an additional parameter ξ - the Coriolis attenuation parameter which multiplies the matrix elements of the Coriolis term in the Hamiltonian. The original Coriolis force turns out to be much too strong and it has to be reduced by a factor $\xi \sim$0.4-0.95 [Rin80].

The electromagnetic transitions considered are $M1$ and $E2$. The $M1$ operator is written as

$$\mathcal{M}(M1) = \sqrt{\frac{3}{4\pi}} (g_R R + g_l l + g_s s), \tag{4.10}$$

where g_R, g_l and g_s are the core, orbital and the spin g-factors, respectively. The $E2$ operator is written schematically

$$\mathcal{M}(E2, \mu) = \sum_i q_i r_i^2 Y_{2\mu}(\theta, \phi), \tag{4.11}$$

where the sum extends over all nucleons and thus splits naturally into contributions from the odd particle and the remaining nucleons (the core). The core contribution is given

by the usual intrinsic $E2$ moments Q_0 and Q_2, which are defined in terms of the shape variables ε_2 and γ. The $M1$ and $E2$ matrix elements are given in Ref. [Lar78].

Model parameters

The main model parameters are the quadrupole deformation ε_2, the asymmetry parameter γ, the moment of inertia Θ_0, usually introduced by the energy of the first excited state of the core $E(2^+)$ and the Coriolis attenuation factor ξ. The variable moment of inertia of the rigid rotor is defined by the so-called VMI-parameters, the ground-state moment of inertia A_{00} and the softness parameter C.

The shape parameters ε_2 and γ for the nucleus under investigation can be determined from the available experimental data, as the $B(E2)$ values or using the lowest excited states of the adjacent even-even nuclei. However, the low-energy spectra of the even-even nuclei in the A$\sim$70 mass region differ from those of a perfect axial or triaxial rotor. In a number of cases, the shapes of the even nuclei rapidly change with the mass number leading to a change in the energies of the low spin states, so that the question arises which of the two neighbors or which average of them should be taken. Moreover, there is evidence that the odd nucleon polarizes the core so that the parameters of even neighbours are not quite applicable to the odd-A nucleus. Being aware of these ambiguities, a certain compromise has to be chosen.

Values of β_2 ($\varepsilon_2 \approx 0.95\beta_2$) extracted from the measured reduced transition probabilities in ^{69}As are given in Table 4.1. Data concerning the adjacent even cores ^{68}Ge and ^{70}Se are also included. Unfortunately, the lifetimes of the excited yrast states in ^{68,69}Se have not been measured yet; this would have practically offered the possible value of β_2 in the calculations for ^{69}Se.

It is obvious from the comparison of Table 4.1 that the even cores ^{68}Ge and ^{70}Se behave in a different way already at low spin. The $B(E2)$ values and the β_2 deformations along the yrast band in ^{68}Ge are rather constant, whereas there is an evident decrease of $B(E2)$ values by a factor of three along the ground band in ^{70}Se. It appears that the slight backbending effect between spin 4^+ and 6^+ visible in the transition energies in ^{70}Se shows up in a more dramatic way in the $E2$ strengths and consequently in the deformation [Myl89]. At low excitation energies ^{69}As exhibits the same irregular behavior in $B(E2)$ values as in ^{70}Se, but the excitation energies show a more regular behavior like in ^{68}Ge.

The values for the $E(2^+)$ parameter should be fixed by the excitation energies of the adjacent even-even cores (^{68,70}Se for ^{69}Se and ^{68}Ge, ^{70}Se for ^{69}As). Since the model deals with quasiparticles, i.e. a mixture of a particle and a hole state, values of $E(2^+)$ parameter slightly different from the experimental energies of the first excited state in the neighboring cores are expected to best fit the experimental data.

The asymmetry parameter γ is usually determined from the energy ratio of the second 2^+ state to the nearest member of the ground state band, in most cases the first 4^+ state ($E(2_2^+)/E(4_1^+)$) [Ter75]. The experimental energy ratios $E_{2_1^+}/E_{2_2^+}$, $E_{4_1^+}/E_{2_2^+}$, $E_{6_1^+}/E_{2_2^+}$ are listed in Table 4.2 for different even-even nuclei in the A$\sim$70 mass-region together with the corresponding theoretical γ values assuming a triaxial rotor [Dav58]. The experimental ratios $E_{2_1^+}/E_{2_2^+}$ of all nuclei included in the systematics point to a maximum triaxiality ($\gamma = -30^\circ$). With increasing spin the asymmetry γ starts to increase ($-30^\circ \leq \gamma \leq -20^\circ$)

Table 4.1: Lifetimes, reduced transition probabilities and deformations in ^{68}Ge [Bur02], ^{69}As [Bha00] and ^{70}Se [Bha93].

Nucleus	E_γ (keV)	$I_i \rightarrow I_f$	τ_{exp} (ps)	$B(E2)_{exp}$ (W.u)	β_2^{exp}
^{68}Ge	1016	$2^+ \rightarrow 0^+$	2.6(3)	17.7(1)	0.20
	1252	$4^+ \rightarrow 2^+$	1.1(1)	13.6(3)	0.18
	1429	$6^+ \rightarrow 4^+$	0.7(2)	12.0(3)	0.17
^{69}As	854	$13/2^+ \rightarrow 9/2^+$	5.0(8)	21(2)	0.21
	1098	$17/2^+ \rightarrow 13/2^+$	<6.05	>5	>0.1
	1204	$21/2^+ \rightarrow 17/2^+$	8.3(13)	2.3(4)	0.07
^{70}Se	945	$2^+ \rightarrow 0^+$	1.4(3)	44(9)	0.29
	1094	$4^+ \rightarrow 2^+$	1.4(3)	21(3)	0.21
	964	$6^+ \rightarrow 4^+$	3.9(9)	14.7(3)	0.17
^{69}Se	1079	$13/2^+ \rightarrow 9/2^+$			
	1246	$17/2^+ \rightarrow 13/2^+$			
	1356	$21/2^+ \rightarrow 17/2^+$			
^{68}Se	853	$2^+ \rightarrow 0^+$			
	1088	$4^+ \rightarrow 2^+$			
	1362	$6^+ \rightarrow 4^+$			

very likely reflecting a certain softness of these nuclei. Since the energy spectrum of the even triaxial rotor is symmetric about $\gamma = -30°$, this procedure cannot distinguish between prolate triaxial shapes ($-30° < \gamma < 0°$) and oblate triaxial shapes ($-60° < \gamma < -30°$).

The value of the γ parameter is at best determined by fitting the signature splitting between the favoured and the unfavoured yrast states. The signature splitting function $S(I)$ is extremely sensitive to any variation of the γ asymmetry parameter and it can provide a good argument in choosing the value of γ. This function is defined as [Zam91]:

$$S(I) = \frac{E(I) - E(I-1)}{E(I) - E(I-2)} \cdot \frac{I(I+1) - (I-2)(I-1)}{I(I+1) - I(I-1)} - 1. \tag{4.12}$$

S(I) describes the relative deviation of the energy of the state with spin I-1 from its presumed energy under the assumption of strong coupling. S(I)=0 holds in the case of a strongly coupled band (E(I)$\sim$I(I+1)) (see Fig. 4.4).

Table 4.2: Ratios of the first 2_1^+, 4_1^+, 6_1^+ energies to the second 2_2^+ energy for some even-even nuclei in the A$\sim$70 mass-region and derived values for the γ asymmetry parameter.

Nucleus	$\frac{E_{2_1^+}}{E_{2_2^+}}$ / γ	$\frac{E_{4_1^+}}{E_{2_2^+}}$ / γ	$\frac{E_{6_1^+}}{E_{2_2^+}}$ / γ
^{68}Se	0.53 / $-30°$	1.22 / $-26°$	2.07 / $-24°$
^{68}Ge	0.57 / $-30°$	1.27 / $-27°$	2.08 / $-23°$
^{70}Se	0.59 / $-30°$	1.27 / $-27°$	1.87 / $-21°$
^{70}Ge	0.61 / $-30°$	1.26 / $-27°$	1.93 / $-22°$
^{72}Ge	0.57 / $-30°$	1.18 / $-25°$	
^{74}Se	0.50 / $-30°$	1.08 / $-23°$	1.76 / $-21°$

For every chosen set of deformation parameters (ε_2 and γ) the single-particle model based on the modified oscillator potential is employed to calculate the single-particle energies and the single-particle wave functions. Next, it is necessary to select a few single-particle states near the Fermi surface which may constitute an adequate truncated single-particle basis space for the non-adiabatic part of the calculation. The model basis can include up to 15 orbitals of a given parity.

RTRP calculations for the low-lying positive-parity states in ^{69}Se

The calculations for the yrast positive-parity band in ^{69}Se were performed by considering values for the quadrupole deformation in the range $0.25 \leq \epsilon_2 \leq 0.35$, as suggested by the systematics of the odd-A Selenium isotopes. Of course, values outside this range have not been excluded from the fit either. In the calculations, $g_{9/2}$, $g_{7/2}$ and $d_{5/2}$ single-particle orbitals have been considered. The best agreement with the experimental data has been obtained for $\varepsilon_2 = 0.33$. This value agrees with the deformation $\beta_2 = 0.32$ for the ground-state band in the even-even core ^{68}Se derived by Petrovici *et al.* [Pet2] from *complex* EXCITED VAMPIR [Pet96] calculations.

An effective core excitation energy of $E(2^+)$=500 keV has been found to reproduce the experimental level energies. This value is smaller than the experimental energy of 854 keV of the first 2^+ state in ^{68}Se. The difference between the experimental and the calculated $E(2^+)$ values are due to the fact that the model treats the coupling to an even-even core of a quasiparticle, i.e. a mixture of a particle and a hole state. Therefore one cannot expect to obtain agreement between experiment and theory when choosing the value of $E(2^+)$ parameter just equal to the energy of the first excited state in the ^{68,70}Se nuclei.

Figure 4.4 displays both the theoretical and experimental signature splitting functions for the spin sequence of the yrast levels. The observed signature splitting cannot be reproduced with an axial oblate shape ($\gamma = -60°$, $\epsilon_2 > 0$). Varying γ between $-60°$ and $-40°$ will produce only small changes in the theoretical function, but the changes become

important when γ approaches the maximum triaxiality where $\gamma = -36°$ reproduces very well the experimental splitting.

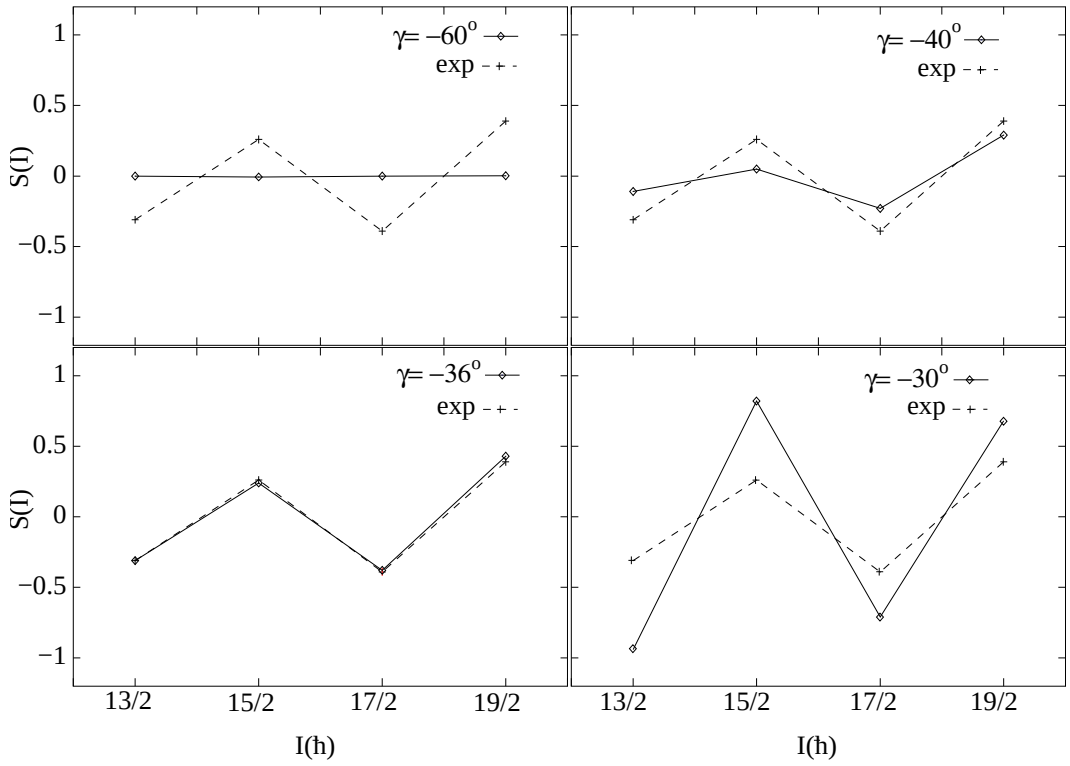

Figure 4.4: *Experimental and calculated signature splitting for the 1qp-states of the positive-parity yrast band in ^{69}Se. The RTRP parameters used in the calculations are given in Table 4.3.*

Only a small attenuation of the Coriolis force was necessary and the optimum results were obtained for ξ=0.95. The model parameters used in the present calculations are given in Table 4.3.

The comparison of the experimental and calculated energy levels in ^{69}Se is shown in Figure 4.5. The calculated levels are normalized to the experimental energy of the bandhead with spin $9/2^+$. In Figure 4.5 only the theoretical yrast and yrare levels which have an experimental partner were represented. The set of parameters which describes very well the experimental signature splitting (Table 4.3) can successfully reproduce the experimental energies of the one quasiparticle yrast positive-parity states. The calculated levels are dominated by the $g_{9/2}$ single particle orbital which gives a contribution of $\sim$80% to the total wave function of the yrast and yrare states. The $d_{5/2}$ and $g_{7/2}$ orbitals contribute only with small amplitudes (see Table 4.4). The amplitudes of the core states in the total wave functions are presented in Figure 4.6. The 2_2^+, 3^+, 4_2^+, ... core states form the quasi-γ-band of a triaxial rotor; there is no β-band of the core in this model. The wave functions associated to the yrast calculated levels reveal that the contribution from the ground-state band of the core is larger than 90% (Figure 4.6, top). The non-yrast

Table 4.3: The RTRP parameters used in the present work: quadrupole deformation ε_2, asymmetry parameter γ, core 2^+ state energy, Coriolis attenuation factor ξ. κ_n and μ_n are the Nilsson parameters for neutrons in the $N = 4$ oscillator shell, taken from Ref. [Ben85].

	ε_2	γ	$E(2^+)$ (MeV)	ξ	κ_n	μ_n
^{69}Se, π=+	0.33	$-36°$	0.50	0.95	0.070	0.39

Table 4.4: Relative single-particle structure of positive-parity states in ^{69}Se calculated with the RTRP model (parameters ε_2=0.33, $\gamma = -36°$ and see Table 4.3). For each spin the squared amplitude is given for the yrast and yrare states.

	yrast states			yrare states		
Spin	$g_{9/2}$	$d_{5/2}$	$g_{7/2}$	$g_{9/2}$	$d_{5/2}$	$g_{7/2}$
$9/2^+$	88.4	9.9	0.7	79.8	14.4	2.7
$11/2^+$	87.0	10.6	1.0			
$13/2^+$	84.9	11.6	1.7	85.7	11.3	1.3
$15/2^+$	85.9	11.1	1.4			
$17/2^+$	80.8	13.4	2.9	84.3	12.2	1.5
$19/2^+$	84.2	11.9	1.9			
$21/2^+$	78.7	14.2	3.6			
$23/2^+$	82.8	12.5	2.4			
$25/2^+$	77.5	14.6	4.2			

Table 4.5: Experimental and theoretical values of the mixing ratios δ, branching ratios λ and $B(M1)/B(E2)$ ratios in ^{69}Se.

		Experiment			RTRP, γ=-36°		
$I_i \to I_f$	E_γ (keV)	λ	δ	$B(M1)/B(E2)$ $(\mu_N/eb)^2$	λ	δ	$B(M1)/B(E2)$ $(\mu_N/eb)^2$
$13/2_1^+ \to 11/2_1^+$	403	0.18(2)	0.16±0.05	2.7(12)	0.20	0.12	3.06
$13/2_1^+ \to 9/2_1^+$	1079						
$13/2_2^+ \to 11/2_1^+$	773	8.7(7)	2.30±0.39	0.25(9)	8.34	0.71	1.18
$13/2_2^+ \to 9/2_2^+$	662						

calculated levels contain an increased contribution from the quasi-γ-band states of the core (Figure 4.6, bottom).

The quasi-γ-band in ^{68}Se was experimentally and theoretically found to have a prolate character with a slightly different quadrupole deformation with respect to the ground-state band. Thus, the non-yrast states may be reproduced with a different set of deformation parameters ε_2 or/and γ. The restriction to a rigid rotor core employed by the model is a limitation in the study of these states.

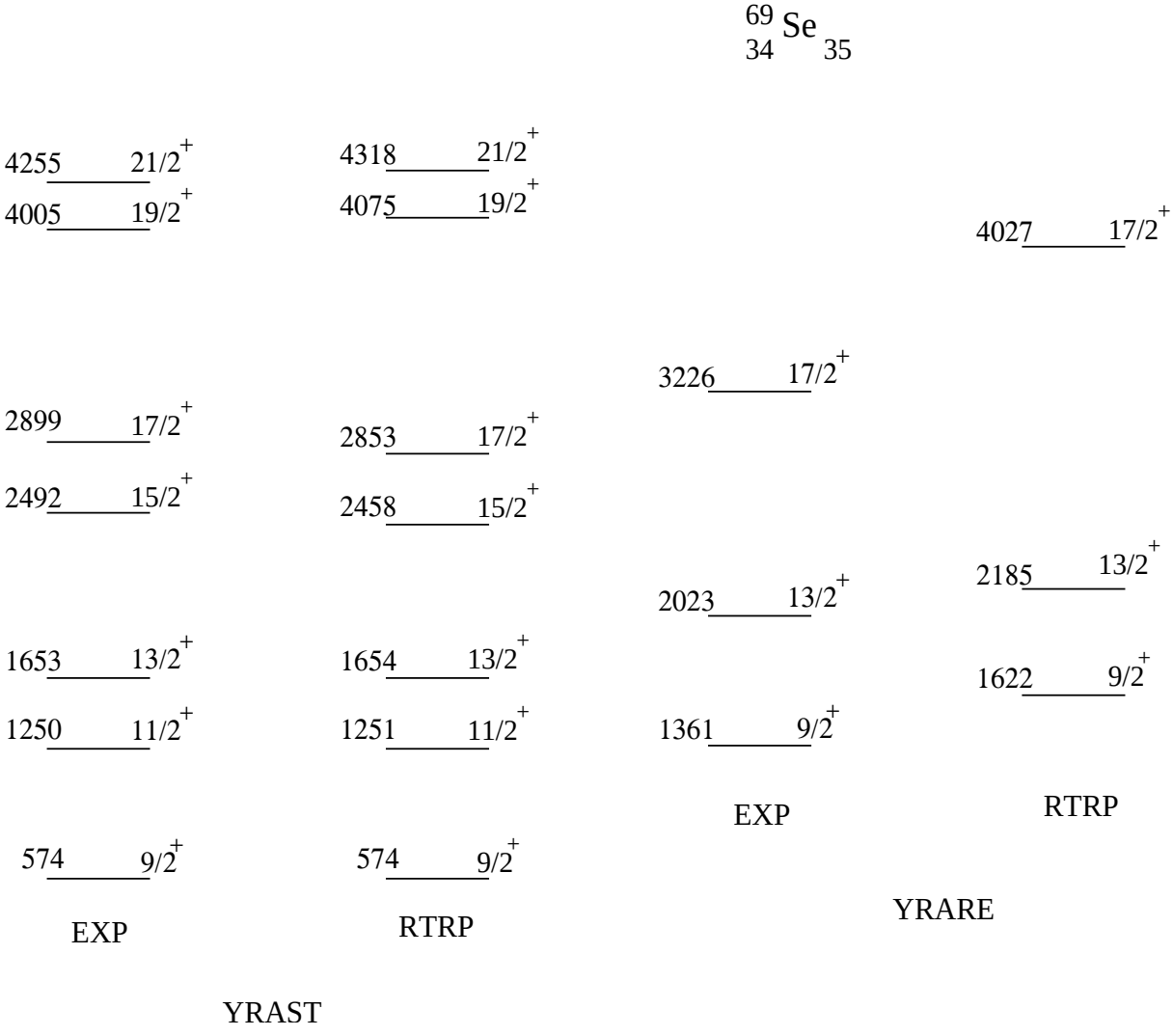

Figure 4.5: *Experimental and calculated positive-parity levels in ^{69}Se. The RTRP parameters used in the calculations are given in Table 4.3.*

The model predicts a $25/2^+$ state at an excitation energy of E_x=6118 keV which may correspond to the experimental state at 5830.8 keV. In this case, the level at 5830.8 keV could be regarded as the continuation of the oblate band. Figure 4.7 shows a comparison

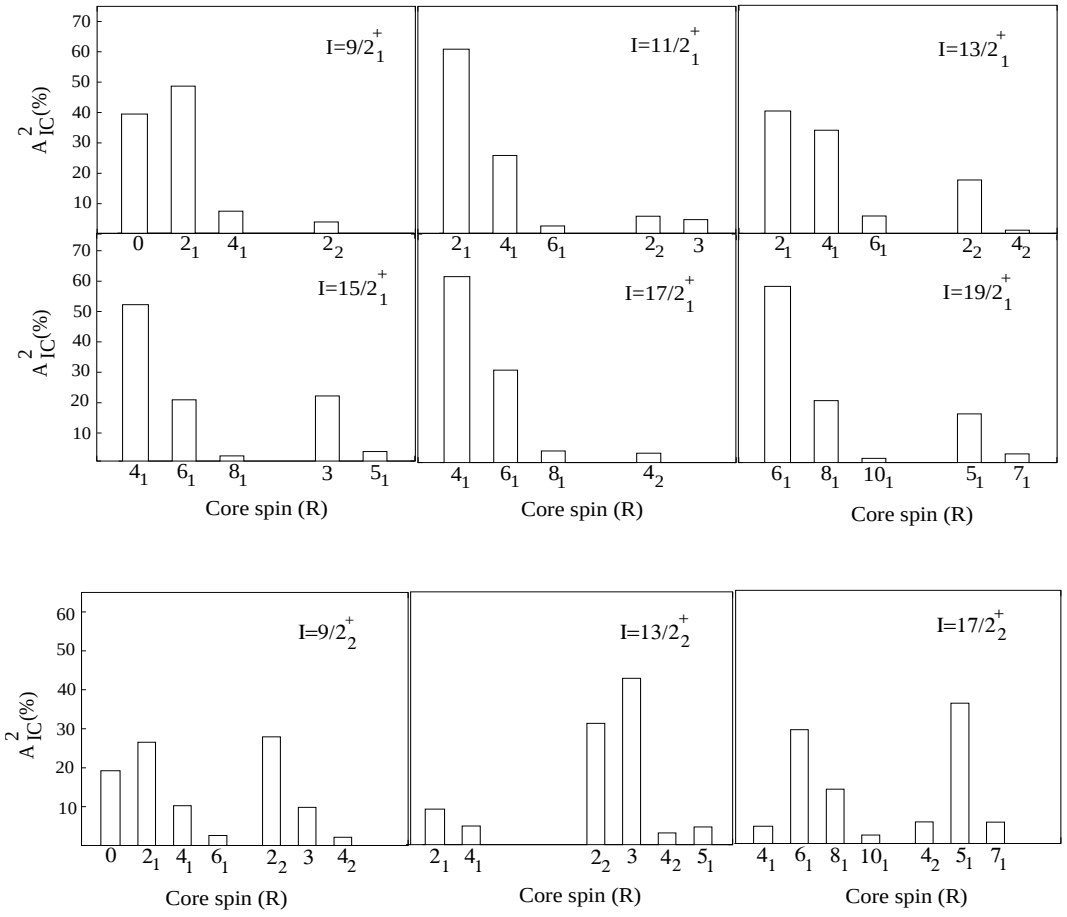

Figure 4.6: *Squared amplitudes A^2_{IC} of core states for positive-parity yrast (top) and yrare (bottom) bands of ^{69}Se calculated with the RTRP model. The model parameters used in the calculations are given in Table 4.3.*

between the experimental and the calculated branching ratios for the yrast and yrare states using the relation

$$\lambda = \left(\frac{T(M1; I \to I-1) + T(E2; I \to I-1)}{T(E2; I \to I-2)} \right)_{RTRP} = \frac{I_\gamma(I \to I-1)}{I_\gamma(I \to I-2)}. \qquad (4.13)$$

The given ratios for the yrare levels are extracted between the inband $I \to I-2$ transition and the corresponding $I \to I-1$ transition populating the levels of the yrast band. The intensity ratio $I_\gamma(I \to I-1)/I_\gamma(I \to I-2)$ for the decay of a given state I has been determined in the most direct way, namely from the coincidence spectrum with a gate on the inband transition populating the state under investigation.

The theoretical branching ratios represented in Fig. 4.7 were calculated using the model parameters given in Table 4.3. In the evaluation of the electromagnetic moments, an effective g_s factor of $0.7 g_s^{free}$ has been used and g_R has been taken as the ratio Z/A=0.492. For comparison, the calculated branching ratios assuming an axial

oblate shape ($\gamma = -60°$) are also represented in the plots. For both yrast and yrare structures, the experimental ratios are better reproduced when assuming a rigid triaxial shape. Calculations with an axial oblate shape predict branching ratios which are larger than the measured ones for the yrast states. The calculations with $\gamma = -36°$ predict a small $B(E2)$ value for the in-band $13/2_2^+ \rightarrow 9/2_2^+$ transition, thus reproducing the observed enhancement of the out-of-band $13/2_2^+ \rightarrow 11/2_1^+$ decay. However, the RTRP results for the yrare band should be regarded with some precaution because due to the shape-coexistence phenomenon, the rigid core approximation assumed for the shape of the ^{69}Se nucleus may not be valid for these states.

The determination of the absolute $B(M1)$ and $B(E2)$ reduced transition probabilities requires the measurement of the nuclear lifetimes and mixing ratios of the levels and transitions involved. However, no lifetimes were determined in the present work and only the mixing ratios of the $13/2_1^+ \rightarrow 11/2_1^+$, 403.1-keV and $13/2_2^+ \rightarrow 11/2_1^+$, 773.3-keV transitions could be determined. One can thus compare the theoretical and the experimental ratios between the in-band $B(M1; I \rightarrow I-1)$ to the $B(E2; I \rightarrow I-2)$ values of the 403.1- and 1079.1-keV transitions depopulating the $13/2^+$ yrast level at 1653.7 keV excitation energy and the ratios between the out-of-band $B(M1; I \rightarrow I-1)$ value to the in-band $B(E2; I \rightarrow I-2)$ value of the 773.3- and 662.3-keV transitions depopulating the $13/2^+$ yrare level at 2023.8 keV excitation energy. The ratios of reduced transition probabilities are given in Table 4.5; the experimental ratios have been calculated using the equation

$$\frac{B(M1; I \rightarrow I-1)}{B(E2; I \rightarrow I-2)} = 0.6967 \cdot \frac{E_\gamma^5(I \rightarrow I-2)}{E_\gamma^3(I \rightarrow I-1)} \cdot \frac{\lambda}{(1+\delta^2)} \quad \mu_N^2/e^2b^2. \tag{4.14}$$

The γ-ray energies E_γ are given in MeV, λ is the measured branching ratio extracted by applying the second part of eq. 4.13 and δ is the $E2/M1$ mixing ratio. The RTRP model reproduces very well the observed electromagnetic properties of the transitions depopulating the $13/2^+$ yrast state and predicts a value of 0.12 for the mixing ratio of the 403.1-keV transition.

In conclusion, the one-quasiparticle yrast positive-parity states in ^{69}Se and their properties can be well reproduced in the framework of Rigid Triaxial Rotor plus Particle model. The fit of the experimental signature splitting and branching ratios demonstrates the importance of a non-axial symmetry calculation. More experimental data, in particular lifetime measurements in the one-quasiparticle bands, would be helpful for a more complete description of the shape of this nucleus.

RTRP calculations for the low-lying positive-parity states in ^{69}As

Figure 4.8 shows the solutions of the RTRP model for the yrast favored and unfavored states up to spin I=$29/2^+$ as function of γ. The calculated energies are given in units of the even-even first excited state $E(2^+)$. The quadrupole deformation ε_2=0.2 and the value $E(2^+)$=0.7 MeV used in the calculations are believed to be appropriate for the nucleus ^{69}As, as suggested by the deformation extracted from the experimental $B(E2)$ values and the excitation energies of the even-even neighboring nuclei ^{68}Ge and ^{70}Se (see Table 4.1).

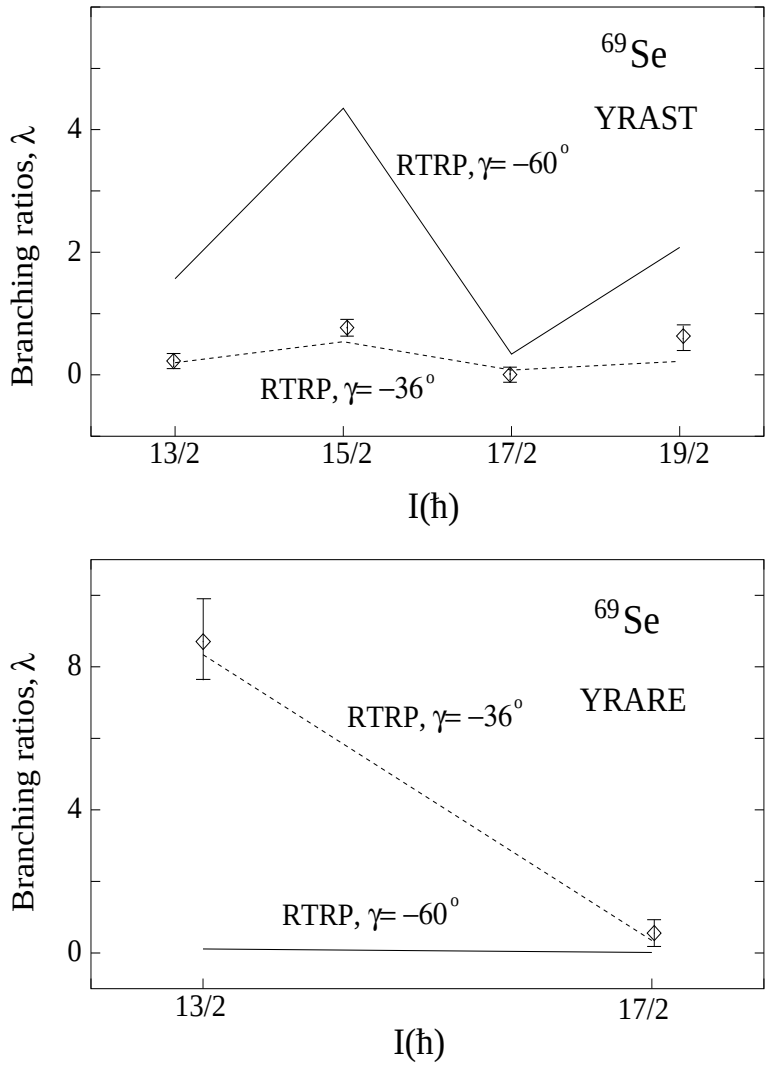

Figure 4.7: *Experimental branching ratios (points) in ^{69}Se compared to the calculated values using the RTRP model for $\gamma = -36°$ (dotted lines) and $\gamma = -60°$ (oblate axial symmetric) (solid lines). The theoretical values are based on calculated matrix elements and experimental γ-ray energies. The RTRP model parameters are those given in Table 4.3.*

At $\gamma = 0°$ (prolate case) the sequence of levels $I = j,\ j+2,\ j+4,\ \ldots$, is favored in energy (favored band). The unfavored band ($I = j+1,\ j+3,\ j+5,\ \ldots$) lies higher in energy and it is expected to be weakly populated. For γ-values above $-15°$, the energy splitting between the favored and unfavored bands remains rather constant, with the order of the favored being lowest always preserved. Varying γ in the interval $(-20°, -40°)$ has a drastic effect on the calculated energies. In this region the unfavored states come down in energy while the favored states slightly increase their energies. For certain γ-values, the favored states $I = j,\ j+2,\ j+4,\ \ldots$, are found to cross their respective unfavored

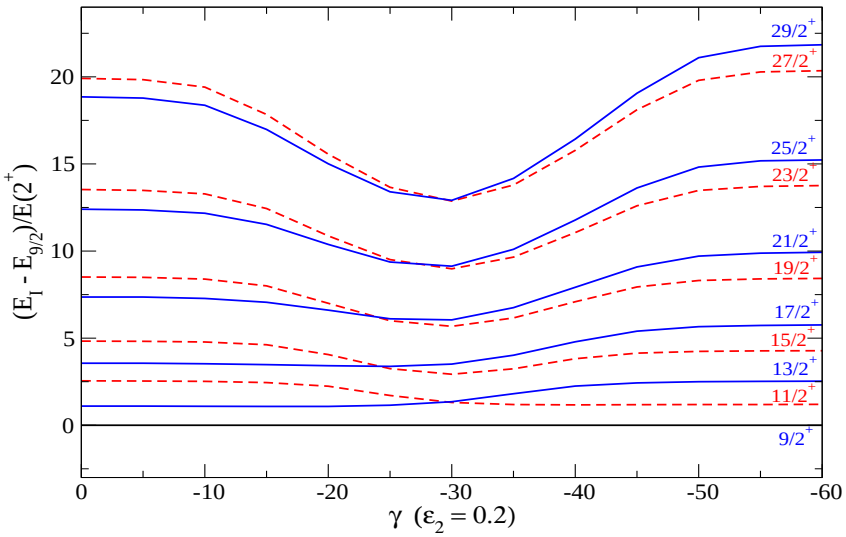

Figure 4.8: *The eigenvalues of the Rigid Triaxial Rotor plus Particle model for one particle sitting in the $g_{9/2}$ orbital, as function of the asymmetry parameter γ and for a fixed value of the quadrupole deformation, ε_2=0.2. The ordinate is the difference between the eigenvalues obtained for each spin value and that of the lowest $I = 9/2^+$ state, in units of $E(2^+)$. The Fermi level is on the first lowest $g_{9/2}$ component.*

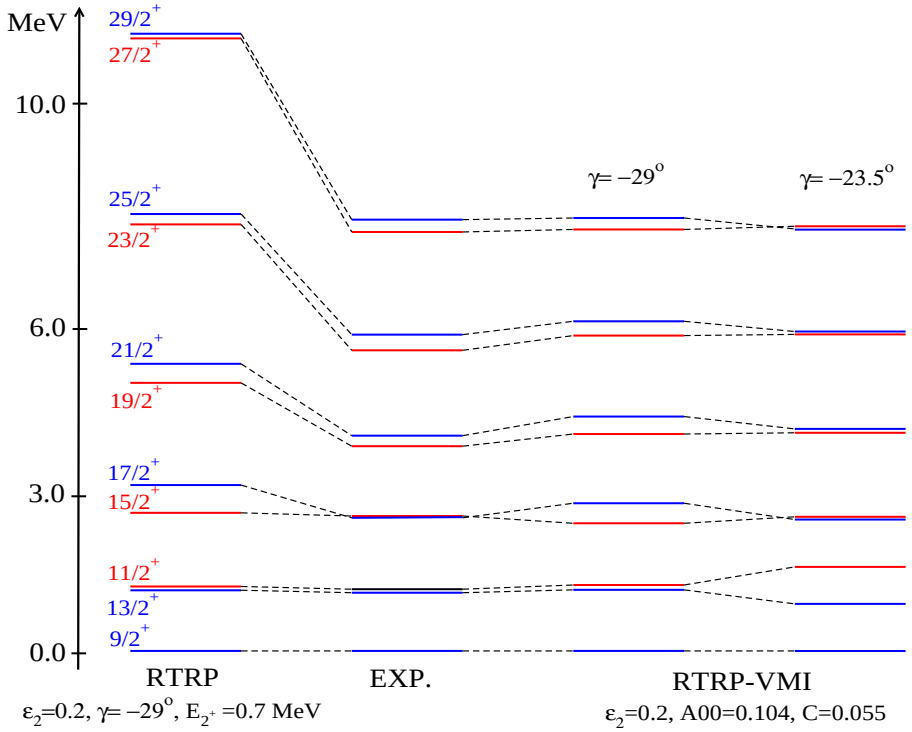

Figure 4.9: *Experimental and calculated excitation energies in ^{69}As. The spectra are (from the left to right): Theoretical results with a triaxial rigid rotor (RTRP); experimental data; results including the softness of the asymmetric core (RTRP-VMI) with $\gamma = -29°$; RTRP-VMI fit with $\gamma = -24.5°$.*

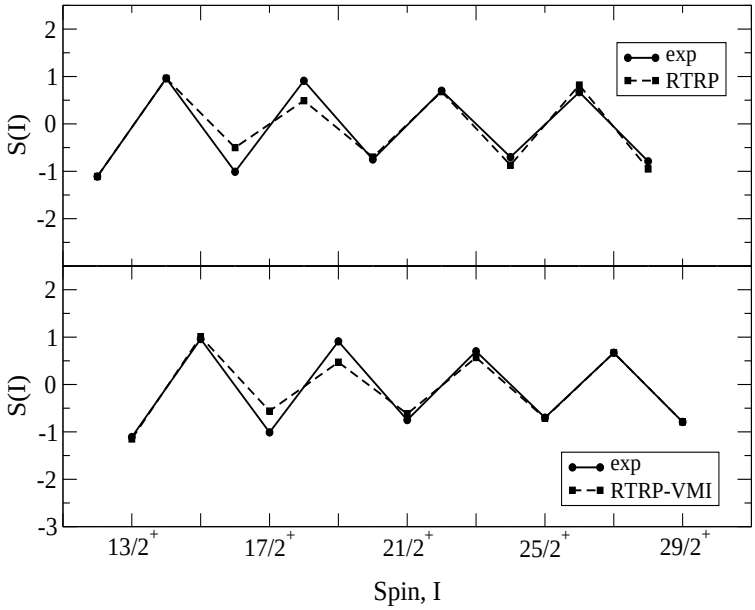

Figure 4.10: *Experimental and calculated signature splitting for the states in Band 1 in* ^{69}*As. The model parameters used in calculations are* ε_2*=0.2,* $\gamma = -29°$*,* $E(2^+)$*=0.7 MeV,* ξ*=1 (RTRP, top panel) and* ε_2*=0.2,* $\gamma = -29°$*, A00=0.104 MeV, C=0.055 MeV*^{3}*,* ξ*=1 (RTRP-VMI, bottom panel).*

partners $I = j + 1,\ j + 3,\ j + 5,\ \ldots$. For example, the crossing of the $11/2^+$ and $13/2^+$ states occurs at $\gamma \approx -30°$, the unfavored $15/2^+$ state crosses the $17/2^+$ favored state at $\gamma \approx -25°$, and so on. Above $\gamma = -30°$ a normal rotational band ($I = j,\ j+1,\ j+2,\ \ldots$) starts to develop. For γ-values in the interval $(-30°, -40°)$ the favored and the unfavored bands lie close together but with decreasing further γ toward $-60°$ (oblate) the energy splitting between the two bands increases.

In ^{69}As, the unfavored $11/2^+$ state lies 50 keV above the favored $13/2^+$ state and the energy splitting between the unfavored $15/2^+$ state and the favored $17/2^+$ state is only 6 keV. This situation could be described by the model assuming a γ-value around $-25°$, as seen in Fig. 4.8. For higher spins, the unfavored levels were found to lie 150-200 keV below their favored partners thus forming a normal sequence of spins I=$19/2^+$, $21/2^+$, $23/2^+$, ..., $29/2^+$. The model can reproduce such level ordering only when employing γ-values smaller than $-29°$. Different γ-values at different spins suggest a γ-soft low-lying spectrum in ^{69}As. Since in the RTRP model the deformation is kept constant throughout the calculations, it is not appropriate in describing the ground-state band in ^{69}As. However, it is interesting to see to which extent the experimental band can be reproduced. The best fit could be obtained with the RTRP model for the ground-state band in ^{69}As is shown in Fig. 4.9 (left). The γ-parameter has been chosen in such a way that the level ordering above spin $I = 19/2^+$ is obtained. As it was already discussed, such γ-value does not reproduce the $15/2^+$ state above the $17/2^+$ state. Moreover, even though the ordering of the higher levels is reproduced, the excitation energies are always

higher than the experimental ones. This is due to the fact that the moment of inertia is fixed for all spin values. In order to obtain a better quantitative agreement of the excitation energies, inclusion of the softness of the core is required (VMI). The values of two VMI parameters (the moment of inertia $A00$ and the stiffness parameter C) used in the calculations were obtained by fitting the first excited 2^+ and 4^+ states of the core nucleus. The results of the RTRP-VMI calculations are shown on the right in Fig. 4.8. The inclusion of the softness of the core does not affect too much the energy of the lower spin states but improves considerably the fit to the higher-spin states.

The signature-splitting function defined by eq. 4.12 is illustrated in Fig. 4.10 for the experimental, RTRP (top panel) and RTRP-VMI (bottom panel) calculated levels in Band 1. The observed splitting is well reproduced in both cases for all spins, except the $17/2^+$ and $15/2^+$ states.

The RTRP calculations in ^{69}Se and ^{69}As indicate that at low spin, ^{69}Se has a more tightly bound ground-state band with substantial deformation (ε_2=0.33, $\gamma = -33°$), stabilized by the large gaps in the oblate and prolate level sequences at $N, Z = 34$. However, this stabilization is delicate: removal of particles leads to lower deformed shapes exhibiting γ-softness, as in ^{69}As. Due to the restriction to a rigid rotor core, the RTRP model is not fully adequate to describe the positive-parity ground-state band in ^{69}As.

4.2.2 Negative-parity states

Low-lying negative-parity states in ^{69}Se

At low energies, the negative-parity states in ^{69}Se do not show a rotational-like structure as observed in the heavier odd-Se isotopes, suggesting a smaller deformation for this part of the level scheme and possibly predominant shell model characteristics. A negative-parity decoupled rotational band develops already at excitation energies around 300 keV in ^{71}Se [Ebe84] and, with increasing the neutron number, the strong-coupled negative-parity structures characterize the ^{73,75,77}Se nuclei. Thus, at low excitation energies, the negative-parity structures of ^{69}Se fits better in the systematics of neighboring odd-Ge isotopes, whose structural and electromagnetic properties at low excitations derive from both neutron and proton shell effects and from small shape deformations connected with the departure from closed shells, defining a transitional region where neither shell nor collective effects can be expected to predominate.

In order to determine whether the low-lying excitations of ^{69}Se are mainly shell excitations or mainly collective modes one needs complete experimental information about the level scheme and electromagnetic properties. Because the experimental information is still far from complete, the discussions implying the negative-parity bands found in ^{69}Se are for the moment only qualitative.

It has been already remarked that the ordering of the low-lying negative-parity levels in ^{63,65}Ni, ^{65,67}Zn and ^{67,69}Ge follows a consistent pattern [Poh90, Mur78, Mur83]. Systematics of these nuclei imply sequences consisting of spins ($\frac{1}{2}^-$, $\frac{5}{2}^-$, $\frac{3}{2}^-$, $\frac{3}{2}^-$) for the ground states and the first three excited states. With the new experimental information found in the present work for the low-energy negative parity states in ^{69}Se, this nucleus can be successfully included in the systematics above and the results and conclusions found in

the previous investigations concerning the nature and the properties of these levels can be applied.

Of the odd-nuclei with 35 neutrons, the low-lying negative-parity states in ^{69}Se closely resemble those of the ^{67}Ge whose properties are probably most similar to ^{69}Se. Some evidence for the shell configuration of the low levels in ^{67}Ge was found in the relative intensities of the γ-rays deexciting the first three excited negative-parity states [Mur78]. A comparison of the $B(M1)$ ratios calculated from their branching ratios has been shown that the transitions from the $3/2^-$ levels to the $5/2^-$ level are inhibited by factors $\sim$3-40 relative to the transitions to the $1/2^-$ ground state. The same degree of inhibition of the analogous transitions in ^{63}Ni has been also reported [Bog67]. The small $B(M1)$ value of the transition to the $5/2^-$ isomeric state suggest l-forbidden transition to this level, such as might arise if the $3/2^-$ and $1/2^-$ levels were principally p-shell configurations, and the $5/2^-$ mostly $f_{5/2}$.

The $B(M1)$ ratio extracted from the experimental branching ratios of the 90.3 keV ($3/2^-_1 \rightarrow 5/2^-_1$) and 129.1 keV ($3/2^-_1 \rightarrow 1/2^-_1$) transitions in ^{69}Se is 0.34, indicating a certain degree of inhibition for the transition to the first excited state, consistent with the observations outlined above concerning the single-particle nature of the ground and the first two excited states. The second $3/2^-$ level decays by the 161.3 keV transition to the first $3/2^-$ level and by the 250.7 keV transition to the $5/2^-$ level. The two transitions have about the same relative intensity. Moreover, the decay to the ground state $1/2^-$ was not observed in ^{69}Se. In contradiction to the expectations of a strong allowed $M1$ transition, the fact that this decay is missing may suggest a different shell structure of the $3/2^-_2$ level with respect to its analogous in the neighboring ^{63}Ni and ^{67}Ge nuclei.

In a simple shell model of $^{69}_{34}\mathrm{Se}_{35}$, 56 nucleons form a closed shell ^{56}Ni core, leaving 6 protons and 7 neutrons to be distributed through the $2p_{3/2}$, $1f_{5/2}$ and $2p_{1/2}$ shells in order to generate negative-parity states. Difficulties arise from the fact that these three valence shells are very close in energy which increases the probability of significant configuration mixing for the 13 nucleons outside the ^{56}Ni core. For simplicity, the discussion can be restricted to only the 7 active neutrons and it is not unreasonable, given the weak Z-dependence of the systematic regularities observed in the odd Ni, Zn and Ge isotopes [Poh90, Mur78, Mur83]. Thus, the results of the shell-model calculations obtained for $^{63}\mathrm{Ni}_{35}$ [Los88, Coh67] may be generalized. In the work of Losano *et al.* [Los88], a detailed study of the odd-Ni isotopes was performed in the framework of a low-seniority shell model with the aim to investigate the mixing of one and three-quasiparticle states in the low-lying negative-parity structures. In addition, the effects of seniority-five configurations on low-lying states has also been studied through the comparison of low-seniority shell-model results with those which arise from the full shell-model calculations. These calculations reproduced the systematics observed in the N=35 nuclei with the $1/2^-$-$5/2^-$-$3/2^-_1$-$3/2^-_2$ low-lying spin sequence, the gap of several keV between these levels and the next excited levels and the general trend of the states at excitation energies between 1 and 3 MeV. Another important result arises from the structure of the wave functions which characterize these states. The $1/2^-$, $5/2^-$ and $3/2^-_1$ have a predominant seniority ν=1 character. The next excited levels, including the second $3/2^-$ state are dominated by ν=3 configurations. As expected, the values of ν increases with increasing the excitation energy.

Low-lying negative-parity states in ^{69}As

As in ^{69}Se, the states below 3 MeV excitation energy in ^{69}As show a non-regular energy spacing, presumably being of single-particle character. Competing with these states, two main configurations could be distinguished. The configuration consisting of states at 1987.5, 2627.6 and 3418.5 keV may be considered the signature partner of the configuration consisting of states at 2311.2, 3045.4 and 3844.6 keV, see 3.4. This is justified by the occurrence of the weak $M1/E2$ crossover transitions between the levels of the two configurations.

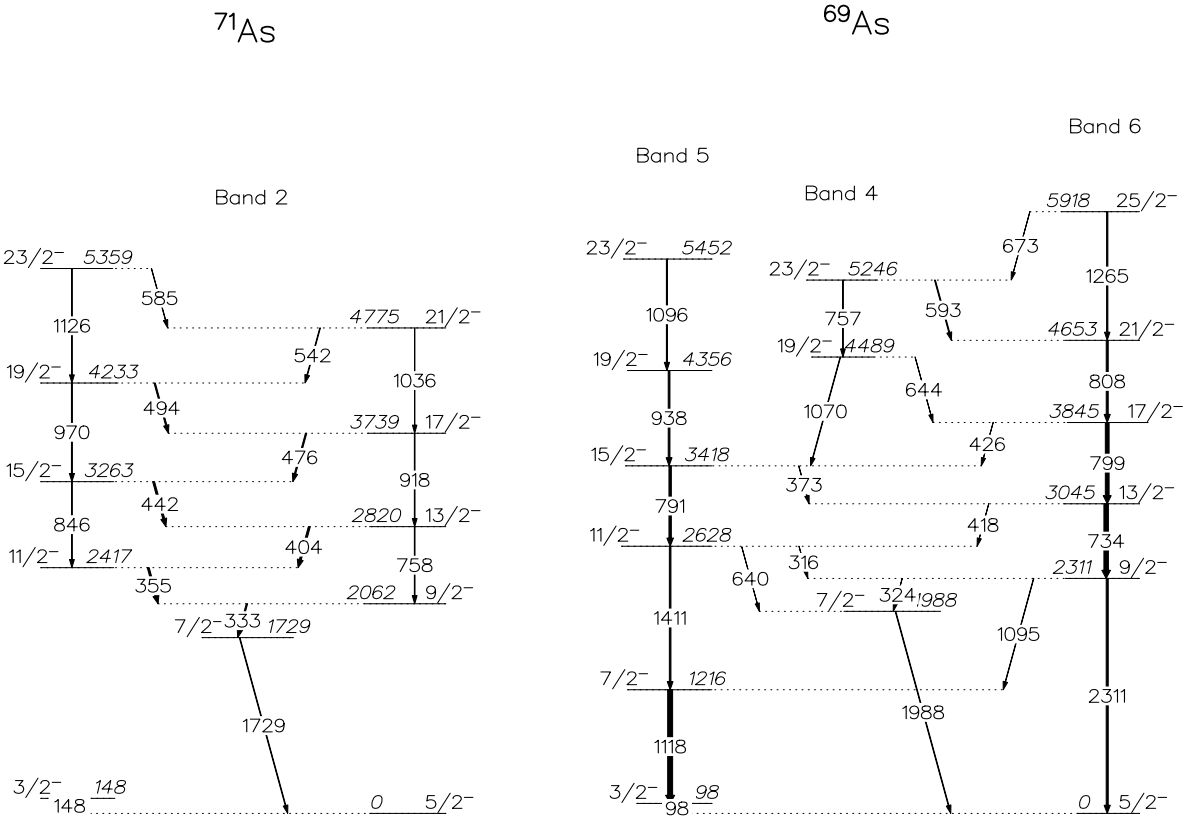

Figure 4.11: *Comparison between the $f_{7/2}$ band identified in ^{71}As [Fot99] and the sequence in ^{69}As which shows similar decay properties and may represent a candidate for the $f_{7/2}$ band in this nucleus. The width of the arrows is proportional to the intensity of the transitions. In ^{71}As, the intensities are relative to the intensity of the 714.0-keV transition [Zig94].*

Similar negative-parity structures have been identified previously in ^{71}As [Zig94]. There, the $E2$ transitions in the band built on the second $9/2^-$ state were found to

show a high collectivity. Total Routhian calculations for the $\pi = -, \alpha = +1/2$ states in ^{71}As showed the presence of three shallow minima for rotational frequencies below 0.4 MeV [Zig94]. The minima were located near 0° and ±60°, exhibiting γ-softness. With increasing rotational frequency one triaxial minimum was calculated to persist. In a recent work, Fotiades *et al.* [Fot99] managed to extend the negative-parity band found in Ref. [Zig94] up to spin $(37/2^-)$ and to observe a new sequence of negative-parity levels developing at low excitation energies (see 4.11). The newly observed structure has been interpreted as being part of a strong-coupled-like band built on $7/2^-[303]$ proton orbital which approaches the Fermi surface for Z=33 at large β_2 >0.3 prolate deformations. The $f_{7/2}$ band in ^{71}As was found to be a ΔI=1 sequence with $B(M1)/B(E2)$ ratios varying between 4 and 6 $\mu_N^2/(e^2b^2)$ and could be reproduced with a moment Q_t=3.1 eb which corresponds to an ϵ_2 value of 0.37 [Fot99].

A possible candidate for a $f_{7/2}$ band in ^{69}As could be the structure containing the levels discussed above. However, the properties of this structure do not really resemble those of the $f_{7/2}$ band found in ^{71}As. In ^{69}As, the $M1/E2$ crossover transitions between the favored and the unfavored members of the presumed $f_{7/2}$ band are very weak with respect to the intraband $E2$ transitions. The corresponding $B(M1)/B(E2)$ ratios calculated with the experimental branching ratios are found to vary between 0.04 and 2.14 $\mu_N^2/(e^2b^2)$. Since the $M1$ strengths are proportional to the difference $(g_K - g_R)$ and the gyromagnetic ratio for collective rotation is $g_R \approx$0.48, such low values of the $B(M1)/B(E2)$ ratios indicate $g_K \approx g_R$ for this sequence. A near cancellation of the $(g_K - g_R)$ difference is expected to occur for a $5/2^-$ structure, but not for a $7/2^-$ band.

As pointed out in the previous section, the two $15/2^-$ states at 3418.5 and 3947.5 keV are candidates for octupole states in ^{69}As. Such states are generated in the odd-A nuclei by coupling the $g_{9/2}$ particle to the 3^- state in the even-even core. Both states show the systematical features characteristic to the octupole states found in the neighboring odd-A nuclei, namely the direct feeding via $E2$ transitions from the higher $19/2^-$ states and the decay via $E1$ transitions into the respective $13/2^+$ yrast level. In ^{68}Ge, the 3^- state has been observed at an excitation energy of 2649 keV [Lim81]. By combining this energy with the excitation energy of the $g_{9/2}$ proton excitation in ^{69}As (1306 keV), an energy of 3955 keV is obtained, very close to the observed energy of 3947.5 keV of the second $15/2^-$ state in ^{69}As. Similarly, two of the three observed $19/2^-$ levels can be interpreted as coupling of the $g_{9/2}$ proton to the 5^- states at 3582 and 3649 keV in ^{68}Ge [Lim81], even though the excitation energy of the $19/2^-$ states in ^{69}As is around 300 keV lower than expected. Analogous discussions could be applied to the higher-spin states like $21/2^-$ (6^-) and $23/2^-$ (7^-).

4.3 High-spin states

With increasing rotational frequency, the yrast line shows drastic changes, as the nucleus in its deexcitation process, follows the path which is at most energetically favored. In the nuclei exhibiting collective rotational bands, these changes in the yrast line are discussed in terms of band crossings. As pointed out at the beginning of this chapter, the band crossings may represent the crossing of different configurations (e.g., the ground-state

band and the 2-quasiparticle band) or the crossing of shapes.

The band-crossings phenomena are usually discussed in terms of rotational frequency, kinematic and dynamic moments of inertia, alignments of single-particle routhians.

The rotational frequency is related to the slope of the curve excitation energy E vs. spin I, considering a rotation about a fixed axis (e.g. O_x):

$$\omega(I) = \frac{dE(I)}{dI_x} \tag{4.15}$$

where I_x denotes the component of the total angular momentum I along the axis of rotation. An approximate relation between I_x and the total angular momentum I is often employed (see, for instance, Refs. [Ben79a, Ben79b]):

$$I_x = \left[I(I+1) - K^2\right]^{1/2} \approx \left[(I+1/2)^2 - K^2\right]^{1/2} \tag{4.16}$$

In Eq. 4.16, K denotes the component of I along the nuclear symmetry axis (the O_z axis). Approximating the differential quotient by a quotient of finite differences, Eq. 4.15 becomes:

$$\omega(I) = \frac{E(I+1) - E(I-1)}{I_x(I+1) - I_x(I-1)}. \tag{4.17}$$

Bohr and Mottelson introduced the quantities [Boh81]

$$J^{(1)} = \left[\frac{2}{\hbar}\frac{dE(I)}{d(I_x)^2}\right]^{-1} = \hbar\frac{I_x}{\omega}, \tag{4.18}$$

referred to as the "kinematic" moment of inertia, and

$$J^{(2)} = \hbar^2\left[\frac{d^2E(I)}{dI_x^2}\right]^{-1} = \hbar\frac{dI_x}{d\omega} = J^{(1)} + \omega\frac{dJ^{(1)}}{d\omega}, \tag{4.19}$$

referred to as the "dynamic" moment of inertia. These two quantities reflect two different physical aspects of the nuclear structure; in particular, the dynamical moment of inertia is related to the curvature of the $E(I)$ line. For a rigid-body rotation the two quantities coincide. The use of the plots involving kinematic or dynamic moments of inertia, being defined as derivatives, reveal more subtle variations in the nuclear structure of nuclei.

In the analysis of the properties of the bands in the crossing region one is not interested in the absolute values of some quantum-mechanical observables like energies and spins but rather in their differences between different configurations (bands). The relative values are obtained from the respective absolute values with a reference subtracted. As a reference rotor one may select the ground-state band.

For a reference rotational band (i.e. the ground-state band) it is convenient to introduce a kinematical moment of inertia $J^{(1)}_{ref}$ that is linear in ω^2:

$$J^{(1)}_{ref} = J^{(1)}_0 + J^{(1)}_2\omega^2. \tag{4.20}$$

This corresponds to the Harris formula of rotational spectra [Har65], which is equivalent to the VMI expression [Mar69]. In the equation above, the constant J_0 and J_1 have to be

adjusted for each nucleus separately. The angular momentum of the reference rotor along the axis of rotation $I_{x,ref}(\omega)$, denoted by $I_{ref}(\omega)$ is given by:

$$I_{ref}(\omega) = \hbar^{-1} J^{(1)}_{ref}\omega = \hbar^{-1}(J^{(1)}_0 + J^{(1)}_2\omega^2)\omega. \tag{4.21}$$

Any contribution to the total angular momentum $I(\omega)$ of the rotating nucleus originating from quasi-particles will show itself by a deviation from the smooth increase described by the equation above. The quasi-particle aligned angular momentum $i(\omega)$ is thus obtained as:

$$i(\omega) = I_x(\omega) - I_{ref}(\omega) \tag{4.22}$$

4.3.1 High-spin states in ^{69}Se

Positive-parity high-spin states

The top panel of Fig. 4.12 shows the kinematic moments of inertia of the oblate ground state structures in ^{68,69}Se and ^{68}Ge [Lim81, Pet89]. The data for ^{68}Se are taken from Refs. [Fis00, Fis03]. The corresponding alignments i_x are plotted in the bottom panel of the figure. The difference in initial alignment at low rotational frequencies ($i(\omega) \approx 4\hbar$) in ^{69}Se with respect to the even-even ^{68}Se and ^{68}Ge nuclei implies a nearly complete alignment of the odd neutron in a $g_{9/2}$ orbital with the axis of rotation.

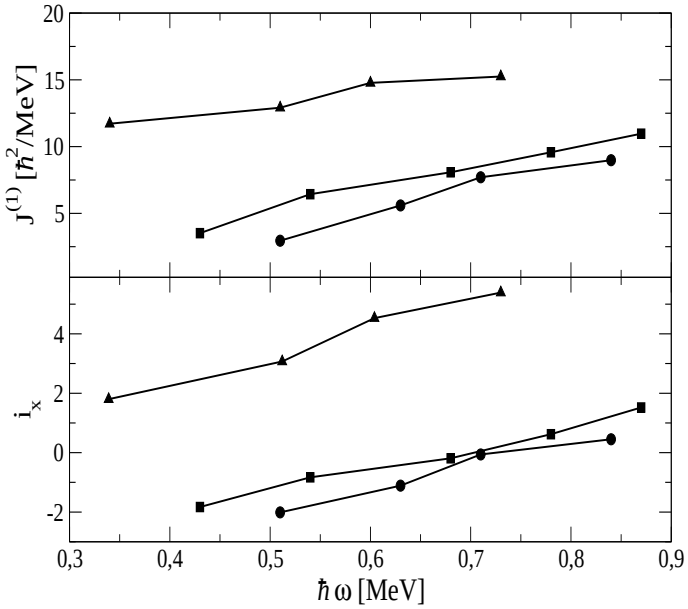

Figure 4.12: *Experimental kinematic moments of inertia $J^{(1)}$ (top) and alignments i_x (bottom) for the oblate ground-state structures in ^{68}Se (closed squares), ^{69}Se (closed triangles) and ^{68}Ge (closed circles). A common set of Harris parameters J_0=6.0 $\hbar^2 MeV^{-1}$ and J_1=3.5 $\hbar^4 MeV^{-3}$ taken from Ref. [Bru00] has been used for all nuclei.*

The properties of the excited prolate configurations in ^{68,69}Se and the proton-aligned band in ^{68}Ge are analyzed in Fig. 4.13. Interesting to note is the similarity between the behavior of the moment of inertia of the excited bands in ^{69}Se and ^{68}Ge (top panel of Fig. 4.13). The sharp backbend at the rotational frequency $\hbar\omega \approx$0.6 MeV and the gain in alignment of $\sim 7\hbar$ units of angular momentum in both nuclei are consistent with the alignment of a pair of $g_{9/2}$ protons occupying the low 1/2[440] orbital at prolate deformation. This indicates a strong polarization of the core and shape change from oblate triaxial shape at low spin to prolate shapes at intermediate spin. The observed similarity between the backbends and the alignments of the excited structure in ^{69}Se and the proton-aligned configuration in ^{68}Ge reciprocally confirms their nature and suggests a similarity in the shape of the two nuclei in this spin region. TRS calculations for ^{68}Ge predicted in this spin region two coexisting prolate minima ($\beta_2 \approx$0.2 and $\gamma \approx 13°$; $\gamma \approx -15°$) one being expected to correspond to the band considered in the present work and the other one corresponding to the proton-aligned band [Ste03].

In ^{68}Se, however, the first irregularity in the kinematic moment of inertia occurs at a lower rotational frequency ($\hbar\omega \approx$0.55 MeV) with respect to ^{69}Se and ^{68}Ge. Despite the low gain in alignment (see Fig. 4.13 bottom), this irregularity has been interpreted in Ref. [Fis00] as due to the alignment of $g_{9/2}$ particles in a near-prolate potential. The much larger backbending above spin I=14$^+$ has been predicted by Sun [Sun02] prior to its experimental observation [Fis03], and it was suggested to correspond to the subsequent 2-*qp* and 4-*qp* alignment of protons and neutrons. TRS calculations for ^{68}Se predict two excited bands, one corresponding to a more collective shape of $\beta_2 \sim$0.33 and $\gamma = -18°$ and the other to a less collective configuration with β_2=0.34 and $\gamma = +32°$ [Wys01]. The predicted bands were found to have characteristics very similar to the experimental bands investigated by Fischer *et al.* [Fis03].

In ^{69}Se and ^{68}Ge, a second crossing occurs in the frequency range $\hbar\omega$=0.8-0.9 MeV. Theoretically, a neutron alignment may take place but a second proton alignment cannot be excluded. An alternative scenario is that the observed irregularities are due to a crossing of shapes. However, the bands need to be developed to substantially higher spin before any firm conclusion can be reached concerning alignments or shape mixing.

Negative-parity high-spin states

Above spin 15/2$^-$ and excitation energies around 3 MeV, collective excitations predominate the high-spin negative-parity part of the level scheme in ^{69}Se. The 15/2$^-$ state at 3206 keV is the only certain candidate for the octupole state in ^{69}Se. Making use of the angular correlation and distribution data from the present work, no other 15/2$^-$ states were identified. The states 15/2$^-$, 19/2$^-$, and 23/2$^-$ at 3205.6, 3673.6, and 4387.8 keV excitation energies may be interpreted as the $g_{9/2}$ particle or hole coupled to the 3$^-$, 5$^-$, and 7$^-$ states in the neighboring even-even nuclei ^{68,70}Se [Fis00, Rai02]. Such a coupling picture follows the trend observed within the chain of Ge isotopes between ^{64}Ge and ^{70}Ge which suggested their interpretation in the framework of the weak-coupling model [Her95, Bec97]. The energies of these states agree very well with the energies of the corresponding core states in ^{70}Se, while the tentatively assigned analogous states in ^{68}Se are about 200-300 keV higher in energy. The occurrence of the two coexisting parallel

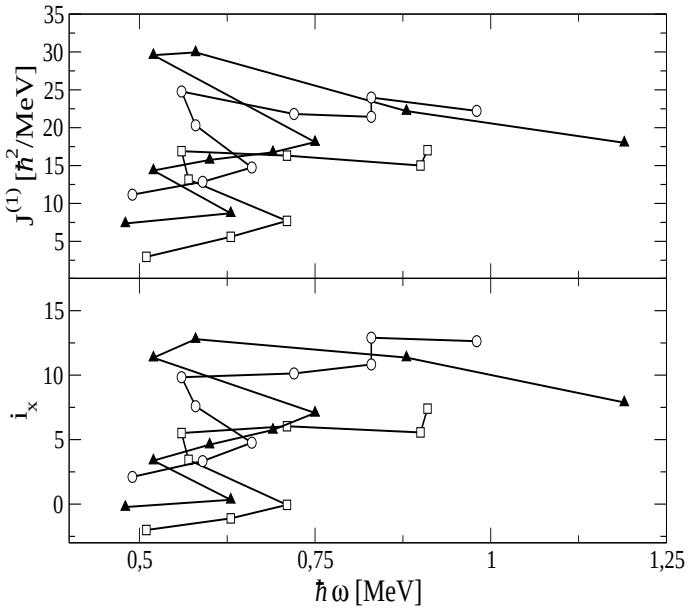

Figure 4.13: *Experimental kinematic moments of inertia $J^{(1)}$ (top) and alignments i_x (bottom) for the excited configurations in ^{68}Se (closed triangles), ^{69}Se (open circles) and the proton aligned band in ^{68}Ge (open squares). A common set of Harris parameters J_0=6.0 $\hbar^2 MeV^{-1}$ and J_1=3.5 $\hbar^4 MeV^{-3}$ taken from Ref. [Bru00] has been used for all nuclei.*

structures (bands 6 and 7 in Fig. 3.3) starting at a tentative spin of $(29/2^-)$ suggests a change in structure at high spin [Jen01].

4.3.2 High-spin states in ^{69}As

Positive-parity high-spin states

Figure 4.15 shows the kinematic ($J^{(1)}$) and the dynamic ($J^{(2)}$) moments of inertia for the three excited positive-parity bands identified in ^{69}As, the excited configuration recently observed in ^{67}As [Jen01] and the neutron-aligned band in ^{68}Ge [War00]. Unfortunately, positive-parity excited configurations in ^{71,73}As are not known to high enough spins to see the first upbend or backbend, preventing a more detailed systematic comparison. Similar behavior of the $J^{(1)}$ and $J^{(2)}$ in both ^{67,69}As may indicate similar shapes in these nuclei at intermediate spin. In ^{67}As, however, more experimental investigations are needed in order to establish firmly the high-spin structure of this nucleus. The sharp backbendings occurring in all nuclei around 0.53 MeV rotational frequency reflect the change in structures attributed in Refs. [Jen01, Bru00, Her92] with the breaking of a pair of $g_{9/2}$ neutrons, as suggested by the gain of $\sim 7\hbar$ units of angular momentum obtained in each of the alignment processes (see Fig. 4.16). In ^{68}Ge, additional experimental evidence for the neutron character of the alignment came from the measured g-factor of the 8^+ state of the band [Bar19].

Above spin $29/2^+$, two modes of rotation are present in ^{69}As, represented by bands 2

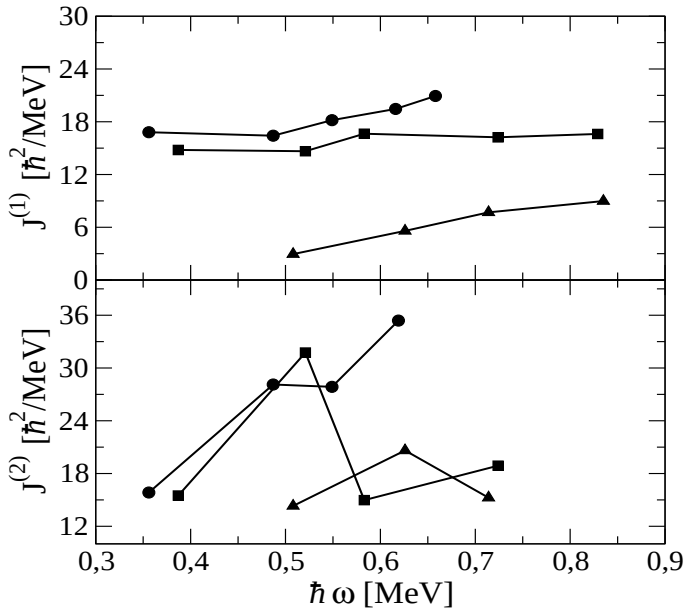

Figure 4.14: *Kinematic ($J^{(1)}$) and dynamic ($J^{(2)}$) moments of inertia for Band 1 in ^{69}As (closed squares), ground state band in ^{71}As (closed circles) and the ground state band in ^{68}Ge (closed triangles). For the As-nuclei, a value of K=5/2 has been used in the analysis.*

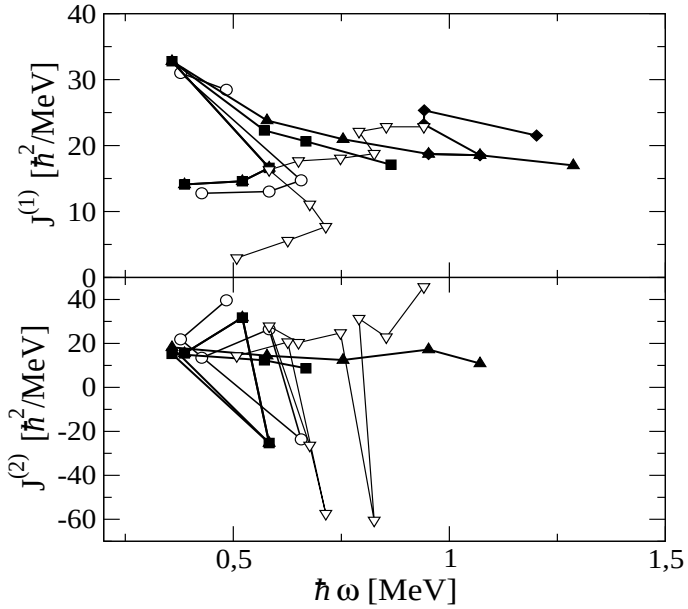

Figure 4.15: *Kinematic ($J^{(1)}$) and dynamic ($J^{(2)}$) moments of inertia for the excited bands in ^{69}As (closed symbols), ^{67}As (open circles) and ^{68}Ge (open triangles). For ^{69}As, the closed squares are the Band 2, the closed triangles are the Band 3 and the closed diamonds are the Band 4. A value of K=5/2 has been used in the analysis. Due to the limited spin range it has been observed, the dynamic moment of inertia for Band 4 has not been presented.*

and 3 in the level scheme of Fig. 3.3. Although Band 3 is not yrast, it involves a larger intensity of the intraband transitions, suggesting a higher collectivity in Band 3 than in Band 2. In Fig. 4.15 the kinematic and the dynamic moments of inertia for the excited bands in ^{69}As, ^{67}As and ^{68}Ge are plotted. The gradual down-sloping of the kinematic moment of inertia of Band 3 in ^{69}As at the highest spins is characteristic of a band moving toward termination and losing collectivity. On contrary, $J^{(1)}$ extracted for the neutron-aligned band in ^{68}Ge increases very smoothly. TRS calculations for ^{68}Ge in this spin region predicted two coexisting prolate minima ($\beta_2 \approx 0.2$ and $\gamma \approx 13°$; $\gamma \approx -15°$) one being expected to correspond to the band considered in the present work and the other one corresponding to the proton-aligned band [Ste03].

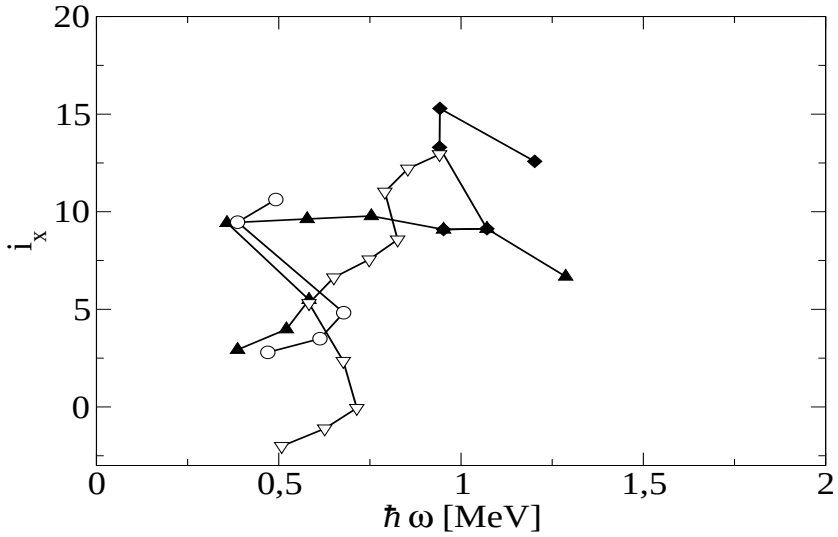

Figure 4.16: *Alignments i_x (i_x=I_x-i_{ref}) in ^{69}As (closed symbols), ^{67}As (open circles) and ^{68}Ge (open triangles). For ^{69}As, the closed triangles are the Band 3 and the closed diamonds are the Band 4. A common set of Harris parameters of J_0=6 $\hbar^2$/MeV and J_1=3.5 $\hbar^4$/MeV^3 taken from Ref. [Bru00] has been used for all nuclei. The alignments in the As-nuclei have been calculated considering K=5/2.*

The irregularity in the kinematic moment of inertia at $\hbar\omega \approx 1$ MeV in ^{69}As (see Fig. 4.15) indicates a second change in the positive-parity yrast line. There, Band 4 crosses Band 3, the former becoming yrast and contributing to the total alignment with $\sim 6\hbar$ units of angular momentum (Fig. 4.16).

Negative-parity high-spin states

The kinematic and the dynamic moments of inertia for the $\pi = -, \alpha = -1/2$ bands 5 and 6 are plotted in Fig. 4.17 (α denotes the signature; its physical meaning is explained in the next section). At $\hbar\omega \approx 0.67$ MeV, Band 5 undergoes a crossing, as suggested by the very irregular behavior of both $J^{(1)}$ and $J^{(2)}$. Although the kinematic moment of inertia for Band 6 shows a smooth increase with increasing rotational frequency, the weak peak

around 0.76 MeV in the dynamic moment of inertia may reflect a band crossing also for this structure.

The $\pi = -, \alpha = +1/2$ yrast structure (Band 7) exhibit a rather sharp backbending at $\hbar\omega \approx$0.7 MeV (see Fig. 4.18) which may be associated with an alignment of $g_{9/2}$ particles in a near prolate potential. The decrease in $J^{(1)}$ with increasing rotational frequency and the smooth drop in $J^{(2)}$ to values lower than $J^{(1)}$ in Band 7 suggest an unpaired regime of rotation typical to the terminating bands. On contrary, both the kinematic and dynamic moments of inertia extracted for Band 8 show a smooth increase with increasing rotational frequency. This behavior is similar to that of the $\pi = -, \alpha = +1/2$ yrast band in ^{71}As [Zig94]. In ^{71}As, TRS calculations for rotational frequencies around 0.4 MeV predict a single prolate γ-soft minimum in the potential energy. Above $\hbar\omega$=0.6 MeV this minimum was found to stabilize at $\gamma \approx 30^\circ$ [Zig94].

4.3.3 Cranked Nilsson-Strutinsky calculations at high spin

One of the most successful models in describing the properties of the high-spin rotational bands is the cranked Nilsson-Strutinsky (CNS) model. This model describes the observed bands in terms of configurations specified by the occupation of the valence orbitals. It makes it possible to study how specific configurations, which show up as collective rotational bands at intermediate spin values, gradually lose their collectivity and terminate in a non-collective state at the maximal spin which can be built within the configuration. This is associated with the fact that in configurations which are not strongly deformed and which can be characterised by a specific number of particles in the N-shells or j-shells, the angular momentum is limited. If one considers the nucleus as consisting of "inner" particles in closed shells forming a spherical core and the "outer" valence particles in partly filled shells, the maximum spin can be reached in a certain configuration (e.g. a specific occupation of the valence orbitals) is the sum of the angular momenta of the valence particles.

The process of building up angular momentum and terminating states is illustrated schematically in Fig. 4.19. At low rotational frequencies, the nucleus rotates around an axis perpendicular to the symmetry axis. This rotation can be described as collective in nature, but considered from a microscopic point of view, the total angular momentum (total spin) is built from the individual valence particle spins all having a small component in the total spin direction. As the total spin increases, these individual contributions will increase and start to become non-negligible compared with a typical single-particle angular momentum j. The valence particles will tend to rotate around the total spin axis with quantization taking place along this axis, i.e. they start to built up a ring of matter around this axis. With increasing angular momentum, the particles will show larger and larger tendencies to rotate around the total spin axis and finally become fully quantized along this axis, thus forming an oblate matter distribution of single-particles. In this single-particle state, the symmetry axis coincides with the rotation axis. Since collective rotation along the symmetry axis is forbidden in quantum mechanics, no further angular momentum can be brought into the system with the same occupation of single-particle orbitals and thus this state represents the termination of a rotational band. In this terminating (aligned) state, the angular momentum has reached its maximal value within

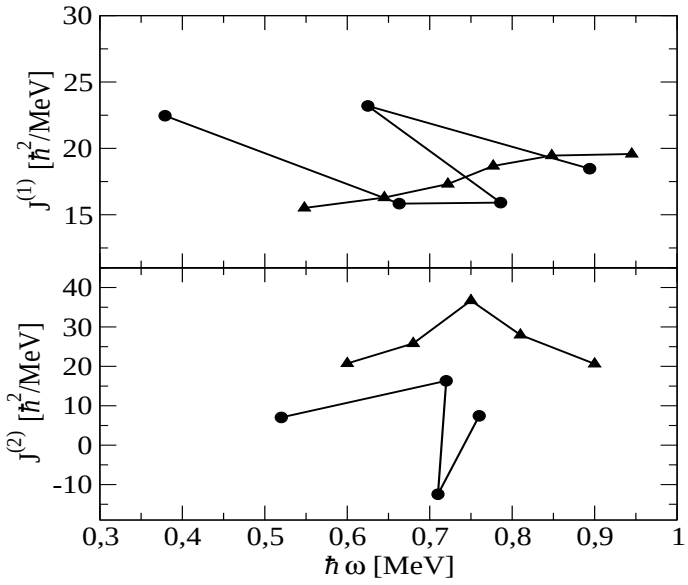

Figure 4.17: *Kinematic ($J^{(1)}$) and dynamic ($J^{(2)}$) moments of inertia for the $\pi = -, \alpha = -1/2$ bands 5 (closed circles) and 6 (closed triangles) in ^{69}As. In the plots, the $19/2^-$ states at 4488.7 and 4356.2 keV, respectively, have been taken as the lowest states. A value of K=5/2 has been used in the analysis.*

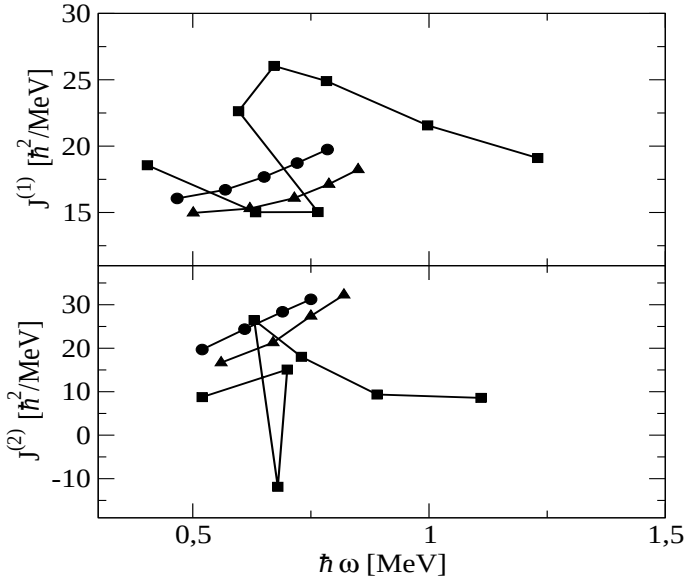

Figure 4.18: *Kinematic ($J^{(1)}$) and dynamic ($J^{(2)}$) moments of inertia for the $\pi = -, \alpha = +1/2$ bands in ^{69}As (closed squares and triangles) and ^{71}As (closed circles). For ^{69}As, the closed squares are the Band 7 and the closed triangles are the Band 8. The $17/2^-$ state at 3844.6 keV has been taken as the lowest state for both bands. For ^{71}As, the closed circles are the band labeled as Band 1 in Ref. [Fot99]. A value of K=5/2 has been used in the analysis.*

this specific configuration, where according to the Pauli principle, one particle in the j-shell will contribute $j\hbar$ to the total angular momentum, the next $(j-1)\hbar$, etc. In the ideal case described above, a specific configuration evolves continously from high collectivity at low spin to an aligned non-collective state at the maximum spin for this configuration, changing its deformed shape from prolate to oblate.

Systematic investigations of terminating bands in different mass-regions have been carried out within the macroscopic-microscopic approach using the standard cranked Nilsson potential. This theoretical method which is usually reffered to as the "configuration-dependent Cranked Nilsson-Strutinsky" (CNS) approach [Afa99], provides a sufficiently accurate physical description of the experimental bands like excitation energies as function of spin, shape trajectories, quadrupole moments or kinematic and dynamic moments of inertia.

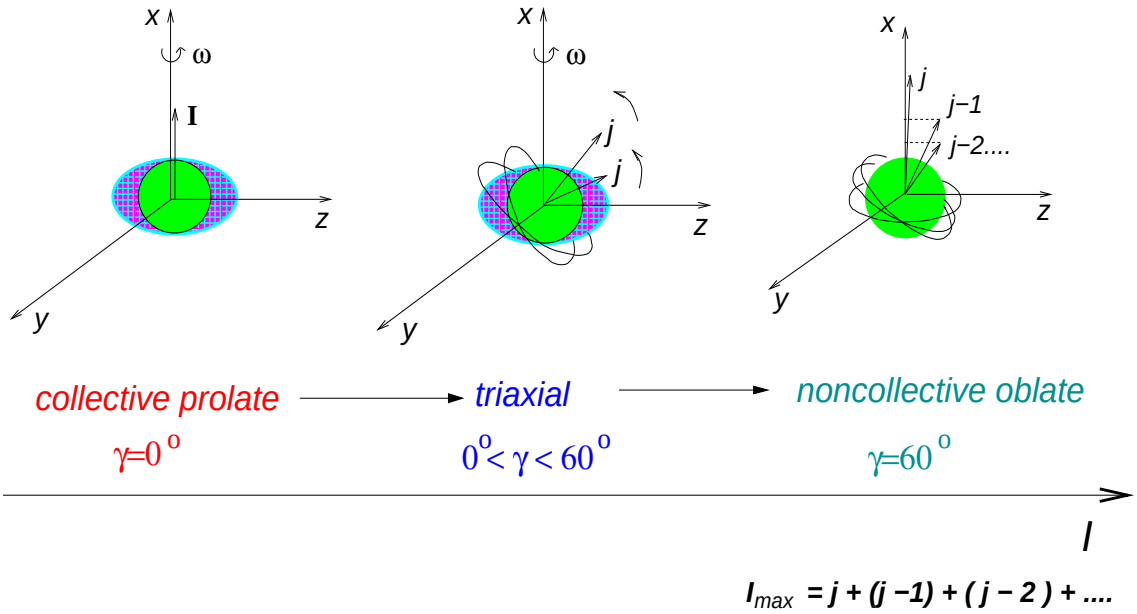

Figure 4.19: *Schematic illustration of a terminating configuration built from a closed core + a number of nucleons in partly filled j-shells. The configuration evolves from prolate and collective rotation at low spin over triaxial shape and partial alignment at indermediate spin to an aligned oblate state at termination. In an ideal terminating state all spin vectors point along the rotation axis.*

Frequently used alternatives for the single-particle potentials are the Wood-Saxon [Naz85] or Folded-Yukawa [Mol74] potentials; these should be essentially equivalent from the physical point of view. The advantage of using the modified Nilsson potential is that all matrix elements can be given in an analytic form. Therefore, compared with other potentials, it is often easier to deduce the physical origin of the new phenomena. The model does not include pairing so the calculations are realistic only at high spin. The neglecting of pairing has the advantage that the tracing of a fixed configuration undergoing drastic deformation changes become possible over the considerable spin range of a band

up to termination.

In the $A \sim 70$ mass-region, the CNS model has been used to describe the properties of the high-spin states in ^{68}Ge [War00], ^{70}Se [Rai02] and ^{70,72,73}Br nuclei [Jen02, Ple00, Ple01].

In the following subsection, a short description of the model is given. A more detailed discussion can be found in Ref. [Afa99].

The CNS model

The simplest way to describe the properties of rotating nuclei in a microscopic way is to use the cranking-model aproximation suggested by Inglis [Ing54, Ing55]. The single-particle cranking Hamiltonian is given as [Ben85]:

$$h^{\omega} = h^{0} - \omega j_{x}, \tag{4.23}$$

where the single-particle potential is the Nilsson potential in the form described by eq. 4.2. The eigenvalues and eigenfunctions of the cranked Nilsson Hamiltonian h^{ω} are determined using the eigenvectors of the cranked harmonic oscillator as basis states [Afa99, Ben85]. The matrix elements between different N-shells are neglected. This introduces a small error but it has the great advantage that N can be considered an approximate quantum number.

The diagonalization of the Hamiltonian 4.23 gives the eigenvalues e^{ω}_{ν}, which are referred to as single-particle energies in the rotation frame or routhians, and the eigenvectors Ψ^{ω}_{ν}. The single-particle energies in the laboratory system e_{ν} and the single-particle angular momentum alignments $< j_x >_{\nu}$ in the rotating system are obtained as

$$e_{\nu} =< \Psi^{\omega}_{\nu} \mid h^{0} \mid \Psi^{\omega}_{\nu} >, \qquad < j_x >_{\nu} =< \Psi^{\omega}_{\nu} \mid j_x \mid \Psi^{\omega}_{\nu} > \tag{4.24}$$

In the limit of high rotational frequencies, the total spin I is given by

$$I \approx I_x = \sum_{\nu \in occ} < \Psi^{\omega}_{\nu} \mid j_x \mid \Psi^{\omega}_{\nu} > \tag{4.25}$$

Since the cranked Hamiltonian 4.23 is invariant with respect to space inversion, parity is a good quantum number. In addition, the Hamiltonian remains invariant in the one-dimensional cranking approximation with respect to a rotation through an angle π around the cranking axis [Voi83],

$$\mathcal{R}_x = \exp(-i\pi j_x), \quad \mathcal{R}_i \Psi_i = \exp(-i\pi j_x)\Psi_i. \tag{4.26}$$

The eigenvalues of $\mathcal{R}_x$ are $\exp(-i\pi\alpha)$, where α is the signature exponent quantum number. The total parity and signature of a system is defined as

$$\pi_{tot} = \prod_{occ} \pi_i, \qquad \alpha_{tot} = \sum_{occ} \alpha_i \bmod 2, \tag{4.27}$$

where the multiplication and the sum extends over the occupied proton and neutron orbitals. For an even nucleus $\alpha_{tot} = 0$ gives I=0, 2, 4, ..., whereas $\alpha_{tot} = +1$ gives I=1, 3, 5, ... In odd nuclei $\alpha_{tot} = -1/2$ gives I=3/2, 7/2, 11/2, ..., whereas $\alpha_{tot} = +1/2$ gives I=1/2, 5/2, 9/2, ... Keeping track of π_{tot} and α_{tot} means that the total yrast line of

the nucleus is separated into four yrast lines, characterized by their parity and signature. The bands are usually denoted by $(\pi_{tot}, \alpha_{tot})$.

The total energy E_{tot} of the nucleus cannot be calculated just summing up the single-particle energies since such procedure fails to reproduce the average nuclear properties (e.g. the absolute binding energies) and their deformation dependence. The difficulties arise from the fact that in the Nilsson model the levels are grouped into shells leading to an oscillating level density and consequently an oscillating binding energy, in contrast to its observed smooth behavior. In fact, only the corresponding average part is wrong. It was the idea of Strutinsky to calculate only the fluctuating part of the total energy within the shell model and to take the average part from the liquid drop model [Str67, Str68].

Following the Strutinsky shell-correction procedure, in the CNS model the total energy E_{tot} of the rotating nucleus at a specific deformation $\bar{\varepsilon} \equiv (\varepsilon_2, \varepsilon_4, \gamma)$ and a specific spin I_0 is calculated as a sum of the rotating liquid drop energy and the shell energy

$$E_{tot}(\bar{\varepsilon}, I_0) = E_{LD}(\bar{\varepsilon}, I = 0) + \frac{I_0^2}{2J_{rig}(\bar{\varepsilon})} + \delta E_{shell}(\bar{\varepsilon}, I_0), \tag{4.28}$$

where the rigid-body moment of inertia J_{rig} is calculated with a sharp nuclear surface and a radius parameter r_0=1.2 fm.

The shell energy is calculated as

$$\delta E_{shell}(\bar{\varepsilon}, I_0) = \sum_{\nu \in conf} e_\nu(\omega, \bar{\varepsilon}, I = I_0) - \sum_\nu \widetilde{e_\nu}(\tilde{\omega}, \bar{\varepsilon}, \tilde{I} = I_0), \tag{4.29}$$

with both expressions evaluated at the same spin value I_0, which means that they are generally evaluated at different rotational energies. The smoothed sum is calculated using the Strutinsky procedure [Str67, Str68]. In the codes used in the present calculations, it is parameterized as

$$\sum_\nu \widetilde{e_\nu}(\tilde{\omega}, \bar{\varepsilon}, \tilde{I} = I_0) = E_0 + \frac{1}{2J_{str}(\bar{\varepsilon})} I_0^2 + bI_0^4, \tag{4.30}$$

where $J_{str}(\bar{\varepsilon})$ is the (Strutinsky) smoothed moment of inertia and $E_0 = \sum_\nu \widetilde{e_\nu}(\tilde{\omega}, \bar{\varepsilon}, \tilde{I} = 0)$. The constants E_0, J_{str} and b are determined by calculating the smoothed sum at several frequencies, e.g, at $\omega = 0$, at a large ω-value corresponding roughly to the highest spin values of interest, and at an intermediate ω-value.

With these formulas the total nuclear energy can be calculated as a function of spin I at any deformation. The minimum energy for different configuration constraints can be found in deformation space at all allowed spins.

The calculations are carried out in a mesh in the $(\varepsilon_2, \varepsilon_4, \gamma)$-deformation space. Then for each configuration and each spin separately, the total energy of a nucleus, is determined by a minimization in the shape degrees of freedom. The γ-parameter is varied in the interval $-120° \leq \gamma \leq 60°$. It is well known that all the ellipsoidal shapes can be described in the interval $0° \leq \gamma \leq 60°$ but the extension of γ to three 60° sectors is necessary to allow for the possibility of cranking around each of the three principal axes (see Fig. 4.20). In the three sectors (namely $-120° \leq \gamma \leq -60°$, $-60° \leq \gamma \leq 0°$ and $0° \leq \gamma \leq 60°$) the intrinsic shape is the same; only the relation between the symmetry-axis and the cranking

axis is different. For a certain mass and deformation ε_2 the liquid drop model yields the largest moment of inertia for $\gamma = 60°$, a smaller value at $\gamma = 0°$, a still smaller value for $\gamma = -60°$ and the smallest value in the case of $\gamma = -120°$ [Voi83]. The largest moments of inertia correspond to rotation with the lowest energies and it is therefore not surprising that most nuclei attain shapes corresponding to the sector between $\gamma = 0°$ and $60°$.

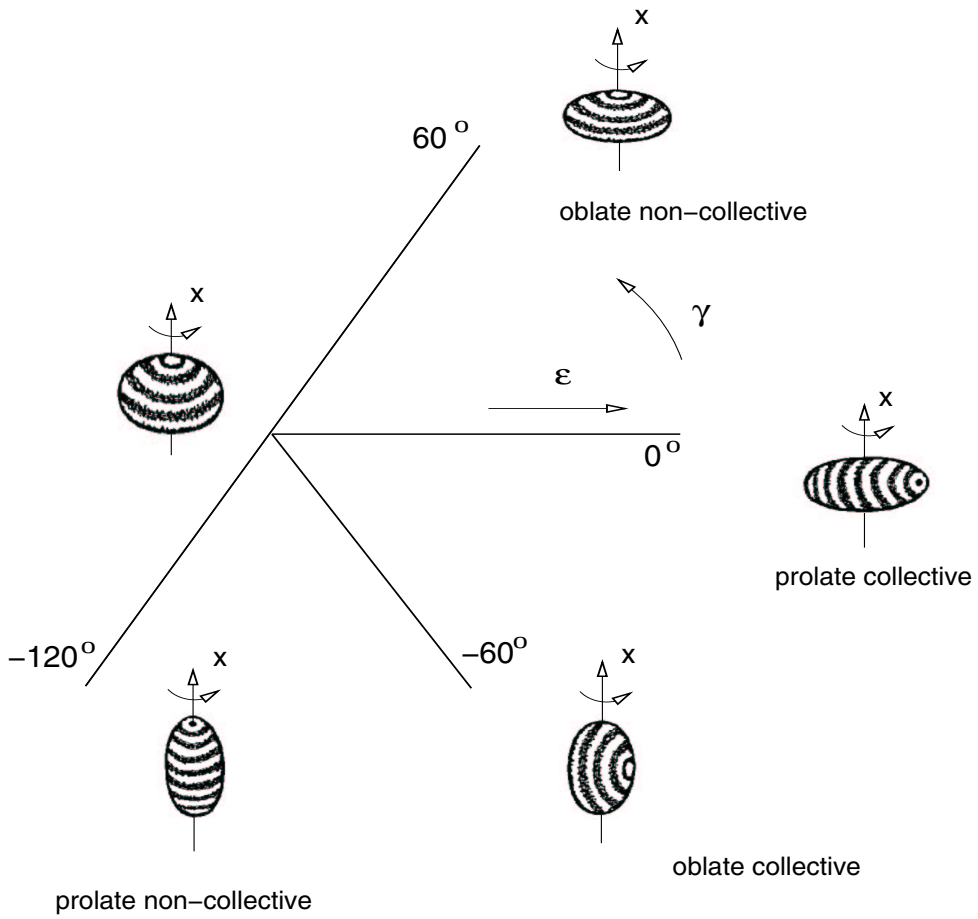

Figure 4.20: *Various nuclear shapes expressed by the deformation parameter ε_2 (plotted radially) and the asymmetry parameter γ. The rotation axis is defined as the x-axis. The maximum collectivity is found for $\gamma = -60° \div 0°$ whereas individual nucleon excitations occur at shapes with $\gamma = 60°$ and $\gamma = -120°$. For $\gamma = 60°$ (oblate shape) and for $\gamma = -120°$ (prolate shape), the nucleus rotates around the symmetry axis while the rotation takes place around the perpendicular axis for $\gamma = 0°$ (prolate shape) and $\gamma = -60°$ (oblate shape). For other γ-values, the nucleus is triaxial with the rotation axis coinciding with the shorter ($\gamma = 0° \div 60°$), the intermediate ($\gamma = 0° \div -60°$) and the longer ($\gamma = -60° \div -120°$) principal axis, respectively.*

In comparing the total energies of the calculated and the experimental bands, $(E(I) - E_{rld}(I))$ plots are used, i.e., excitation energies with an "average" rigid rotor reference subtracted. Such plots provide considerably more detailed information about individual

and relative properties of the rotational bands. Considering that most terminating bands start at a near-prolate ($\gamma \sim 0°$) deformation of $\varepsilon_2 \sim 0.25 - 0.30$ and terminate at oblate ($\gamma = 60°$) deformation of $\varepsilon_2 \sim 0.15$, a reasonable rigid rotor reference can be specified as [Rag86]

$$E_{rld} = \frac{1}{2J_{rig}} I(I+1), \qquad \frac{1}{2J_{rig}} \approx 32.32 A^{-5/3} \frac{MeV}{\hbar^2}, \tag{4.31}$$

with A being the mass number.

The present formalism neglects the pairing correlations, so that the calculations are realistic only above spin I=15$\hbar$.

Model parameters

The parameters appearing in the calculations can generally be divided into two types:

- Parameters like κ and μ describing the $l \cdot s$ and l^2-strengths of the single particle potential or the liquid-drop model constants a_ν, a_s, etc. Such parameters are fixed from fits to experimental quantities and are valid over a large range of nuclei. The liquid-drop parameters widely used are those of Myers and Swiatecki [Mye67]. The Nilsson parameters (κ,μ) are dependent on the main oscillator quantum number N and the set defined in Ref. [Ben85] is usually called "standard". Although this standard set facilitate the study of a wide range of nuclei, it is sometimes necessary to fit the parameters of the Nilsson potential for a specific region in order to obtain a more accurate description of the experimental data. The set of parameters used in the calculation of the nuclei in the $A \sim$70 mass region are those proposed by Galeriu *et al.* [Gal86] and referred to as "A=80 parameters". This latter set of parameters has been used in the present work.

- Parameters like those describing the deformation of the mean field ($\varepsilon_2, \varepsilon_4, \gamma$). Such parameters are calculated self-consistently (e.g. from the minimization of the total energy) or they may be fixed, for example, from measured quadrupole moments. In the present calculations, the total energies corresponding to Eq. 4.28 have been calculated using a rectangular mesh of Cartesian variables,

  $$x = \varepsilon_2 \cos(\gamma + 30°); \quad y = \varepsilon_2 \sin(\gamma + 30°), \tag{4.32}$$

  with the mesh points defined by

  $$x = 0.0, 0.04, 0.08, \ldots, 0.56; \quad y = -0.56, -0.52, \ldots, 0.52, 0.56. \tag{4.33}$$

  The hexadecapole deformation is defined to take the values

  $$\varepsilon_4 = -0.06, -0.03, 0.0, 0.03, 0.06. \tag{4.34}$$

A flow chart of the codes associated to the cranked Nilsson-Strutinsky model and used in the present calculations is given in Appendix A.3.

Single-particle routhians - illustrative example

Figure 4.21 shows the effects on the spherical shells of breaking the spherical symmetry

(left), the axial symmetry (middle) and the time-reversal symmetry (right). Starting from spherical shape, the static orbitals are first drawn for prolate shape up to ε_2=0.3. This is the typical Nilsson diagram for prolate nuclei in the $A \sim$70 mass-region. In the middle panel of Fig. 4.21, the value of the γ asymmetry parameter is increased from 0° to 20° for a constant quadrupole deformation of ε_2=0.3.

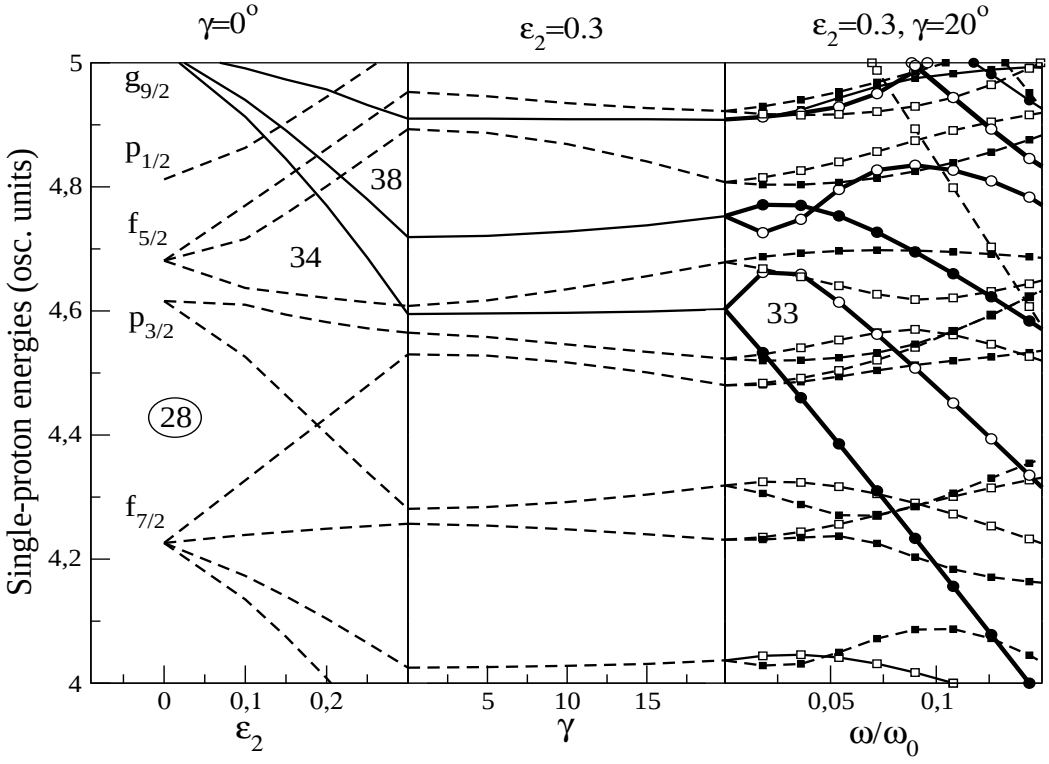

Figure 4.21: *Single-proton energies as function of the quadrupole deformation ε_2 (left), asymmetry parameter γ (middle) and rotational frequency ω/ω_0 (right). The A=80 parameters have been used for the Nilsson potential. The (ε_2, γ) values are those found to be specific to the nuclei in the A$\sim$70 mass-region. Solid and dashed lines correspond to positive- and negative-parity orbitals, respectively. In the right panel, the closed and open symbols describe the states with signatures $\alpha = +1/2$ and $\alpha = -1/2$, respectively.*

Each state can be occupied by a maximum of 2 particles, i.e., the states with a projection of the particle angular momentum j on the symmetry axis with Ω and -Ω are indistinguishable. When the deformed nucleus experiences a rotation, Coriolis and centrifugal forces act on the individual nucleons in the rotating frame, the extra term -$\hbar\omega j_x$ must be added to the intrinsic Hamiltonian for independent-particle motion (see eq. 4.23). The Coriolis interaction depends on the angular velocity and therefore violates time-reversal invariance and lifts the two-fold degeneracy of the Nilsson levels, each level being split into two components. This is illustrated in the right panel of Fig. 4.21 where the eigenvalues e_ν^ω of the cranking Hamiltonian 4.23 (single-particle Routhians) are plotted as functions of angular velocity ω/ω_0 for the Nilsson potential with deformation ε_2=0.3 and γ=20°.

The closed and open symbols describe states with signature $\alpha = +1/2$ and $\alpha = -1/2$, respectively. Those Routhians corresponding to orbitals most sensitive to rotation decrease very steeply with ω and can be approximately characterized by a large angular momentum j and its large projection j_x to the cranking axis. They lead to the strongest alignment of the nucleonic angular momenta with the rotation axis. In fact, the aligned angular momentum $< \nu \mid j_x \mid \nu >$ can be seen as directly related to the slope of the curve e^{ω}_{ν} vs ω at a fixed deformation:

$$\frac{de^{\omega}_{\nu}}{d\omega} = -\hbar < \nu \mid j_x \mid \nu >, \tag{4.35}$$

with the minus sign originating from the minus sign in the formula for the Routhian. The rotation-sensitive orbitals are found to be the lowest members of high-j multiplets, such as $g_{9/2(\Omega=1/2)}$ and $g_{9/2(\Omega=3/2)}$ in the example considered here or the $h_{11/2(\Omega=1/2)}$, $h_{11/2(\Omega=3/2)},\ldots$, $h_{9/2(\Omega=1/2)}$, $h_{9/2(\Omega=3/2)},\ldots$, or $i_{13/2(\Omega=1/2)}$, $i_{13/2(\Omega=3/2)},\ldots$, for heavier nuclei.

Configuration labeling

Figure 4.22 shows the single-particle routhians calculated as function of rotational frequency ω for a fixed deformation ε_2=0.3 and γ=5°. Such deformation is believed to characterize the intermediate-spin region of the yrast positive-parity bands in ^{69}Se and ^{69}As.

As was discussed in the previous subsection, the eigenstates of the cranking Hamiltonian have a definite signature and parity. Moreover, the principle quantum number N (usually denoted as N_{rot}) is a preserved quantum number. Thus, the parity π, the signature α and the principal quantum number N_{rot} can be used to label the routhians. In the example considered in Fig. 4.22, the positive parity orbitals are those from the N=4, $g_{9/2}$ subshell and they are drawn with full lines whereas the dashed lines indicate the negative-parity orbitals emerging from the N=3, $f_{7/2}$, $p_{1/2}$, $f_{5/2}$ and $p_{1/2}$ subshells. For a given parity, the orbitals with positive signature are represented with closed symbols and those with negative signature with open symbols.

In a deformed rotating potential, the orbitals within the same N_{rot} shell strongly mix, but in some cases a distinction between high-j and low-j orbitals into different group of subshells is possible. Considering for example the N=4 shell, it is known that for a spherical shape, the spin-orbit term $l \cdot s$ lowers the $g_{9/2}$ subshell with respect to the other N=4 subshells, such as $d_{5/2}$ or $g_{7/2}$. As the nucleus becomes more deformed, the $d_{5/2}$ and $g_{7/2}$ orbitals are expected to mix strongly since they are very close together, but still separated from the $g_{9/2}$ subshell. Thus, for not to large deformations and/or rotational frequencies, the orbitals from the $g_{9/2}$ subshell remain rather pure and they can be classified as high-j orbitals whereas the mixed $d_{5/2}g_{7/2}$ orbitals are the low-j orbitals. In the N=3 shell, a similar division is generally appropriate, e.g. treating the $f_{7/2}$ subshell as high-j orbitals and the group of $f_{5/2}p_{3/2}$ subshells as low-j orbitals. Thus, when a configuration is labeled as having n particles, e.g. in the $f_{5/2}p_{3/2}$ subshells, the meaning is not that the particles are in these pure subshells but instead that they are

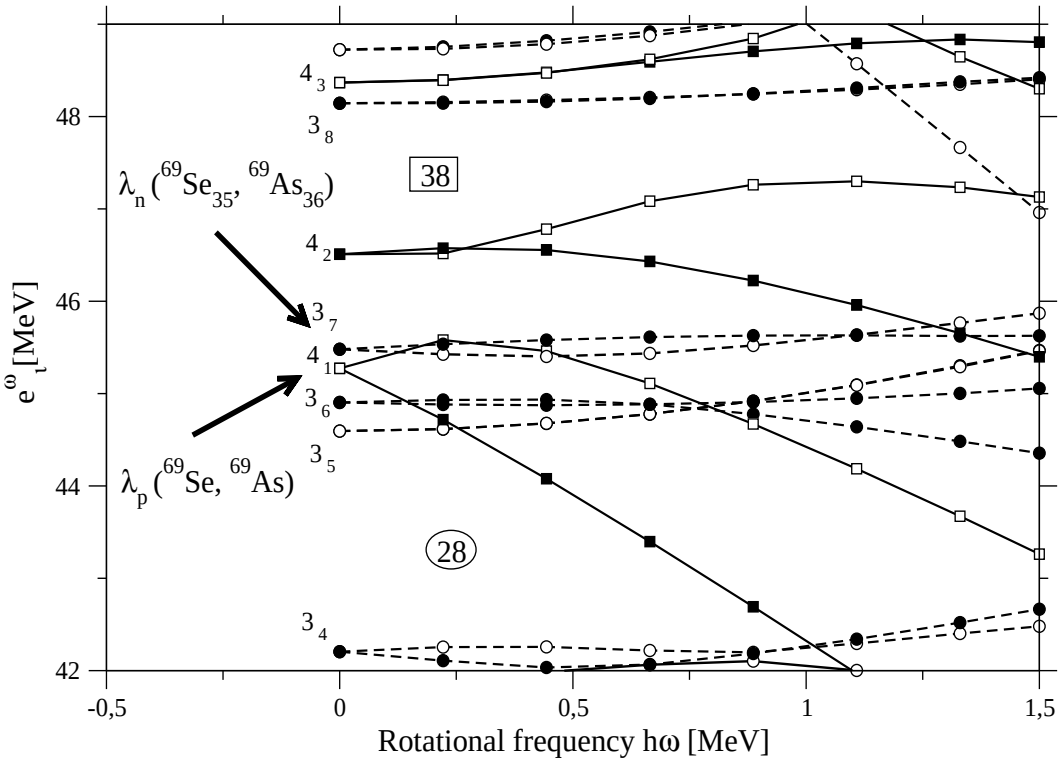

Figure 4.22: *Calculated single-particle energies at constant deformation ε_2=0.3, ε_4=0.0 and $\gamma = 5°$. The orbitals are labeled according to their N-shell with the ordering in the shell as a subscript. Solid and dashed lines correspond to positive- and negative-parity orbitals, respectively. The closed and open symbols describe the states with signatures $\alpha = +1/2$ and $\alpha = -1/2$, respectively. A=80 parameters have been used for the Nilsson potential.*

distributed over the orbitals of the deformed rotating potential, whose wave functions have their main components in these subshells. An example of configuration specification in terms of occupation of different N_{rot}-shells consisting of high- and low-j orbitals of different signature α, is given in Table 4.6.

Choosing the configurations

In performing the calculations for the nucleus of interest, one has to start by specifying the configurations likely to correspond to the experimental bands. These configurations will consist of "inner" particles in closed shells forming a spherical core and the "outer" valence particles in partly filled shells, the former determining the main properties of the nucleus. In the $A \sim 70$ nuclei the closed shells are N=0, 1 and 2 and they define the doubly-magic core $^{40}_{20}Ca_{20}$. The remaining particles will then fill the orbitals of the N=3 and N=4 shells. The $N = Z$=28 magic numbers leads to the $f_{7/2}$ subshell of the N=3

Table 4.6: Configuration in ^{69}As specified in terms of the occupation of different high- and low-j N_{rot} orbitals of different signature α.

	N_{rot}=	0	1	2	3	4	5
Proton configuration							
$\alpha = -1/2$	low-j	0	1	3	2	0	0
$\alpha = -1/2$	high-j	1	2	3	4	0	0
$\alpha = +1/2$	low-j	0	1	3	2	0	0
$\alpha = +1/2$	high-j	1	2	3	4	1	0
Neutron configuration							
$\alpha = -1/2$	low-j	0	1	3	3	0	0
$\alpha = -1/2$	high-j	1	2	3	4	1	0
$\alpha = +1/2$	low-j	0	1	3	3	0	0
$\alpha = +1/2$	high-j	1	2	3	4	1	0

shell to be completely occupied, so that the valence particles expected to play a role in the structure of the yrast line in the nuclei in the $A \sim$70 mass-region are those outside the doubly-magic nucleus $^{56}_{28}$Ni$_{28}$. The configurations included in calculations will then differ only by the way of arranging the valence particles in the N=3, low-j, $f_{5/2}p_{3/2}$ subshells, and N=4, high-j, $g_{9/2}$ subshell.

An example of defining configurations independent of parity or signature is illustrated in Fig. 4.22. For 33 protons, the lowest energy is obtained if the orbitals below the spherical Z=28 gap are filled, one proton is in the N=4, 4_1 orbital of $\alpha = +1/2$ signature and the four remaining valence protons are placed in the N=3 orbitals, 3_5 and 3_6. With the division in low- and high-j discussed above, this specific way of arranging the valence particles will correspond to the $(f_{5/2}p_{3/2})^4(g_{9/2})^1$ configuration. It is evident that at the deformation chosen, this is the lowest energy proton configuration at low spin. Examining the single-particle routhians shown in Fig. 4.22, some general features can be extracted. It is seen that at the deformation and for the rotational frequencies considered, the two signatures of the orbitals in the N=3 shells are almost degenerate. Consequently, the most favourable way to distribute the valence particles in the $f_{7/2}$ subshell or $f_{5/2}p_{3/2}$ group of subshells is to have an equal number of particles in both signatures (α_{tot}=0). Configurations involving an odd number of $N = 3$ particles will be doubly degenerate, depending on whether the hole is in the positive or the negative signature.

In defining excited configurations, one is obviously interested to find the favored configurations (i.e. the lowest in energy) of maximal spin. Such configurations are those which involve several particles in the $g_{9/2}$ orbitals, since these particles are easy to align and the gain in alignment is maximal. This is achieved by exciting particles from the N=3 shell into the N=4, $g_{9/2}$ subshell. In the case considered in Fig. 4.22, these are the configurations obtained by lifting one proton from either 3_5 or 3_6 orbitals into the 4_1, $\alpha = -1/2$ orbital, thus forming the $(f_{5/2}p_{3/2})^3(g_{9/2})^2$ configurations. However, in the calculations, there is no way to distinguish between the 3_5, 3_6 or 3_7 orbitals, since all are classified as low-j, $f_{5/2}p_{3/2}$ orbitals.

Configurations with more than two $g_{9/2}$ protons are formed in the same way, but they

are expected to lie at high energies since it is energetically very expensive to excite a third proton from the N=3 orbitals near the Fermi surface to the higher lying, e.g. 4_2, $\alpha = +1/2$ orbital. Even higher spin can be obtained by exciting particles across the Z=28 gap, i.e. by making holes in the $f_{7/2}$ subshells. This kind of configuration will be discussed in the next subsection.

Figure 4.22 is drawn for protons but it is straigtforward to define configurations for neutrons in an analogous manner. Furthermore, the deformation is chosen to be illustrative and a similar procedure is carried out for all other deformations in a mesh in the $(\varepsilon_2, \varepsilon_4, \gamma)$-space. Consequently, configurations can be defined consistently in the full deformation space, and the energy vs. spin curves can be calculated for these fixed configurations at the different mesh points. Thus, it becomes possible to draw total energy surfaces at fixed spins and find the energy minimum in the $(\varepsilon_2, \varepsilon_4, \gamma)$-space for each configuration. In this way, the total energy E and the equilibrum deformation as functions of the spin I are obtained.

CNS calculations at high spin in ^{69}As

In the calculations for ^{69}As, 12 proton configurations have been considered as containing the most favoured ways of arranging the 5 valence protons in the $f_{5/2}p_{3/2}$ and $g_{9/2}$ valence orbitals outside the doubly-magic core $^{56}_{28}\mathrm{Ni}_{28}$. For the 8 valence neutrons, 15 neutron configurations have been considered. In building the configurations, the main idea was that the configurations with the lowest energy will be those having up to 3 protons and 4 neutrons in the $g_{9/2}$ orbital. Furthermore, the most favoured way to arrange the valence particles in the $f_{5/2}p_{3/2}$ and $g_{9/2}$ valence orbitals is to have an approximately equal number of particles in each signature.

By combining the 12 proton and 15 neutron configurations, four groups of total configurations were obtained, depending on the total parity and signature: $\pi = +, \alpha \pm 1/2$ and $\pi = -, \alpha \pm 1/2$. The theoretical bands built on these configurations were investigated separately and the results obtained were compared with the experimental bands. Since the model does not include pairing, only states above spin I=10 are discussed.

The detailed structure of the configurations which appear relevant when assigning theoretical counterparts to the observed bands in ^{69}As are summarized in Table 4.7. The calculated configurations are labeled as $[p, n]_{\gamma_{av}}$, where $[p, n]$ represents the number of protons and neutrons in the $g_{9/2}$ orbitals and the index γ_{av} is the average γ deformation of the configuration. This indexing was introduced in order to distinguish between the configurations with the same distribution of the particles over the valence j-shells which were found in the calculations to exhibit two low-lying minima in the potential-energy surfaces. The labeling $(\ldots)^q_s$ used in Table 4.7 refers to the number of particles q in the respective subshell or group of subshells whose spins couple to the total angular momentum s in the maximal-spin state. The maximal-spin states of these configurations are in the I=25-30 range, as specified in the table. In the corresponding terminating states at oblate shape, $\gamma = 60°$, the deformation is generally rather large, $\varepsilon_2 \approx 0.30$.

In the top panel of Fig. 4.23, the $(E - E_{rld})$ curves for the lowest calculated $\pi = +, \alpha = +1/2$ bands are shown. The energy of the rigid rotor reference E_{rld} is calculated is indicated in Eq. 4.31. At low spin, bands with one proton and two neutrons in the $g_{9/2}$

Table 4.7: The structure of the calculated bands which are likely to correspond to the experimental bands observed in ^{69}As. The columns 5 and 6 give the calculated deformation parameters in the maximum spin state of each fixed configuration. In the last column, the terminating spin value I_{term} is given, where a star indicates that this value coincides with I_{max}, the maximum spin value which can be built for a specific distribution of the particles over the subshells.

Label	Configuration	Exp. band	I^{exp}_{max} [$\hbar$]	ε_2	γ	I_{term} [$\hbar$]
	$\pi = +, \alpha = +1/2$					
$[1,2]_{\gamma\sim 50^\circ}$	$\pi(g_{9/2})^1_{4.5}(f_{5/2}p_{3/2})^4_4 \otimes \nu(g_{9/2})^2_8(f_{5/2}p_{3/2})^6_4$	Band 2	37/2	0.26	60°	41/2
$[1,2]_{\gamma\sim 30^\circ}$	$\pi(g_{9/2})^1_{4.5}(f_{5/2}p_{3/2})^4_6 \otimes \nu(g_{9/2})^2_8(f_{5/2}p_{3/2})^6_6$	Band 3	45/2	0.22	53°	49/2*
$[2,3]$	$\pi(g_{9/2})^2_8(f_{5/2}p_{3/2})^3_{4.5} \otimes \nu(g_{9/2})^3_{10.5}(f_{5/2}p_{3/2})^5_{5.5}$	Band 4	53/2	0.31	60°	57/2*
	$\pi = -, \alpha = -1/2$					
$[1,3]$	$\pi(g_{9/2})^1_{4.5}(f_{5/2}p_{3/2})^4_4 \otimes \nu(g_{9/2})^3_{10.5}(f_{5/2}p_{3/2})^5_{2.5}$	Band 5	39/2	0.32	60°	43/2
$[2,2]_{\gamma\sim 50^\circ}$	$\pi(g_{9/2})^2_8(f_{5/2}p_{3/2})^3_{3.5} \otimes \nu(g_{9/2})^2_8(f_{5/2}p_{3/2})^6_0$	Band 5		0.34	60°	39/2
$[2,2]_{\gamma\sim 15^\circ}$	$\pi(g_{9/2})^2_8(f_{5/2}p_{3/2})^3_{5.5} \otimes \nu(g_{9/2})^2_8(f_{5/2}p_{3/2})^6_6$	Band 6	43/2	0.26	22°	55/2*
$[2,2]$	$\pi(g_{9/2})^2_8(f_{5/2}p_{3/2})^3_{2.5} \otimes \nu(g_{9/2})^2_8(f_{5/2}p_{3/2})^6_5$	Band 6		0.29	60°	47/2
	$\pi = -, \alpha = +1/2$					
$[2,2]_{\gamma\sim 15^\circ}$	$\pi(g_{9/2})^2_8(f_{5/2}p_{3/2})^3_{4.5} \otimes \nu(g_{9/2})^2_8(f_{5/2}p_{3/2})^6_4$	Band 7	49/2	0.30	60°	49/2
$[1,3]$	$\pi(g_{9/2})^1_{4.5}(f_{5/2}p_{3/2})^4_6 \otimes \nu(g_{9/2})^3_{10.5}(f_{5/2}p_{3/2})^5_{5.5}$	Band 8	41/2	0.26	60°	53/2*

orbitals ($[1,2]$) are calculated to be the lowest in energy, whereas above spin $41/2^+$, the $[2,3]$ configuration is predicted to be yrast. These calculated configurations are compared in the lower panel of Fig. 4.23 with the relative energies ($E - E_{rld}$) of the experimental positive-parity bands 2, 3 and 4. Configurations $[1,2]_{\gamma\sim 50^\circ}$ and $[1,2]_{\gamma\sim 30^\circ}$ correspond to the two minima in the potential-energy surface of the same fixed configuration (see Fig. 4.24). The two configurations are very good candidates for bands 2 and 3, respectively. The experimental and the calculated bands show about the same curvature in the energy graphs. The terminating calculated spins for the $[1,2]_{\gamma\sim 50^\circ}$ and $[1,2]_{\gamma\sim 30^\circ}$ configurations (see Table 4.7 and Fig. 3.3) suggest that bands 2 and 3 were observed up to two units of angular momentum lower than their respective terminations. The crossing between the

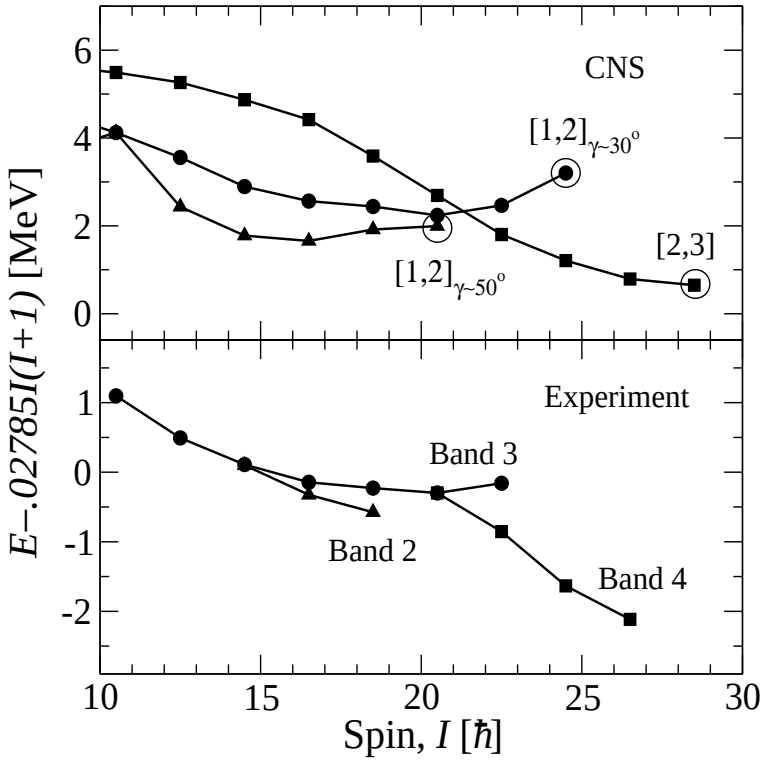

Figure 4.23: *Calculated (top) and experimental (bottom) energies of the ($\pi = +, \alpha = +1/2$) configurations relative to a standard rotor reference. The calculated bands are labeled by the number of the $g_{9/2}$ protons and neutrons. The aligned states (γ=60°) are indicated by large open circles. The maximum spin for the [1,2]$_{\gamma\sim30°}$ configuration is predicted at $\gamma \sim 53°$, which can in principle be considered a terminating state.*

two experimental bands, observed around spin $29/2^+$ is not well described by the theory. However, the exact crossing point is sensitive to the detailed features of the single-particle energies used in the model. Moreover, in this spin region pairing correlations could still be important so the CNS calculations should be considered with some caution.

In the spin range $45/2^+$-$57/2^+$, the [2,3] configuration is calculated to be the lowest in energy. This is in very close agreement with the experimental situation where at spin $45/2^+$, Band 4 becomes yrast by crossing Band 3 (Fig. 4.23, bottom). Thus, the crossing between Band 3 and Band 4 may be interpreted as the crossing between configurations with different numbers of $g_{9/2}$ particles ([1,2] and [2,3], respectively) and slightly different deformations. At the predicted crossing spin, I=$41/2^+$, the calculated shapes for the [1,2]$_{\gamma\sim30°}$ and [2,3] configurations are ε_2=0.24, γ=22° and ε_2=0.33, γ=26°, respectively. In this region of rather high rotational frequencies, it is reasonable to believe that at crossing, the $g_{9/2}$ particles in the $[2, 3]$ configuration have their angular momentum almost fully aligned with the axis of rotation. A gain in alignment of $\sim 6\hbar$ units is expected from the additional $g_{9/2}$ proton and neutron in the $[2, 3]$ configuration with respect to the [1,2]$_{\gamma\sim30°}$ configuration. This is in a very good agreement with the experimental observations (see

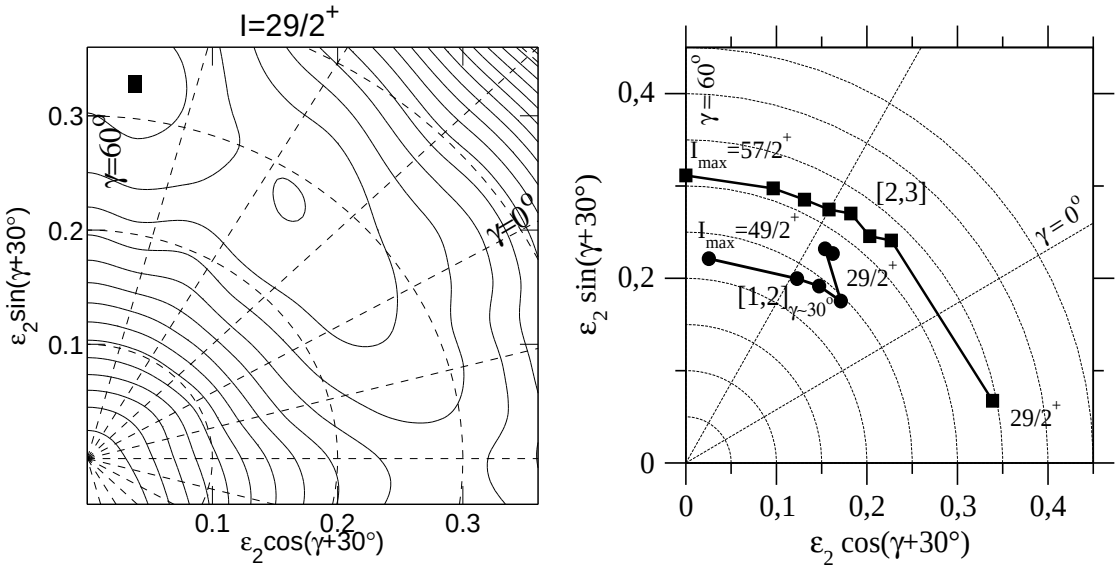

Figure 4.24: *Left: Potential-energy surface for the [1,2] configuration ($\pi = +, \alpha = +1/2$) at spin I=14.5$^+$. The lowest minimum is marked with a closed square. The energy difference between neighboring equipotential lines is 0.4 MeV. Right: Shape trajectories for the calculated configurations [1,2]$_{\gamma\sim30°}$ and [2,3] ($\pi = +, \alpha = +1/2$), believed to correspond to the experimental bands 3 and 4 in ^{69}As.*

Fig. 4.16).

In the $I = 45/2^+$ spin region, the TRS calculations for ^{69}As performed in Ref. [Bru00] predicted a strongly deformed minimum ($\beta_2 \approx 0.45$) coexisting with a triaxial prolate minimum ($\beta_2 \approx 0.20$, $\gamma \approx 25°$). The strongly deformed band is expected to contain an additional pair of particles which have been moved from the $f_{7/2}$ into the $g_{9/2}$ orbits [Bru00]. In such case, the two excited $f_{7/2}$ particles are more likely to be protons, since in a nucleus with 36 neutrons it is energetically very unfavorable to make holes in the $f_{7/2}$ neutron orbital. A superdeformed band obtained by promoting two protons from the $f_{7/2}$ orbital into the $g_{9/2}$ orbital has been reported in the neighboring even-even core ^{68}Ge and interpreted within the CNS approach [War00]. The experimental excitation energy is not known so that the calculated configurations with two proton holes in the $f_{7/2}$ subshell were compared with the superdeformed band in ^{68}Ge assuming different spin values and arbitrary excitation energies [War00].

^{69}As is only one proton away from ^{68}Ge, so, in principle, a $f_{7/2}^{-2}$ strongly deformed band is likely to occur, although is not expected to become yrast until very high spin. Calculations for few low-lying configurations of this kind have been carried out. It was found that the $f_{7/2}^{-2}$ bands are predicted to lie in general 1-2 MeV higher in energy than the lowest pure valence space configurations and become yrast around spin $I = 30$ when the spin is exhausted in the valence-space configurations.

The deformation paths for the [1,2]$_{\gamma\sim30°}$ and [2,3] configurations are represented in Fig. 4.24. The paths show the change in the intrinsic nuclear shape of the calculated bands as a function of spin in the (ε_2,γ)-plane. Both bands have collective near-prolate ($\gamma \sim 15°$)

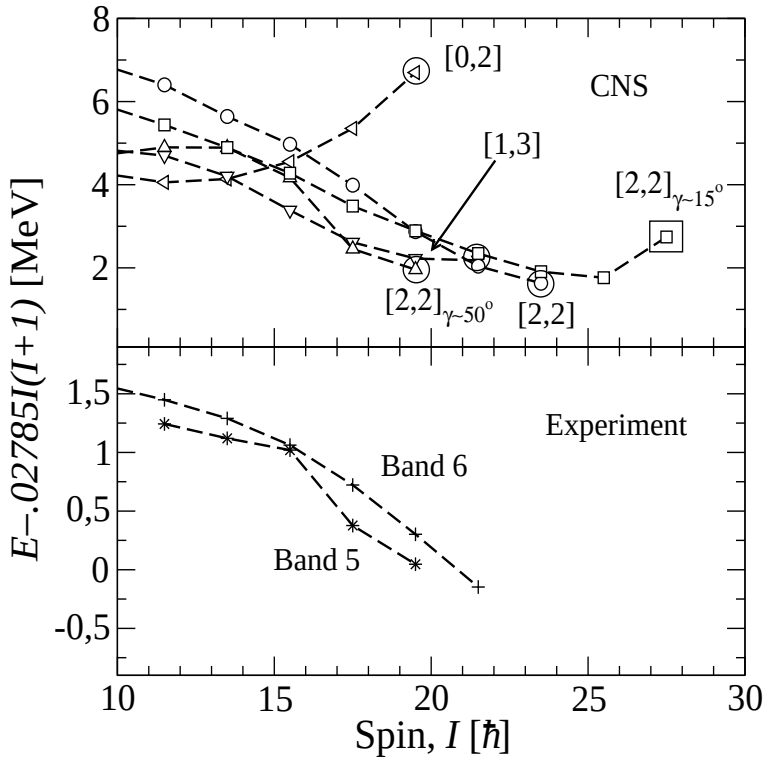

Figure 4.25: *Same as Fig. 4.23 but for negative-parity bands with signature* $\alpha = -1/2$. *The open square indicate a collective state of maximum spin,* I_{max}.

shapes at moderate spins. The bands thus initially involve collective rotations about an axis perpendicular to the symmetry axis. As the rotational frequency increases, the Coriolis and the centrifugal forces acting on the valence particles become strong enough to initiate the spin alignment of these particles. This causes a reduction in collectivity of the bands. The configuration [2,3] changes gradually its nuclear shape from prolate to non-collective oblate ($\gamma \sim 60°$), through the triaxial (γ) plane, at an almost constant quadrupole deformation ($\varepsilon_2 \approx 0.3$). The $[1,2]_{\gamma\sim 30°}$ configuration prefers to stay longer close to $\gamma \sim 30°$ for a greater part of its trajectory, approaching the non-collective axis only in the maximum spin state (I_{max}=$49/2^+$).

The lowest calculated $\pi = -, \alpha = -1/2$ configurations are represented in the top panel of Fig. 4.25. Above spin $15\hbar$, four configurations are predicted to lie close to the yrast line, all of which being energetically favored at some spin. The calculations indicate that the $[1,3]$ configuration competes in the $31/2^-$-$43/2^-$ spin range with three configurations of [2,2] nature. As seen in Table 4.7, all [2,2] calculated bands have the same number of particles in the $g_{9/2}$ and (fp) orbitals, the structural differences arising only from the signature of the (fp) particles.

The [1,3] and $[2,2]_{\gamma\sim 50°}$ configurations (or some mixture of them) are both candidates for Band 5 above spin $31/2^-$ (Fig. 4.25, lower panel). The latter configuration corresponds to the non-collective minimum in the potential-energy surface drawn in Fig.

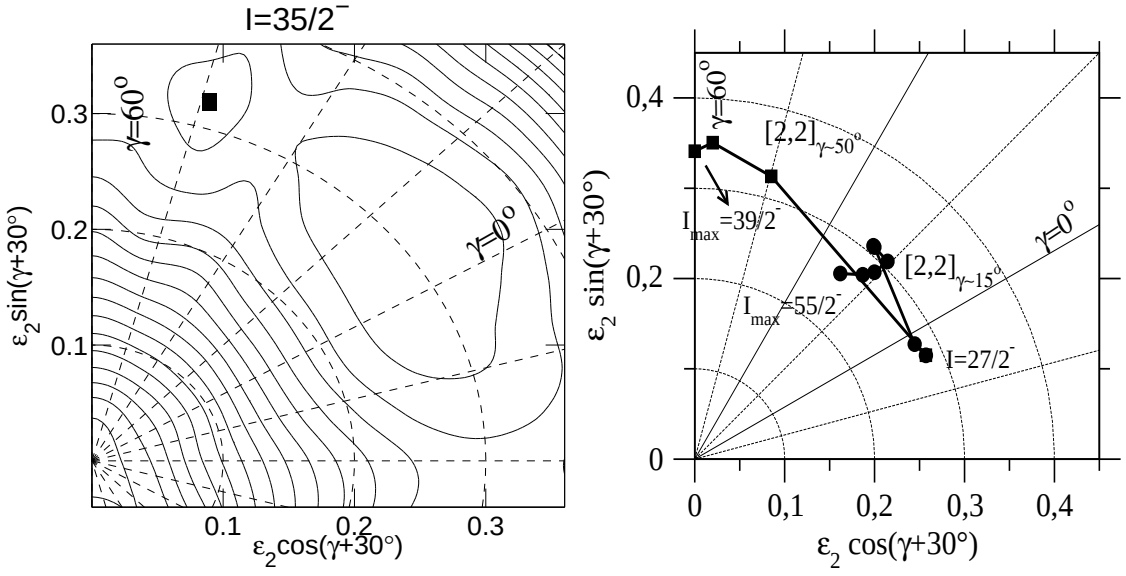

Figure 4.26: *Left: Potential-energy surface for the $\pi = -, \alpha = -1/2$, [2, 2] configuration at spin I=17.5⁻. The two minima correspond to the [2,2]$_{\gamma\sim 15^\circ}$ and [2,2]$_{\gamma\sim 50^\circ}$ configurations. The first minimum is marked with with a closed square. The energy difference between neighboring equipotential lines is 0.4 MeV. Right: Shape trajectories for the calculated configurations [2,2]$_{\gamma\sim 50^\circ}$ and [2,2]$_{\gamma\sim 15^\circ}$, candidates for the experimental bands 5 and 6 in* ^{69}As.

4.26. The second, triaxial prolate minimum, corresponds to the configuration labeled as [2,2]$_{\gamma\sim 15^\circ}$. The theoretical band [1,3] is calculated to terminate at spin $43/2^-$, whereas the termination for the band [2,2]$_{\gamma\sim 50^\circ}$ is reached at spin $39/2^-$.

When drawn relative to a rigid rotor reference, the energy graph of the Band 6 decreases smoothly with increasing spin, as illustrated in the lower panel of Fig. 4.25. This behavior is similar to that of the calculated bands [2,2] and [2,2]$_{\gamma\sim 15^\circ}$. Since below spin $39/2^-$, [2,2]$_{\gamma\sim 15^\circ}$ is lower in energy than [2,2], the former is favored in the interpretation of the experimental Band 6. Furthermore, at spin $31/2^-$, the two minima supporting the [2,2]$_{\gamma\sim 50^\circ}$ and [2,2]$_{\gamma\sim 15^\circ}$ configurations are predicted very close in energy, in agreement with the observed near degeneracy of bands 5 and 6. Due to the similar structures of these two configurations and the rather small potential-energy barrier between them, it is expected that they will strongly mix. Such mixing may be the cause for the irregularities observed in the dynamic moments of inertia of the two bands, as discussed in the previous section (see also Fig. 4.17). For the last two states observed in Band 6, the calculations predict a crossing of the [2,2]$_{\gamma\sim 15^\circ}$ and [2,2] configurations. The latter becomes lowest after crossing but remains degenerate with the former and the question arises whether in this spin region the high-spin part of the [2,2] configuration should rather be considered when making configuration assignments to the experimental Band 6. In fact, the relative energies and the crossings of the calculated bands depend on the parameterization of the Nilsson potential. In order to investigate this effect, calculations have been carried out using the set of single-particle parameters from Ref. [Ben85]. Employing this set

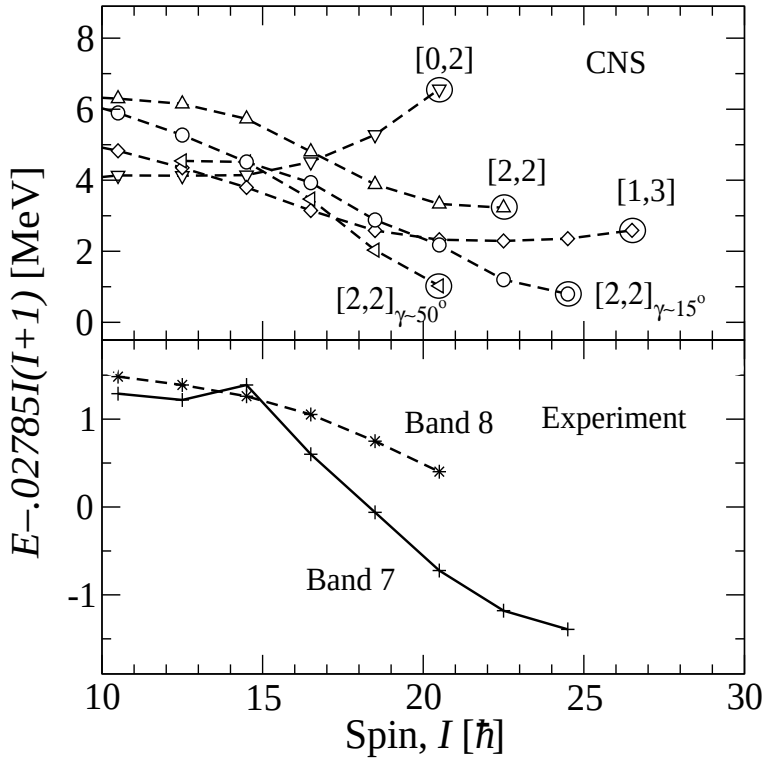

Figure 4.27: *Same as Figs. 4.23 and 4.25 but for negative-parity bands with signature* $\alpha = +1/2$.

of parameters, it was found that the configurations discussed above do not exhibit any crossing, they only come very close in energy in the spin region of interest.

The process of building angular momentum in the $[2,2]_{\gamma\sim 50^\circ}$ and $[2,2]_{\gamma\sim 15^\circ}$ bands above spin $29/2^-$ and up to the calculated maximum spin can be followed in figure 4.26 as a function of deformation. While the second minimum stays rather stable near the collective prolate axis ($\gamma \approx 15^\circ$), the first minimum makes a sudden transition from collective prolate ($\gamma \approx -50^\circ$) to non-collective oblate ($\gamma \approx 50^\circ$) in the spin interval $27/2^-$-$31/2^-$ and then terminates smoothly.

The lowest calculated $\pi = -, \alpha = +1/2$ configurations are displayed in the top panel of Fig. 4.27. The positive signature of the theoretical bands is obtained by changing the signature of a (fp) neutron in the [1,3] configuration and the signature of a (fp) proton in all other configurations, with respect to their negative signature partners discussed above. From the comparison of the theoretical $(E - E_{rld})$ curves with that of Band 7 (Fig. 4.27) it is clear that Band 7 cannot be identified with the configuration labeled $[2,2]_{\gamma\sim 50^\circ}$, because this configuration is predicted to terminate below the maximum spin observed in Band 7. The theoretical band is calculated to be non-collective and may not have a counterpart in the observed spectrum. The next lowest calculated configuration which might be taken into account in the interpretation of Band 7 is the [1,3] configuration. However, it is preferred to associate Band 7 with the configuration $[2,2]_{\gamma\sim 15^\circ}$ because of

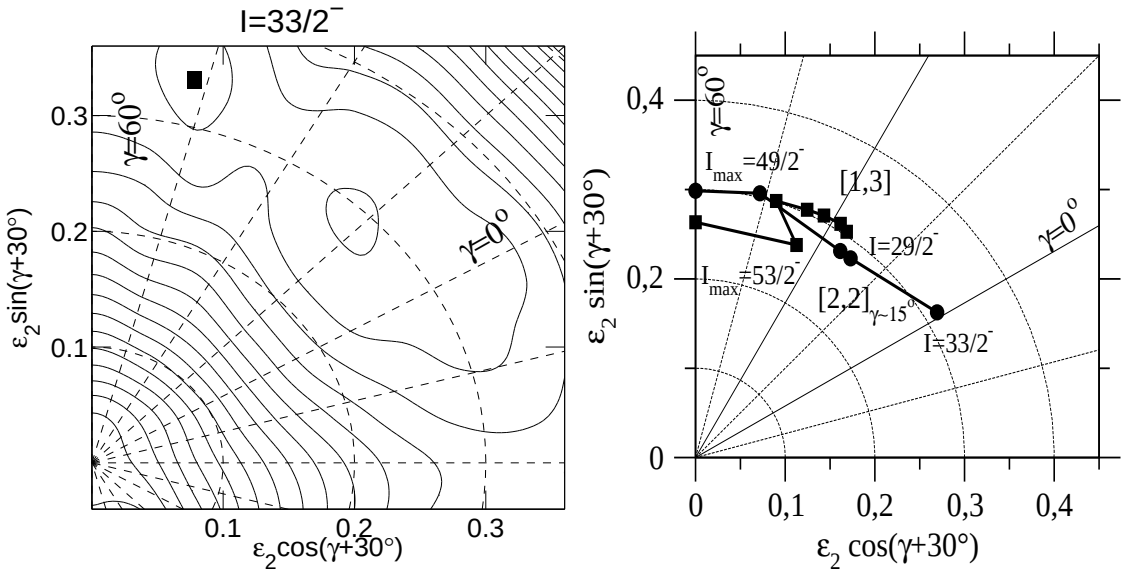

Figure 4.28: *Left: Potential-energy surface for the $\pi = -, \alpha = -1/2$, $[2,2]$ configuration at spin I=16.5⁻. The two minima correspond to the [2,2]$_{\gamma\sim15°}$ and the [2,2]$_{\gamma\sim50°}$ configurations. The lowest minimum is marked with a closed square. The energy difference between neighboring equipotential lines is 0.4 MeV. Right: Shape trajectories for the calculated configurations [2,2]$_{\gamma\sim15°}$ and [1,3], candidates for the experimental bands 7 and 8 in ^{69}As.*

the better agreement in the slopes of the corresponding energy graphs above spin $29/2^-$. The calculated termination for the $[2,2]_{\gamma\sim15°}$ configuration is at spin $49/2^-$, this being also the maximum spin observed in Band 7.

The correspondence between the slopes of the theoretical and experimental $(E - E_{rld})$ curves suggests that the configurations $[1,3]$ and $[2,2]$ may be considered when making assumptions for Band 8. For this band, however, more experimental information at higher spin than is needed in order to make a more firm assignment.

The shape trajectories of the $[2,2]_{\gamma\sim15°}$ and [1,3] configurations, candidates for the experimental bands 7 and 8 are shown in Fig. 4.28. The shape of the theoretical band $[2,2]_{\gamma\sim15°}$ is calculated to be collective prolate at intermediate spin ($\varepsilon_2 \approx 0.27$, $\gamma \approx 10°$) and to terminate at γ=60° with a quadrupole deformation of $\varepsilon_2 \approx 0.3$ (see Fig. 4.28). This can also be read out from Table 4.7 where the detailed structure of the $\pi = -, \alpha = +1/2$ configurations is given.

CNS calculations at the high-spin in ^{69}Se

The nucleus ^{69}Se has 6 valence protons and 7 valence neutrons outside the doubly-magic core $^{56}_{28}Ni_{28}$. The configurations considered in the present calculations were defined in a manner analogous to those discussed in the case of ^{69}As. The detailed description of the configurations which are believed to correspond to the experimental bands in ^{69}Se is listed in Table 4.8.

Table 4.8: The structure of the calculated bands which are likely to correspond to the experimental bands observed in ^{69}Se. The labeling $(\ldots)^q_s$ refers to the number of particles q in the respective subshell or group of subshells whose spins couple to the total angular momentum s. Columns 5 and 6 give the calculated deformation parameters at the termination of each fixed configuration. In the last column, the terminating spin value I_{term} is given. The spin value marked by * represents the maximum spin can be obtained for the respective configuration.

Label	Configuration	Exp. band	I^{exp}_{max} [$\hbar$]	ε_2	γ	I_{term} [$\hbar$]
	$\pi = +, \alpha = +1/2$					
$[2,3]_{\gamma\sim-30^\circ}$	$\pi(g_{9/2})^2_8(f_{5/2}p_{3/2})^4_6 \otimes \nu(g_{9/2})^3_{10.5}(f_{5/2}p_{3/2})^4_6$	Band 2	45/2	0.27	-13°	$61/2^\star$
$[2,3]_{\gamma\sim30^\circ}$	$\pi(g_{9/2})^2_8(f_{5/2}p_{3/2})^4_4 \otimes \nu(g_{9/2})^3_{10.5}(f_{5/2}p_{3/2})^4_4$	Band 2		0.35	60°	53/2
	$\pi = -, \alpha = +1/2$					
$[2,2]_{\gamma\sim30^\circ}$	$\pi(g_{9/2})^2_8(f_{5/2}p_{3/2})^4_4 \otimes \nu(g_{9/2})^2_8(f_{5/2}p_{3/2})^5_{2.5}$	Band 6	41/2	0.33	60°	45/2

In the top panel of Fig. 4.29, the $(E - E_{rld})$ curves for the lowest calculated ($\pi = +, \alpha = +1/2$) configurations are plotted. The calculations show that there are a number of competing configurations which are yrast or close to yrast in the spin range of interest. Configurations [1,2] and [2,1] are of low-collectivity, as indicated by the large open circles marking the aligned states within each configuration. The lowest calculated collective configuration is [2,3]. The bands labeled as $[2,3]_{\gamma\sim-30^\circ}$ and $[2,3]_{\gamma\sim30^\circ}$ were calculated in the two minima of the potential-energy surfaces for the [2,3] configuration.

The excitation energies with a rigid rotor reference subtracted $(E - E_{rld})$ for the experimental positive-parity bands 2 and 3 are illustrated in the lower panel of Fig. 4.29. In the spin region $25/2^+$-$37/2^+$, Band 2 appears to have regular spacing, as expected for a collective band.

In making assignments to this experimental band, one has two alternatives. If one follows the calculated yrast line, then, below spin $37/2^+$, Band 2 may be interpreted as being the band built in the $\gamma \sim -30^\circ$ minimum of the [2,3] configuration. Above this spin value, the band built in the $\gamma \sim -30^\circ$ minimum of the same configuration may be assigned to the highest observed part of Band 2. The alternative interpretation is to consider the $[2,3]_{\gamma\sim30^\circ}$ configuration the only candidate for this experimental band and assume that the experimental counterpart for the $[2,3]_{\gamma\sim-30^\circ}$ configuration was not yet identified. The $[2,3]_{\gamma\sim30^\circ}$ configuration is predicted to terminate at spin $I = 53/2^+$, four units of angular momentum above the maximum spin experimentally observed.

An assignment for Band 3 is not easy to make since in the spin region this band has been observed the pairing correlations are expected to be still important.

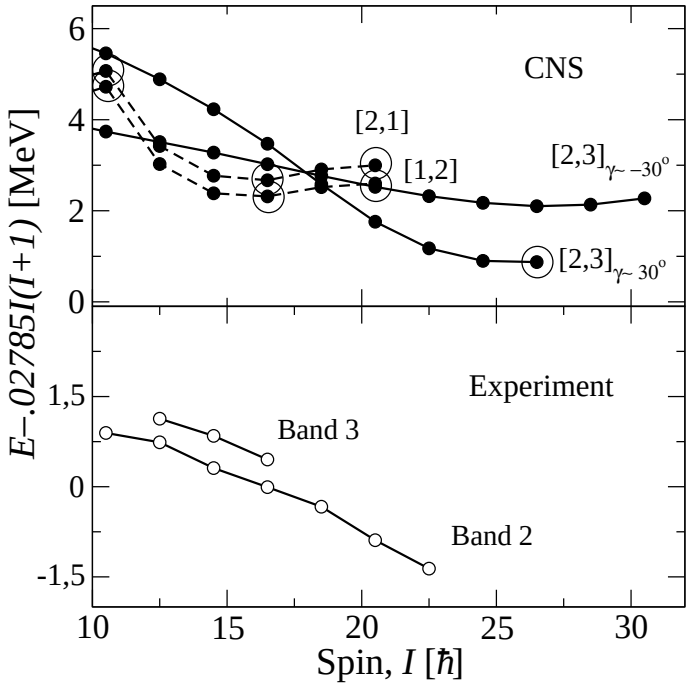

Figure 4.29: *Calculated (top) and experimental (bottom) energies of the* ($\pi = +, \alpha = +1/2$) *bands in* ^{69}Se.

Some selected potential-energy surfaces for the [2,3] configuration are shown in Fig. 4.30. At low spin, the minimum at $\gamma \sim -30°$ is calculated lowest being separated by a potential-energy barrier of 0.8 MeV from the $\gamma \sim 30°$ minimum. There is also a third minimum showing up in the calculations at a deformation of ε_2=0.4 and $\gamma \sim 0°$. It is, however, located $\approx$1 MeV higher in energy than the lowest minimum and it does not seem to play an important role in the structure of the yrast line. With increasing spin, the energy of the $\gamma \sim 30°$ minimum decreases smoothly and, around spin $I \approx 37/2^+$, it becomes equal to the energy of the $\gamma \sim -30°$ minimum. Above this spin value, the latter minimum becomes energetically unfavored and exhibits γ-softness. In such a case, the calculated energy as function of spin for the $[2,3]_{\gamma\sim-30°}$ configuration may not be very accurate since the energies are calculated through the minimisation of the total energy, therefore a well-defined deformation is needed.

The change in the intrinsic nuclear shape as a function of spin in the (ε_2,γ)-plane for the calculated $\pi = +, \alpha = +1/2$ configurations is presented in Fig. 4.31. The band built on the $\gamma \sim -30°$ minimum evolves smoothly in the direction toward somewhat smaller ε_2 and higher γ-values, but retains the initial large collectivity up to the maximum spin I_{max}=$53/2^+$. The band built in the $\gamma \sim 30°$ minimum loses collectivity with increasing spin, as the band approaches termination and the valence particles become more and more aligned with the axis of rotation.

In Fig. 4.32, the excitation energies with a rigid rotor reference substracted for the lowest calculated ($\pi = -, \alpha = +1/2$) configurations are compared with those for the experimental bands 6 and 7. The detailed description of the calculated configurations

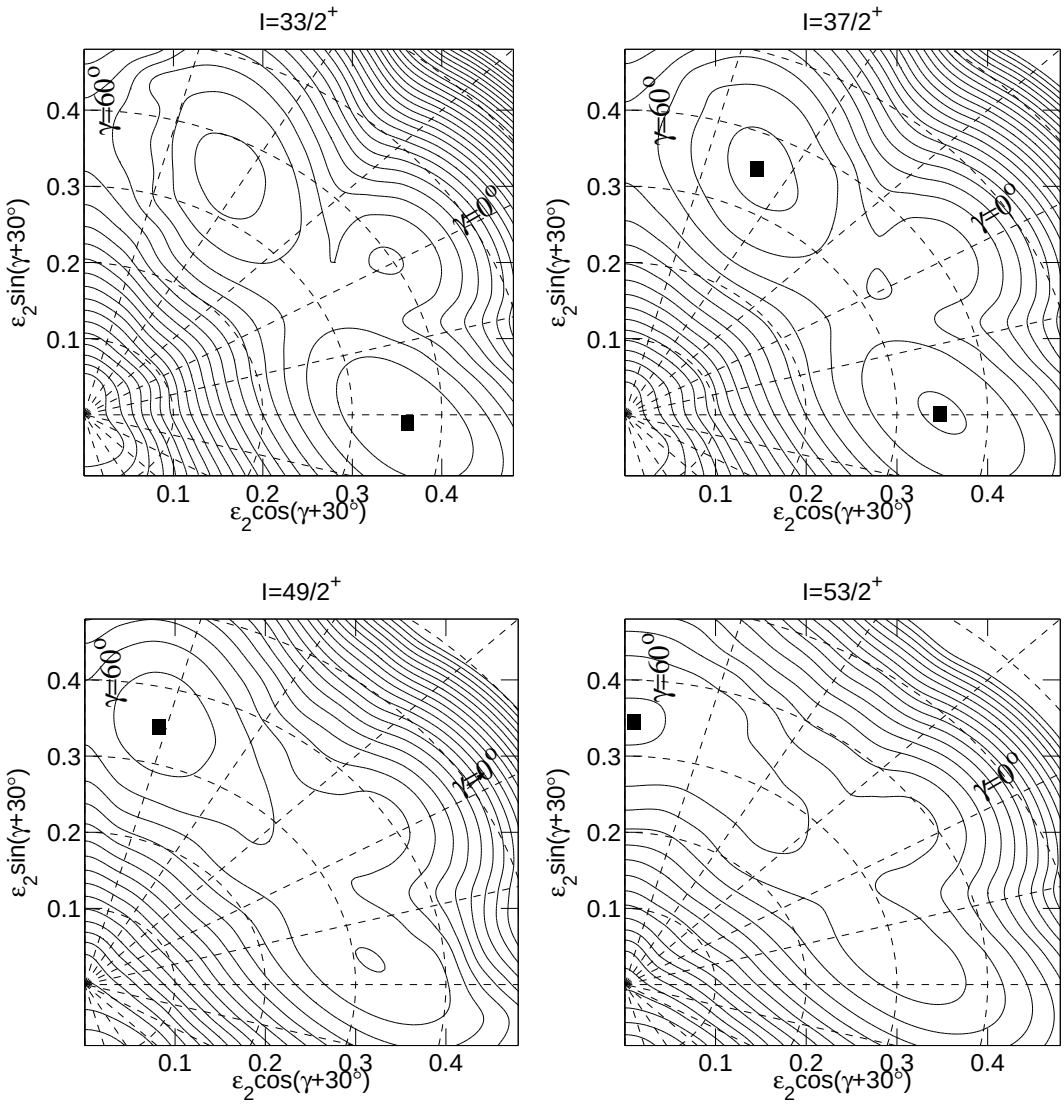

Figure 4.30: *Potential-energy surfaces for the $\pi = +, \alpha = +1/2$, [2,3] configuration calculated in ^{69}Se. The energy difference between two neighboring equipotential lines is equal to 0.4 MeV. The lowest minimum is marked by a closed square.*

is listed in Table 4.8. The predictions of the CNS model for the lowest negative-parity configurations calculated in ^{69}Se are very similar to those for the positive-parity configurations discussed above. The bands built in the $\gamma \sim -30°$ and $\gamma \sim 30°$ minima of the potential-energy surface of a configuration with two protons and two neutrons in the $g_{9/2}$ orbitals are found to dominate the yrast line of negative-parity. The potential-energy surfaces for the [2,2] configuration are plotted in Fig. 4.33 for different spin values. The $\gamma \sim -30°$ minimum is deeper at low rotational frequencies but its energy increases with increasing spin. The two minima cross around spin $29/2^-$. Above this spin value, the $\gamma \sim -30°$ minimum becomes energetically unfavored and exhibits γ-softness.

Band 6 is best described by the $[2,2]_{\gamma\sim 30°}$ configuration which terminates in a non-

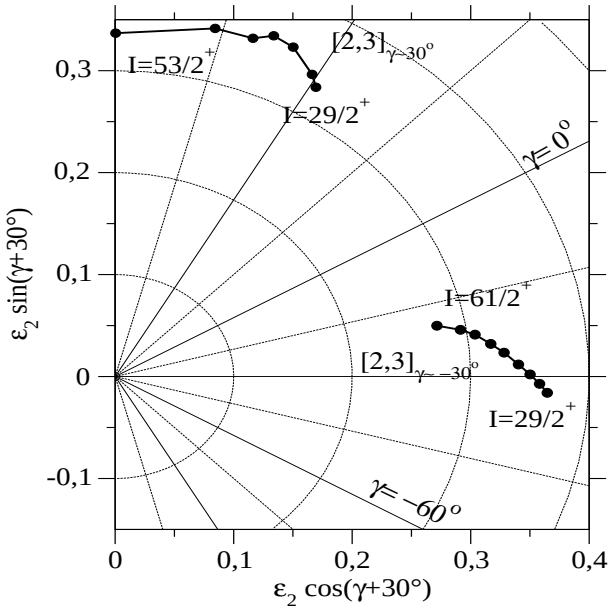

Figure 4.31: *Shape trajectories for the lowest calculated $\pi = +, \alpha = +1/2$ configurations which are believed to correspond to the experimental bands 2 and 3 in ^{69}Se.*

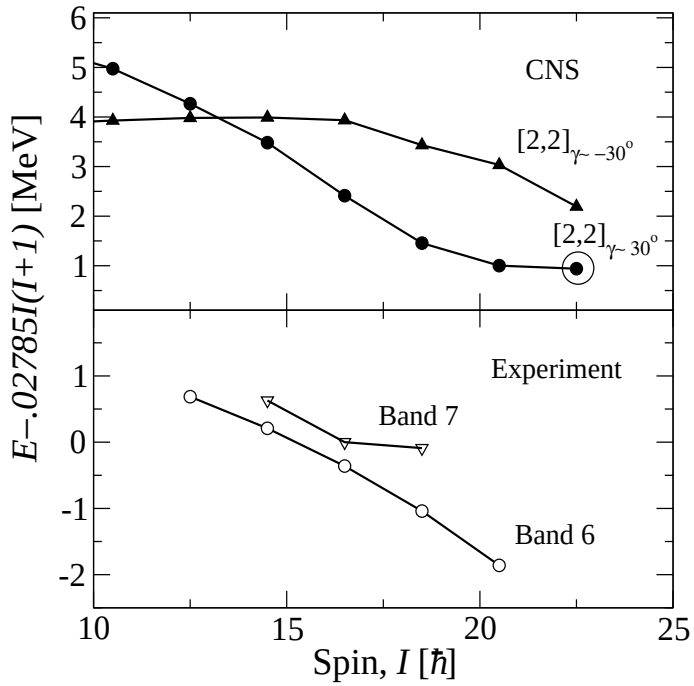

Figure 4.32: *Calculated (top) and experimental (bottom) energies of the ($\pi = -, \alpha = +1/2$) bands in ^{69}Se.*

collective oblate state at I=45/2$^-$. Calculations indicate that the experimental band has been observed up to one transition below termination. Due to the limited spin range

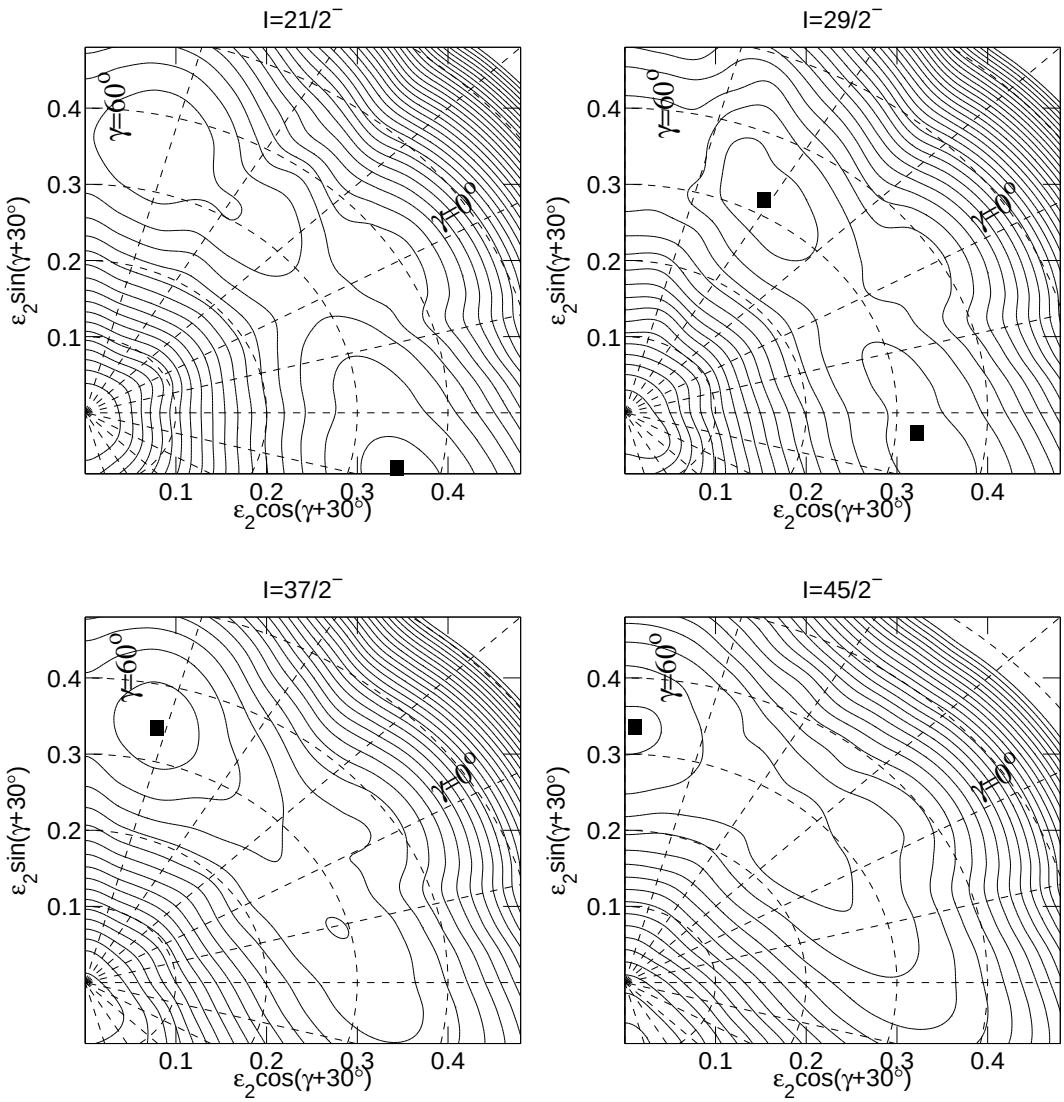

Figure 4.33: *Potential-energy surfaces for the $\pi = -, \alpha = +1/2$, [2,2] configuration calculated in ^{69}Se. The energy difference between two neighboring equipotential lines is equal to 0.4 MeV. The lowest minimum is marked by a closed square.*

in which Band 7 is observed, it is difficult to make assumptions about its nature. A candidate for this band may be the $[2, 2]_{\gamma\sim-30^\circ}$ configuration.

In conclusion, the CNS calculations showed that at high spin, the properties of yrast line in ^{69}Se are essentially determined by two competing minima in the potential-energy surface of the same configuration, one located at $\gamma \sim -30^\circ$ and one at $\gamma \sim 30^\circ$. However, it is interesting to note that, according to the CNS calculations, the coexistence seems to survive to quite high spin values. At low spin, the $\gamma \sim -30^\circ$ minimum is deeper and is separated from the $\gamma \sim 30^\circ$ minimum by a potential-energy barrier of around 0.8 MeV. At higher spin, the former minimum becomes energetically unfavoured and exhibits γ-softness, while the latter evolves smoothly toward $\gamma = 60^\circ$.

4.3.4 Comparison with the CNS calculations for neighboring nuclei

The competition of shapes predicted by the CNS model in ^{69}Se is not surprinsing, since it is well known that the coexistence of different shapes plays an important role in the structure of the nuclei in the A$\sim$70 mass-region. Shape coexistence at high spin has been already reported in the neighboring nuclei ^{70}Se [Rai02] and ^{70}Br [Jen02]. In ^{68}Ge, however, the shape coexistence was found to not affect the high-spin structure of this nucleus very much [War00].

In all three nuclei, the high-spin rotational bands were discussed within the CNS framework, therefore it will be interesting to compare the reported results with the results obtained for ^{69}Se and ^{69}As in the present work. By using the available data, it is possible to investigate how the extra-proton in the $g_{9/2}$ orbital influences the properties of the yrast or near-yrast bands, when going from the Z to the $Z+1$ nucleus. The configurations found to be the best candidates for the observed bands in the nuclei mentioned above and those investigated in the present work are summarized in Table 4.9.

In ^{70}Br, the CNS model indicates that the yrast line in the spin-range I=15-25 is dominated by ($\pi = +, \alpha = +1$) odd-spin states [Jen02]. Competing configurations of [2,2] and [3,3] nature were found to be yrast or close to yrast in the spin region of interest. The [3,3] configuration led to two coexisting minima in the potential-energy surface, one at $\gamma \approx -20^\circ$ and one at $\gamma \approx 30^\circ$. Detailed comparisons of experimental quantities such as $E - E_{rld}$, kinematic and dynamic moments of inertia and alignments with the predictions of the CNS model strongly suggested the assignment of the $[3,3]_{\gamma\sim-20^\circ}$ configuration for the $I = 15^+ - 25^+$ yrast states [Jen02]. An upbend seen in the dynamic moment of inertia at the highest rotational frequency observed in ^{70}Br has been interpreted as the crossing of the $[3,3]_{\gamma\sim-20^\circ}$ and $[3,3]_{\gamma\sim30^\circ}$ configurations.

^{70}Br is only one proton away from ^{69}Se, so the interpretation proposed for the positive-parity yrast band in ^{70}Br gives confidence to the results obtained in the calculations for ^{69}Se.

Perhaps interesting to note is that when going from ^{69}Se to ^{70}Br, the extra proton in the latter nucleus seems to affect the minimum with $\gamma < 0^\circ$ more than that with $\gamma > 0^\circ$. Moreover, it shows a tendency to drive the $\gamma < 0^\circ$ minimum toward somewhat larger γ-values but in the same time to increase the energy difference between the two minima, by favoring the minimum located at negative-γ values. Thus, the band built in this minimum remains yrast over a wide spin interval.

In ^{70}Se, the positive-parity band which develops yrast above spin $I = 16^+$ has been proposed to correspond to the second minimum of the $[2, 2]$ configuration [Rai02]. This minimum was found to start at $\varepsilon_2 \sim 0.29$ and $\gamma \sim 24^\circ$, remaining stable in the spin range from $I = 14^+$ to $I = 26^+$. Two other minima were predicted for the same configuration, one non-collective ($\gamma \sim 52^\circ$) and one triaxial-oblate ($\gamma \sim -45^\circ$), but not clear relation between these minima and the other observed positive-parity bands could be made [Rai02]. At low spins, the minimum at $\gamma \sim -45^\circ$ is calculated lowest in energy, but above spin $I = 15$ it is crossed by the $\gamma \sim 24^\circ$ and $\gamma \sim 52^\circ$ minima.

The potential-energy surface calculated for the ($\pi = -, \alpha = -1/2$) structures in ^{70}Se showed two minima that developed from configurations of [2,3] nature. While the

Table 4.9: The structure of the calculated bands which are likely to correspond to the experimental bands observed in ^{70}Br, ^{69,70}Se, ^{69}As, and ^{68}Ge. The configurations are labeled as $[p,n]_{\gamma(av)}$, where $p(n)$ is the number of protons(neutrons) in the $g_{9/2}$ orbital and γ_{av} is the average γ deformation of the configuration at spins $I \approx$16. For a specific nucleus, the configurations are given regardless of signature and in the increased order of their energies. Configurations not labeled by their γ-value were found to show only a well defined prolate minimum in the potential-energy surfaces for spins $I >$10.

Nucleus	$\pi = +$	$\pi = -$	Ref.
$^{70}_{35}$Br$_{35}$	$[3,3]_{\gamma\sim-20^\circ}$ $[3,3]_{\gamma\sim+30^\circ}$		[Jen02]
$^{69}_{34}$Se$_{35}$	$[2,3]_{\gamma\sim-30^\circ}$ $[2,3]_{\gamma\sim+30^\circ}$	$[2,2]_{\gamma\sim-30^\circ}$ $[2,2]_{\gamma\sim+30^\circ}$	present work
$^{70}_{34}$Se$_{36}$	$[2,2]_{\gamma\sim+52^\circ}$ $[2,2]_{\gamma\sim+24^\circ}$ $[2,2]_{\gamma\sim-45^\circ}$	$[2,3]_{\gamma\sim-20^\circ}$ $[2,3]_{\gamma\sim40^\circ}$	[Rai02]
$^{69}_{33}$As$_{36}$	$[1,2]_{\gamma\sim+50^\circ}$ $[1,2]_{\gamma\sim+30^\circ}$ [2,3]	[1,3] $[2,2]_{\gamma\sim+50^\circ}$ $[2,2]_{\gamma\sim+15^\circ}$	present work
$^{68}_{32}$Ge$_{36}$	[1,3] [2,2]	[1,2] [2,3]	[War00]

first minimum stays near the non-collective oblate axis ($\gamma = 60^\circ$) and reaches it at spin I=25, the second minimum moves smoothly from $\gamma \approx -37^\circ$ to $\gamma \approx 18^\circ$ in the spin range from I=15 to I =27. The two observed negative-parity bands were believed to belong to such different minima. This interpretation is also supported by the smoother behavior of the kinematic moment of inertia of the band associated to the collective minimum compared with irregularities observed in the second band, corresponding to the non-collective minimum [Rai02].

With decreasing the proton number and going away from Z=34 along the N=36 path, prolate deformed configurations are predicted to form the high-spin yrast line in nuclei like ^{69}As or ^{68}Ge. In ^{69}As, coexisting oblate and prolate minima in the potential-energy surfaces of the configurations found to be the candidates for the observed bands are predicted only at low spin, $I <$21/2. Above this spin value, the energy difference between the two minima increases rapidly and, above spin I=33/2, the oblate minimum is too

high in energy to play a role in the structure of the yrast line.

As discussed in subsection 4.3.3, the bands built in the prolate and non-collective minima of the $(\pi = +, \alpha = +1/2)$ [1,2] configuration are assigned to the positive-parity bands observed in ^{69}As. The candidates for the negative-parity high-spin states are the bands built in the prolate minima of the potential-energy surfaces of the [1,3] and [2,2] configurations. By adding one $g_{9/2}$ proton to the $(\pi = +, \alpha = +1/2)$ [1,2] and $(\pi = +, \alpha = \pm 1/2)$ [1,3] configurations, the energy difference between the prolate and oblate minima is considerably lowered, leading in ^{70}Se to the high-spin triaxial-oblate bands $[2,2]_{\gamma\sim -45^\circ}$ and $[2,3]_{\gamma\sim -20^\circ}$ (see Table 4.9).

In ^{68}Ge, configurations of [2,2] and [1,3] nature were believed to correspond to the observed $(\pi = +, \alpha = 0, 1)$ yrast bands, respectively, whereas the configurations [2,3] and [1,2] were the believed to correspond to the observed negative parity yrast bands $(\pi = -, \alpha = 0, 1)$, respectively [War00]. All configurations start prolate or nearly prolate and have deformations in the range ε_2=0.25-0.31. The model predicts that the experimental bands were observed up to their terminations. However, the configurations associated to the observed bands were generally not calculated lowest in energy. For the [1,3] configuration, associated with the band terminating at $I = 25^+$, a shape-coexisting band at approximately the same energy was also found. This band was predicted to terminate at a lower spin of $I = 21^+$ and could not be assigned to the observed band.

From the CNS calculations in the nuclei considered in this section, some general features concerning the positive-parity yrast line can be extracted. It turns out that with decreasing the proton number from Z=35 to Z=33, the number of $g_{9/2}$ protons in the configurations found to best describe the positive-parity yrast lines decreases from three to one, see Table 4.9. The configurations were found to lead to coexisting minima in the potential-energy surfaces, with $\gamma \sim -30^\circ$, $\gamma \sim 30^\circ$, and $\gamma \sim 50^\circ$. The coexistence of two shapes shows a maximum in ^{70}Br were the minima at $\gamma \sim -20^\circ$ and $\gamma \sim 30^\circ$ are predicted to survive separately and close to the yrast line over a wide spin range. When protons are removed as going from $^{70}_{35}$Br to $^{69}_{33}$As, the negative-γ minimum becomes less bound and the spin range where the bands built on this minimum are yrast decreases. The minima with $\gamma > 0$ become more favored and the non-collective minima more pronounced.

Since configurations with one $g_{9/2}$ proton are assigned to the yrast line at intermediate spins in ^{69}As, configurations with no protons excited in this orbital are then expected to lie close to yrast in the Z=32, ^{68}Ge. With such small number of particles in the $g_{9/2}$ orbital these configurations will have a low collectivity and they cannot be assigned to the observed bands. Therefore, the [1,3] and [2,2] excited configurations were associated to the positive-parity experimental bands, see Table 4.9.

Similar systematical trends for the calculated negative-parity yrast bands in these nuclei are not easy to establish. These bands are, in general, less populated in experiments and therefore more difficult to observe at high-spin. Only in ^{68}Ge and ^{70}Se the negative-parity bands were investigated to high enough spin, allowing an unambiguous configuration assignment.

4.3.5 Summary and conclusions

The present analysis reports on new experimental information of the level schemes of ^{69}Se and ^{69}As. These nuclei are interesting to study because they lie in a region of nuclei where the shape is rapidly changing with the particle number. The proximity of the N=Z=34 prolate and oblate and N=Z=36 oblate shell gaps implies that nuclei may exhibit different structures at different excitation energies.

The level schemes of ^{69}Se and ^{69}As obtained from the present analysis are presented in Figs. 3.1 and 3.2-3.4, respectively. The level scheme of ^{69}Se consists of 111 transitions, about a factor of 2 more than reported in the work of Jenkins *et al.* [Jen01], whereas the level scheme of ^{69}As includes 188 transitions, about a factor of 7 more than reported in the earlier works [Mit97, Bru00].

Spins were assigned to many of the new states on the basis of angular distributions and correlation measurements. The spectroscopic information such as level and γ-ray energies, γ-ray intensities, mixing ratios and spin assignments are listed in Tables A.1 and A.2, respectively.

Many low-lying positive-parity non-yrast states were identified in both nuclei. They show features which agree very well with the systematics of light odd-Ge isotopes [Her95, Bec97] and heavier odd-As isotopes [Zig94, Hei77], such as the yrare $9/2^+$ state close in energy to the yrast $11/2^+$ state and several $17/2^+$ states strongly populated from the $19/2^-$ states. This suggests similar underlying structures and deformations for these parts of the level schemes.

The continuation of the positive-parity ground state band in ^{69}As was established up to spin $29/2^+$. The newly observed states were found to show the same degree of signature splitting as the previously known states below spin $21/2^+$. In ^{69}Se, however, the ground-state oblate band was extended by the $(19/2^+)$ level. No continuation of the band above spins $21/2^+$ could be identified, despite a careful search. This suggests that the minimum in the potential-energy surface corresponding to the ground-state band survives in ^{69}As at much higher excitation energies than in ^{69}Se.

At spin $21/2^+$ a change in the yrast structure occurs in both nuclei as shown by the strong backbendings in the kinematic moments of inertia. These backbendings are interpreted in Refs. [Jen01, Bru00] as being caused by the alignment of a pair of $g_{9/2}$ particles.

The present analysis brings a large amount of new information about the structure of ^{69}As at high spin. The positive-parity excited band reported in Ref. [Bru00] up to spin $(37/2^+)$ is extended up to spin $(45/2^+)$. Around spin $41/2^+$, this band was found to be crossed by another structure which was observed up to spin $(53/2^+)$. The coincidence data reveal also the existence of a new short sequence which develops parallel to the band investigated in Ref. [Bru00]. The regular spacing of the levels within the sequence and the results of the directional correlation measurements suggest that this is the yrast band in the spin region $29/2^+ - (37/2^+)$.

The present analysis confirms the high-spin bands in ^{69}Se reported in Ref. [Jen01]. Two short sequences are newly found, developing parallel to the yrast positive-parity band above spin $21/2^+$.

The low-lying negative-parity parts of the level schemes were considerably enlarged

in both nuclei. Based on the coincidence data, no evidence for a $f_{7/2}$ band could be found in ^{69}As. Instead, a rotational-like sequence exhibiting properties consistent with those of a $f_{5/2}$ band was identified. This band, however, coexists with states of single-particle character, indicating that at low spin, ^{69}As is less deformed than ^{71}As. In ^{69}Se, the negative-parity states below 3 MeV show irregular spacing, suggesting a small deformation for this part of the level scheme.

Shapes with small deformation seem to characterize also the intermediate-spin region in ^{69}Se and ^{69}As. The excitation energy of the states in the spin-range $15/2^-$-$23/2^-$ agree very well with the energies of the 3^--7^- states in the even-even neighboring nuclei, ^{68,70}Se and ^{68}Ge, respectively. This may indicate that the $15/2^-$-$23/2^-$ states are generated by the $g_{9/2}$ particle or hole weakly coupled to the 3^--7^- states of the neighboring even-even nuclei. Such a coupling picture follows the trend observed in ^{65,67,69}Ge and ^{71}As isotopes, which suggested their interpretation in the framework of the weak-coupling model [Her95, Bec97, Zig94]. Above spin $23/2^-$, rotational bands start to develop in both nuclei, indicating an increased deformation at high-spin.

Prior to this work only one high-spin negative-parity band was known in ^{69}As. It was identified by Sefzig [Sef88] and only partially confirmed in Refs. [Mit97, Bru00]. The present measurements support the existence of the levels forming this band, but not their ordering. Based on the γ-rays intensities measured in the coincident data, a new level order is proposed. The band is extended up to spin $(49/2^-)$ corresponding to an excitation energy of $\sim$16 MeV. Further three new bands are observed up to spins $39/2^-$, $(43/2^-)$, and $(41/2^-)$, respectively.

The excitation energies of the low-lying positive-parity states in both nuclei are compared with the predictions of the Rigid Triaxial Rotor plus Particle model [Lar78]. The model describes an odd system of nucleons by coupling a quasiparticle to a triaxial Davydov even-even core [Dav58]. The shape of the core is defined by the quadrupole deformation parameter ε_2 and the asymmetry parameter γ. These parameters are kept constant throughout the calculations (rigid rotor).

In ^{69}Se, the set of deformation parameters ε_2=0.33, $\gamma = -33°$ is found to reproduce very well the properties of the yrast states such as signature splitting, excitation energies and branching ratios. The yrare band could not be reproduced with the same set of parameters which described very well the yrast band; this suggests different deformations for the two bands, i.e. shape-coexistence at low-spin.

In ^{69}As, the model fails to reproduce the ordering of the levels of the positive-parity yrast band. According to the calculations, the observed small splitting between the $15/2^+$ and $17/2^+$ states can only be reproduced for γ-values in the interval from $-25°$ to $-20°$ whereas in order to fit the splitting between the higher spin states γ-values in the interval from $-35°$ to $-29°$ need to be employed.

The fact that the yrast states in ^{69}Se could be reproduced by assuming a fixed shape for the core suggests that at low spin, this nucleus has a tightly bound ground-state band with substantial deformation, stabilized by the large gaps at N, Z=34 oblate and prolate. However, this stabilization is delicate; removal of particles leads to less deformed shapes exhibiting γ-softness, as in ^{69}As.

Generally, the properties of the high-spin bands are determined by more than one quasiparticle, the particle-rotor model employed to describe the low spin states does not

apply here anymore. Thus, for the description of the high-spin states in ^{69}Se and ^{69}As the Cranked Nilsson-Strutinsky model is used.

Within the Cranked Nilsson Strutinsky (CNS) model [Afa99] the observed bands are described in terms of configurations specified by the occupation of the valence orbitals. A configuration consists of "inner" particles in closed shells forming a spherical core and the "outer" particles in partly filled shells. These valence particles occupy specific orbitals which are generally dominated by a specific j-shell. Each configuration has a maximum (terminating) spin which reflects the limited angular momentum content of the valence space of the fixed configuration. The process of approaching the maximum spin value within the configuration is associated with smooth shape changes in the (ε_2, γ)-deformation plane, from collective-prolate shapes at low spin ($\gamma = 0°$) to triaxial shapes at intermediate spins ($0° < \gamma < 60°$) achieving an oblate non-collective shape at the termination ($\gamma = 60°$).

In the case of the nuclei ^{69}Se and ^{69}As the valence orbitals are those outside the doubly-magic core ^{56}Ni, the $N = 3$, $p_{3/2}f_{5/2}$ subshells and $N = 4$, $g_{9/2}$ orbital. The configurations are labeled as $[p, n]$, where $p(n)$ is the number of protons (neutrons) in the $g_{9/2}$ orbital. By comparing the experimental and the calculated excitation energies, configurations could be assigned to each of the observed bands and therefore information about shape evolution at different rotational frequencies and terminating spins could be obtained.

In ^{69}Se, the positive-parity [2,3] and negative-parity [2,2] configurations are calculated lowest in energy above spin $I = 10$. These configurations are found to lead to two coexisting minima in the potential-energy surfaces, one triaxial-oblate with $\gamma \approx -30°$ and one triaxial-prolate with $\gamma \approx 30°$. At low spin, the triaxial oblate minimum is deeper and is separated from the prolate minimum by a potential-energy barrier of around 0.8 MeV. With increasing spin, the energy difference between the two minima decreases until the minima become degenerate. Above spin $I = 15$, the oblate minimum becomes energetically unfavored and exhibits γ-softness while the prolate minimum evolves smoothly toward $\gamma = 60°$.

The bands built on these minima are the candidates for the bands identified in ^{69}Se. Thus, they represent a coexistence of different shapes at high spin. The yrast bands were observed up to spin values very close to the predicted terminations.

For ^{69}As, triaxial oblate deformations are predicted by the model at low excitation energies. In the intermediate spin region ($10 < I < 20$), the oblate minimum lies too high in energy and it does not play an important role in the structure of the yrast line. In this spin region, the positive-parity bands were found to be best described by the structures built in the triaxial ($\gamma \approx 30°$) and non-collective ($\gamma \approx 50°$) competing minima of the [1,2] configuration. At high spin, the [2,3] configuration is lowest and constitutes a very good candidate for the highest observed positive-parity band in ^{69}As. In all cases, the configurations are predicted to terminate two units of angular momentum above the maximum spin experimentally observed.

Configurations of [2,2] and [1,3] nature are assigned to the negative-parity bands. The maximum spin predicted for these configurations is in the I=18-26 interval, very close to the highest spins experimentally observed.

There is an overall reasonable agreement between the CNS calculations and experi-

ment. The comparison of the measured level schemes and with the predicted configurations does illustrate rather clearly how the underlying microscopic shell structure leads to configuration changes along the yrast line of the nuclei investigated in this work.

An important aspect for the future work will be the measurements of the lifetimes of the excited states in both nuclei, which will allow the determination of the reduced transition probabilities and quadrupole moments, needed for a more detailed verification of the deformations and their development with spin. Investigations on the high-spin states of the neighboring isotopes ^{67,71}Se or ^{67,71}As would be also of a great help for the general understanding of the influence of the extra-particle or hole on the shape evolution and band structure, making possible a systematic study of the behaviour at high spin and allowing for consistent description of the mass-region.

The models employed in this work to describe the structure of the nuclei ^{69}Se and ^{69}As are too simple as the issue of shape coexistence and shape mixing make their level schemes very difficult to interpret. However, the models allowed to describe special aspects in different regions of spin and excitation energies. For a more global and consistent description of all properties like shape-coexistence, shape mixing and development of shapes with increasing spin, more complex nuclear models need to be developed. A more realistic description of the structure of these nuclei can be obtained, for instance, by including the pairing correlations in the CNS formalism. This would then allow for a more accurate description of the band crossings and deformations especially at low rotational frequencies.

The large amount of experimental data presented in this work for the nuclei ^{69}Se and ^{69}As will be very helpful for a critical test of the new theoretical models.

Appendix A

Tables

A.1 Spectroscopic information in ^{69}Se

Table A.1: Energies, relative intensities and DCO ratios of γ-ray transitions assigned to ^{69}Se. The intensities are normalized to the 773.3-keV transition, set to be 100.

E_{level}(keV)	E_γ(keV)	I_γ^a	R_{DCO}^b	Gate	σL	$I_i^\pi \rightarrow I_f^\pi$
0.0						$\frac{1}{2}^-$
39.4	39.4[1]				$E2$	$\frac{5}{2}^- \rightarrow \frac{1}{2}^-$
129.1	129.1(2)	23.8(12)	0.33(7)	468.0	$M1/E2$	$\frac{3}{2}^- \rightarrow \frac{1}{2}^-$
	90.3(1)	7.1(6)			$M1/E2$	$\frac{3}{2}^- \rightarrow \frac{5}{2}^-$
290.1	161.3(4)	5.3(4)	0.51(27)	807.0	$M1$	$\frac{3}{2}^- \rightarrow \frac{3}{2}^-$
	250.7(2)	5.6(18)	1.53(20)	844.0	$M1/E2$	$\frac{3}{2}^- \rightarrow \frac{5}{2}^-$
574.6	534.5[1]				$E2$	$\frac{9}{2}^+ \rightarrow \frac{5}{2}^-$
713.1	422.6(1)	0.8(1)	1.06(77)	129.1	$M1/E2$	$\frac{5}{2}^- \rightarrow \frac{3}{2}^-$
	673.7(3)	3.3(4)			$M1/E2$	$\frac{5}{2}^- \rightarrow \frac{5}{2}^-$
914.6	786.4(5)	17.7(11)	0.93(18)	807.0	$E2$	$\frac{7}{2}^- \rightarrow \frac{3}{2}^-$
	876.2(4)	35.2(78)	0.84(14)	807.0	$M1/E2$	$\frac{7}{2}^- \rightarrow \frac{5}{2}^-$
1101.8	1061.7(4)	1.1(4)	1.53(41)	468.0	$E2$	$\frac{9}{2}^- \rightarrow \frac{5}{2}^-$
1123.5	993.9(2)	19.6(12)	0.97(18)	468.0	$E2$	$\frac{7}{2}^- \rightarrow \frac{3}{2}^-$
	1084.1(3)	18.1(30)	0.64(11)	468.0	$M1/E2$	$\frac{7}{2}^- \rightarrow \frac{5}{2}^-$
	833.2(3)	0.7(3)			$E2$	$\frac{7}{2}^- \rightarrow \frac{3}{2}^-$
1134.7	844.0(4)	3.3(10)	0.92(31)	129.1	$M1/E2$	$\frac{5}{2}^- \rightarrow \frac{3}{2}^-$
	1004.8(2)	1.1(3)			$M1/E2$	$\frac{5}{2}^- \rightarrow \frac{3}{2}^-$
	1095.3(5)	3.1(4)			$M1/E2$	$\frac{5}{2}^- \rightarrow \frac{5}{2}^-$
1193.8	1155.4(2)	8.2(6)	0.89(16)	807.0	$E2$	$\frac{9}{2}^- \rightarrow \frac{5}{2}^-$
1250.7	675.9(3)	210.8(90)	0.95(16)	714.2	$M1/E2$	$\frac{11}{2}^+ \rightarrow \frac{9}{2}^+$
1361.8	110.7(2)	3.3(3)	0.29(8)	675.9	$M1/E2$	$\frac{9}{2}^+ \rightarrow \frac{11}{2}^+$
	787.2(3)	15.3(41)			$M1/E2$	$\frac{9}{2}^+ \rightarrow \frac{9}{2}^+$

1653.7	403.1(6)	57.0(3)	0.53(10)	675.9	$M1/E2$	$\frac{13}{2}^+ \rightarrow \frac{11}{2}^+$
	1079.1(4)	309.2(110)	1.04(8)[c]	1355.7	$E2$	$\frac{13}{2}^+ \rightarrow \frac{9}{2}^+$
2023.8	773.3(2)	100	1.08(11)	714.2	$M1/E2$	$\frac{13}{2}^+ \rightarrow \frac{11}{2}^+$
	662.3(3)	1.5(5)			$E2$	$\frac{13}{2}^+ \rightarrow \frac{9}{2}^+$
2079.4	944.7(2)	4.7(4)	1.83(78)	129.1	$E2$	$\frac{9}{2}^- \rightarrow \frac{5}{2}^-$
	956.3(1)	1.2(2)			$M1/E2$	$\frac{9}{2}^- \rightarrow \frac{7}{2}^-$
	1163.8(2)	1.0(2)			$M1/E2$	$\frac{9}{2}^- \rightarrow \frac{7}{2}^-$
	1366.1(4)	3.2(8)			$E2$	$\frac{9}{2}^- \rightarrow \frac{5}{2}^-$
2158.9	1244.3(4)	1.0(2)			$(M1/E2)$	$(\frac{9}{2}^-) \rightarrow \frac{7}{2}^-$
	1446.2(1)	0.7(4)			$(E2)$	$(\frac{9}{2}^-) \rightarrow \frac{5}{2}^-$
2398.6	1205.2(2)	3.6(3)	0.22(7)	807.0	$M1/E2$	$\frac{11}{2}^- \rightarrow \frac{9}{2}^-$
	1275.2(3)	12.4(12)	1.14(15)	468.0	$E2$	$\frac{11}{2}^- \rightarrow \frac{7}{2}^-$
	1484.0(4)	5.2(5)	0.93(17)	468.0	$E2$	$\frac{11}{2}^- \rightarrow \frac{7}{2}^-$
2433.9	1240.3(4)	4.5(11)	0.57(13)	468.0	$M1/E2$	$\frac{11}{2}^- \rightarrow \frac{9}{2}^-$
	1311.1(2)	1.9(4)	1.13(47)	468.0	$E2$	$\frac{11}{2}^- \rightarrow \frac{7}{2}^-$
	1333.3(4)	0.7(3)	0.76(30)	468.0	$M1/E2$	$\frac{11}{2}^- \rightarrow \frac{9}{2}^-$
	1519.3(2)	1.9(2)	1.05(26)	468.0	$E2$	$\frac{11}{2}^- \rightarrow \frac{7}{2}^-$
2492.7	469.2(4)	2.7(4)			$M1/E2$	$\frac{15}{2}^+ \rightarrow \frac{13}{2}^+$
	838.6(2)	6.3(17)	0.37(14)	675.9	$M1/E2$	$\frac{15}{2}^+ \rightarrow \frac{13}{2}^+$
	1242.2(3)	47.8(34)	1.11(24)	714.2	$E2$	$\frac{15}{2}^+ \rightarrow \frac{11}{2}^+$
2581.0	557.3(4)	3.1(3)	0.85(11)	773.3	$M1/E2$	$\frac{13}{2}^+ \rightarrow \frac{13}{2}^+$
	926.8(4)	4.7(2)	0.81(11)	1079.1	$M1/E2$	$\frac{13}{2}^+ \rightarrow \frac{13}{2}^+$
	1219.2(3)	3.3(7)			$E2$	$\frac{13}{2}^+ \rightarrow \frac{9}{2}^+$
2618.1	1424.3(4)	5.3(4)	0.79(14)	1154.4	$E2$	$\frac{13}{2}^- \rightarrow \frac{9}{2}^-$
2900.0	406.7(5)	4.2(5)	0.53(21)	1079.1	$M1/E2$	$\frac{17}{2}^+ \rightarrow \frac{15}{2}^+$
	876.2(2)	6.7(8)			$E2$	$\frac{17}{2}^+ \rightarrow \frac{13}{2}^+$
	1246.3(4)	272.6(114)	0.95(7)[c]	1079.1	$E2$	$\frac{17}{2}^+ \rightarrow \frac{13}{2}^+$
2935.5	856.1(4)	1.4(6)	1.36(67)	844.1	$E2$	$\frac{13}{2}^- \rightarrow \frac{9}{2}^-$
2979.6	546.2(5)	<0.1			$M1/E2$	$\frac{13}{2}^- \rightarrow \frac{11}{2}^-$
	581.1(3)	1.1(3)			$M1/E2$	$\frac{13}{2}^- \rightarrow \frac{11}{2}^-$
	821.1(3)	2.2(2)			$(M1/E2)$	$\frac{13}{2}^- \rightarrow (\frac{11}{2}^-)$
	901.2(5)	6.9(6)	1.37(35)	844.0	$E2$	$\frac{13}{2}^- \rightarrow \frac{9}{2}^-$
	1729.8(2)	6.7(6)			$E1$	$\frac{13}{2}^- \rightarrow \frac{11}{2}^+$
3205.6	807.0(3)	14.9(14)	1.05(10)	468.0	$E2$	$\frac{15}{2}^- \rightarrow \frac{11}{2}^-$
	772.3(4)	6.8(5)	1.06(15)	1154.4	$E2$	$\frac{15}{2}^- \rightarrow \frac{11}{2}^-$
	1183.2(5)	6.1(3)	0.59(11)	468.0	$E1$	$\frac{15}{2}^- \rightarrow \frac{13}{2}^+$
	1553.1(3)	17.2(18)	0.56(10)	468.0	$E1$	$\frac{15}{2}^- \rightarrow \frac{13}{2}^+$
3227.1	734.2(21)	18.7(2)	0.8(2)	1079.1	$M1/E2$	$\frac{17}{2}^+ \rightarrow \frac{15}{2}^+$
	1203.3(2)	31.0(19)	0.91(17)	714.2	$E2$	$\frac{17}{2}^+ \rightarrow \frac{13}{2}^+$
	1573.5(4)	11.7(9)			$E2$	$\frac{17}{2}^+ \rightarrow \frac{13}{2}^+$
3498.3	598.3(5)	0.8(4)			$M1/E2$	$\frac{17}{2}^+ \rightarrow \frac{17}{2}^+$
	917.3(4)	2.7(6)			$E2$	$\frac{17}{2}^+ \rightarrow \frac{13}{2}^+$
	1005.4(2)	0.3(2)			$M1/E2$	$\frac{17}{2}^+ \rightarrow \frac{15}{2}^+$

	1474.5(4)	7.8(12)	0.82(17)	773.3	$E2$	$\frac{17}{2}^+ \rightarrow \frac{13}{2}^+$
3576.5	677.2(10)	3.2(1)	0.36(11)	1079.1	$M1/E2$	$\frac{17}{2}^+ \rightarrow \frac{17}{2}^+$
	996.3(4)	3.5(9)			$E2$	$\frac{17}{2}^+ \rightarrow \frac{13}{2}^+$
	1083.8(1)	3.1(7)	1.05(27)	1079.1	$M1/E2$	$\frac{17}{2}^+ \rightarrow \frac{15}{2}^+$
	1553.0(3)	2.1(2)	0.70(15)	773.3	$E2$	$\frac{17}{2}^+ \rightarrow \frac{13}{2}^+$
	1923.2(4)	3.2(4)	0.84(26)	1079.1	$E2$	$\frac{17}{2}^+ \rightarrow \frac{13}{2}^+$
3617.6	412.0(2)	7.3(7)	0.52(4)	807.0	$M1/E2$	$\frac{17}{2}^- \rightarrow \frac{15}{2}^-$
	638.0(2)	3.3(4)	2.12(56)	129.1	$E2$	$\frac{17}{2}^- \rightarrow \frac{13}{2}^-$
	1000.1(4)	3.7(5)	1.18(24)	1154.4	$E2$	$\frac{17}{2}^- \rightarrow \frac{13}{2}^-$
3673.6	56.2(3)	$\sim 18^d$			$M1/E2$	$\frac{19}{2}^- \rightarrow \frac{17}{2}^-$
	97.3(3)	2.4(2)	0.31(8)	714.2	$E1$	$\frac{19}{2}^- \rightarrow \frac{17}{2}^+$
	176.2(2)	1.4(1)	0.55(7)	714.4	$E1$	$\frac{19}{2}^- \rightarrow \frac{17}{2}^+$
	448.2(2)	14.1(12)	0.46(5)	714.2	$E1$	$\frac{19}{2}^- \rightarrow \frac{17}{2}^+$
	468.0(5)	11.4(9)	0.91(8)	714.2	$E2$	$\frac{19}{2}^- \rightarrow \frac{15}{2}^-$
3722.7	517.1(5)	3.7(5)	0.43(12)	1275.2	$M1/E2$	$\frac{17}{2}^- \rightarrow \frac{15}{2}^-$
	743.3(2)	1.6(3)			$E2$	$\frac{17}{2}^- \rightarrow \frac{13}{2}^-$
4006.3	1106.3(4)	<1.0			$(M1/E2)$	$(\frac{19}{2}^+) \rightarrow \frac{17}{2}^+$
	1512.6(5)	1.6(5)			$(E2)$	$(\frac{19}{2}^+) \rightarrow \frac{15}{2}^+$
4255.7	1355.7(3)	190.7(95)	$1.09(9)^c$	1079.1	$E2$	$\frac{21}{2}^+ \rightarrow \frac{17}{2}^+$
4271.8	549.4(4)	1.2(2)			$E2$	$\frac{21}{2}^- \rightarrow \frac{17}{2}^-$
	598.2(5)	20.6(14)	0.41(9)	1275.2	$M1/E2$	$\frac{21}{2}^- \rightarrow \frac{19}{2}^-$
4387.8	116.4(3)	1.8(2)	0.37(15)	468.0	$M1/E2$	$\frac{23}{2}^- \rightarrow \frac{21}{2}^-$
	714.2(5)	17.2(18)	1.12(11)	468.0	$E2$	$\frac{23}{2}^- \rightarrow \frac{19}{2}^-$
4435.7	762.1(3)	8.8(8)	1.1(2)	468.0	$(E2)$	$\frac{23}{2}^- \rightarrow \frac{19}{2}^-$
5257.9	1002.2(4)	21.1(7)			$(E2)$	$(\frac{25}{2}^+) \rightarrow \frac{21}{2}^+$
5386.9	996.8(4)	3.1(4)			$(M1/E2)$	$(\frac{25}{2}^-) \rightarrow \frac{23}{2}^-$
	1115.1(2)	33.2(21)			$(E2)$	$(\frac{29}{2}^-) \rightarrow (\frac{25}{2}^-)$
5438.0	1182.3(3)	109.4(65)	$1.09(10)^c$	1355.7	$E2$	$\frac{25}{2}^+ \rightarrow \frac{21}{2}^+$
5830.8	1575.1(4)	41.8(34)	$1.34(27)^c$	1355.7	$E2$	$\frac{25}{2}^+ \rightarrow \frac{21}{2}^+$
6147.8	761.4(4)	1.7(4)			$(M1/E2)$	$(\frac{27}{2}^-) \rightarrow (\frac{25}{2}^-)$
	1760.0(2)	5.6(21)			$(E2)$	$(\frac{27}{2}^-) \rightarrow \frac{23}{2}^-$
6467.0	1080.1(3)	2.5(11)			$(E2)$	$(\frac{29}{2}^-) \rightarrow (\frac{25}{2}^-)$
6477.2	1219.3(2)	11.9(18)			$(E2)$	$(\frac{29}{2}^+) \rightarrow (\frac{25}{2}^+)$
6568.2	1130.2(3)	72.8(42)	$1.12(15)^c$	1079.1	$E2$	$\frac{29}{2}^+ \rightarrow \frac{25}{2}^+$
6887.7	1501.2.3(4)	8.4(27)			$(E2)$	$(\frac{29}{2}^-) \rightarrow (\frac{25}{2}^-)$
7104.3	1273.5(3)	29.9(17)			$(E2)$	$(\frac{29}{2}^+) \rightarrow (\frac{25}{2}^+)$
	1666.2(3)	8.2(5)			$(E2)$	$(\frac{29}{2}^+) \rightarrow \frac{25}{2}^+$
7684.4	1217.4(4)	3.4(11)			$(E2)$	$(\frac{33}{2}^-) \rightarrow (\frac{29}{2}^-)$
8035.0	1466.8(5)	46.2(32)	$1.08(15)^c$	1355.7	$(E2)$	$(\frac{33}{2}^+) \rightarrow \frac{29}{2}^+$
8044.3	1156.3(4)	5.1(3)			$(E2)$	$(\frac{33}{2}^-) \rightarrow (\frac{29}{2}^-)$
8056.0	1910.2(4)	1.2(2)			$(E2)$	$(\frac{31}{2}^-) \rightarrow (\frac{27}{2}^-)$
8494.1	1389.8(4)	4.5(14)			$(E2)$	$(\frac{33}{2}^+) \rightarrow (\frac{29}{2}^+)$
9008.1	1323.7(3)	3.2(4)			$(E2)$	$(\frac{37}{2}^-) \rightarrow (\frac{33}{2}^-)$

9714.2	1679.2(4)	9.9(12)	$(E2)$	$(\frac{37}{2}^+)\rightarrow(\frac{33}{2}^+)$
9956.2	1911.9(3)	3.3(7)	$(E2)$	$(\frac{37}{2}^-)\rightarrow(\frac{33}{2}^-)$
10414.4	1406.3(5)	2.7(2)	$(E2)$	$(\frac{41}{2}^-)\rightarrow(\frac{37}{2}^-)$
11382.6	1668.4(7)	7.4(3)	$(E2)$	$(\frac{41}{2}^+)\rightarrow(\frac{37}{2}^+)$
13363.1	1980.5(9)	3.1(11)	$(E2)$	$(\frac{45}{2}^+)\rightarrow(\frac{41}{2}^+)$

[a] Relative intensity derived from the $\gamma-\gamma$ matrix sorted from the self-suporting target experiment.
[b] DCO ratio deduced from the $\gamma-\gamma$ matrix sorted from the backed-target experiment except for where indicated otherwise.
[c] The DCO was determined from the $\gamma-\gamma$ matrix sorted from the self-suporting target experiment.
[d] From the balance of the intensities.

A.2 Spectroscopic information in ^{69}As

Table A.2: Energies, relative intensities and DCO ratios of γ-ray transitions assigned to ^{69}As. The intensities are normalized to the 853.8-keV transition, set to be 100.

E_{level}(keV)	E_γ(keV)	I_γ^a	R_{DCO}^b	Gate	σL	I_i^π	I_f^π
0.0						$5/2^-$	
98.2	98.2	7.8(3)	0.50(5)	1097.6	$M1/E2$	$3/2^-$	$5/2^-$
761.8	663.6	2.5(2)	0.67(18)^c	601.3	$M1/E2$	$5/2^-$	$3/2^-$
	761.8	4.9(7)	1.05(19)^c	601.3	$M1$	$5/2^-$	$5/2^-$
863.2	765.0	11.9(29)	1.85(15)	442.4	$E2$	$7/2^-$	$3/2^-$
	863.2	69.1(29)	0.61(5)	1097.6	$M1/E2$	$7/2^-$	$5/2^-$
933.4	835.2	4.0(3)	0.76(1)^c	799.2	$E2$	$7/2^-$	$3/2^-$
1216.3	1118.1	15.8(10)	1.36(12)^c	799.2	$E2$	$7/2^-$	$3/2^-$
	1216.3	6.9(14)	0.41(6)^c	799.2	$M1/E2$	$7/2^-$	$5/2^-$
1305.6	89.3	3.5(10)	0.46(6)	1097.6	$E1$	$9/2^+$	$7/2^-$
	442.4	91.7(44)	0.65(5)	1204.2	$E1$	$9/2^+$	$7/2^-$
	1305.6	58.4(62)	1.05(7)	1097.6	$M2$	$9/2^+$	$5/2^-$
1470.3	1470.3	18.9(16)	0.98(7)	808.3	$E2$	$9/2^-$	$5/2^-$
1534.0	228.4	0.22(3)			$(E2)$	$(5/2^+)$	$9/2^+$
	1435.8	3.1(3)			$(E1)$	$(5/2^+)$	$3/2^-$
1670.4	1670.4	2.8(3)			$(M1/E2)$	$(7/2^-)$	$5/2^-$
1713.2	779.8	0.6(1)			$(M1)$	$(5/2^-)$	$5/2^-$
	1615.0	3.3(2)	0.5(1)^c	601.3	$(M1/E2)$	$(5/2^-)$	$3/2^-$
	1713.2	0.6(2)			$(M1/E2)$	$(5/2^-)$	$3/2^-$
1987.5	1987.5	0.19(1)	0.42(1)^c	790.9	$M1/E2$	$7/2^-$	$5/2^-$
2159.4	853.8	100	1.01(6)	1097.6	$E2$	$13/2^+$	$9/2^+$
2169.0	635.0	0.33(6)	2.2(7)	648.5	$(E2)$	$9/2^{(+)}$	$(5/2^+)$
	952.7	0.20(3)			$(E1)$	$9/2^{(+)}$	$7/2^-$
	1305.8	2.1(3)	2.5(3)^c	863.2	$(E1)$	$9/2^{(+)}$	$7/2^-$
2199.7	1336.5	4.1(2)	2.3(2)^c	863.2	$E2$	$11/2^-$	$7/2^-$
2210.7	905.1	19.5(10)	0.19(4)^c	756.9	$M1/E2$	$11/2^+$	$9/2^+$
2311.2	323.7	0.18(4)	0.64(13)^c	808.3	$M1/E2$	$9/2^-$	$7/2^-$
	598.0	1.4(1)	0.98(9)^c	799.2	$E2$	$9/2^-$	$5/2^-$
	640.8	0.35(2)			$(M1/E2)$	$9/2^-$	$(7/2^-)$
	1005.6	1.5(1)	0.61(6)^c	808.3	$E1$	$9/2^-$	$9/2^+$
	1094.9	1.18(9)			$M1/E2$	$9/2^-$	$7/2^-$
	1377.8	0.20(1)	0.68(22)	799.2	$M1/E2$	$9/2^-$	$7/2^-$
	1448.0	0.8(5)			$M1/E2$	$9/2^-$	$7/2^-$
	2311.2	6.4(7)	1.08(9)	808.3	$E2$	$9/2^-$	$5/2^-$
2444.1	730.9	0.16(1)			$(E2)$	$9/2^-$	$(5/2^-)$
	773.7	0.19(1)			$(M1/E2)$	$9/2^-$	$(7/2^-)$
	1227.8	1.6(3)			$M1/E2$	$9/2^-$	$7/2^-$
	1682.3	0.9(1)	1.27(20)^c	601.3	$E2$	$9/2^-$	$5/2^-$
2627.6	316.4	0.18(3)	0.57(13)^c	790.9	$M1/E2$	$11/2^-$	$9/2^-$
	468.2	<0.1	0.7(3)	790.9	$E1$	$11/2^-$	$13/2^+$

	640.1	0.2(4)	1.3(2)[c]	790.9	$E2$	$11/2^-$	$7/2^-$
	957.2	2.9(3)	1.20(14)[c]	790.9	$E2$	$11/2^-$	$7/2^-$
	1322.0	2.4(1)	0.67(6)[c]	790.9	$E1$	$11/2^-$	$9/2^+$
	1411.3	5.0(3)	0.95(18)[c]	756.9	$E2$	$11/2^-$	$7/2^-$
2666.0	1449.7	2.1(5)	1.27(13)[c]	799.2	$E2$	$11/2^-$	$7/2^-$
2711.0	551.6	5.7(8)			$(E1)$	$(11/2^-)$	$13/2^+$
	1405.4	4.7(3)			$(E1)$	$(11/2^-)$	$9/2^+$
2777.1	1306.8	11.4(12)	1.01(8)	1470.3	$E2$	$13/2^-$	$9/2^-$
2808.0	597.3	3.6(7)	0.34(5)[c]	756.9	$M1/E2$	$13/2^+$	$11/2^+$
	639.0	1.2(1)	1.7(2)	648.5	$E2$	$13/2^+$	$9/2^{(+)}$
	648.6	2.1(2)			$M1$	$13/2^+$	$13/2^+$
	1502.4	4.7(10)	2.1(3)	648.5	$E2$	$13/2^+$	$9/2^+$
3045.4	268.3	0.12(1)	0.68(9)[c]	1470.3	$M1$	$13/2^-$	$13/2^-$
	334.4	5.3(4)	0.51(5)[c]	799.2	$M1/E2$	$13/2^-$	$11/2^-$
	379.4	1.6(1)			$M1/E2$	$13/2^-$	$11/2^-$
	417.8	0.41(3)	0.52(7)[c]	808.3	$M1/E2$	$13/2^-$	$11/2^-$
	601.3	0.91(6)	0.96(17)[c]	808.3	$E2$	$13/2^-$	$9/2^-$
	734.2	14.3(17)	1.15(11)	808.3	$E2$	$13/2^-$	$9/2^-$
	886.0	3.2(2)	1.1(1)[c]	808.3	$E1$	$13/2^-$	$13/2^+$
3216.8	1006.1	1.1(2)			$M1/E2$	$13/2^+$	$11/2^+$
	1057.4	2.5(2)	0.24(3)[c]	853.8	$M1/E2$	$13/2^+$	$13/2^+$
3257.0	449.0	<0.1			$E2$	$17/2^+$	$13/2^+$
	1097.6	90.2(44)	0.95(6)	1204.2	$E2$	$17/2^+$	$13/2^+$
3263.2	455.2	0.11(3)			$M1/E2$	$15/2^+$	$13/2^+$
	1052.5	1.55(4)	1.08(21)[c]	756.9	$E2$	$15/2^+$	$11/2^+$
	1103.8	1.9(5)	0.19(2)[c]	756.9	$M1/E2$	$15/2^+$	$13/2^+$
3418.5	373.1	1.0(2)			$M1/E2$	$15/2^-$	$13/2^-$
	641.4	1.7(4)	0.67(10)[c]	1470.3	$M1/E2$	$15/2^-$	$13/2^-$
	752.5	0.8(2)	1.2(2)	937.7	$E2$	$15/2^-$	$11/2^-$
	790.9	7.6(14)	1.2(1)	756.9	$E2$	$15/2^-$	$11/2^-$
	1218.8	2.1(4)	0.77(10)[c]	756.9	$E2$	$15/2^-$	$11/2^-$
	1259.1	6.1(3)	0.49(6)	756.9	$E1/M2$	$15/2^-$	$13/2^+$
3507.1	290.3	≈ 0.1			$M1/E2$	$15/2^+$	$13/2^+$
	699.1	<0.1			$M1/E2$	$15/2^+$	$13/2^+$
	1296.4	0.32(4)	1.12(6)	1305.6	$E2$	$15/2^+$	$11/2^+$
	1347.7	0.24(3)	0.41(16)[c]	756.9	$M1/E2$	$15/2^+$	$13/2^+$
3660.4	153.3	0.16(1)			$M1/E2$	$17/2^+$	$15/2^+$
	397.2	0.17(1)	0.57(13)[c]	1052.5	$M1/E2$	$17/2^+$	$15/2^+$
	403.4	2.7(2)			$M1$	$17/2^+$	$17/2^+$
	852.4	4.4(3)	1.24(5)	853.8	$E2$	$17/2^+$	$13/2^+$
	1501.0	4.1(3)	1.76(14)[c]	853.8	$E2$	$17/2^+$	$13/2^+$
3840.2	333.1	1.9(6)	0.49(23)[c]	756.9	$M1/E2$	$17/2^+$	$15/2^+$
	577.0	3.5(12)	0.39(6)[c]	756.9	$M1/E2$	$17/5^+$	$15/2^+$
	583.2	<0.1			$M1$	$17/2^+$	$17/2^+$
	623.4	1.3(1)	0.81(2)[c]	756.9	$E2$	$17/2^+$	$13/2^+$
	1032.2	5.7(4)	1.3(1)	853.8	$E2$	$17/2^+$	$13/2^+$
	1680.8	1.9(6)	1.15(27)[c]	756.9	$E2$	$17/2^+$	$13/2^+$
3844.6	426.1	0.17(1)	0.76(13)[c]	790.9	$M1/E2$	$17/2^-$	$15/2^-$

	587.6	0.86(6)	1.25(20)[c]	808.3	$E1$	$17/2^-$	$17/2^+$
	799.2	12.1(12)	1.01(8)	808.3	$E2$	$17/2^-$	$13/2^-$
	1067.5	8.9(8)	1.01(8)	808.3	$E2$	$17/2^-$	$13/2^-$
3947.5	529.1	0.6(2)			$M1$	$15/2^-$	$15/2^-$
	902.3	1.00(5)			$M1/E2$	$15/2^-$	$13/2^-$
	1748.0	3.1(4)	2.91(55)[c]	863.2	$E2$	$15/2^-$	$11/2^-$
	1788.7	2.6(3)	0.44(9)[c]	853.8	$E1$	$15/2^-$	$13/2^+$
4148.2	641.1	0.25(2)	0.80(14)[c]	756.9	$M1/E2$	$17/2^+$	$15/2^+$
	885.0	0.14(2)	0.56(8)[c]	756.9	$M1/E2$	$17/2^+$	$15/2^+$
	891.2	<0.1			$M1$	$17/2^+$	$17/2^+$
	931.4	<0.1			$E2$	$17/2^+$	$13/2^+$
4306.1	465.9	<0.1			$(M1/E2)$	$(19/2^+)$	$17/2^+$
	645.7	0.12(3)			$(M1/E2)$	$(19/2^+)$	$17/2^+$
	1042.9	0.24(5)			$(E2)$	$(19/2^+)$	$15/2^+$
4356.2	937.7	5.4(3)	1.23(12)	853.8	$E2$	$19/2^-$	$15/2^-$
	1099.2	5.6(6)			$E1$	$19/2^-$	$17/2^+$
4461.2	1204.2	68.2(31)	1.16(7)	1097.6	$E2$	$21/2^+$	$17/2^+$
4488.7	340.5	0.8(1)	0.42(3)[c]	756.9	$E1$	$19/2^-$	$17/2^+$
	541.0	0.22(3)	1.23(25)[c]	756.9	$E2$	$19/2^-$	$15/2^-$
	644.1	<0.1			$M1/E2$	$19/2^-$	$17/2^-$
	648.5	1.4(2)	0.55(6)[c]	756.9	$E1$	$19/2^-$	$17/2^+$
	828.3	0.8(1)	0.53(7)[c]	756.9	$E1$	$19/2^-$	$17/2^+$
	1070.2	1.6(1)	1.04(8)	756.9	$E2$	$19/2^-$	$15/2^-$
	1231.7	0.12(2)	0.53(11)	756.9	$E1$	$19/2^-$	$17/2^+$
4551.2	1334.4	0.15(3)					$13/2^+$
4554.0	197.8	<0.1	0.60(14)[c]	790.9	$M1/E2$	$19/2^-$	$17/2^-$
	405.8	2.1(5)			$E1$	$19/2^-$	$17/2^+$
	606.3	2.5(8)			$E2$	$19/2^-$	$15/2^-$
	709.4	0.17(4)	0.33(7)[c]	799.2	$M1/E2$	$19/2^-$	$17/2^-$
	893.6	2.4(4)	0.39(10)[c]	1097.6	$E1$	$19/2^-$	$17/2^+$
	1135.5	2.9(12)	1.4(3)[c]	790.9	$E2$	$19/2^-$	$15/2^-$
	1297.0	1.4(4)	0.54(4)	1097.6	$E1$	$19/2^-$	$17/2^+$
4652.9	808.3	6.3(4)	0.93(8)	1470.3	$E2$	$21/2^-$	$17/2^-$
4713.3	565.1	<0.1					$17/2^+$
4847.2	194.3	0.11(2)	0.54(7)[c]	808.3	$M1$	$21/2^-$	$21/2^-$
	1002.6	2.3(2)	0.94(7)	1470.3	$E2$	$21/2^-$	$17/2^-$
4929.4	468.2	0.27(2)			$M1$	$21/2^+$	$21/2^+$
	1672.4	1.2(1)	1.39(14)	1097.6	$E2$	$21/2^+$	$17/2^+$
5150.0	436.7	<0.1					
5152.3	598.3	3.1(7)					$19/2^-$
5193.3	263.8	0.5(1)			$E2$	$25/2^+$	$21/2^+$
	732.1	57.6(27)	0.94(6)	1097.6	$E2$	$25/2^+$	$21/2^+$
5245.6	398.4	1.13(8)	0.51(8)[c]	808.3	$M1/E2$	$23/2^-$	$21/2^-$
	592.7	2.8(2)	0.36(3)[c]	808.3	$M1/E2$	$23/2^-$	$21/2^-$
	691.6	1.25(9)	0.9(2)	799.2	$E2$	$23/2^-$	$19/2^-$
	756.9	1.35(1)	0.94(13)	790.9	$E2$	$23/2^-$	$19/2^-$
5452.4	1096.2	3.4(2)	0.94(7)	937.7	$E2$	$19/2^-$	$15/2^-$
5711.1	1249.9	17.4(8)	0.47(5)	1097.6	$M1/E2$	$23/2^+$	$21/2^+$

5831.5	1280.3	<0.1					
5918.3	672.7	0.29(2)	0.51(9)[c]	756.9	$M1/E2$	$25/2^-$	$23/2^-$
	1265.4	4.0(3)	1.00(8)	799.2	$E2$	$25/2^-$	$21/2^-$
5941.0	1479.8	12.3(5)	0.84(6)	1204.2	$E2$	$25/2^+$	$21/2^+$
6089.2	843.6	0.43(3)			$M1/E2$	$25/2^-$	$23/2^-$
	1242.0	1.6(1)	1.22(14)	799.2	$E2$	$25/2^-$	$21/2^-$
6359.7	1166.4	12.5(6)	1.03(19)	1097.6	$E2$	$29/2^+$	$25/2^+$
6369.4	1176.1	25.4(11)	1.04(12)	1097.6	$E2$	$29/2^+$	$25/2^+$
6571.5	1325.9	1.1(1)	1.07(8)	756.9	$E2$	$27/2^-$	$23/2^-$
6742.0	1289.6	2.5(2)	1.28(13)	937.7	$E2$	$27/2^-$	$23/2^-$
6847.3	477.9	0.62(17)	1.28(13)	1176.1	$E2$	$25/2^+$	$29/2^+$
	1136.2	6.0(17)	0.47(7)	1097.6	$M1/E2$	$25/2^+$	$23/2^+$
7446.5	1505.5	5.6(7)	0.35(3)	1204.4	$E2$	$27/2^+$	$25/2^+$
	1735.4	0.23(3)			$E2$	$27/2^+$	$23/2^+$
7448.3	1359.1	1.08(8)			$E2$	$29/2^-$	$25/2^-$
	1530.0	2.8(2)	1.49(11)	1265.4	$E2$	$29/2^-$	$25/2^-$
7519.5	1430.3	0.73(6)	0.93(10)	799.2	$E2$	$29/2^-$	$25/2^-$
7614.5	1696.2	1.8(6)	1.43(10)	808.3	$E2$	$29/2^-$	$25/2^-$
7627.2	1686.2	1.2(2)	1.2(3)	1204.2	$E2$	$29/2^+$	$25/2^+$
7689.9	842.6	1.8(4)	0.45(13)	1136.2	$M1/E2$	$27/2^+$	$25/2^+$
	1320.5	4.9(13)	0.36(5)	1176.1	$M1/E2$	$27/2^+$	$29/2^+$
7716.7	1347.4	4.9(3)	1.2(2)	1176.1	$E2$	$33/2^+$	$29/2^+$
	1357.1	4.1(2)	1.32(10)	1166.4	$E2$	$33/2^+$	$29/2^+$
7896.6	1527.2	18.9(8)	1.15(8)	1176.1	$E2$	$33/2^+$	$29/2^+$
8142.8	1571.3	0.64(5)	0.98(10)	756.9	$E2$	$31/2^-$	$27/2^-$
8185.8	1443.8	1.3(2)	1.06(8)	937.7	$E2$	$31/2^-$	$27/2^-$
8382.4	692.5	0.12(2)	0.50(11)	1320.5	$M1/E2$	$29/2^+$	$27/2^+$
	1535.1	0.3(1)	1.16(13)	1136.2	$E2$	$29/2^+$	$25/2^+$
8455.4	765.5	0.9(2)			$(M1/E2)$	$(25/2^+)$	$27/2^+$
	1608.1	1.98(55)			$(M1)$	$(25/2^+)$	$25/2^+$
	2095.7	6.1(17)	1.27(11)	1204.2	$(E2)$	$(25/2^+)$	$29/2^+$
8641.5	1193.2	2.9(2)	1.05(9)	799.2	$E2$	$33/2^-$	$29/2^-$
	1027.0	1.1(3)			$E2$	$33/2^-$	$29/2^-$
9095.4	1575.9	0.6(1)			$(E2)$	$(33/2^-)$	$29/2^-$
9393.0	1250.2	0.18(2)	1.25(17)	756.9	$E2$	$35/2^-$	$31/2^-$
9472.2	1755.4	3.1(2)	0.97(20)	1166.4	$E2$	$37/2^+$	$33/2^+$
9738.5	1552.7	0.8(1)	0.90(8)	937.7	$E2$	$35/2^-$	$31/2^-$
9819.4	1922.8	6.2(3)	1.4(1)	1204.2	$E2$	$37/2^+$	$33/2^+$
9985.7	1344.2	2.3(2)	1.03(8)	1265.4	$E2$	$37/2^-$	$33/2^-$
10097.0	1641.6	3.9(3)			$(E2)$	$(29/2^+)$	$25/2^+$
10795.8	1700.4	0.80(5)			$(E2)$	$(37/2^-)$	$(33/2^-)$
11180.3	1787.3	0.16(2)	1.2(2)	757.6	$E2$	$39/2^-$	$35/2^-$
11434.6	1696.1	0.4(1)	1.5(2)	937.7	$E2$	$39/2^-$	$35/2^-$
11551.8	1566.1	2.3(2)	1.15(10)	1265.4	$E2$	$41/2^-$	$37/2^-$
11977.2	2157.8	2.9(1)	1.15(14)	1176.1	$E2$	$41/2^+$	$37/2^+$
12287.4	2468.0	0.7(2)			$(E2)$	$(41/2^+)$	$37/2^+$
13325.0	1890.4	0.2(1)			$(E2)$	$(43/2^-)$	$39/2^-$
13545.8	1994.0	0.50(6)	0.96(10)	1193.2	$E2$	$45/2^-$	$41/2^-$

13871.5	1894.3	2.1(3)	$(E2)$	$(45/2^+)$	$(41/2^+)$
	1584.1	0.3(1)		$(45/2^+)$	$(41/2^+)$
14567.0	2589.8	1.8(4)	$(E2)$	$(45/2^+)$	$41/2^+$
15765.0	1893.5	1.6(4)	$(E2)$	$(49/2^+)$	$(45/2^+)$
16005.6	2459.8	0.3(2)	$(E2)$	$(49/2^-)$	$45/2^-$
18180.6	2415.6	1.23(6)	$(E2)$	$(53/2^+)$	$(49/2^+)$

[a] Relative intensity derived from the $\gamma - \gamma$ matrix sorted from the self-supporting target experiment.
[b] DCO ratio deduced from the $\gamma - \gamma$ matrix sorted from the self-supporting target experiment
except for where indicated otherwise.
[c] The DCO was determined from the $\gamma - \gamma$ matrix sorted from the backed-target experiment.

A.3 Model codes

A.3.1 RTRP codes for low-spin calculations

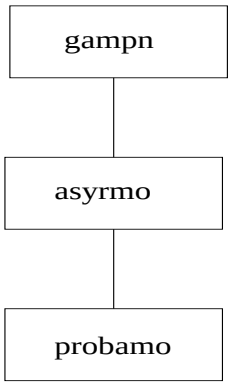

Figure A.1: *Flow chart of the RTRP codes used in the present calculations.*

- **gampn** - calculates the single-particle energies and various matrix elements in a modified oscillator (Nilsson) potential;
- **asyrmo** - diagonalizes the particle + triaxial rotor Hamiltonian in the strong-coupling basis;
- **probamo** - calculates the $E2$ and $M1/E2$ matrix elements.

A.3.2 CNS codes for high-spin calculations

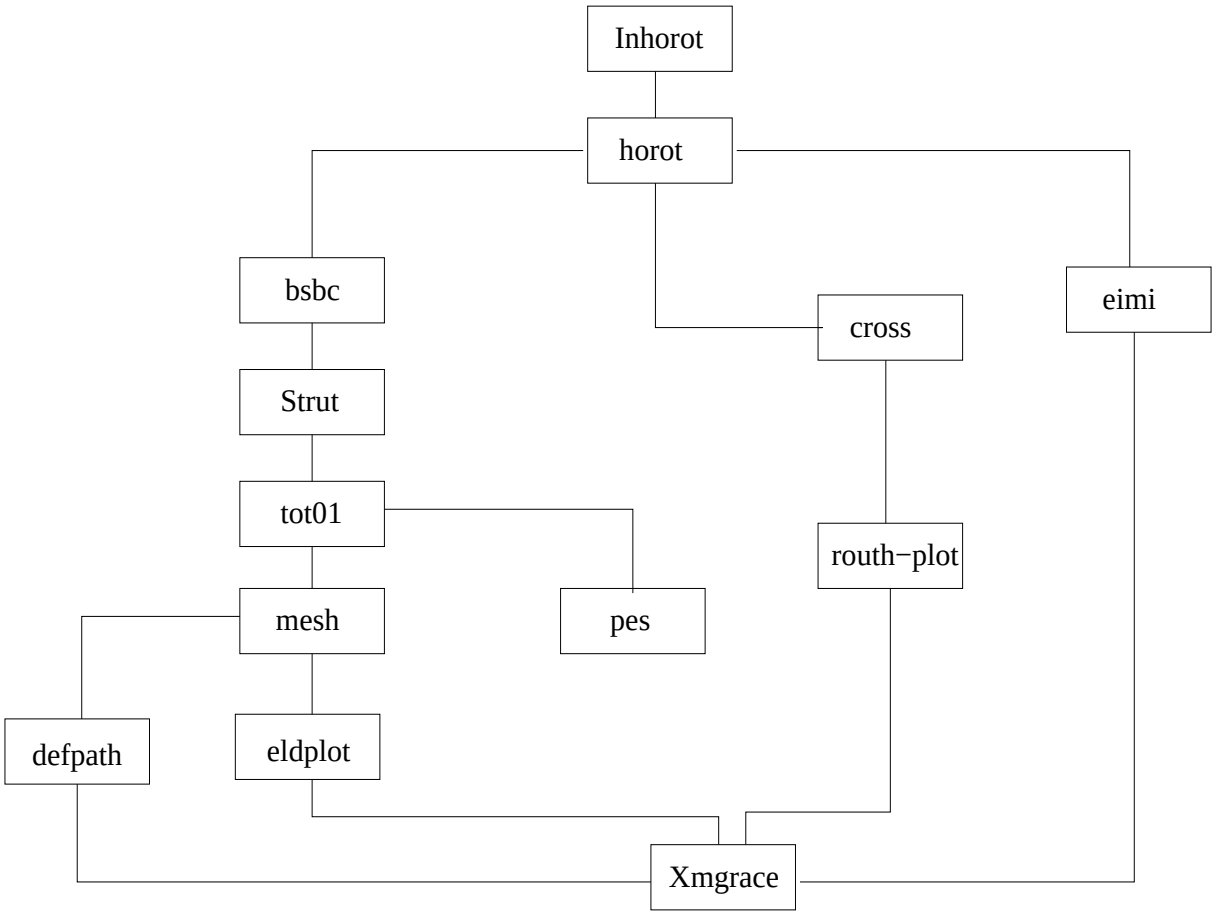

Figure A.2: *Flow chart of the CNS codes used in the present calculations.*

- **Inhorot** - sets up a mesh in the deformation and frequency space that is to be diagonalized;
- **horot** - diagonalizes the cranking Hamiltonian at each of the mesh points;
- **bsbc** - calculates liquid-drop energies and moments of inertia;
- **Strut** - it carries out the Strutinsky smearing procedure.
- **tot01** - calculates total energies in the different mesh points for the specified configurations;
- **mesh** - finds the energy minimum in the deformation space;
- **pes** - generates plots of the potential-energy surfaces as a function of spin for a given configuration;
- **defpath** - generates plots of the deformation paths;

- **eldplot** - generates $E - E_{rld}$ plots;
- **cross** - removes virtual crossings;
- **routh-plot** - plots single-particle energies as a function of rotational frequency (routhians);
- **eimi** - generates plots of tilted Fermi surfaces for fixed deformations.
- **Xmgrace** - plotting program (an older version is **Xmgr**).

Bibliography

[Afa99] A.V. Afanasjev, D.B. Fossan, G.J. Lane, and I. Ragnarsson, Phys. Rep. **322**, 1(1999).

[And76] G. Andersson *et al.* Nucl. Phys. A, **268**, 205(1976).

[Ari75] A. Arima and F. Iachello, Phys. Rev. Lett. B, **57** 39(1975).

[Arr89] J.W. Arrison *et al.*, Phys. Rev. C, **40**, 2010(1989).

[Arr90] J.W. Arrison, T. Chapuran, U.J. Hüttmeier and D.P. Balamuth, Phys. Lett. B, **248**, 39(1990).

[Asy] I. Ragnarsson and P. Seems, *Code ASYRMO*, Private Communication, 1991.

[Bar19] M.E. Barclay *et al.*, J. Phys. G **12**, L295(1986).

[Bazz97] D. Bazzacco *"GASP Data Analysis Program Package"*, Private Communication, 1997.

[Bec92] F.A. Beck, Prog. Part. Nucl. Phys., **28**, 443(1992).

[Bec97] F. Becker *et al.*, Nucl. Phys. A, **626**, 799(1997).

[Ben79a] R. Bengtsson and S. Frauendorf, Nucl. Phys. A, **314**, 27(1979).

[Ben79b] R. Bengtsson and S. Frauendorf, Nucl. Phys. A, **327**, 139(1979).

[Ben84] R. Bengtsson, P. Möller, J. R. Nix, and J. Zhang, Phys. Scr. **29**, 402(1984).

[Ben85] T. Bengtsson *et al.*, Nucl. Phys. A, **436**, (1985).

[Ber80] F.J. Bergmeister, A. Henriquez Frings, A. Gelberg, and K. P. Lieb, Z. Phys. A, **296**, 181(1980).

[Bet71] R.R. Betts, D. J. Pullen, W. Scholz, and B. Rosner, Phys. Rev. Lett, **26**, 25, 1576(1971).

[Bha93] M.R. Bhat, Nucl. Data Sheets **68**, 117 (1993).

[Bha00] M.R. Bhat and J. K. Tuli, Nucl. Data Sheets **90**, 269(2000).

[Bog67] A.P. Bogdanov *et al.*, Yad. Fiz. **5**, 1161(1967).

[Boh52] A. Bohr, Dan. Mat. Fys. Medd. Selsk. **26**, 33(1952).

[Boh69] A. Bohr and B. Mottelson, *Nuclear Structure Vol I,II, W. A. Benjamin Edit., New York 1969*

[Boh81] A. Bohr and B. R. Mottelson, Physica Scripta, **24**, 71(1981).

[Bos72] M. Bosterli *et al.*, Phys. Rev. C, **5**, 1050(1972).

[Bou03] E. Bouchez *et al.*, Phys. Rev. Lett. **90**, 082502(2003).

[Bra72] M. Brack *et al.*, Rev. Mod. Phys. **44**, 320(1972).

[Bru00] A. M. Bruce *et al.*, Phys. Rev. C, **62**, 027303(2000).

[Bur02] T.W. Burrows, Nucl. Data Sheets **97**, 1(2002).

[But73] P.A. Butler *et al.*, Nucl. Instrum. Methods **108**, 497(1973).

[Cha97] C. Chandler *et al.*, Phys. Rev. C, **56**, R2924(1997).

[Coh67] S. Cohen, R.D. Lawson, M.H. Macfarlane, S. P. Pandya, and M. Soga, Phys. Rev., **160**, 903(1967).

[Dav58] A.S. Davydov and G. F. Filippov, Nucl. Phys., **8**, 237(1958).

[Dew87] A. Dewald *et al.*, Z. Phys. A, **326**, 509(1987).

[Dra70] J.E. Draper and R. M. Leider, Nucl. Phys. **A141**, 211(1970).

[Duc99] G. Duchêne *et al.*, Nucl. Instrum. Methods A **432**, 90(1999).

[Ebe84] J. Eberth, L. Cleeman, and N. Schmal, Proc.Intern.Sym. on In-Beam Nuclear Spectroscopy, Debrecen, Hungary, May 14-18, 1984, Zs.Dombradi, T.Fenyes, Eds., p.23 (1984).

[Ebe93] J. Eberth *et al.*, Nuclear Physics News, Vol. 3, 3(1993)8.

[Eks92] L. P. Ekström and A. Nordlund, Nucl. Instrum. Methods Phys. Res. A **313**, 421(1992).

[Enn91] P.J. Ennis *et al*, Nucl. Phys. A, **535**, 392(1991).

[Fis00] S.M. Fischer *et al.*, Phys. Rev. Lett. **84**, 4064(2000).

[Fis03] S.M. Fischer, C.J. Lister, and D.P. Balamuth, Phys. Rev. C **67**, 064318(2003).

[Fot99] N. Fotiades *et al.*, Phys. Rev. C, **59**, 2919(1999).

[Gad99] A. Gadea *et al.*, LNL Annual Report **160/00**, 151(1999).

[Gal86] D. Galeriu, D. Bucurescu, and M. Ivascu, J. Phys. **G12**, 329(1986).

[Gam] I. Ragnarsson and P. Seems, *Code GAMPN1*, Private Communication, 1999.

[Grz98] R. Grzywacz *et al.*, Phys. Lett. B, **429**, 247(1998).

[Ham74] J.H. Hamilton *et al.*, Phys. Rev. Lett. **32**, 239(1974).

[Ham76] J.H. Hamilton *et al.*, Phys. Rev. Lett. **36**, 340(1976).

[Har65] S.M. Harris, Phys. Rev. **138**, 509b(1965).

[Hee86] J. Heese *et al.*, Z. Phys. A **325**, 45(1986).

[Hei76] B. Heits *et al.*, Phys. Lett. B, **61**, 33(1976).

[Hei77] B. Heits, H. G. Friederichs, A. Rademacher, K. O. Zell and P. von Brentano, Phys. Rev. C. **15**, 1742(1977).

[Hel76] H.A. Helms, W. Hogervorst, G.J. Zaal, and J. Blok, Phys. Scr. **14**, 138(1976).

[Hel78] H. P. Hellmeister *et al.*, Phys. Rev. C, **17**, 2113(1978).

[Her87] M.A. Herath-Banda *et al.*, J. Phys. G **13**, 43(1987).

[Her90] U. Hermkens, Diplom Thesis, Cologne, 1990.

[Her92] U. Hermkens *et al.*, Z. Phys. A **343**, 371(1992).

[Her95] U. Hermkens *et al.*, Phys. Rev. C, **52**, 1783(1995).

[Hsi92] S.T. Hsieh, H.C. Chiang, and Der-San Chuu, Phys. Rev. C, **46**, 195(1992).

[Ing54] D.R. Inglis, Phys. Rev., **96**, 1059(1954).

[Ing55] D.R. Inglis, Phys. Rev., **97**, 701(1955).

[Iva76] M.A. Ivanow, I.Kh. Lemberg, and I.S. Michin, in *Annual Conference on Nuclear Spectroscopy*, Soviet Academy of Science, Baku, URSS, 1976, p.410.

[Jen01] D.G. Jenkins *et al.*, Phys. Rev. C, **64**, 064311(2001).

[Jen02] D.G. Jenkins *et al.*, Phys. Rev. C, **65**, 064307(2002).

[Joh72] A. Johnson, H. Ryde, and J. Hjorth, Nucl. Phys. A, **179**, 753(1972).

[Joh97] G.D. Johns, J. Döring, R.A. Kaye, G.N. Sylvan, and S.L. Tabor, Phys. Rev. C, **55**, 660(1997).

[Kel01] N.S. Kelsall *et al.*, Phys. Rev. C. **64**, 024309(2001).

[Kis63] L.S. Kisslinger and R.A. Sorensen, Rev. Mod. Phys. **35**, 853(1963).

[Kor01] A. Korichi *et al.*, Phys. Rev. Lett. **86**, 2746(2001).

[Kra73] K.S. Krane, R.M. Steffen and R.M. Wheeler, Nucl. Data Tables **11**, 351(1973).

[Kra89] A. Krämer-Flecken *et al.*, Nucl. Instrum. Methods Phys. Res. A **275**, 333(1989).

[Lar73] S.E. Larsson, Physica Scripta, **8**, 17(1973).

[Lar78] S.E. Larsson, G. Leander, and I. Ragnarsson, Nucl. Phys. A, **307**, 189(1978).

[Lim81] A.P de Lima *et al.*, Phys. Rev. C, **23**, 213(1981).

[Lis00] C.J. Lister, S.M. Fischer, and D.P. Balamuth, Proccedings *PINGST2000-Selected Topics on N=Z Nuclei*, Lund, Sweden, June 2000, Eds. D. Rudolph and M. Hellström, p.46.

[Los88] L. Losano, H. Dias, F. Krmpotić, and B.H. Wildenthal, Phys. Rev. C, **38**, 2902(1988).

[Luh85] L. Lühmann *et al.*, Phys. Rev. C **31**, 828(1985).

[Mac77] J.A. Macdonald *et al.*, Nucl. Phys. A, **288**, 1(1977).

[Mar69] M.A.J. Mariscotti, G. Sharff-Goldhaber, and B. Buck, Phys. Rev. **178**, 1864(1969).

[Mat74] E. Der Mateosian and A.W. Sunyar, Atomic Data and Nuclear Data Tables **13**, 1391(1974).

[Mit97] S. Mitarai *et al.*, JAERI Rev. 97-010, 23(1997).

[Mol74] P. Möller, S.G. Nilsson, and J.R. Nix, Nucl. Phys. A, **229**, 292(1974).

[Mur78] M.J. Murphy, C.N. Davids, E.B. Norman, and R.C. Pardo, Phys. Rev. C, **17**, 1574(1978).

[Mur83] M.J. Murphy and C.N. Davids, Phys. Rev. C, **28**, 1069(1983).

[Mye67] W.D Myers and W.J. Swiatecki, Ark. Phys. **36**, 343(1967).

[Myl89] T. Mylaeus *et al.*, J. Phys. G, **15**, L135(1989).

[Naz85] W. Nazarewicz, J. Dudek, R. Bengtsson, T. Bengtsson and I. Ragnarsson, Nucl. Phys. A, **435**, 397(1985).

[New60] T.D. Newton, Can. J. Phys. **38**, 70(1960).

[New67] J.O. Newton, F. S. Stephens, R. M. Diamond, K. Kotajima and E. Matthias, Nucl. Phys. **A95**, 357(1967).

[Nol74] E. Nolte, Y. Shida, W. Kutschera, R. Prestele, and H. Morinaga, Z. Phys. **268**, 267(1974).

[Paa76a] V. Paar, E. Coffou, U. Eberth, and J. Eberth, J. Phys. G, **2**, 917(1976).

[Paa76b] V. Paar, U. Eberth, and J. Eberth, Phys. Rev. C, **13**, 2532(1976).

[Pet89] A. Petrovici, K.W. Schmid, F. Grümmer, and A. Faessler, Nucl. Phys. A, **504**, 277(1989).

[Pet90] A. Petrovici, K.W. Schmid, F. Grümmer, and A. Faessler, Nucl. Phys. A, **517**, 108(1990).

[Pet96] A. Petrovici, K.W. Schmid, and A. Faessler, Nucl. Phys. A, **605**, 290(1996).

[Pet02] A. Petrovici, K.W. Schmid, and A. Faessler, Nucl. Phys. A, **708**, 190(2002).

[Pet2] A. Petrovici, K.W. Schmid and A. Faessler, Nucl. Phys. A **710**, 246(2002).

[Pie81] R.B. Piercey *et al.*, Phys. Rev. Lett. **47**, 1514(1981).

[Ple00] C. Plettner *et al.*, Phys. Rev. Let. **85**, 2454(2000).

[Ple01] C. Plettner *et al.*, Phys. Rev. C **62**, 014313(2000).

[Pod95] Zs. Podolyak, T. Fenyes, and J. Timar, Nucl. Phys. A, **584**, 60(1995).

[Poh90] K.R. Pohl, D.F. Winchell, J.W. Arrison, and D.P. Balamuth, Phys. Rev. C, **42**, R1175(1990).

[Poh95] K.R. Pohl, D.F. Winchell, J.W. Arrison, and D.P. Balamuth, Phys. Rev. C, **51**, 519(1995).

[Pro] I. Ragnarsson and P. Seems, *Code PROBAMO*, Private Communication, 1991.

[Pul77] F. Pühlhofer, Nucl. Phys. A **280**, 267(1977).

[Rad95] D.C. Radford, Nucl. Instrum. Methods Phys. Res. A **361**, 297(1995).

[Rag86] I. Ragnarsson, Z. Xing, T. Bengtsson, M.A. Riley, Phys. Scr. **34**, 651(1986).

[Rag88] I. Ragnarsson *et al.*, Hyperfine Interactions, **43**, 425(1988).

[Rai02] G. Rainovksi *et al.*, J. Phys. G: Nucl. Part. Phys., **28**, 2617(2002).

[Ram88] M. Ramdane *et al.*, Phys. Rev. C, **37**, 645(1988).

[Rin80] P. Ring and P. Schuck, *The nuclear many-body problem, New York, (1980)120*

[Sch68] W. Scholz and F.B. Malik, Phys. Rev. **176**, 1355(1968).

[Sch84] K.W. Schmid, F. Grümmer, and A. Faessler, Nucl. Phys. A, **431**, 205(1984).

[Sef88] R. Sefzig *PhD Thesis*, Cologne, 1988.

[Sie65] K. Siegbahn (Ed), Alpha-, Beta- and Gamma-Ray Spectroscopy, North-Holland (1965).

[Sim97] J. Simpson, Z. Phys. A **358**, 39(1997).

[Ske99] Ö. Skeppstedt *et al.*, Nucl. Instrum. Methods A **421**, 531(1999).

[Sko90] S. Skoda *et al.*, Z. Phys. A, **336**, 391(1990).

[Sko98] S. Skoda *et al.*, Il Nuovo Cimento, **111A**, 6-7, 669(1998).

[Soh97] D. Sohler *et al.*, Nucl. Phys. A **618** 35(1997).

[Soh98] D. Sohler *et al.*, Nucl. Phys. A, **644**, 141(1998).

[Soh99] D. Sohler *et al.*, Phys. Rev. C, **59**, 1328(1999).

[Sou82] R. Soundranayagam *et al.*, Phys. Rev. C, **25**, 1575(1982).

[Ste72] F.S. Stephens, R.M. Diamond, J.R. Leigh, T. Kammuri, and K. Nakai, Phys. Rev. Lett. **29**, 438(1972).

[Ste75b] R.M. Steffen and K. Alder, in *The Electromagnetic Interaction in Nuclear Spectroscopy*, ed. W. D. Hamilton, North-Holland, Amsterdam, 1975, p. 505.

[Ste03] E. Stefanova *et al.*, Phys. Rev. C, **67**, 054319(2003).

[Str67] V.M. Strutinsky, Nucl. Phys. A, **95**, 420(1967).

[Str68] V.M. Strutinsky, Nucl. Phys. A, **122**, 1(1968).

[Sun02] Y. Sun, in Proceedings of the Conference on Nuclear Structure with Large Gamma-Arrays: Status and Perspectives, Legnaro, Italy, 2002, edited by G. de Angelis, in press.

[Tar75] P. Taras and B. Haas, Nucl. Instrum. Methods **123**, 73(1975).

[Ter75] J. Meyer-Ter-Vehn, Nucl. Phys. A **249**, 141(1975).

[Tok75] H. Toki and A. Faessler, Nucl. Phys. A **253** 231(1975).

[Tok76] H. Toki and A. Faessler, Phys. Lett. B **63** 121(1976).

[Voi83] M.J.A. de Voigt, J. Dudek, and Z. Szymanski, Rev. Mod. Phys. **55**, 320(1983).

[Zam91] N.V. Zamfir and R. Casten, Phys. Let. B, **260**, 256(1991).

[Zig94] R.S. Zighelboim *et al.*, Phys. Rev. C, **50**, 2, 716(1994).

[Zob80] V. Zobel, L. Cleemann, J. Eberth, T. Heck, and W. Neumann, Nucl. Phys. A, **346**, 510(1980).

[Zob80b] V. Zobel, L. Cleemann, J. Eberth, H.P. Hellmeister, W. Neumann, N. Wiehl, Nucl. Instr. Meth., **171**, 223(1980).

[War00] D. Ward *et al.*, Phys. Rev. C, **63**, 014301(2000).

[Wei94] D. Weil, R. Wirowski, E. Ott, A. Dewald and P. von Brentano, Nucl. Phys. **A567**, 431(1994).

[Wio88a] M. Wiosna *et al.*, Phys. Lett. B, **200**, 255(1988).

[Wio88b] M. Wiosna, PhD thesis, Cologne, 1988.

[Wys01] R.A Wyss and W. Satula, Acta Phys. Pol. B **32**, 2457(2001).

[Yam67] T. Yamazaki, Nucl. Data Tables **A3**, 1(1967).